Negative Ion Photoelectron Spectroscopy: Testing the Limits of Normal Mode Analysis

by

K. M. Lemke

B.A., Smith College, 2006

A thesis submitted to the

Faculty of the Graduate School of the

University of Colorado in partial fulfillment

of the requirements for the degree of

Doctor of Philosophy

Department of Chemistry and Biochemistry

2012

This thesis entitled:
Negative Ion Photoelectron Spectroscopy: Testing the Limits of Normal Mode Analysis
written by K. M. Lemke
has been approved for the Department of Chemistry and Biochemistry

_____

W. Carl Lineberger

_____

Veronica M. Bierbaum

Date _____

The final copy of this thesis has been examined by the signatories, and we find that both the content and the form meet acceptable presentation standards of scholarly work in the above mentioned discipline.

Lemke, K. M. (Ph.D., Physical Chemistry)

Negative Ion Photoelectron Spectroscopy: Testing the Limits of Normal Mode Analysis

Thesis directed by Prof. W. Carl Lineberger

Negative ion photoelectron spectroscopy has been used to study the furanide anion ($C_4H_3O^-$), dihalomethyl anions (CHX_2^-, where X = Cl, Br, and I), the cyanopolyyne anions HC_4N^- and $HCCN^-$, propadienylidenide (H_2CCC^-), and propargylenide ($HCCCH^-$). Using this experimental technique in combination with calculations and Franck-Condon simulations, we learn about the electronic and vibrational structures of these molecules.

Furanide is an ideal anion to interrogate using photoelectron spectroscopy. The five-membered ring structure of furanide constrains it to a relatively small geometry change upon photodetachment. Thus, there is substantial Franck-Condon overlap between the wavefunctions of the ground vibrational state of the anion and of the ground vibrational state of the neutral. A prominent origin peak is observed in the photoelectron spectrum, from which we measure its electron affinity (EA). Our standard Franck-Condon analysis, which assumes uncoupled and harmonic normal modes, reproduces the observed photoelectron spectrum. The excellent agreement between simulation and experiment enables the identification of individual vibronic transitions that give rise to the peaks in the spectrum. With peak assignments, we measure the frequencies of several active vibrational modes.

In sharp contrast to the rigid furanide anion, the dihalomethyl anions undergo a large geometry change upon photodetachment. When an electron is removed, the pyramidal anion becomes nearly planar, exciting multiple large-amplitude vibrations. As a result of the large geometry change between the anion and the neutral, the best Franck-Condon overlap occurs with high vibrational levels of the neutral—where mode-coupling and anharmonicity become important. Our standard Franck-Condon analysis breaks down under these circumstances, and the origin peak is unobservable. Only by applying sophisticated theoretical methods can we interpret the structure

of the photoelectron spectra of the dihalomethyl anions.

The cyanopolyyne anions HC_4N^- and $HCCN^-$ are also challenging to investigate *via* photoelectron spectroscopy. The bent anions become quasilinear upon photodetachment to the $^3A''$ ground states of these neutral cyanopolyynes. However, unlike the spectra of the dihalomethyl anions, the origin peaks of HC_4N and $HCCN$ have observable intensity in their photoelectron spectra. The geometries of the $^1A'$ excited states are very similar to that of their respective anions, leading to short vibrational progressions and intense origin peaks of the excited states.

Propadienylidenide and propargylenide, both m/z 38, display very different photoelectron spectra. The rational synthesis made possible by the flowing-afterglow anion source allows us to selectively prepare the different isomers by choosing the appropriate precursor. Reacting O^- with allene produces primarily H_2CCC^-, which is a relatively rigid molecule that exhibits modest, resolved vibrational progressions with an intense origin peak. Reacting O^- with propyne yields a mixture of both H_2CCC^- and $HCCCH^-$; we subtract the spectrum of H_2CCC^- to obtain the spectrum of $HCCCH^-$. Unlike its isomer, $HCCCH^-$ undergoes a significant geometry change when an electron is detached, and the photoelectron spectrum of the ground state of propargylene is characterized by an extended vibrational progression. Again, because the best Franck-Condon overlap occurs with higher vibrational levels of the neutral, assignment of the origin peak is not straightforward, and our standard Franck-Condon simulations are of no help.

In this work, we investigate several floppy molecules using negative ion photoelectron spectroscopy. It is particularly challenging to elucidate the photoelectron spectra of these molecules because they test the limits of the normal mode analysis that is typically applied to these spectra. These species illustrate the difficulties involved in probing the electronic and vibrational structure of floppy molecules, as well as the theoretical methods that are required to understand their complex spectra.

Dedication

To sweet Adeline.

Acknowledgements

I would first like to thank my advisor, Carl, for his guidance, encouragement, and patience along my graduate school journey. Thank you for the opportunity to work in the PES lab and for your genuine care for the education and well-being of your students. I'd also like to thank the past and present Lineberger lab members. Thank you, Scott, for teaching me so much about the experiment. Thank you, Lenny, for your help in refurbishing the instrument. I'd like to thank Wilson, Elisa, Amanda, Yu-Ju, and Josh for always being willing to lend advice and a helping hand. I'm lucky to have been able to work with such a talented group of people who are also good friends.

Thanks to the Negative Ion Supergroup—Barney Ellison, Veronica Bierbaum, Mathias Weber, Chuck DePuy, and group members—for enlightening and motivating discussions. I am so thankful to have been able to work in a cooperative environment with such talented scientists.

I've also had the privilege of working with several collaborators and Visiting Fellows. I'd like to thank Kent Ervin, who wrote the PESCAL normal mode simulation program and who is always willing to give advice (both experimental and theoretical). Thanks to Anne McCoy and John Stanton for their theoretical assistance and collaboration on several projects. Thank you, David Osborn and Bob McMahon, for your helpful discussions and assistance, particularly on the propargylene and propadienylidene work.

I am grateful to have worked in JILA, where we have such excellent resources. The Instrument Shop is truly world class, and everyone is extremely knowledgeable and skilled. I'd especially like to thank Kim, Blaine, Hans, and Dave for their help in rebuilding the Wien Filter a couple years

ago. I'd also like to thank the Electronics Shop. James, Terry, and Chris have come to our rescue numerous times. Thanks to the guys in Computing, as well, for their assistance on numerous occasions.

I'd like to thank my friends for their academic help and for making the last several years so fun. Thanks to my parents, Rosanne and Curt, for your love and encouragement. You always made my education the priority, and I appreciate all that you sacrificed to make sure that I had the best instruction. Thank you, Adeline, for your help taking some of this data; you have been the best motivator. Thank you, Nathan, for your love and support.

Contents

Chapter

Tables

Table

Figures

Figure

Chapter 1

Introduction

1.1   Negative Ion Photoelectron Spectroscopy

Photoelectron spectroscopy is a powerful technique used to study the electronic and vibrational structure of atoms and molecules. In conventional photoelectron spectroscopy, a photon with fixed energy in excess of the binding energy of an electron is used to detach an electron from either a charged or neutral species. The kinetic energy of the outgoing electron is then measured. Conservation of energy dictates that since the energy of the photodetachment radiation and the kinetic energy of the detached electron are known, the energy with which the electron was bound can be deduced:

$$\mathrm{eBE} = h\nu - \mathrm{eKE} \tag{1.1}$$

where eBE is the electron binding energy, $h\nu$ is the photon energy, and eKE is the electron kinetic energy.

The probability that a molecule will absorb a photon and undergo a transition is determined by the transition moment of the molecule.[1] The electric and magnetic fields of a photon interact with the electric and magnetic fields present in the molecule, and the probability of photon absorption depends on the coupling between these fields. Specifically, the transition probability is $|\boldsymbol{M}|^2$, where $\boldsymbol{M}$ is the transition dipole moment for the transition from a lower energy level to a higher energy level. The transition dipole moment describes the instantaneous change in the dipole moment that results from the movement of electrical charge during the transition. In the electric dipole

moment approximation, for a molecule with wavefunctions Ψ'' and Ψ' of the lower and upper states, respectively, the transition moment is given by Eq. 1.2,

$$\boldsymbol{M} = \int \Psi' \mu \Psi'' \mathrm{d}\tau \tag{1.2}$$

where $\mathrm{d}\tau$ includes all spatial and spin coordinates, and μ is the electric dipole moment operator. For a system of n number of particles with charges Q_n at positions $\mathbf{x}_n$, the electric dipole moment operator is given by Eq. 1.3.

$$\mu = \sum Q_n \mathbf{x}_n \tag{1.3}$$

We will later find it useful to separate the summation into terms involving the electrons and those involving the nuclei: $\mu = \mu_e + \mu_n$.

If the transition dipole moment is zero, the probability of the transition is zero, and the transition is forbidden in the electric dipole moment approximation. Using the symmetries of the wavefunctions of the upper and lower states, we establish selection rules that govern electronic, vibrational, and rotational transitions. One of the advantages of photoelectron spectroscopy is that its unique selection rules enable us to investigate electronic states that are inaccessible using other spectroscopic methods.

The Born-Oppenheimer approximation allows us to factor the total wavefunction of the molecule. The Born-Oppenheimer approximation states that because the nuclei are orders of magnitude more massive than electrons, electrons can rearrange on a much faster time-scale than the nuclei. As a result, electrons are able to relax to the ground-state configuration at each nuclear configuration. Thus, we can separate the electronic, vibrational, and rotational parts of the wavefunction of a molecule with $\boldsymbol{r}$ electronic and $\boldsymbol{R}$ nuclear coordinates as follows (Eq. 1.4):

$$\Psi(\boldsymbol{r}, \boldsymbol{R}) = \psi_{\mathrm{e}}(\boldsymbol{r}, \boldsymbol{R}_{\mathrm{e}}) \, \psi_{\mathrm{v}}(\boldsymbol{R}) \, \psi_{\mathrm{r}}(\boldsymbol{R}) \tag{1.4}$$

This expression assumes that during a vibration, the electronic wavefunction ψ_e can be approximated by the wavefunction at its equilibrium nuclear coordinates ($\boldsymbol{R}_{\mathrm{e}}$). Substituting Eq. 1.4 into

the transition dipole moment equation (Eq. 1.2),

$$M = \int \int \psi'_e(r, R_e) \, \psi'_v(R) \, (\mu_e + \mu_n) \, \psi''_e(r, R_e) \, \psi''_v(R) \, dr \, dR. \tag{1.5}$$

We can then separate the variables in Eq. 1.5 into the sum of terms involving μ_n and those involving μ_e. The portion involving μ_n is the product of two integrals, one of which is the integral of ψ'_e and ψ''_e; because the wavefunctions of different electronic states are orthogonal, this integral is zero. Thus, only the terms involving μ_e remain:

$$M = \int \psi'_e(r, R_e) \, \mu_e \, \psi''_e(r, R_e) \, dr \, \int \psi'_v(R) \, \psi''_v(R) \, dR. \tag{1.6}$$

These two integrals form the basis of the electronic and vibrational selection rules.

During an electronic transition, the total spin of the system must be conserved. Upon photodetachment, the ejected electron carries with it a spin of $\pm\frac{1}{2}\hbar$. Thus, the spin of the neutral daughter must also change by $\pm\frac{1}{2}\hbar$ relative to the parent anion; i.e., $\Delta S = \pm\frac{1}{2}$.[2] In this way, photoelectron spectroscopy offers an advantage over traditional absorption spectroscopy: electronic states with different spin multiplicities can be probed, and term energies can be measured directly.

Using Eq. 1.6, we determine vibrational selection rules. As previously stated, the intensity of a transition is proportional to the square of the transition dipole moment:

$$I \propto M^2 = \left[\int \psi''_v(R) \, \psi'_v(R) \, dR \right]^2 \left[\int \psi''_e(r, R_e) \, \mu_e \, \psi'_e(r, R_e) \, dr \right]^2. \tag{1.7}$$

According to the Condon approximation, for a given pair of electronic states the electronic transition strength, $\left[\int \psi''_e(r, R_e) \, \mu_e \, \psi'_e(r, R_e) \, dr \right]^2$, is the same for all vibrational transitions. This is a reasonable assumption because the electronic transition probability is a slowly varying function of the nuclear coordinates; most transitions arise from the ground vibrational state of the anion, limiting the range of vibrational overlap.[3] Thus, the relative intensities of vibrational transitions are proportional to the square of the overlap of the vibrational wavefunctions, called Franck-Condon factors (FCFs). In order to observe a vibrational transition, the product $\int \psi''_v(R) \, \psi'_v(R) \, dR$ must be totally symmetric. Therefore, any Δv is allowed for a totally symmetric vibration. For non-

totally symmetric modes, symmetry dictates that the FCF will be zero for $\Delta v = \pm 1, \pm 3, \pm 5,...$ but may be non-zero for $\Delta v = 0, \pm 2, \pm 4,....$

With an understanding of the theory and the selection rules governing photoelectron spectroscopy, we will next discuss the great utility of this technique for probing the electronic and vibrational structure of molecules and the geometry change that takes place upon photodetachment.

1.2   What We Learn from Photoelectron Spectra

The vibronic transitions observed in a photoelectron spectrum are governed by the aforementioned selection rules, and from the spectrum we obtain information about the final state formed upon photodetachment. Photoelectron spectroscopy of a neutral molecule yields information about its cation states, including the ionization energy of the molecule (Eq. 1.8), while negative ion photoelectron spectroscopy (NIPES) yields information about the neutral molecule (Eq. 1.9).[4]

$$M + h\nu \rightarrow M^+ + e^-(eKE) \tag{1.8}$$

$$M^- + h\nu \rightarrow M + e^-(eKE) \tag{1.9}$$
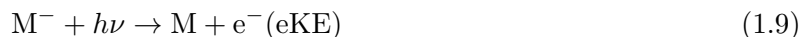
In the work presented in this thesis, NIPES is used to measure the electron affinity (EA) and other valuable spectroscopic quantities of neutral molecules.

NIPES of a simple diatomic AB is illustrated in Fig. 1.1. The potential energy curves of the ground electronic state of AB^- and the ground and excited electronic states of the neutral AB are shown. Energy is plotted as a function of the internuclear distance, R, and the resulting photoelectron spectrum is shown along the y-axis. We begin with the anion AB^-; in our experiment, described in detail in Chapter 2, the majority of anions are formed in the ground vibrational state ($v'' = 0$) of the ground electronic state. A photon imparts energy to the anion (green arrow). The photon energy is greater than the energy with which the excess electron is bound, so an electron is ejected. The neutral AB molecule is formed in various vibrational levels of the ground X and excited A electronic states. The electron carries away the energy in excess of its binding energy in the form

of kinetic energy. We measure the eKE of the ejected electron (blue arrows). Through Eq. 1.1, we know the energy with which the electron was bound, depicted as a red arrow corresponding to a quantized vibrational level of the neutral AB.

From the photoelectron spectrum, we learn about several important properties of the molecule. In the $X(AB) \leftarrow X(AB^-)$ photoelectron spectrum of Fig. 1.1, the peak corresponding to the transition between the ground vibrational state of the anion and the ground vibrational state of the ground electronic state of the neutral (the 0-0 transition) is known as the origin peak. The eBE of the origin peak corresponds to the adiabatic EA of AB. Peaks in the photoelectron spectrum correspond to vibrational levels of the neutral. Thus, from the peak spacing we can measure the harmonic frequency, ω_e (red arrows), of the AB stretch. Though most anions are generated in the ground vibrational state, there is some population—usually determined by the Boltzmann distribution (Eq. 1.10)—in vibrationally excited states of the anion:

$$\frac{N_2}{N_1} = \frac{g_2}{g_1} exp \left[-\frac{(E_2 - E_1)}{kT} \right] \tag{1.10}$$

where $\frac{N_2}{N_1}$ is the population ratio in states 1 and 2, g_1 and g_2 are the degeneracies of the two levels, and E_1 and E_2 are the energies of the levels. Photodetachment from a vibrationally excited anion to the ground vibrational state of the neutral is known as a hot band, and it appears lower in energy than the origin. The difference in energy between the origin and the hot band corresponds to the vibrational frequency of the anion.

We may also observe transitions to the excited A state of AB. The difference in energy between the origin peak of the X state and the origin peak of the A state of AB corresponds to the term energy, T_e. In the X state of AB, the equilibrium bond length is very similar to that of the anion; however, in the excited A state the bond length is significantly lengthened, and the potential energy curves are displaced with respect to each other along the x-axis (ΔR, purple arrows). The intensity of the peaks in a photoelectron spectrum is governed by the aforementioned FCFs, the square of the overlap between the ground vibrational wavefunction of the anion and the various vibrational levels of the neutral; this concept is discussed more thoroughly in the following

Figure 1.1: Schematic of negative ion photoelectron spectroscopy.
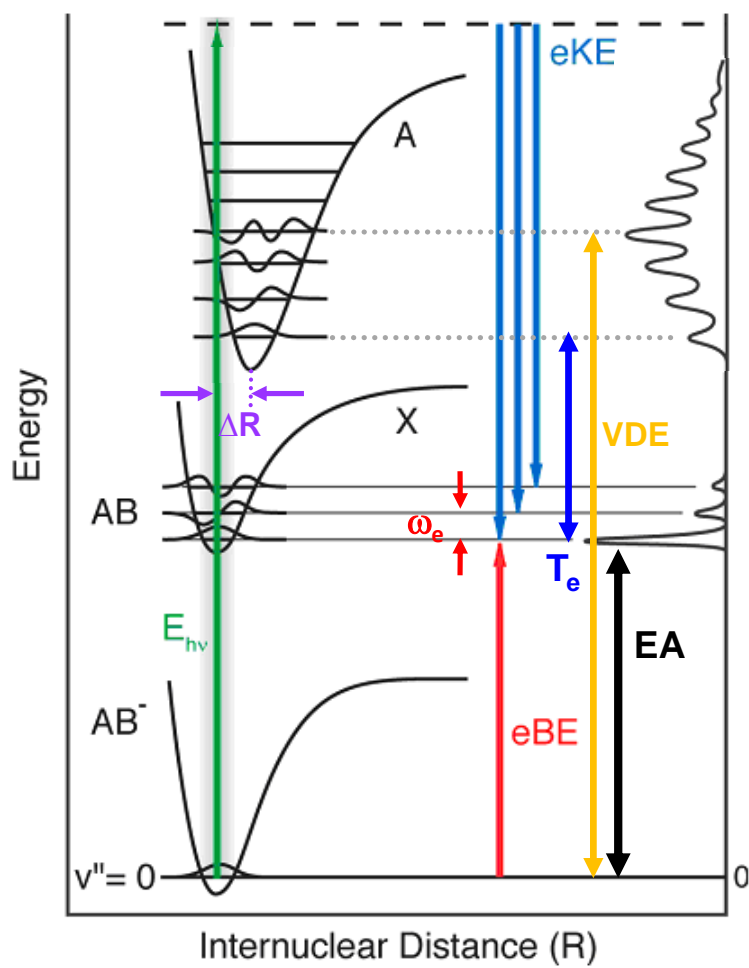
section (Section 1.3). Because the equilibrium bond lengths of the anion and the excited-state neutral are quite different, the best Franck-Condon overlap occurs with high vibrational levels of the neutral. The eBE of the most intense transition—termed the vertical detachment energy, or VDE (yellow arrow)—corresponds to the amount of energy required to remove an electron with no geometry change. Thus, the vibrational structure of the photoelectron spectrum lends insight into the geometry change, ΔR, that takes place upon photodetachment.

Additional information about the symmetry of the orbital from which photodetachment occurred can also be obtained from the photoelectron spectrum using eKE-dependent photoelectron angular distributions. The angular dependence of the photoelectron intensity is given by Eq. 1.11, which relates the observed intensity to the angle θ between the electric field vector of the light and the photoelectron collection axis:[5]

$$\frac{\mathrm{d}\sigma}{\mathrm{d}\Omega} = \frac{\sigma_0}{4\pi}(1 + \beta P_2(\cos\theta)) \tag{1.11}$$

where σ_0 is the total photodetachment cross section, β is the anisotropy parameter, and $P_2(\cos\theta)$ is the second Legendre polynomial. When $\theta = 54.7°$ (the so-called "magic angle"), the photoelectron intensity is independent of β and directly reflects the relative photodetachment cross section. The relative intensities at $\theta = 0°$ (I_0) and $\theta = 90°$ (I_{90}) are related by Eq. 1.12.

$$\beta = \frac{I_0 - I_{90}}{\frac{1}{2}I_0 + I_{90}} \tag{1.12}$$

For atoms, the photoelectron angular distribution directly reflects the angular momentum state of the orbital of the detached electron. Because the total angular momentum of the system must be conserved, upon photodetachment the angular quantum number l must change by ± 1. For example, an electron detached from a spherical s-orbital ($l = 0$) will detach as a p-wave ($l = 1$). In this case, the maximum peak intensity occurs when the electric field vector and the photoelectron collection axis are aligned ($\theta = 0°$), and $\beta = 2$. If, instead, an electron is removed from an atomic p-orbital, the photoelectron will depart as an s- ($l = 0$) or a d- ($l = 2$) wave. Close to threshold, the lower angular momentum state will dominate and yield an isotropic distribution with $\beta = 0$.

At higher energy, the anisotropy distribution will reflect the interference of the s- and d-waves, resulting in $\beta < 0$.[5,6]

Angular distributions of molecules are not as straightforward to interpret, but they are nonetheless valuable. Analogous to atomic photodetachment, the angular distribution of photo-electrons ejected from molecular anions reflects the symmetry of the molecular orbital from which it was removed.[7] Electrons removed from an s-like σ orbital can be expected to have $\beta \approx 2$. Furthermore, each electronic state has a characteristic β value; interference between the outgoing waves causes the β value to vary slightly with kinetic energy. Thus, relative β values of peaks in a photoelectron spectrum are very instructive: a sharp change in the β value indicates a different electronic state of the neutral.

1.3   Franck-Condon Analysis

In the approximation of separable electronic, vibrational, and rotational parts of the wave-function and a slowly varying electronic transition moment, transition probabilities are proportional to the square of the vibrational overlap integrals between the initial and final states (the FCFs).[8] The Franck-Condon integral is given by

$$C(v', v'') = \int \psi_{v'}(\mathbf{Q'}) \, \psi_{v''}(\mathbf{Q''}) \, \mathrm{d}\mathbf{Q'}, \tag{1.13}$$

where $\psi_{v'}(\mathbf{Q'})$ is the full, multidimensional vibrational wavefunction of the neutral (final state) in quantum state v' as a function of $\mathbf{Q'}$, the mass-weighted normal coordinates of the neutral. Likewise, $\psi_{v''}(\mathbf{Q''})$ is the full, multidimensional vibrational wavefunction of the anion (initial state) in quantum state v'' as a function of its mass-weighted normal coordinates, $\mathbf{Q''}$.[3]

It is very challenging to solve the Franck-Condon integral exactly, as the true wavefunctions of polyatomics are extremely complex and difficult or impossible to compute. In order to tackle this problem and evaluate the Franck-Condon integral for polyatomic molecules, we must make certain approximations and assumptions. In the next two sections, we will outline the standard normal mode analysis by which photoelectron spectra are simulated. Within this approximation, there are

two approaches to computing the FCFs that differ in their representation of the normal modes of vibration. First, we will discuss the approach most commonly taken for simulating photoelectron spectra, in which the normal modes are described as displacements in a Cartesian coordinate basis (Section 1.3.1). We will then review a second approach that better treats molecules undergoing a large geometry change upon photodetachment, in which a molecule's internal coordinates are used to define the normal mode displacements (Section 1.3.2). As we will see in the following chapters, molecules that undergo a large geometry change upon photodetachment (i.e., the equilibrium geometries of the anion and neutral are significantly different) test the applicability of these methods and the validity of their assumptions and approximations.

1.3.1   Normal Mode Analysis using Cartesian Coordinates

The normal mode analysis using orthogonal Cartesian displacement coordinates is easily implemented computationally for molecules of arbitrary size and connectivity, and therefore has become the conventional method.[9] In this method, we treat the vibrational modes of the molecule as harmonic normal modes of vibration. In doing so, we assume the following: each normal mode acts as a simple harmonic oscillator, the normal modes are independent and do not interact, the center of mass does not move during the vibration, and all atoms pass through their equilibrium positions at the same time.[10] Under the assumption that the normal modes in each electronic state are uncoupled, the wavefunctions can be expressed as the product of one-dimensional wavefunctions in each normal coordinate (Eq. 1.14).

$$\psi_{\mathrm{v}}(\mathbf{Q}) = \psi_{\mathrm{v}_1}(Q_1)\ \psi_{\mathrm{v}_2}(Q_2)\ \psi_{\mathrm{v}_3}(Q_3)... \tag{1.14}$$

In order to evaluate the Franck-Condon integral in Eq. 1.13, the wavefunctions must be expressed in terms of the same coordinates for both states. Thus, we perform a transformation that relates the normal coordinates of the neutral ($\mathbf{Q}'$) to those of the anion ($\mathbf{Q}''$):

$$\mathbf{Q}'' \ = \ \mathbf{J}''\mathbf{Q}' \ + \ \mathbf{K}''. \tag{1.15}$$

Equation 1.15 is the Duschinsky transformation. The $(3N-6)$-dimensional vector $\mathbf{K}''$ describes the difference in the nuclear equilibrium positions between the anion and neutral in terms of the normal coordinates of the anion. The $(3N-6) \times (3N-6)$ Duschinsky rotation matrix $\mathbf{J}''$ accounts for the mixing of normal modes that result from the discrepancy between the normal mode coordinates of the anion and neutral.[8,11]

A simple picture can help us understand these two parameters. Fig. 1.2 illustrates Duschinsky translation and rotation for two normal vibrations of a molecule.[11,12] The two orthogonal normal coordinates of the initial state ($\mathbf{Q}_1''$ and $\mathbf{Q}_2''$) are shown in black, and the corresponding normal coordinates of the final state ($\mathbf{Q}_1'$ and $\mathbf{Q}_2'$) are given in red. We can consider this as a picture of the potential energy surfaces of the states reduced from three dimensions to two (eliminating the energy axis). In the first case, shown in Fig. 1.2(a), the potential energy surface of the final state is distorted—as a consequence of different force constants in the initial and final states—and displaced—resulting from different equilibrium geometries in the two states. There is a one-to-one correspondence between the normal coordinates of the upper and lower states, and $\mathbf{Q}_1''$ and $\mathbf{Q}_2''$ are independent during the photodetachment process. The $\mathbf{K}''$ vector is necessary to describe the difference in geometry between the two states, while $\mathbf{J}'' = \mathbf{I}$, the identity matrix.

In Fig. 1.2(b) we find a more complicated case. Here, the normal coordinates of the final state are distorted, translated, and *rotated* by the angle α with respect to the initial state. The geometry of the upper state has changed such that the character of its normal modes is different from those of the lower state. The normal mode $\mathbf{Q}_1'$ is partially projected onto both $\mathbf{Q}_1''$ and $\mathbf{Q}_2''$; i.e., the normal modes are mixed. Therefore, we can think of the $\mathbf{K}''$-displacement vector as describing a translation of the upper state potential energy surface with respect to that of the lower state, while the $\mathbf{J}''$ matrix accounts for rotation of the neutral potential energy surface with respect to that of the anion.

We can express the normal mode vectors of a molecule with N atoms in terms of Cartesian coordinates ξ as

$$\mathbf{Q} = \mathbf{T}^{\dagger}\mathbf{m}^{1/2}(\xi - \xi_{eq}), \tag{1.16}$$

Figure 1.2: Illustration of Duschinsky (a) translation and (b) rotation.
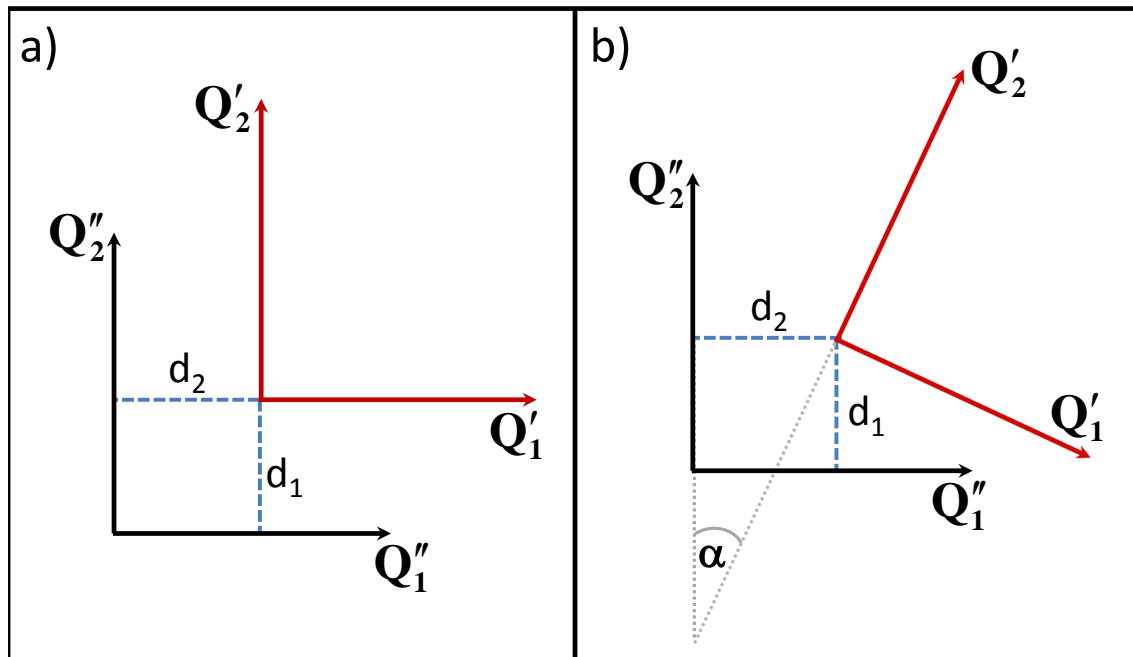
where $\mathbf{m}$ is the $(3N \times 3N)$ diagonal matrix of the atomic masses, $\mathbf{T}$ is the normal mode matrix (containing the vibrational eigenvectors of the appropriate mass-weighted Hessian), and ξ_{eq} is the equilibrium position vector.[8,13] Therefore,

$$\mathbf{J}''^{(x)} = \mathbf{T}''^\dagger \mathbf{m}^{-1} \mathbf{T}' \quad \text{and} \quad \mathbf{K}''^{(x)} = \mathbf{T}''^\dagger \mathbf{m}^{-1/2}(\xi'_{eq} - \xi''_{eq}) \tag{1.17}$$

Finally, a rotation matrix is applied to the normal mode matrix and the equilibrium position vector structured to ensure that the Duschinsky transformation (Eq. 1.15) does not introduce rotation or translation of the molecule, thereby satisfying the Eckart conditions.[14–19]

Treating the vibrations as independent, harmonic, normal modes expressed in Cartesian coordinates, we can compute the FCFs in a couple of ways. First, if we set $\mathbf{J}'' = \mathbf{I}$ we ignore Duschinsky rotation and invoke the parallel-mode approximation.[4] In this case, transitions involving combinations of vibrational modes are treated as the product of the FCFs of one-dimensional systems. Clearly, this approach most accurately simulates the spectra of molecules that undergo very little geometry change upon photodetachment and whose normal modes are essentially the same in both electronic states (e.g., Fig. 1.2(a)).

For systems in which the equilibrium geometries of the initial and final states are modestly different, the character of the normal modes in each state is likely to be different. In these cases, like the one illustrated in Fig. 1.2(b), Duschinsky rotation is an important consideration. To account for differences in the normal modes of the anion and neutral, the FCFs are calculated using the Chen algorithm[20] that is based on the generating function method developed by Sharp and Rosenstock[8] in the normal-mode approximation. The Fortran program PESCAL[21] is used to compute the FCFs of the photodetachment processes presented in this thesis.

Having computed the FCFs, we can now simulate the photoelectron spectrum. Relative intensities of the vibronic transitions for anions with vibrational temperature T'' are given by

$$\mathbf{I}(\nu'', \nu') = C\ v_e\ \text{FCF}(\nu'', \nu'; \mathbf{K}) \exp\left[\frac{-G_0''(\nu'')}{kT''}\right] \tag{1.18}$$

where C is a scaling factor, v_e is the electron velocity (or the final eKE), and $G_0''(\nu'')$ and $G_0'(\nu')$

are the initial and final vibrational energies, respectively, calculated according to the harmonic-oscillator model. The peak positions of the transitions are given by Eq. 1.19

$$\text{eKE}(\nu'', \nu') = h\nu - \text{EA} - G_0'(\nu') + G_0''(\nu'') \tag{1.19}$$

Using these equations, we can generate a stick spectrum in terms of eKE.[2]

The independent harmonic-oscillator model, in which the normal modes are described in terms of nuclear Cartesian displacements, is extremely useful: it can be applied to any molecule of arbitrary size or geometry, very accurately simulating electronic spectra that involve relatively small displacements of equilibrium geometries.[13,22–24] When a small geometry change takes place upon photodetachment, as in the $X(AB) \leftarrow X(AB^-)$ detachment shown in Fig. 1.1, the most prominent features in the photoelectron spectrum arise from overlap between the lowest vibrational levels of each state, where the vibrations are well described as decoupled harmonic oscillators. Furthermore, if the equilibrium geometries and bonding of the two states are very similar, the character of their normal modes is essentially the same, and the Duschinsky rotation may be minor.

Difficulties arise, however, when a molecule undergoes a large geometry change upon photodetachment, as in the $A(AB) \leftarrow X(AB^-)$ detachment shown in Fig. 1.1. In this case, the best Franck-Condon overlap occurs with high vibrational levels of the neutral, where anharmonicity and coupling between vibrational modes can become important factors. Molecules with very different geometries will have qualitatively different normal modes, and the Duschinsky rotation will be significant. The use of rectilinear Cartesian coordinates to represent the normal modes can lead to the additional problem of mode mixing.[10,13,19,25,26] Mode mixing occurs when a large geometry displacement in one coordinate is partially projected onto the others, resulting in a spurious displacement in another mode. This results in the appearance of non-physical vibrational progressions in the simulation that are not experimentally observed. We can avoid mode mixing by instead defining the normal modes of a molecule in terms of curvilinear internal coordinates (its bond lengths and angles), discussed in the following section.

1.3.2 Normal Mode Analysis using Internal Coordinates

Alternatively, we can express the normal modes in terms of internal coordinates, using changes to a molecule's bond lengths and angles to define the geometry difference between the anion and neutral. This method essentially eliminates mode mixing and artificial nuclear displacements that are introduced when a large geometry change is represented in a Cartesian coordinate basis. The use of curvilinear internal coordinates in normal mode analysis has been shown to yield more accurate Franck-Condon simulations of systems with large geometry changes.[13,19,24] Though internal coordinates more naturally represent the vibrational potential energy surfaces, this treatment[10,27] is not commonly used because it requires calculations specific to each system and therefore cannot be generally applied.

To compute the Franck-Condon integrals in the harmonic approximation, one must obtain the vibrational frequencies of the normal modes of the initial and final states (from electronic structure calculations), along with the $\mathbf{J}''$ matrix and $\mathbf{K}''$ vector expressed in terms of a set of the $3N$ - 6 nonredundant internal coordinates $\mathbf{s}$ of a molecule with N atoms. To compute the $\mathbf{J}''^{(s)}$ matrix and $\mathbf{K}''^{(s)}$ vector in internal coordinates, we first define the following:

$$\mathbf{Q} = \mathbf{L}^{-1}(\mathbf{s} - \mathbf{s}_{eq}), \tag{1.20}$$

where $\mathbf{Q}$ is the normal mode vector, $\mathbf{s}_{eq}$ is the vector of the equilibrium internal coordinates, and $\mathbf{L}$ is the matrix whose columns contain the eigenvectors for the normal coordinates in terms of the internal coordinates. If the same set of internal coordinates $\mathbf{s}$ is used for the initial and final states,

$$\mathbf{J}''^{(s)} = (\mathbf{L}'')^{-1}\mathbf{L}' \quad \text{and} \quad \mathbf{K}''^{(s)} = (\mathbf{L}'')^{-1}(\mathbf{s}'_{eq} - \mathbf{s}''_{eq}). \tag{1.21}$$

Most electronic structure calculations generate vibrational normal mode vectors in Cartesian coordinates. The matrix $\mathbf{L}$ can be found by expanding the internal coordinates in a power series of Cartesian coordinates about the equilibrium position and truncating the expansion at the first order:[10]

$$\mathbf{s} = \mathbf{s}_{eq} + \mathbf{B}(\xi - \xi_{eq}) \tag{1.22}$$

where $\mathbf{B}$ is the first derivative matrix, known as the Wilson matrix, and ξ_{eq} is the equilibrium position vector.[28]

Using the inverse transformation,

$$\xi = \xi_{eq} + \mathbf{G}^{-1}\mathbf{B}^{\dagger}\mathbf{m}^{1/2}(\mathbf{s} - \mathbf{s}_{eq}) \tag{1.23}$$

with

$$\mathbf{G} = \mathbf{B}^{\dagger}\mathbf{m}^{-1/2}\mathbf{B} \tag{1.24}$$

where $\mathbf{m}$ is the diagonal matrix of the atomic masses. Using Eqs. 1.16 and 1.21, we arrive at the following expressions for the $\mathbf{J}''^{(s)}$ matrix and $\mathbf{K}''^{(s)}$ vector in internal coordinates:[13,19]

$$\mathbf{J}''^{(s)} = \mathbf{T}''^{\dagger}\mathbf{m}^{-1/2}\mathbf{B}''(\mathbf{G}'')^{-1}\mathbf{B}'\mathbf{m}^{-1/2}\mathbf{T}' \tag{1.25}$$

and

$$\mathbf{K}''^{(s)} = \mathbf{T}''^{\dagger}\mathbf{m}^{-1/2}\mathbf{B}''(\mathbf{G}'')^{-1}(\mathbf{s}''_{eq} - \mathbf{s}'_{eq}), \tag{1.26}$$

where, again, $\mathbf{T}$ is the normal mode matrix in Cartesian coordinates. With the $\mathbf{J}''^{(s)}$ matrix and $\mathbf{K}''^{(s)}$ vector and the harmonic normal mode frequencies obtained from electronic structure calculations, the Franck-Condon integrals can be computed using recurrence relations.[29,30] The Fortran program PESCAL[21] is used to compute the FCFs for the photoelectron spectra presented in this thesis.

Although this method addresses the issue of mode mixing—an artifact of using Cartesian coordinates to represent the geometry change—it does not treat the very real problem of vibrational mode coupling within one electronic state. To treat the mode coupling that can arise when multiple vibrational modes of similar frequencies are active, we must take a more sophisticated approach. For example, in Chapter 4 we show that a multidimensional anharmonic coupled-mode approach is required to interpret the photoelectron spectra of the dihalomethyl anions.[24] Such methods are significantly more computationally expensive and are, like normal mode analysis using internal coordinates, specific to each molecule studied.

1.4   Dissertation Preview

This dissertation is organized into several chapters describing the experimental apparatus, theoretical methods employed for the analysis of the data, and the results of investigations of several different molecular systems. First, the experimental apparatus used to collect the data presented in subsequent chapters is described in detail in Chapter 2. Various theoretical approaches were taken to interpret the photoelectron spectra, and these methods are also discussed in Chapter 2.

With an understanding of the methods used to collect and interpret our data, we proceed with the results of investigations of several molecular systems. In Chapter 3, furanide ($C_4H_3O^-$) provides a nice example of the information one can obtain from the photoelectron spectrum of a well-behaved molecule that does not undergo a significant geometry change upon photodetachment. Because the gas-phase acidity of furan is known,[31,32] we employ a well-established thermochemical cycle[33] to determine the C-H bond energy of furan. The decomposition mechanisms of furan are of particular interest to the biomass community, and knowledge of its C-H bond dissociation energy validates the current decomposition models.

The photoelectron spectra of the dihalomethyl anions CHX_2^-, where X = Cl, Br, and I, are presented in Chapter 4. Upon photodetachment, the pyramidal anions become nearly planar. This large geometry change effects activity of multiple large-amplitude vibrations. These vibrations couple, and the standard normal-mode, uncoupled, harmonic oscillator approximations no longer apply to the spectra of these challenging molecules. Various methods for calculating the spectra of these molecules are examined, and the difficulties associated with analyzing the photoelectron spectra of such molecules is discussed.

The photoelectron spectra of the cyanopolyyne anions HC_4N^- and $HCCN^-$ are shown in Chapter 5. In both cases, a large geometry change occurs upon photodetachment from the bent anion to the quasilinear $^3A''$ ground state, resulting in an extended vibrational progression. Unlike the dihalomethyl anions, however, the origin peaks of these molecules have observable intensity, enabling measurement of their EAs. There is little geometry change between the bent anion and

the bent $^1A'$ excited state, and its origin is very prominent. We measure the singlet-triplet splitting of these molecules, as well as the frequency of the CN stretch, which displays unexpected condition-dependent behavior.

We take a brief interlude from the floppy molecules to examine the photoelectron spectrum of propadienylidenide (H_2CCC^-) in Chapter 6. Because the excess electron is localized primarily on the terminal carbon of this chain, only modest geometry changes occur upon photodetachment. The photoelectron spectrum of the $^1A_1$ ground state is straightforward to analyze. This work was done in collaboration with Velocity-map Imaging (JILA) and Slow Electron Velocity-map Imaging (Berkeley) experiments, enabling the observation of several higher-lying excited states. Significant vibronic coupling in the excited states leads to complex spectra of the higher-lying states of this astrophysically-relevant molecule.

We conclude with the spectrum of propargylene anion ($HCCCH^-$) in Chapter 7. As another floppy molecule, the photoelectron spectrum of $HCCCH^-$ is difficult to model, and assignment of the origin is difficult. A large change in the $\angle CCH$ upon photodetachment leads to significant activity of the "W" bending mode, resulting in an extended vibrational progression in the ^3B ground state. By comparing the photoelectron spectra of $HCCCH^-$ and $DCCCD^-$, we assign the origin peak and measure the EA. We observe three distinct electronic states in the NIPES spectra; using calculations of the orbitals involved in photodetachment, along with our chemical intuition, we assign the vibrational progressions to the $\tilde{X}^3B$, $\tilde{a}^1A$, and $\tilde{b}^1B$ states of HCCCH. Velocity-map Imaging of $HCCCH^-$ reveals additional vibronic structure at higher binding energies, but a conclusive assignment of these features is not made.

Chapter 2

Methodology

2.1   Experimental Methods

2.1.1   Introduction

The negative-ion photoelectron spectrometer consists of four main parts: a negative-ion source, elements for focusing and mass selecting ions, an ultraviolet (UV) laser, and an electrostatic energy analyzer. A schematic overview of the photoelectron spectrometer is given in Fig. 2.1. Anions are born and thermalized in a flowing afterglow ion source, accelerated and focused into a Wien velocity filter for mass selection, and then decelerated into the interaction region, where they meet the output of an Ar-ion laser operating in the near-UV. Electrons are detached from the anions; those that exit orthogonal to both the anion and laser beams are focused into a hemispherical energy analyzer, where they are separated on the basis of their electron kinetic energies (eKEs). In this way, a photoelectron spectrum is collected as a function of eKE.

2.1.2   Flowing Afterglow Ion Source

A flowing afterglow microwave discharge source was used to generate the negative ions studied in this thesis. The flowing afterglow is very versatile; it can be used in conjunction with various ion sources, including electron impact ionization, metal cathode discharge, and microwave discharge. In contrast to other gas discharge sources, we can selectively prepare the desired ion by carrying out rational ion-molecule syntheses.[34] Furthermore, the microwave discharge source provides a

Figure 2.1: Schematic of photoelectron spectrometer.
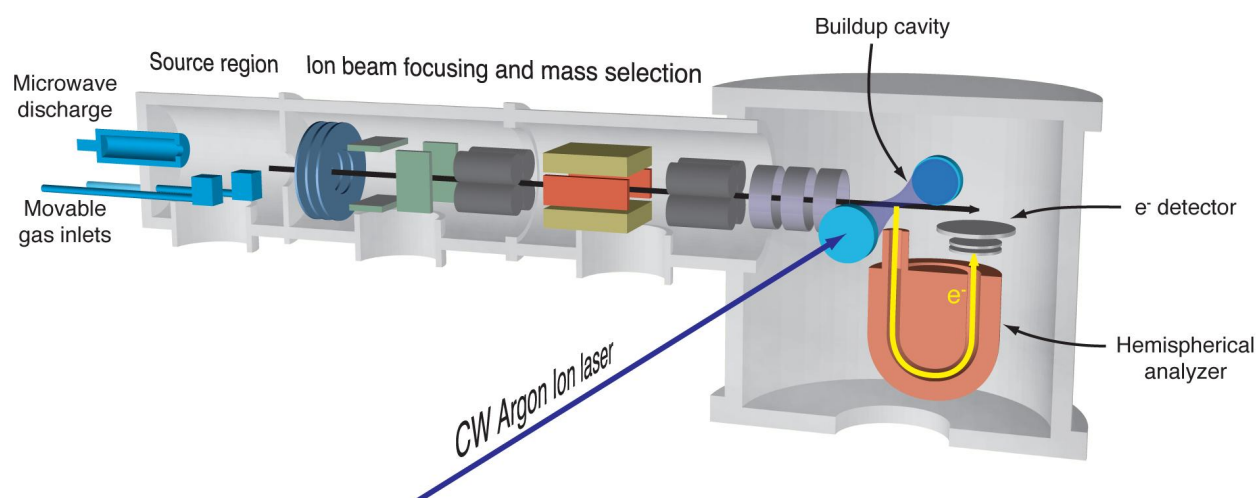
continuous source of thermalized (approximately 300 K) negative ions. This suppresses hot bands, reducing congestion in the photoelectron spectrum and facilitating peak assignment.

The microwave discharge source consists of a brass microwave cavity with a quartz cylinder, depicted in Fig. 2.2. Helium buffer gas is purified using a molecular sieve trap cooled with liquid N_2; purified He flows through the cylinder at a rate of approximately $7 - 10$ std. L sec^{-1}, controlled by a Tylan flow controller. The flow is maintained by a 330 L sec^{-1} Stokes Roots blower such that the pressure in the source region is approximately 0.5 Torr. A trace amount of O_2 is also added at a rate of approximately $5 - 10$ std. cm^3 min.$^{-1}$

Figure 2.2: Microwave discharge flowing afterglow ion source.
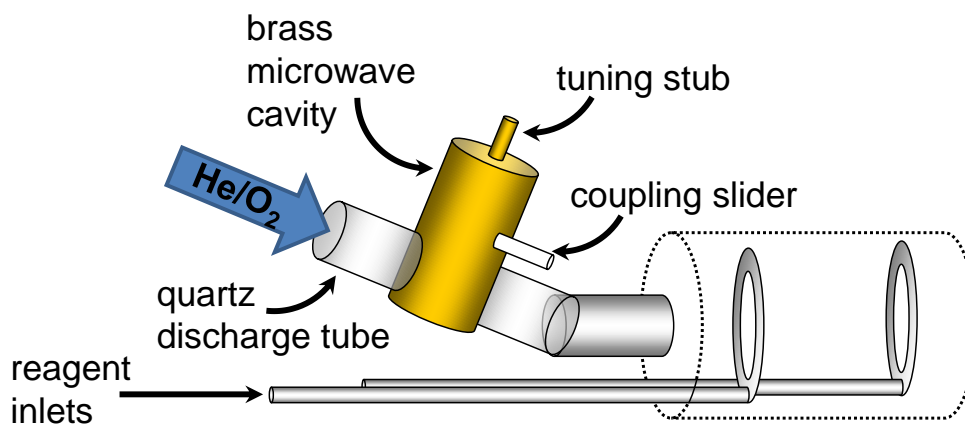
To light the discharge, approximately 70 W of forward power from the Opthos MPG 4 Microwave Power Generator is supplied to the discharge cavity, and an energized Tesla coil makes contact with the quartz tube. Power from the 2.45-GHz microwave discharge is transferred to the gas in the quartz tube. A plasma containing metastable He atoms, He ions, and free electrons is produced. Once the stable plasma has been formed, the forward power is reduced to approximately 10 W. The resonant microwave discharge cavity increases the electric field in the gas; the tuning stub (see Fig. 2.2) is used to fine-tune the resonant frequency of the cavity, while the coupling slider is adjusted to match the impedance of the cavity to that of the coaxial cable of the microwave power supply to minimize the reflected power.[35] The reflected power should be nearly zero during

operation so as to protect the magnetron in the microwave power supply.

The ion-molecule reactions used to prepare the anions presented here employ O^-. O^- is generated in the flowing afterglow *via* dissociative electron attachment (Eq. 2.1), in which a low energy electron formed in the plasma attaches to O_2, causing it to dissociate into O^- and neutral O.[36]

$$O_2 + e^- \rightarrow (O_2^*)^- \rightarrow O^- + O. \tag{2.1}$$
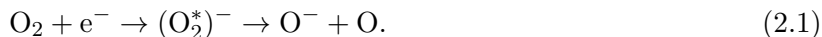
O^- has been shown to react efficiently and often with good specificity with neutral hydrogen-containing species[36] to abstract H^+ or H_2^+. Neutral reagents are added downstream of O^- formation through the movable ring inlets shown in Fig. 2.2, and the following reactions take place:

$$O^- + RH_2 \rightarrow R^- + H_2O \tag{2.2}$$

$$O^- + RH_2 \rightarrow RH^- + OH \tag{2.3}$$

$$O^- + RH_2 \rightarrow RH + OH^- \tag{2.4}$$

$$O^- + RH_2 \rightarrow RHO^- + H \tag{2.5}$$

If removal of only one proton is desired, O^- is first reacted with methane (CH_4) to produce hydroxide (OH^-) through a hydrogen transfer reaction:

$$O^- + CH_4 \rightarrow OH^- + CH_3. \tag{2.6}$$
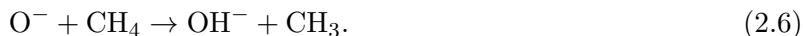
The appropriate neutral precursor is added and undergoes the following H^+ abstraction:

$$OH^- + RH_2 \rightarrow H_2O + RH^-. \tag{2.7}$$

Flow rates of He, O_2, and neutral precursors are optimized, and the positions of the movable ring inlets are adjusted to maximize the ion current of the desired anion.

Anions undergo $10^4 - 10^5$ collisions with the He buffer gas and are thermalized to room temperature.[2] The ions can be further cooled to approximately 150 K by flowing liquid N_2 through a jacket surrounding the flow tube.

2.1.3   Ion Focusing and Mass Selection

An overview of the photoelectron spectrometer is shown in Fig. 2.3. Ions are extracted from the ion source region through a molybdenum nosecone with an aperture approximately 1 mm in diameter. The voltage applied to the nosecone $(0 - 2$ V$)$ is adjusted for maximum ion current. A 2000 L sec^{-1} 6-inch diffusion pump maintains a pressure of approximately 10^{-4} Torr in what is referred to as the afterglow lensing region. The purpose of the afterglow lenses, L1 – L6, is to steer, focus, and accelerate the ion beam. Lenses 1 - 4 are independently adjusted daily to maximize ion current, while L5 and L6 are fixed at 400 V and 735 V, respectively. The first deflector, D1, has independent vertical and horizontal deflectors; it is referenced to the L3 voltage. The second deflector (D2) is referenced to the voltage applied to L4, and it also has independent deflectors in both the horizontal and vertical directions. The final deflector in the afterglow lensing region is D3. This lens controls the horizontal deflection only, steering anions through the 10° bend. The purpose of the 10° bend is to separate the anions from neutrals, as the undesired neutrals and photons generated in the flowing afterglow will not be steered by D3 and will instead hit the chamber walls and be pumped away.

After the 10° bend, the ions enter the first of four triple quadrupoles (Q1). Unlike quadrupoles that are used for mass selection, the triple quadrupole einzel lenses in this apparatus act to steer and focus the anions.[37] Each triple quadrupole consists of three quadrupole elements, with a total of 12 poles, as illustrated in Fig. 2.4. The poles are supplied with six separate voltages: outer horizontal (OH), outer vertical (OV), center up (CU), center down (CD), center left (CL), and center right (CR). The center elements primarily steer the ion beam, while the outer elements focus the ions.

After Q1, the focused ions pass through aperture A2, which has a diameter of approximately 1.5 mm. A Keithley 600A electrometer is used to measure the ion current on the A2 plate. Ions can be directed onto the plate or through the aperture using Q1, thereby enabling the user to maximize the total ion current arriving at A2 and to focus the ions through the aperture. Typically, 10 nA of total ion current reaches A2, and at least 75% exits the skimmer. An 8-inch, 3000 L s^{-1} diffusion

Figure 2.3: Detailed overview of the negative-ion photoelectron spectrometer.

Faraday cup

laser beam

interaction spot

DL 1 − 4

D5

Q4

A3

Q3

electro-magnet

Wien filter

Q2

D4

A2

D3

Q1

L4 − 6

D2

D1

L1 − 3

nose-cone

liquid N$_2$ jacket

flowing afterglow
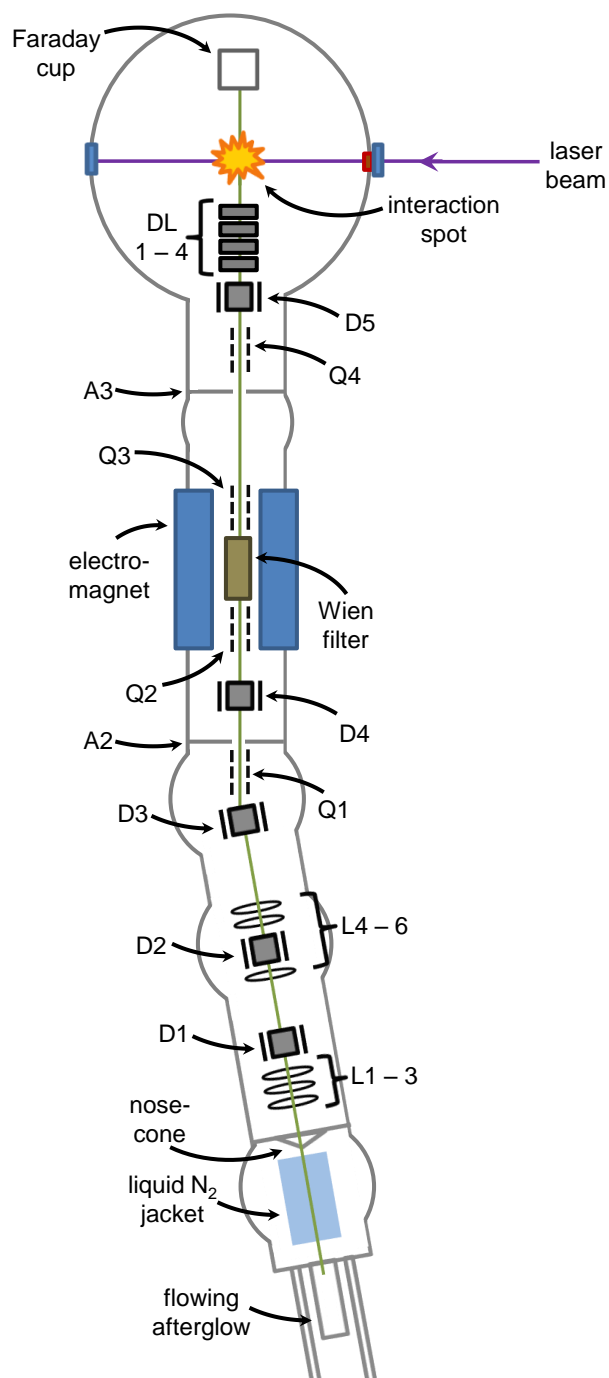
Figure 2.4: Diagram of a triple quadrupole lens. Six separate voltages are supplied to the 12 poles of the triple quadrupole einzel lens: outer vertical (OV), outer horizontal (OH), center up (CU), center down (CD), center left (CL) and center right (CR). The center elements primarily steer the ions, while the outer elements focus the beam.
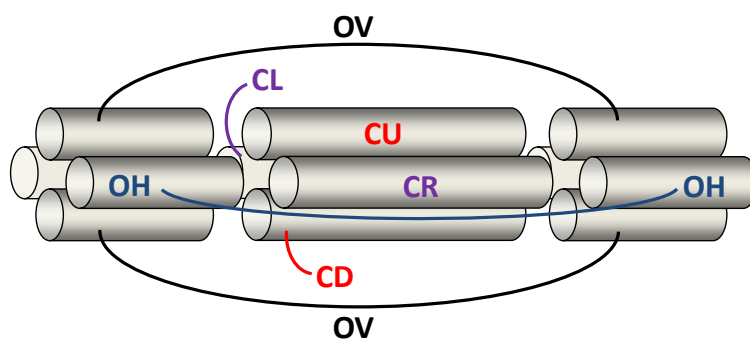
pump maintains a pressure of 10^{-6} Torr in this region.

After A2, the ions travel through a fourth deflector, D4, and into the Wien filter assembly. The Wien filter assembly comprises the Wien velocity filter and two triple quadrupoles (Q2 and Q3), sandwiching the Wien filter. The entire Wien filter assembly was rebuilt in 2010.[38] A photo showing the new Wien filter assembly is provided in Fig. 2.5. Q1 and Q2 were refurbished and the Wien filter was rebuilt using a completely new design. Additionally, electrically isolated faceplates, each with a 5 mm aperture, were added at the entrance and exit of the Wien filter to give the operator additional places to measure ion current. The Q1 and Q2 elements function as a pair to tightly focus the ion beam into the Wien filter; specifically, Q1 focuses more tightly in the horizontal direction, while Q2 focuses more tightly in the vertical direction.

Figure 2.5: A photo of the rebuilt Wien filter assembly. The ions first enter (a) Q2, where they are focused into (b) the Wien filter. Plates are mounted at the entrance and exit of the Wien filter on which ion current can be measured. Ions then enter (c) Q3.
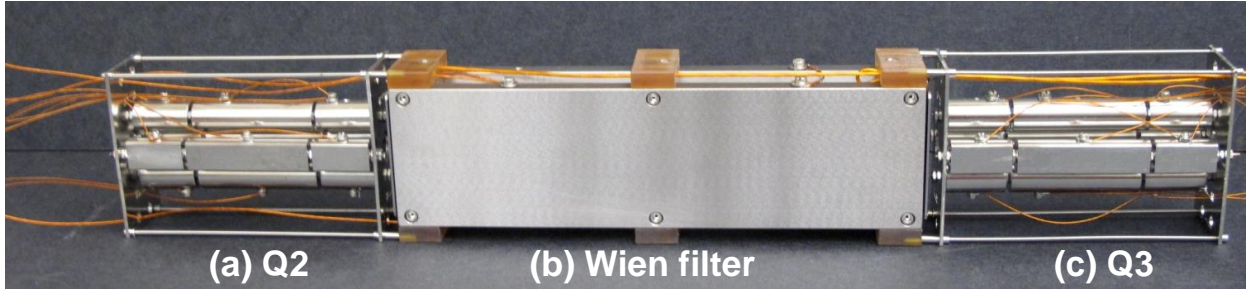
The Wien filter utilizes perpendicular electric and magnetic fields to separate ions on the basis of their mass-to-charge ratio (m/z). The force $\vec{F}$ felt on a particle with charge q in an electric field $\vec{E}$ is

$$\vec{F_E} = q\vec{E}. \tag{2.8}$$

The force on a charged particle in a magnetic field $\vec{B}$ is given by Eq. 2.9:

$$\vec{F_B} = q\vec{v} \times \vec{B} \tag{2.9}$$

where $\vec{v}$ is the velocity of the charged particle. Thus, anions travelling through the Wien filter will feel forces in opposite directions from the perpendicular electric and magnetic fields. If these forces

are equal, an ion will pass through the filter undeflected. All ions have the same charge q and therefore feel the same $\vec{F_E}$. They also have the same kinetic energy (KE); because KE = 735 eV $= \frac{1}{2}mv^2$, the force from the magnetic field is different for ions of different mass. In this way, the Wien filter separates ions on the basis of their m/z ratio.

In the newly rebuilt Wien filter, shown in Fig. 2.6, the electric field is supplied by two electrodes (+50 V and -50 V relative to the float voltage of 735 V) separated by silicon-coated glass so that the electrodes will mimic infinite plates.[38] Voltage to the electrodes is provided by a voltage divider with a 0 – 40 mA, 0 – 500 V power supply. The magnetic field is supplied by a water-cooled electromagnet external to the Wien filter assembly with a Kepco DC voltage supply (0 – 10 A, 0 – 60 V). To select ions of the desired mass, the magnetic field is varied while the electric field is held constant. The $m/\Delta m$ mass resolution of the new Wien filter is routinely 60. This is a significant improvement over the previous Wien filter ($m/\Delta m \sim 40$). The resolution can be further improved by increasing $\vec{E}$.

Figure 2.6: A cartoon of the rebuilt Wien filter. Panel (a) shows the side view; the electrodes are located at the top and bottom of the Wien filter, and silicon-coated glass plates are located on either side of the filter. Ions of different masses travelling through the Wien filter are dispersed, and only those for which the forces from the $\vec{E}$ and $\vec{B}$ fields balance pass through undeflected. Panel (b) shows a cross-sectional view of the Wien filter. Purple arrows indicate the electric field lines.

(a) Wien filter: side view

(b) Wien filter: cross-section
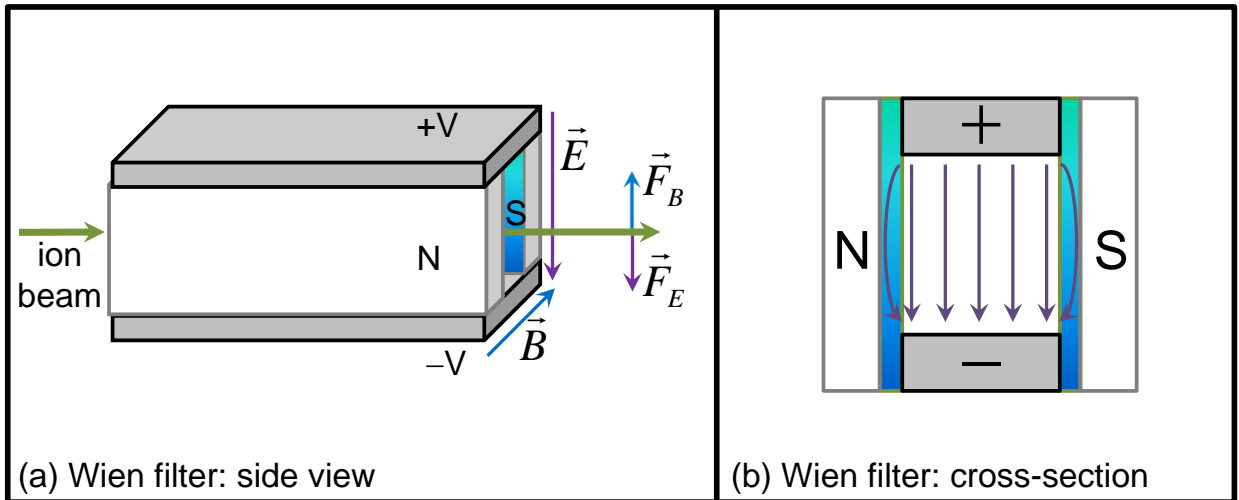
After exiting Q3 of the Wien filter assembly, the ions pass through a short field-free region before reaching the A3 aperture. The on-axis A3 aperture selects the ions of the desired m/z ratio from the spatially dispersed ion beam; therefore, the size of the A3 opening affects the mass resolution of the Wien filter. A3, shown in Fig. 2.7, was recently rebuilt and now consists of a series of three electrically isolated plates with apertures of decreasing diameter: 10 mm, 6 mm, and 2 mm. While monitoring the ion current on each plate, the lenses and quadrupoles can be adjusted to focus the ion beam through A3. Typically, a total of 3 nA is measured on the A3 assembly.

After A3, the mass-selected ion beam enters the fourth quadrupole (Q4) and another set of horizontal and vertical deflectors (D5). These elements focus and steer the ions into the deceleration stack. This set of four deceleration lenses (DL1 – 4) decelerates and focuses the ions to 35 eV in order to reduce the effects of Doppler broadening and increase the residence time of the ions in the interaction region.[34] DL1 is held at the beam velocity of 735 eV, and DL4 is kept at 35 eV. DL2 and DL3 are adjusted to optimize ion current and spectral resolution.

A Faraday cup, on which ion current is measured, is situated beyond the interaction region. Ion currents as low as 1 pA to upwards of 1 nA are measured using a Kiethley 602 Electrometer. Two Varian turbomolecular pumps—a 6-inch, 250 L sec^{-1} pump and an 8-inch, 280 L sec^{-1} pump— backed by a Varian SH-110 scroll pump maintains a pressure of 10^{-9} Torr in the interaction region.

2.1.4   Ar-ion Laser System

The ion beam next enters the interaction region, where it meets a fixed-frequency, 363.8-nm or 351.1-nm laser beam. Because photodetachment cross sections are small ($< 10^{-18}$ cm^2), laser power in excess of 10 W is necessary to observe sufficient photoelectron signal.[2] In order to achieve the high power required from a continuous-wave UV source, an external buildup cavity[39,40] is used in conjunction with an Ar-ion laser.[2,41] At resonance, the circulating power in the buildup cavity is at least a hundred times that of the incoming laser beam. The external buildup cavity is fundamentally a Fabry-Perot interferometer locked to its resonant frequency. A servoamplifier system actively adjusts the lengths of the buildup and laser cavities using piezoelectric translators

Figure 2.7: Photos of the rebuilt A3 assembly. A3 consists of three separate plates with diameters of decreasing size: 10 mm, 6 mm, and 2 mm. Ion current can be measured on each plate separately. The inset shows the head-on view of A3, as seen by the ions.
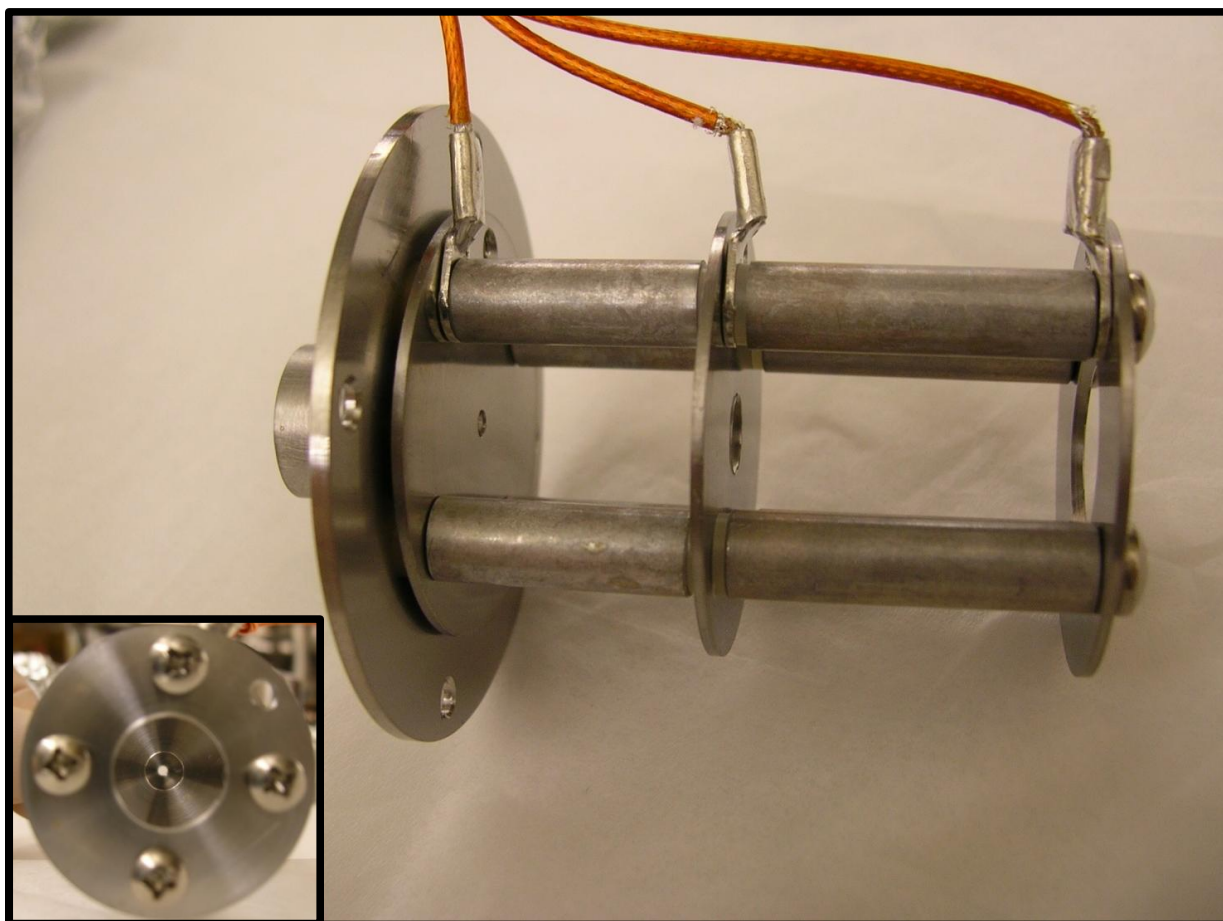
to maintain resonance. The optical setup is depicted in Fig. 2.8.

The Ar-ion laser (Spectra Physics 2085-25) emits at several frequencies in the UV, visible, and infrared. We choose to use either the 363.8 nm (3.40814 eV) line or the 351.1 nm (3.53119 eV) line in order to extend the observable spectral range. The desired line is chosen by the wavelength-specific output coupler. It is necessary to select a single longitudinal mode to amplify in the external buildup cavity, and this is accomplished with an automated, temperature-controlled etalon (Spectra-Physics Model 587 Z-Lok Etalon and 5870 Controller). A Coherent 300 MHz FSR spectrum analyzer is used to ensure that the laser output is single-mode. The high reflector at the rear of the laser is mounted on a piezoelectric translator, controlled by the servoamplifier system, that can adjust the length of the laser cavity to compensate for noise up to approximately 5 kHz.

As shown in Fig. 2.8, the $1 - 2$ W laser beam is steered and coupled into the buildup cavity. The laser beam radius and wave-front curvature are adjusted using the telescope and mirrors to efficiently couple the beam into the buildup cavity. Light transmitted through the buildup cavity is monitored on a photodiode (PD1) to achieve the best match of spatial parameters. A half-wave plate is located before the entrance to the buildup cavity. The laser light is approximately vertically polarized exiting the laser, and it is rotated by the periscope to become nearly horizontal. The half-wave plate enables collection of photoelectron spectra at any polarization, from which we can measure the anisotropy of the photoelectrons (see Section 1.2).

The buildup cavity mirrors are mounted to the vacuum chamber using bellows and kinematic mounts; the input mirror is 99.6% reflective, and the output mirror is 99.8% reflective at 351 nm. Like the high reflector on the laser cavity, the input mirror of the buildup cavity is mounted on a piezoelectric translator and controlled by the servoamplifier system. This piezoelectric translator corrects for thermal drift and noise up to 100 Hz.[2] It also maintains the resonant frequency of the buildup cavity within the free spectral range (FSR) of the laser:

$$\text{FSR} = \frac{c}{2l} \tag{2.10}$$

where c is the speed of light, and l is the length of the cavity. For the Ar-ion laser used in these

Figure 2.8: Diagram of the optical setup.
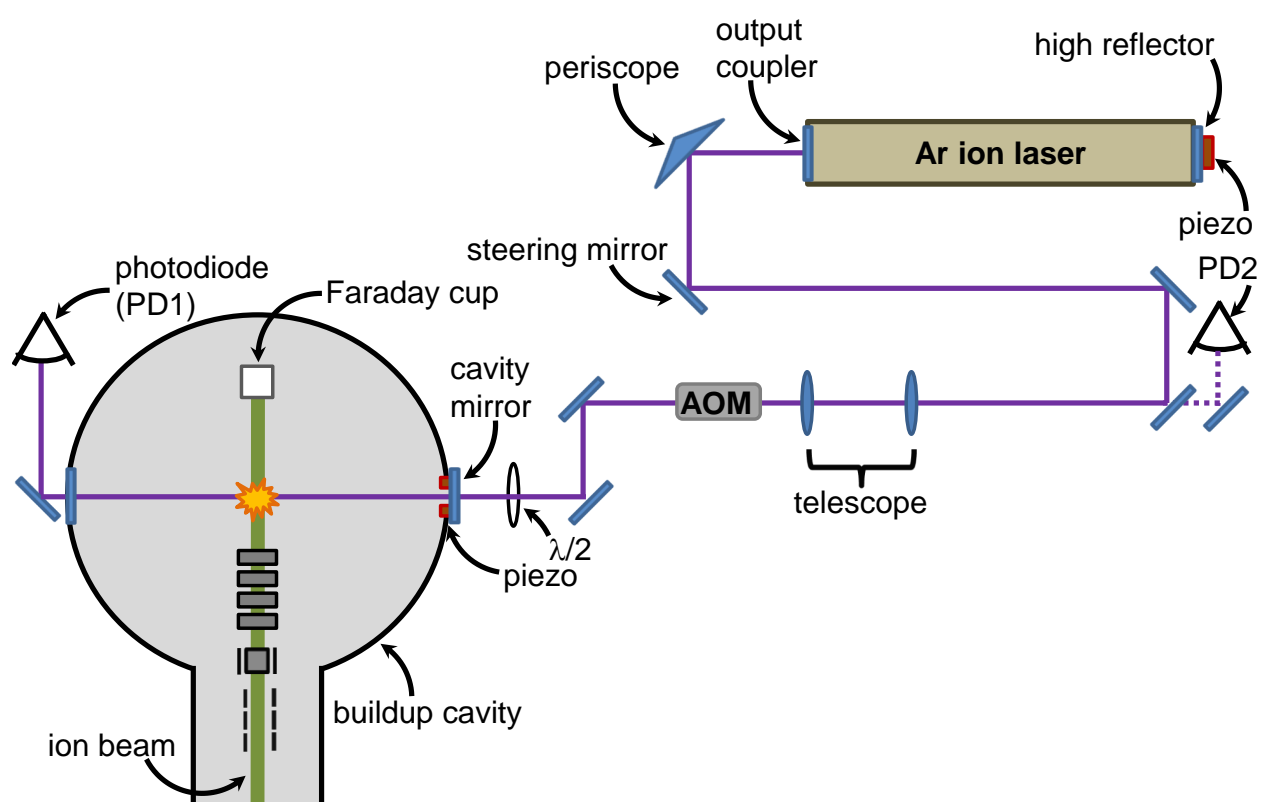
experiments, $l = 178$ cm, and FSR $= 84$ MHz.

The servoamplifier system maintains resonance between the laser and external buildup cavities.[41] The acousto-optic modulator (AOM) plays a central role in locking the laser cavity to the buildup cavity. The AOM (Inter-Action AOM 704) contains a quartz crystal to which an acoustic frequency is applied, generating a standing wave that acts as a Bragg diffraction grating.[42] The applied frequency, 50 – 80 MHz, shifts the laser light to optically isolate the laser and buildup cavities. A 1-MHz dither is also added to the laser frequency. The servoamplifier system extracts an error signal from the modulated light reflected from the buildup cavity (and measured on photo-diode PD2). Using this error signal, the servoamplifier system adjusts the laser and buildup cavity piezoelectric translators, as well as the frequency offset of the AOM, to ensure that the resonance condition is met. The AOM is capable of making the fastest corrections—greater than 5 kHz—to the laser frequency.

2.1.5   Electron Kinetic Energy Analyzer

When the laser and ion beams intersect perpendicularly in the interaction region, electrons are ejected in all directions. Only those ejected orthogonal to both beams are collected and analyzed on the basis of their kinetic energy by an electrostatic hemispherical energy analyzer. The energy analyzer consists of two concentric hemispheres; the electric field gradient disperses the electrons according to their kinetic energies.[43]

The hemispherical energy analyzer is shown in Fig. 2.9. It has an acceptance half-angle of 5°, collecting only 0.2% of the detached electrons. The hemisphere is set to transmit a fixed energy (approximately 4 eV); electrons within 2% of the transmission energy are transmitted through the analyzer (a window of approximately 150 meV at this transmission energy). The cylindrical lenses V_{IR}, V1, V2, and V_{HC} form two zoom lenses that accelerate the photoelectrons to the transmission energy. The first stage of the zoom lens (V_{IR}, V1, and V2) magnifies the initial kinetic energy. The second zoom lens consists of V1, V2, and V_{HC}; the voltage on the center focusing element (V2) has been optimized for resolution and collection efficiency at each eKE.

Figure 2.9: Diagram of the electrostatic hemispherical energy analyzer. Ions are decelerated to 35 eV (V_{IR}) into the interaction region, where they meet the amplified laser beam. Ions are ejected in all directions; only those ejected orthogonal to both the ion and laser beams enter the energy analyzer. A series of lenses accelerates and magnifies the photoelectrons. The potentials applied to the inner and outer hemispheres separate the ions on the basis of their kinetic energies. After acceleration and magnification, the electrons are imaged onto a position-sensitive array detector.
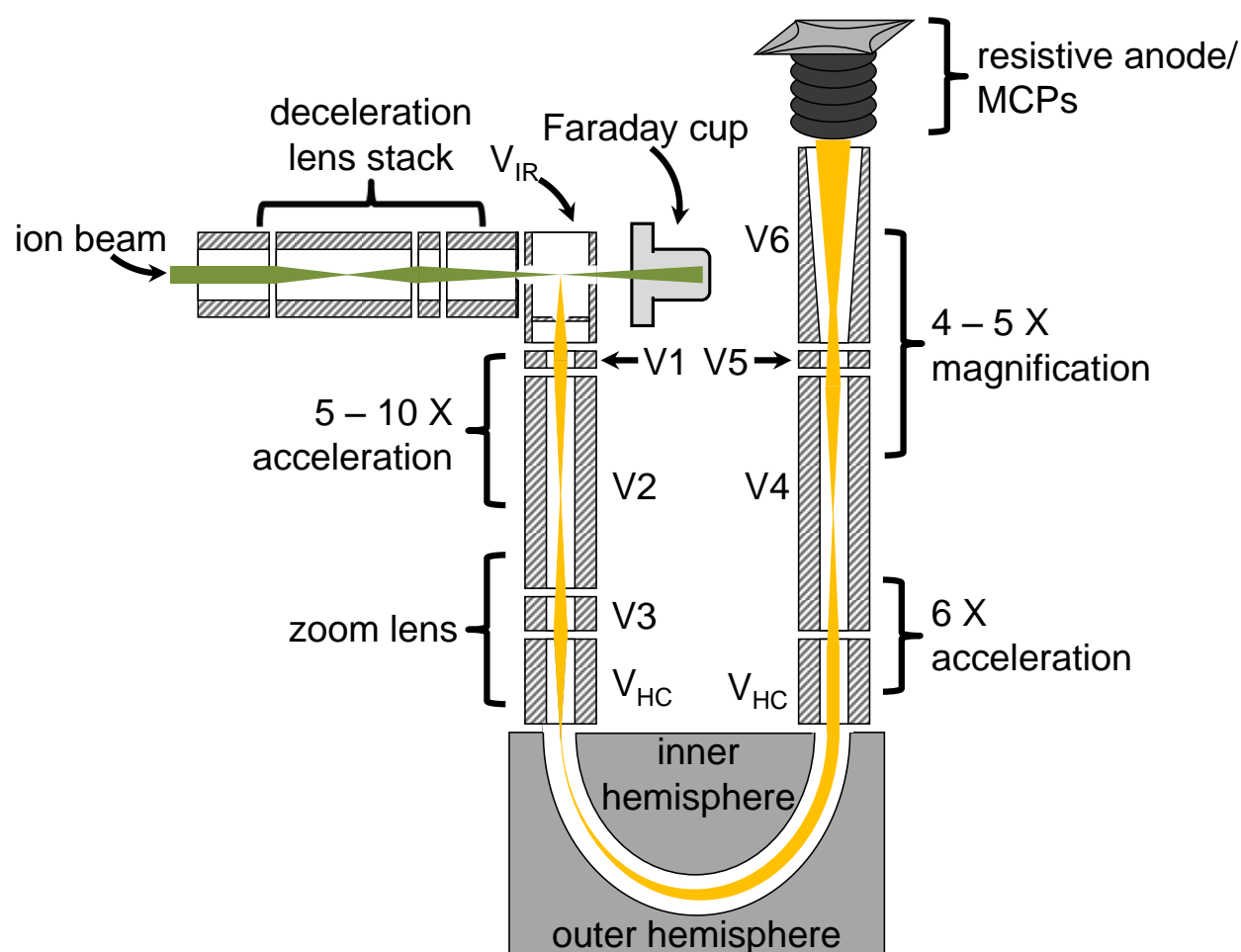
There are no entrance or exit slits to the hemispherical energy analyzer. Herzog correction lenses (V_{HC}) correct for fringe fields at the entrance and exit of the analyzer. Photoelectrons exiting the analyzer are accelerated and magnified by lenses V4 – V6 (Fig. 2.9). They are then imaged onto a two-dimensional position-sensitive array detector, which comprises a five-stage microchannel plate electron multiplier in front of a resistive anode (Quantar Technology 3318A). Photoelectrons with different eKEs are detected at different points on the resistive anode.

2.1.6   Data Acquisition and Processing

The position-sensitive detector is accompanied by a position analyzer (Quantar 2401B) that determines the spatial position of the detected electrons from the voltage outputs measured on the four corners of the anode.[44] The two-dimensional resistive anode contains 256 x-channels in the energy-dispersing direction and 16 y-channels; for a given x-channel, the photoelectron counts in the y-dimension are summed, yielding the number of photodetachment events as a function of eKE.

The computer output is connected to an oscilloscope—for real-time viewing of the photo-electrons' positions—and to a PC equipped with a DAQ card (National Instruments DIO 6533, PCI-DIO-32HS), where the data are recorded by a LabVIEW program. To collect a photoelectron spectrum over the entire eKE range, the center eKE of the 150-meV segment is scanned, and the overlapping segments are combined to produce the full photoelectron spectrum as a function of eKE. Because the transmission energy of the analyzer is fixed, the center eKE of the segment is changed by adjusting the voltages applied to the elements in the detection region. To do so, the LabVIEW program sends digital signals to a home-built Voltage Programmer box (JILA LC036).[44] Photo-electrons with eKE < 0.3 eV are not efficiently collected. The energy resolution of the analyzer is approximately 10 meV.

The electron kinetic energy scale is calibrated before and after each data set using the well-known EA of oxygen.[45] The kinetic energy scale of the analyzer is slightly compressed. To empir-ically determine this compression factor, we collect the photoelectron spectrum of an anion with transitions spanning the eKE range of the analyzer.[2] Recently, W^- and O_2^- have been used.[46,47]

The spectral simulation Fortran program PESCAL[21] is capable of fitting the experimental O_2^- spectrum and extracting the compression factor, which is less than 1.0%.

2.2   Theoretical Methods

2.2.1   Electronic Structure Calculations

In order to analyze the photoelectron spectra, it is helpful to know the equilibrium geometries and vibrational frequencies of the initial and final states. Often, these are not known experimentally; to obtain the best estimate of the frequencies, geometries, and normal mode vectors of the states involved in photodetachment, we perform electronic structure calculations using the Gaussian 03 program package.[48] Geometries are optimized and frequencies are calculated with density functional theory using the B3LYP hybrid functional.[49,50] Generally, the calculations employ the 6-311++G(d,p) basis set.[51,52]

The theoretical EA, vertical detachment energy (VDE), and term energy (T_e) are calculated using Gaussian output. The EA is the difference between the energy (including the zero-point energy, ZPE) of the ground-state neutral at its equilibrium geometry, $E_{eq,\text{neutral}}$, and the energy (including ZPE) of the anion at its equilibrium geometry, $E_{eq,\text{anion}}$:

$$\text{EA} = E_{eq,\text{neutral}} - E_{eq,\text{anion}}. \tag{2.11}$$

The vertical detachment energy is the energy of the most intense transition, corresponding to the amount of energy required to remove an electron with no geometry change. The VDE is calculated using Eq. 2.12:

$$\text{VDE} = E_{\text{neutral}}(\text{anion eqm geom}) - E_{eq,\text{anion}}, \tag{2.12}$$

where $E_{\text{neutral}}(\text{anion eqm geom})$ is the energy of the neutral at the equilibrium geometry of the anion. The T_e is the difference in energy between the ground state and an excited state of the neutral. The T_e is calculated using the following equation:

$$T_e = E_{eq,\text{neutral}'} - E_{eq,\text{neutral}}, \tag{2.13}$$

where $E_{eq,\text{neutral}'}$ is the energy, including ZPE, of an excited state of the neutral. For comparison with experiment, we report theoretical EAs, VDEs, and T_es calculated using the above equations.

2.2.2   Franck-Condon Simulations

We typically use a Franck-Condon analysis of the vibrational structure in photoelectron spectra to obtain frequencies and equilibrium geometries of the neutral species and to identify the origin transition. For more information on Franck-Condon analysis, see Section 1.3. Briefly, the intensity of a vibronic transition I_{FC} is proportional to the square of the Franck-Condon overlap integral

$$I_{FC} = \left[\int \Psi_{v'}(\mathbf{Q}')\Psi_{v''}(\mathbf{Q}'')\mathrm{d}\mathbf{Q}' \right]^2 \qquad (2.14)$$

where $\Psi_{v'}(\mathbf{Q}')$ is the vibrational wavefunction of the neutral in quantum state v' as a function of the normal coordinates of the neutral $\mathbf{Q}'$, and $\Psi_{v''}(\mathbf{Q}'')$ is the corresponding vibrational wavefunction of the anion in terms of its normal coordinates $\mathbf{Q}''$. The normal modes are treated as uncoupled and harmonic.[3]

The Franck-Condon profiles of the photoelectron spectra are simulated using the PESCAL program,[21] as detailed by Ervin *et al.*[4] Simulations use theoretical geometries, normal mode vectors, and vibrational frequencies of the anion and neutral states calculated using the Gaussian 03 software package.[48] The Fortran program FCFGAUS uses the Gaussian output to determine $\mathbf{K}''$ vectors and $\mathbf{J}''$ matrices, generating files that are used as input for PESCAL. The output files from FCFGAUS express the normal mode eigenvectors ($\mathbf{Q}'$, $\mathbf{Q}''$) in terms of mass-weighted Cartesian atomic displacement coordinates.

PESCAL is capable of simulating the photoelectron spectrum in a number of ways (e.g., using the parallel-mode approximation, including Duschinsky rotation, etc.). For the simulations presented here, the Franck-Condon intensities are computed in the harmonic-oscillator approximation including Duschinsky rotation using the Sharp-Rosenstock-Chen method.[4,8,20] This method requires input files containing vibrational frequencies, normal mode vectors, and displacements generated by FCFGAUS and extracted from Gaussian output. The individual vibronic peak contours

are approximated as a Gaussian function with a full-width at half-maximum that is consistent with the instrumental resolution (11 – 12 meV). Alternatively, the stick spectrum can be convoluted with the rotational contours calculated by the Fortran program ROTCONT.[21]

The simulated spectrum is used to aid in the interpretation of the measured photoelectron spectrum. The vibrational modes observed in a photoelectron spectrum generally correspond to those that mimic the geometry change that occurs upon photodetachment. When the vibrational structure of the simulation displays good agreement with the experiment, the simulation can be used as a tool to assign peaks in the experimental spectrum. In addition, the extent of the vibrational progression is determined by the difference in the equilibrium geometries of the anion and neutral: a short vibrational progression arises from a small geometry difference, while an extended progression is the result of a large geometry change. By adjusting the $\mathbf{K''}$ displacements to match the observed spectral envelope, we can determine the net change in geometry between the anion and the neutral. PESCAL is equipped with a least-squares optimization option in which the user can select the input parameters (vibrational frequencies, $\mathbf{K''}$ displacements, temperature, EA, etc.) to optimize in order to obtain the best fit to the experimental data.

The normal-mode analysis in Cartesian coordinates that is employed by PESCAL is the standard method of simulating photoelectron spectra. It can be arbitrarily applied to molecules of any size or geometry, generally producing near-quantitative agreement with the experimental spectrum. However, when a large geometry change takes place upon photodetachment, the approximations invoked in normal-mode analysis are no longer valid. In such cases, the upper portion of the neutral potential energy surface is sampled, where vibrations do not resemble independent harmonic oscillators. The molecules presented here test the limits of normal-mode analysis, and many require a more sophisticated approach to interpret their photoelectron spectra.

Chapter 3

Furanide Anion

3.1 Introduction

Furan, C_4H_4O, has attracted considerable attention due to its key role in combustion chemistry as well as to some intriguing aspects of its thermochemistry—namely, to its unusually high calculated C-H bond strength.[53–55] Furan is one of the primary structural units of coal;[56,57] consequently, knowledge of its reactivity has the potential to improve current technology of coal combustion.[58] Furan is also an important intermediate in the pyrolysis of biomass,[59–62] where it is generally thought to originate in the breakdown of polysaccharides that make up cell walls.[63–65] Conversion of biomass (and, more specifically, its major components: lignin, cellulose, and hemicellulose[66]) into ethanol or other fuels has recently stimulated strong interest as a potential alternative to petroleum-based energy production.[67–69] However, at present, thermal biomass processing is not commercially viable because it is inefficient and plagued by undesired reaction products,[70] such as polycyclic aromatic hydrocarbons (PAH).[71–74] Furan chemistry is central to biomass decomposition; thus, understanding its bond-specific reactivity has far-reaching implications for commercial fuel production, the environment, and the energy economy.

Because of its importance in combustion chemistry and biomass pyrolysis, the thermochemistry of furan has been the subject of several experimental and theoretical investigations. Initial studies focused on thermal decomposition of furan in shock tubes,[75–77] flow reactors,[78,79] and *via* laser pyrolysis.[80] These experiments established that the two primary product channels of unimolecular furan decomposition are (1) $CO + CH_3C{\equiv}CH$, and (2) $CH_2{=}C{=}O + HC{\equiv}CH$.[75–80]

More recently, Vasiliou *et al.* used photoionization mass spectrometry and matrix IR spectroscopy to examine the thermal decomposition products of furan.[81] In addition to the products mentioned above, they detected propargyl radicals (CH_2CCH). Benzene, which is known to form from propargyl radicals,[82] and other aromatic species were also observed in the study,[81] demonstrating the role of furan in the chemistry of PAH formation.

Although the primary decomposition products of furan have been characterized, the mechanisms of their formation are not yet fully known. Several computational studies have been aimed at determining the relative energies of chemical bonds in furan to better understand the mechanistic details of furan decomposition.[53,54,83] One possible pathway begins with the loss of a hydrogen atom bonded to the alpha-carbon in the furan ring; i.e., the cleavage of the C-H_α bond. Yet, the first comprehensive theoretical investigation of the unimolecular decomposition channels of furan[83] concluded that cleavage of the C-H_α bond requires too much energy and therefore cannot be the initial step in any of the major decomposition pathways. Since then, multiple high-level calculations (CBS-QB3,[54] CBS-APNO,[54] G3,[54,55] B3LYP,[55] and CASPT2[53]) agree that the C-H_α bond is prohibitively strong, approximately 121 kcal mol^{-1}. However, this is an unusually high C-H BDE, which makes its experimental verification a particularly valuable contribution. Because there has been no experimental determination of the C-H_α BDE of furan ($DH_{298}(C_4H_3O\text{-}H_\alpha)$) until now, current decomposition models are based on the calculated C-H_α BDE and assume that pathways involving cleavage of the C-H_α bond or H abstraction are unimportant.

The C-H_α BDE of furan can be determined through the well-established methodology of a thermochemical cycle[33] involving the electron affinity (EA) of the α-furanyl radical (α-C_4H_3O), the gas-phase acidity of furan, and the ionization energy of hydrogen. The latter quantity is well-known.[84] Likewise, in 1988, DePuy *et al.* investigated the gas-phase acidities of the two distinct hydrogen atoms in furan.[31] As in our experiment, they prepared furanide in a flowing afterglow apparatus by deprotonation of furan with OH^-, and they reported H^+ loss from both the α- and β-positions. They showed that the α-position was the more acidic of the two, but the exact acidity of the β-position was not determined. Calculations and our own observations confirm

the higher relative acidity of the α-site, since under our experimental conditions we only observe photodetachment from the α-furanide species. A more precise measurement of the gas-phase acidity of furan was subsequently made by Grabowski and Owusu.[32] In the present work we determine the remaining thermodynamic quantity necessary to obtain the C-H$_\alpha$ BDE of furan: the EA of the α-furanyl radical.

We report a photoelectron spectroscopy study of the furanide anion, which provides several new spectroscopic constants and allows the first direct measurement of the C-H$_\alpha$ BDE of furan. We collect the 364-nm negative ion photoelectron spectrum of $C_4H_3O^-$. From the spectrum, we make the first experimental determination of the EA and of several vibrational frequencies of α-C_4H_3O. We observe both the $\tilde{X}^2A'$ σ-radical ground state and $\tilde{A}^2A''$ π-radical excited state of α-C_4H_3O and determine the term energy (T_e) of the excited state.

3.2   Experimental Methods

The negative ion photoelectron spectrometer used in this experiment has been described in detail elsewhere.[2,34,41] The apparatus consists of four main sections: an ion source, a mass filter, an interaction region with crossed laser and ion beams, and an electrostatic electron kinetic energy analyzer. Negative ions are formed in a flowing afterglow ion source. A microwave discharge containing trace amounts of O_2 gas in He buffer gas ($\sim$0.4 Torr) generates atomic oxygen radical anion, O^-. Methane is added downstream of O^- to form hydroxide anion (OH^-), which then reacts with furan (C_4H_4O, $\geq$99%, Sigma-Aldrich) to generate furanide anions: $OH^- + C_4H_4O \rightarrow C_4H_3O^- + H_2O$. Because the H$_\alpha$ of furan is more acidic,[31] we deprotonate predominantly at the α-position under our experimental conditions to produce the α-furanide anion. We confirm the absence of β-furanide using experimental observations in conjunction with theoretical simulations (see Section 3.4.1.3). We do not generate $C_4H_2O^-$; the m/z 66 peak is absent from our mass spectrum, and it has been shown that $C_4H_2O^-$ is not produced efficiently in the reaction of O^- with furan.[85] Collisions with He buffer gas cool the ions to approximately 300 K. The flow tube can be further cooled with a liquid nitrogen jacket to obtain a "cold spectrum" of ions with temperatures

near 150 K. Anions are extracted into a differentially pumped region and are accelerated to 735 eV before entering a Wien velocity filter with a mass resolution of $m/\Delta m \sim 60$. The mass-selected ion beam (typically 200 pA) is decelerated to 35 eV and focused into the laser interaction region. Here, the 1 W output from a single-mode continuous-wave argon ion laser operating at 364 nm (3.40814 eV) is built up to approximately 100 W of circulating power in an optical buildup cavity located within the vacuum system. Photoelectrons ejected in the direction orthogonal to both the laser and ion beams enter a hemispherical energy analyzer. The photoelectron signal is recorded as a function of electron kinetic energy with a position-sensitive detector. The energy analyzer has a resolution of approximately 11 meV under the conditions used for the present experiments.

The electron kinetic energy (eKE) can be converted to electron binding energy (eBE) through the relationship eBE = $h\nu$ - eKE. The absolute kinetic energy scale is calibrated[2,43] before and after each experiment using the well-known EA of atomic oxygen.[45] Additionally, the energy scale is corrected for a slight linear compression $(<1\%)$[2] using the photoelectron spectrum of O_2^-, which provides a number of known transitions spanning the photoelectron energy range.[21,47] After making these corrections and accounting for the resolution of the spectrometer and rotational peak profiles, absolute electron binding energies can be determined with an accuracy of better than 5 meV.

A rotatable half-wave plate positioned outside the buildup cavity varies the polarization of the photodetachment radiation in order to control the angle θ between the electric field vector of the laser beam and the photoelectron collection axis. The photoelectron angular distribution is described by the equation[5]

$$I(\theta) = \frac{\sigma_0}{4\pi}(1 + \beta P_2(\cos \theta)) \tag{3.1}$$

where σ_0 is the total photodetachment cross section, β is the anisotropy parameter, and $P_2(\cos \theta)$ is the second Legendre polynomial. We measure the anisotropy parameter explicitly by recording the photoelectron signal at the kinetic energy of one suitable intense peak in the photoelectron spectrum as a function of θ (between $\theta = 0°$ and $\theta = 360°$ in steps of 10°). The photoelectron angular distribution is fit with Eq. 3.1, and full spectra collected at $\theta = 0°$ and $\theta = 90°$ are scaled to

match β at the energy at which it was measured. Separately, we collect a photoelectron spectrum at $\theta = 54.7°$ (the so-called "magic angle"), where the photoelectron intensity is independent of β and directly reflects the relative photodetachment cross section.

3.3   Theoretical Methods

All electronic structure calculations were performed using the Gaussian 03 program package.[48] Optimized geometries, harmonic vibrational frequencies, and normal mode coordinates were calculated at the B3LYP/6-311++G(d,p) level of theory/basis[52] for the $\tilde{X}^2A'$ state of both the α- and β-furanide anion, as well as for the $\tilde{X}^2A'$ and $\tilde{A}^2A''$ states of the neutral α- and β-furanyl radical. All molecules were constrained to C_s symmetry.

We use a Franck-Condon analysis of the vibrational structure in the furanide photoelectron spectrum to identify the active vibrational modes of the furanyl radical and the geometry change upon photodetachment. The Franck-Condon profiles of the photoelectron spectra are simulated using the PESCAL program,[21] using as a point of departure the calculated geometries, normal mode vectors, and vibrational frequencies of the anion and neutral states. The normal modes and the Duschinsky $\mathbf{J}''$ matrix and $\mathbf{K}''$ displacements are calculated. The Franck-Condon factors are computed in the harmonic oscillator approximation including Duschinsky rotation using the Sharp-Rosenstock-Chen method.[4] The individual vibronic peak contours are simulated by a Gaussian function with a FWHM of 11 meV, consistent with instrumental resolution. Comparison of the simulations to the experimental spectra enables the determination of experimental frequencies.

3.4   Results

3.4.1   Photoelectron Spectra of the Furanide Anion

Chemical intuition suggests that the rigid five-membered ring structure constrains furanide to a relatively small geometry change upon photodetachment. Thus, we expect substantial Franck-Condon overlap near the bottom of the $\tilde{X}^2A'$ potential well, making the determination of the

Table 3.1: Measured and calculated (B3LYP/6-311++G(d,p)) electron affinities and term energies (T_e) of the α- and β-furanyl radicals.

		$\tilde{X}\,^2\mathbf{A}' \leftarrow \tilde{X}\,^1\mathbf{A}'$	T_e
α-furanyl radical	*Experiment*	1.853(4) eV	0.68(7) eV
	Theory	1.8866 eV	0.61647 eV
β-furanyl radical	*Experiment*	--	--
	Theory	1.6712 eV	1.0713 eV

origin—and hence the EA—straightforward. We also expect the most significant changes in the geometry of α-furanide upon photodetachment to be localized near the site from which the electron is removed; therefore, we anticipate the active vibrational modes in the photoelectron spectrum to be limited to only a few normal modes involving changes in the bond lengths and angles surrounding the deprotonated C_α.

This simple picture is supported by the well-resolved nature of the photoelectron spectrum we observe. The 364-nm, magic angle, cold (about 150 K) photoelectron spectrum of $C_4H_3O^-$ is presented in Fig. 3.1(a). We assign the intense, sharp peak at the lowest eBE to the transition from the ground vibrational state of α-furanide to the ground vibrational state of $\tilde{X}^2A'$ α-furanyl radical. The eBE of this origin peak, 1.853(4) eV, directly corresponds to the EA of furanyl radical (Table 3.1). The photoelectron spectrum is dominated by only a few active vibrational modes. From the spectrum we can directly extract three vibrational frequencies of the furanyl radical: 855(25) cm^{-1}, 1064(25) cm^{-1}, and 1307(40) cm^{-1}. These frequencies are typical of in-plane ring-distortion and ring-breathing modes.

The photoelectron spectra of $C_4H_3O^-$ collected at 300 K with the laser polarization set at 90° and 0° relative to the direction of photoelectron collection are displayed in Fig. 3.1(c). In these spectra, a hot band resulting from photodetachment of vibrationally excited anions is visible at lower binding energy than the origin peak. Comparison of the $\theta = 0°$ and $\theta = 90°$ spectra reveals two distinct spectral regions with different anisotropies. Specifically, the anisotropy parameter,

plotted in Fig. 3.1(b), changes near eBE $= 2.5$ eV from positive values at lower binding energies to negative values at higher binding energies. In the simplest view, the anisotropy parameter depends on the electronic orbital from which photodetachment occurred. Therefore, a significant variation in β for different features in a photoelectron spectrum is often a signature of different neutral electronic states. Evidently, two different electronic states of neutral C_4H_3O are observed in the photoelectron spectra: the ground state at lower binding energy, and an excited state that appears at higher binding energy and is suppressed at $\theta = 0°$.

The electronic orbitals and valence electrons of α-furanide anion are presented in Fig. 3.2. Intuitively, we expect the ground state of the α-furanyl radical to result from the removal of an electron from the in-plane σ orbital of the deprotonated C_α, corresponding to a $^2A'$ σ-radical. Higher in energy lies the $^2A''$ π-radical resulting from the removal of an electron from the out-of-plane π orbital of a$''$ symmetry (see Fig. 3.3 for an illustration of the π molecular orbitals). Between 0 and 3 eV of kinetic energy, "s-like" electrons give rise to $\beta > 0$ and "p-like" electrons yield $\beta < 0$. These labels reflect the character of the parent orbital: s-like electrons originate from orbitals with greater symmetry or fewer nodes than those that generate p-like electrons.[7] In other words, electrons removed from in-plane σ orbitals tend to have the greatest photodetachment cross-sections parallel ($\theta = 0°$) to the laser polarization, whereas electrons in out-of-plane π orbitals have a maximum photodetachment cross-section at $\theta = 90°$. As a result, positive β values are often associated with photoelectrons detached from in-plane orbitals of aromatic systems,[7,86,87] and negative β values are often found for photoelectrons detached from π orbitals of aromatic systems.[7,86,88,89] Thus, the positive β values observed at lower eBE in our spectra confirm that the lower energy vibrational progression corresponds to the $^2A'$ σ-radical ground state of the furanyl radical, i.e. the removal of an electron from the in-plane σ orbital of furanide. In contrast, $\beta < 0$ for the higher-lying $\tilde{A}^2A''$ features because in this case the electron is detached from an out-of-plane π orbital. Furthermore, using the same simple picture, we can rule out the possibility that the two progressions represent the ground states of α- and β-furanyl radicals. Regardless of the deprotonation site, the ground-state furanyl radical is generated when an electron is removed from an in-plane σ orbital; thus, we

Figure 3.1: (a) The 364-nm, magic angle, cold photoelectron spectrum of the furanide anion. The fundamental transitions of the ν_6, ν_9, and ν_{13} vibrational modes are marked. (b) β values of the major photoelectron peaks, indicating which features are due to the $\tilde{X}^2A'$ ground state ($\beta > 0$) and which are attributed to the $\tilde{A}^2A''$ excited state of α-furanyl radical ($\beta < 0$). (c) Spectra of the furanide anion, taken at 0° and 90° polarizations at room temperature and scaled to match the β anisotropy parameter of the origin peak (1.853 eV).
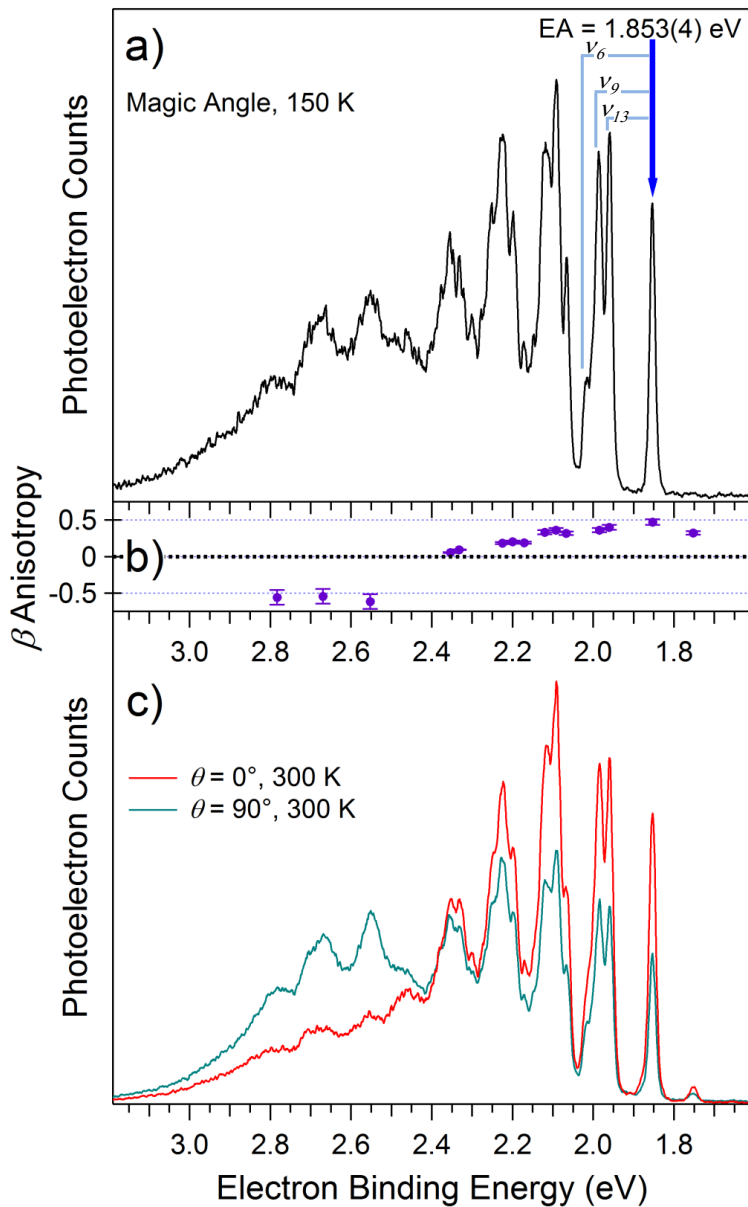
expect $\beta > 0$ for the ground states of both α- and β-furanyl radicals.

Figure 3.2: Electronic orbitals and valence electrons of α-furanide, $\tilde{X}^1A'$. Photodetachment from the in-plane σ orbital of the deprotonated C_α yields the $\tilde{X}^2A'$ σ-radical ground state of the neutral furanyl radical. Photodetachment from the out-of-plane π cloud yields the $\tilde{A}^2A''$ π-radical excited state of the neutral furanyl radical.
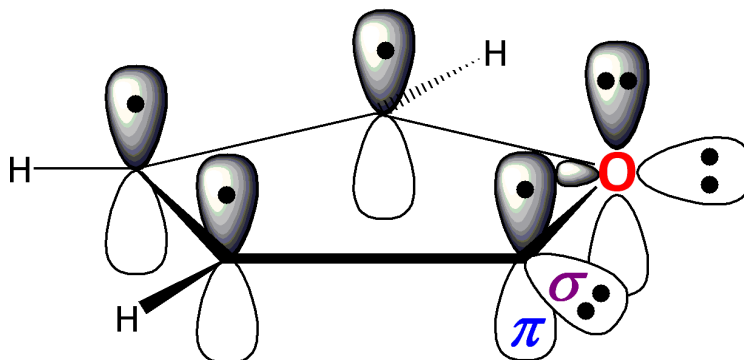
3.4.1.1   The $^2A'$ σ-radical ground state of the α-furanyl radical

Calculations and simulations of the photoelectron signal (plotted in Fig. 3.4) confirm our spectral assignments and enable a quantitative determination of several spectroscopic parameters. Table 3.1 lists the calculated and measured relative energies of the α- and β-furanyl species. The measured EA is in accord with the calculated origin of the α-furanyl radical. Fig. 3.4(b) shows the Franck-Condon simulation of α-furanide photodetachment. The simulated $\tilde{X}^2A' \leftarrow \tilde{X}^1A'$ photoelectron spectrum, bracketed with a purple bar, reproduces the lower binding energy portion of the magic angle spectrum shown in Fig. 3.4(a). The agreement between the simulated and observed spectra further substantiates our assignment of the lower binding energy progression to the $\tilde{X}^2A'$ state of α-furanyl radical.

The relatively modest geometry change upon photodetachment implied by the well-resolved nature of the spectrum is supported by DFT calculations. Table 3.2 shows that detachment of an in-plane σ electron to generate the $\tilde{X}^2A'$ σ-radical distorts the ring to increase the O-•C-C angle about the radical center (•C) and shortens several bonds, especially the •C-C bond. Because the largest geometry change is the increase in the O-•C-C angle, the modes calculated to be most

Figure 3.3: Generalized valence bond diagrams of the π orbitals of $\tilde{A}^2A''$ α-furanyl radical.
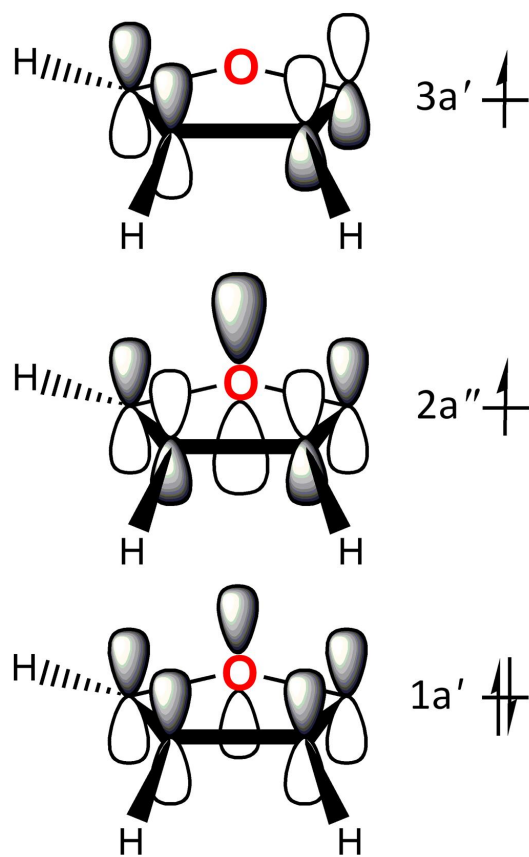
Figure 3.4: (a) The 364-nm magic angle, cold photoelectron spectrum of the furanide anion. (b) The simulated photoelectron spectrum of α-furanide anion. The simulation employs the experimentally measured EA (Table 3.1) and the three experimental frequencies of the neutral ν_6, ν_9, and ν_{13} listed in Table 3.3, determined from the comparison of the *ab initio* simulation to the experimental spectrum; we use calculated values for the remaining harmonic frequencies and all $\mathbf{K}''$ displacements (Table 3.3). (c) The simulated photoelectron spectrum of β-furanide anion. The simulation uses *ab initio* EA, T_e, harmonic vibrational frequencies, and $\mathbf{K}''$ displacements, listed in Table 3.1 and Table 3.5. In panels (b) and (c), the photoelectron signal due to the ground-state furanyl radical is marked with a purple bar, and the excited-state features are designated with a blue bar.
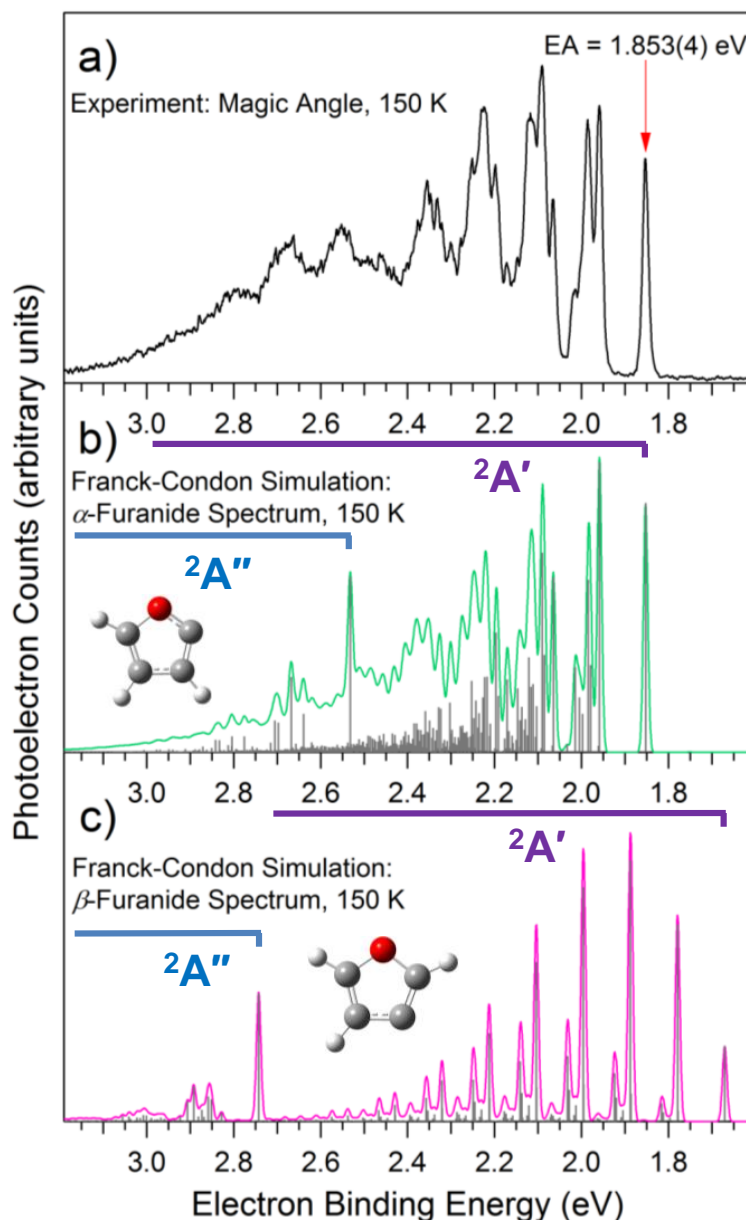
active in the Frank-Condon simulation are ν_{13} (a ring deformation mode dominated by the O-$\bullet$C-C bend), ν_{12} (ring deformation that involves the C-C-C bend), and ν_9 (a ring breathing mode), illustrated in Fig. 3.5. Frank-Condon activity of the various vibrational modes is indicated by their calculated $\mathbf{K}''$ displacements, which are vectors describing the difference in the nuclear equilibrium positions between the anion and the neutral radical. A large $\mathbf{K}''$ value indicates a vibrational normal mode vector that plays a large part in the net geometry change between the anion and the neutral. The calculated $\mathbf{K}''$ displacements are listed in Table 3.3; as we intuitively expect, the largest $\mathbf{K}''$ displacements are for the ν_9, ν_{12}, and ν_{13} ring breathing and ring deformation modes.

The excellent agreement between the α-furanide $\tilde{X}^2\mathrm{A}' \leftarrow \tilde{X}^1\mathrm{A}'$ Franck-Condon simulation and the lower energy vibrational progression allows for partial characterization of the $\tilde{X}^2\mathrm{A}'$ state. Despite most peaks in the spectrum arising from multiple congested vibronic transitions (gray sticks in Fig. 3.4(b)), comparison of the *ab initio* simulation to the experimental spectrum enables us to assign features and measure vibrational frequencies based on photoelectron peaks dominated by a single vibronic transition. In this way, we extract three experimental vibrational frequencies of the ground-state radical (ν_6, ν_9, ν_{13}) and one experimental vibrational frequency of the anion (ν_{13}), which are listed along with the unscaled calculated frequencies in Table 3.3. Though ν_6 is not one of the most active vibrational modes mentioned above, its fundamental transition is sufficiently well-resolved in the photoelectron spectrum to allow a confident determination of its frequency. The calculated and measured frequencies give rise to a simulated spectrum with peak positions that agree reasonably well with the observed vibrational structure. This is especially true at lower binding energy, which corresponds to the portion of the $\tilde{X}^2\mathrm{A}'$ potential energy surface where anharmonic effects are not significant. This suggests that the calculated harmonic vibrational frequencies accurately represent the vibrational frequencies of the $\tilde{X}^2\mathrm{A}'$ state of α-furanyl radical. In addition, the extent of the vibrational progression in the simulation, governed by the computed $\mathbf{K}''$ displacements (Table 3.3), matches the observed spectral envelope. This agreement indicates that the calculated geometry change upon photodetachment is also consistent with the experimental spectrum.

Table 3.2: Optimized geometries of α-furanide anion ($\tilde{X}^1A'$) and α-furanyl radical ($\tilde{X}^2A'$, $\tilde{A}^2A''$), and the calculated net geometry change upon photodetachment (B3LYP/6-311++G(d,p)). Bond lengths are in units of Å, and bond angles are in units of degrees. The net geometry change is defined as the difference in the values of the internal coordinates for the anion and the radical. The bond lengths and angles that undergo the greatest change are boldfaced.
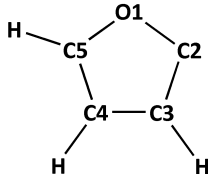
Internal Coordinate	α-Furanide $\tilde{X}^1A'$	α-Furanyl Radical $\tilde{X}^2A'$	$\tilde{A}^2A''$	Geometry Change $\tilde{X}^2A' \leftarrow \tilde{X}^1A'$	$\tilde{A}^2A'' \leftarrow \tilde{X}^1A'$
O1 – C2	1.431	1.329	1.398	-0.012	$\mathbf{-0.033}$
C2 – C3	1.392	1.354	1.468	$\mathbf{-0.038}$	$\mathbf{+0.076}$
C3 – C4	1.440	1.446	1.384	$+0.006$	$\mathbf{-0.056}$
C4 – C5	1.362	1.357	1.393	-0.005	$\mathbf{+0.031}$
O1 – C5	1.366	1.385	1.350	$+0.019$	-0.016
C3 – H	1.084	1.076	1.080	-0.008	-0.004
C4 – H	1.084	1.079	1.079	-0.005	-0.005
C5 – H	1.082	1.076	1.081	-0.006	-0.001
$\angle$ O1 – C2 – C3	103.3	114.1	102.5	$\mathbf{+10.8}$	-0.8
$\angle$ C2 – C3 – C4	110.9	103.4	110.7	$\mathbf{-7.5}$	-0.2
$\angle$ C3 – C4 – C5	105.4	107.3	105.0	$+1.9$	-0.4
$\angle$ C4 – C5 – O1	109.9	109.6	110.9	-0.3	$+1.0$
$\angle$ C5 – O1 – C2	110.5	105.7	110.9	$\mathbf{-4.8}$	$+0.4$

Table 3.3: α-Furanide anion ($\tilde{X}^1A'$) and α-furanyl radical ($\tilde{X}^2A'$, $\tilde{A}^2A''$) vibrational frequencies. All but four of the frequencies listed in the table are unscaled calculated harmonic frequencies (B3LYP/6-311++G(d,p)). The ν_6, ν_9, and ν_{13} neutral frequencies and the ν_{13} anion frequency were determined from the Frank-Condon simulation of the $C_4H_3O^-$ photoelectron spectrum; these frequencies are listed in italics directly below the calculated value. The most active modes, based on the calculated geometry change and experimental peak intensities, are boldfaced.

Mode		Description	Frequencies $\tilde{X}^1A'$, cm^{-1}	$\tilde{X}^2A' \leftarrow \tilde{X}^1A'$		$\tilde{A}^2A'' \leftarrow \tilde{X}^1A'$	
				K''	$\tilde{X}^2A'$, cm^{-1}	K''	$\tilde{A}^2A''$, cm^{-1}
A'	ν_1	C-H stretch	3202.5	-0.0055219	3288.8	-0.0039291	3248.8
	ν_2	C-H stretch	3172.9	-0.0043554	3274.1	-0.0053742	3232.4
	ν_3	C-H stretch	3157.6	1.7468x10^{-4}	3238.7	3.2151x10^{-4}	3224.8
	ν_4	C-C str + H-wag	1537.2	-0.0096266	1568.1	0.013785	1400.0
	ν_5	C-C str + H-wag	1369.2	-0.14452	1453.2	**0.16825**	**1096.9**
	ν_6	C-C str + H-wag	1347.5	0.036363	1356.7 *1307(40)^a*	-0.016990	1475.3
	ν_7	C-C str + H-wag	1161.1	-0.011293	1229.9	**0.081375**	**1332.1**
	ν_8	H-wag	1105.5	0.079981	1167.5	-0.025052	1008.4
	ν_9	**C-O stretch**	**802.0**	**-0.18952**	**1093.7** *1064(25)^a*	**-0.081214**	**718.62**
	ν_{10}	C-O str + H-wag	1072.6	-0.0067749	1019.9	-0.099751	1132.2
	ν_{11}	C-O str + H-wag	982.1	0.036308	1000.3	0.068089	1029.0
	ν_{12}	**C-C-C bend**	**897.5**	**0.19493**	**875.0**	-0.062708	913.4
	ν_{13}	**O-C-C bend**	**852.0** *815(30)^a*	**0.35265**	**867.7** *855(25)^a*	**0.10232**	**865.5**
A''	ν_{14}	o-o-p H-wag	765.0	2.8862x10^{-5}	861.5	-5.9561x10^{-6}	919.4
	ν_{15}	o-o-p H-wag	740.8	2.4088x10^{-6}	777.3	8.1634x10^{-6}	813.8
	ν_{16}	o-o-p H-wag	628.2	-2.2699x10^{-6}	711.2	-1.6492x10^{-5}	901.7
	ν_{17}	o-o-p ring deformation	604.1	-9.2735x10^{-6}	602.3	2.3750x10^{-7}	499.8
	ν_{18}	o-o-p ring deformation	591.3	1.4156x10^{-6}	482.2	-3.7229x10^{-6}	699.9

^{a} Experiment, this work

Figure 3.5: Vector diagrams of the most active vibrational modes upon photodetachment to the $\tilde{X}^2\mathrm{A}'$ ground state and the $\tilde{A}^2\mathrm{A}''$ excited state of α-furanyl radical.
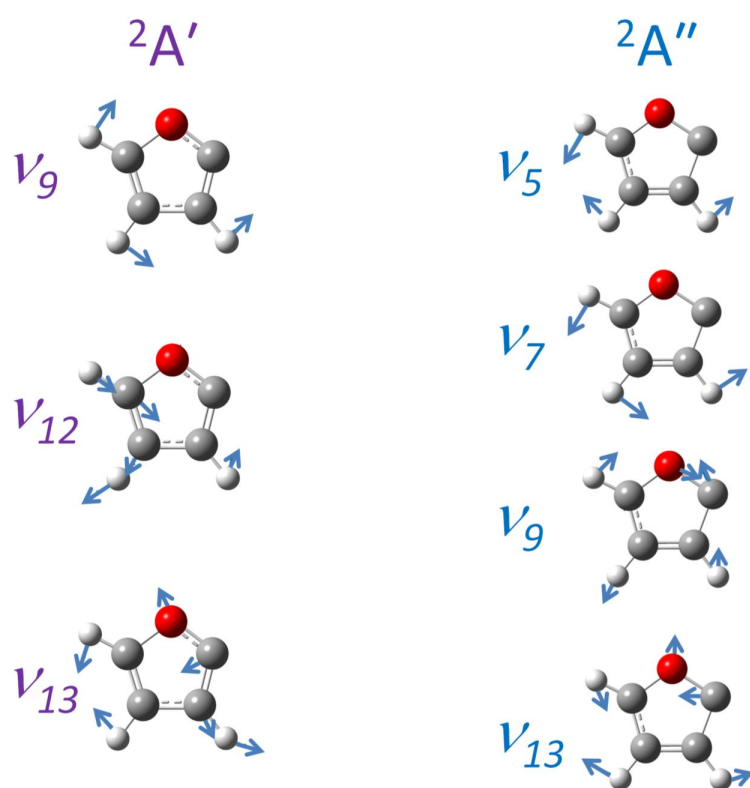
3.4.1.2   The ^{2}A$''$ π-radical excited state of the α-furanyl radical

We assign the higher energy vibrational progression to the $\tilde{A}^2$A$''$ π-radical excited state of α-furanyl, in which an electron has been removed from the out-of-plane π molecular orbital of a$''$ symmetry (Figs. 3.2 and 3.3). The Franck-Condon simulation of the excited state is bracketed in blue in Fig. 3.4(b). The origin transition of the $\tilde{A}^2$A$''$ state of α-furanyl radical is predicted to be an intense peak at eBE = 2.5031 eV. The onset of the first intense feature for which $\beta < 0$, appearing at eBE = 2.53(7) eV, is assigned to the origin of the $\tilde{A}^2$A$''$ state. Accordingly, its term energy is 0.68(7) eV, also in good agreement with the calculated T_e value. The ground-state α-furanyl radical lends some intensity to the photoelectron spectrum above 2.5 eV, as well; there is an underlying unresolved continuum resulting from transitions to high vibrational levels of the $\tilde{X}^2$A$'$ σ-radical. This continuum can be seen in the $\theta = 0°$ spectrum (Fig. 3.1(c)), which minimizes contribution from the π-radical, and it is reproduced in the ground state Franck-Condon simulation.

The $\tilde{A}^2$A$''$ features predicted by the Franck-Condon simulation appear in the experimental spectra, but are much broader than expected. Broad, diffuse spectral bands, such as those observed in the higher binding energy portion of the $C_4H_3O^-$ spectrum, are often characteristic of nonadiabatic effects.[90] Vibronic coupling between the $\tilde{X}^2$A$'$ and $\tilde{A}^2$A$''$ states of α-furanyl radical *via* their A$''$ vibrational modes can result in a large number of vibronic levels into which intensity can be distributed. The generally forbidden A$''$ modes of α-furanyl radical have frequencies between approximately 500 and 900 cm^{-1}; activity of these modes would fill in the excited state spectrum and broaden the resolved peaks predicted in the simulation by approximately 50 meV, which is consistent with the width of the peaks in the $\tilde{A}^2$A$''$ progression. Such broadening of excited state features has also been observed in the photoelectron spectra of pyrrole (C_4H_5N) and thiophene (C_4H_4S),[91–94] as well as N-methyl-5-pyrazolide.[87] In all three cases, the width of the structure that could not be accounted for using Franck-Condon analysis[95,96] was attributed to vibronic coupling.[87,97]

We thus conclude that the higher binding energy vibrational progression in the $C_4H_3O^-$

magic angle spectrum is due to the $\tilde{A}^2\mathrm{A}''$ π-radical state of α-furanyl radical. The experimental T_e agrees well with calculations, and the discrepancy between the simulation and the observed spectrum is attributed to nonadiabatic effects.

3.4.1.3   Contribution from the β-Furanyl Radical

Calculations and Franck-Condon simulations of β-furanide photodetachment are shown in Fig. 3.4(c). Calculated equilibrium structures of the β-furanyl anion and radical states are given in Table 3.4; vibrational frequencies and $\mathbf{K}''$ displacements used in the simulation are listed in Table 3.5. The simulation predicts a significantly more structured β-furanide photoelectron spectrum than the one observed experimentally, as well as a higher excited-state term energy, $T_e(\tilde{A}^2\mathrm{A}'') = 1.07$ eV. Even more importantly, the calculated EA of β-furanyl radical is 182 meV below that of the α-furanyl radical (Table 3.1). We expect the calculated EA of β-furanyl radical to be reasonably reliable, as analogous calculations for the α-furanide species predict the EA to within 35 meV of the actual value. Likewise, the success of the Franck-Condon simulation of the α furanide photoelectron spectrum lends credibility to the simulation of β-furanide. Thus, the discrepancies between the experimental $\mathrm{C_4H_3O^-}$ spectrum and the calculated energy and vibrational structure of the β-furanide spectrum indicate that we do not observe significant signal from the β-furanyl radical under our experimental conditions. Furthermore, we observe no change in the relative intensity of features in the $\mathrm{C_4H_3O^-}$ spectrum when experimental conditions are varied, which one might expect if signal from two different species were present in the photoelectron spectrum. Lastly, as noted earlier, the negative β values above 2.5 eV binding energy rule out the possibility that the higher energy progression is due to the ground state of β furanyl radical.

3.4.2   C-H$_\alpha$ Bond Dissociation Energy

One of the most significant results of this study is a direct measurement of the C-H$_\alpha$ BDE in order to evaluate the plausibility of various decomposition pathways of furan. The C-H$_\alpha$ BDE of furan, or $\mathrm{DH}_{298}(\mathrm{C_4H_3O\text{-}H_\alpha})$, can be determined through the following thermochemical cycle:[33]

Table 3.4: Optimized geometries of β-furanide anion ($\tilde{X}^1A'$) and β-furanyl radical ($\tilde{X}^2A'$, $\tilde{A}^2A''$), and the calculated net geometry change upon photodetachment (B3LYP/6-311++G(d,p)). Bond lengths are in units of Å, and bond angles are in units of degrees. The net geometry change is defined as the difference in the values of the internal coordinates for the anion and the radical. The bond lengths and angles that undergo the greatest change are boldfaced.
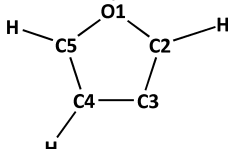
Internal Coordinate	β-Furanide $\tilde{X}^1A'$	β-Furanyl Radical $\tilde{X}^2A'$	$\tilde{A}^2A''$	Geometry Change $\tilde{X}^2A' \leftarrow \tilde{X}^1A'$	$\tilde{A}^2A'' \leftarrow \tilde{X}^1A'$
O1 – C2	1.430	1.377	1.374	**− 0.053**	**− 0.056**
C2 – C3	1.361	1.348	1.433	− 0.013	**+ 0.072**
C3 – C4	1.465	1.422	1.428	**− 0.043**	**− 0.037**
C4 – C5	1.366	1.363	1.376	− 0.003	+ 0.010
O1 – C5	1.362	1.364	1.373	+ 0.002	+ 0.011
C2 – H	1.083	1.075	1.082	− 0.008	− 0.001
C4 – H	1.087	1.077	1.082	− 0.010	− 0.005
C5 – H	1.083	1.077	1.081	− 0.006	− 0.002
∠ O1 – C2 – C3	114.9	107.7	115.4	**− 7.2**	+ 0.5
∠ C2 – C3 – C4	100.7	109.9	99.7	**+ 9.2**	− 1.0
∠ C3 – C4 – C5	110.3	103.8	110.4	**− 6.5**	+ 0.1
∠ C4 – C5 – O1	110.4	111.4	111.3	+ 1.0	+ 0.9
∠ C5 – O1 – C2	103.6	107.2	103.2	+ 3.6	− 0.4

Table 3.5: α-Furanide anion ($\tilde{X}^1$A′) and α-furanyl radical ($\tilde{X}^2$A′, $\tilde{A}^2$A″) vibrational frequencies. All frequencies listed in the table are unscaled calculated harmonic frequencies (B3LYP/6-311++G(d,p)). The modes predicted to be most active, based on the geometry change upon photodetachment and the calculated $\mathbf{K}''$ displacements, are boldfaced.

Mode		**K″ Displacements**		**Frequencies, cm^{-1}**		
		$\tilde{X}^2$A′ ← $\tilde{X}^1$A′	$\tilde{A}^2$A″ ← $\tilde{X}^1$A′	$\tilde{X}^1$A′	$\tilde{X}^2$A′	$\tilde{A}^2$A″
A′	ν_1	-0.0098619	-0.0044959	3191.3	3296.4	3237.8
	ν_2	0.0032261	0.0034002	3186.0	3274.5	3227.9
	ν_3	-0.0063679	-0.0052879	3127.3	3253.9	3206.1
	ν_4	0.038371	-0.019575	1490.5	1542.3	1457.5
	ν_5	-0.0079697	**0.12618**	1432.2	1486.0	**1204.2**
	ν_6	-0.0055620	0.083905	1319.5	1372.1	1054.4
	ν_7	-0.0076154	0.059351	1240.5	1238.5	1319.1
	ν_8	-0.056815	0.019551	1135.2	1170.2	1121.2
	ν_9	-0.096202	-0.011265	1069.8	1136.9	1357.7
	ν_{10}	0.063479	0.0077681	1030.0	1043.3	1013.8
	ν_{11}	**-0.37625**	-0.083552	**785.5**	**1012.6**	688.7
	ν_{12}	**0.28587**	0.055680	**861.5**	**873.74**	878.2
	ν_{13}	**-0.13114**	**0.17189**	**911.7**	**865.8**	**935.9**
A″	ν_{14}	5.7696x10^{-5}	6.1224x10^{-6}	832.5	848.2	920.9
	ν_{15}	-4.6103x10^{-5}	-1.0604x10^{-5}	711.7	762.1	870.5
	ν_{16}	8.1657x10^{-6}	9.0672x10^{-6}	664.8	700.8	792.8
	ν_{17}	-1.1655x10^{-5}	-8.1271x10^{-6}	600.6	613.0	477.5
	ν_{18}	-1.8384x10^{-5}	-6.3188x10^{-6}	608.9	540.7	598.9

[a] Experiment, this work

$$
\begin{array}{rcll}
\text{RH} & \longrightarrow & \text{R}^- + \text{H}^+ & \Delta_{\text{acid}}H_{298}\,(\text{C}_4\text{H}_3\text{O} - \text{H}_\alpha) \\[4pt]
\text{R}^- & \longrightarrow & \text{R} + \text{e}^- & \text{EA}\,(\alpha - \text{C}_4\text{H}_3\text{O}) \\[4pt]
+ \quad \text{H}^+ + \text{e}^- & \longrightarrow & \text{H} & -\text{IE}\,(\text{H})
\end{array}
$$

$$
\overline{\qquad\qquad \text{DH}_{298}\,(\text{RH}) \qquad\quad \text{DH}_{298}\,(\text{C}_4\text{H}_3\text{O} - \text{H}_\alpha) \qquad\qquad} \tag{3.2}
$$
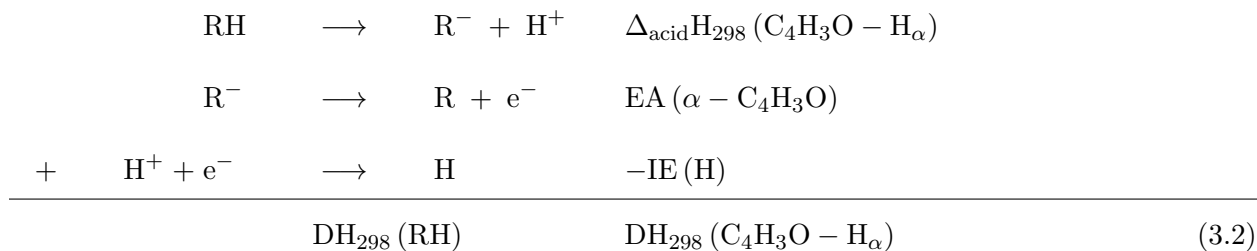
The gas-phase acidity of furan was first measured in 1988 by DePuy, *et al.*,[31] to be 388(3) kcal mol^{-1}, and more recently by Grabowski and Owusu[32] to be 390.7(2) kcal mol^{-1}. The ionization energy of hydrogen is well known: 313.6 kcal mol^{-1}.[84] Now, our measured value for the electron affinity of the α-furanyl radical (1.853(4) eV) enables the first experimental determination of the C-H$_\alpha$ BDE of furan: 119.8(2) kcal mol^{-1}.

In the currently accepted model of the unimolecular decomposition of furan, there are two fragmentation pathways that lead to the experimentally observed products, both of which involve H-rearrangement to a carbene intermediate as the initial step (Fig. 3.6).[53,81] In one pathway, an H$_\alpha$ migrates to the β-position of furan to form the α-carbene, which directly separates into HC$\equiv$CH + CH$_2$=C=O. Alternatively, an H$_\beta$ can move to the α-position to form the β-carbene; further isomerization and decomposition of the β-carbene yields CO + CH$_3$C$\equiv$CH. The CH$_2$=C=CH-CHO intermediate could also lead to the formation of propargyl radical, CH$_2$=C=CH.[81] Our result for the C-H$_\alpha$ BDE substantiates the calculated value[53–55] and validates the accepted decomposition model of furan, in which C-H$_\alpha$ bond scission is prohibitively high in energy to be a viable route to furan decomposition.

This unusually high C-H$_\alpha$ BDE is more than 7 kcal mol^{-1} greater than the C-H BDE of the prototypical aromatic molecule benzene.[33] However, it is in accordance with other five-member heterocycles, which, like furan, have been shown to have very high C-H BDEs. For example, the C-H$_\alpha$ BDE of pyrrole (C$_4$H$_5$N) is 118(1) kcal mol^{-1}.[98] The C-H$_\alpha$ BDEs of the C$_3$H$_4$N$_2$ isomers imidazole[88] and pyrazole[86] are 119(4) kcal mol^{-1} and 121(4) kcal mol^{-1}, respectively. As in the case of the azoles, we attribute the high C-H$_\alpha$ BDE of furan to thermodynamic instability of the

Figure 3.6: Unimolecular decomposition pathways of furan.
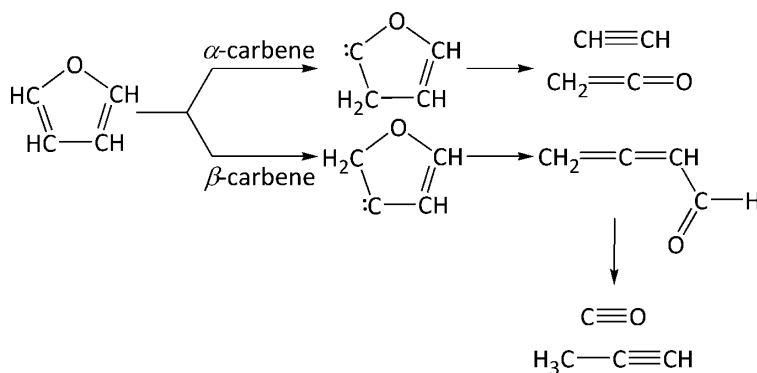
resulting radical. A computational study by Barckholtz *et al.* examined the effects of geometry and spin density on C-H BDEs of aromatic heterocycles[99] and concluded that the primary cause of the instability of the furanyl radical involves the localization of the unpaired electron. As a general rule, a radical is stabilized, thereby decreasing the C-H BDE, when its unpaired electron is delocalized over multiple atoms. In the case of furan, the unpaired electron of the α-furanyl radical is calculated to be almost completely localized on the $\bullet C_\alpha$. In fact, the excess spin density at the $\bullet C_\alpha$ radical center of furanyl radical is calculated to be slightly higher than the excess spin density at the radical center of phenyl radical, indicating that the extent of localization of the unpaired electron of the furanyl radical is slightly greater than that of the phenyl radical.[99] This effectively destabilizes the furanyl radical, leading to the high C-H$_\alpha$ BDE of furan.

3.5 Conclusion

We report the 364-nm photoelectron spectrum of the α-furanide anion. Two electronic states of the α-furanyl radical are observed. At lower binding energy, we find a well-resolved vibrational progression due to α-furanide $\tilde{X}^2A' \leftarrow \tilde{X}^1A'$ photodetachment. The adiabatic EA of the α-furanyl radical is determined to be 1.853(4) eV. Agreement between the $\tilde{X}^2A' \leftarrow \tilde{X}^1A'$ Franck-Condon simulation and the observed spectrum enables identification of several vibrational frequencies of the $\tilde{X}^2A'$ σ-radical ground state, given in Table 3.3.

At higher binding energy, the photoelectron spectrum is dominated by photodetachment to the $\tilde{A}^2 A''$ π-radical excited state of α-furanyl radical. The $\tilde{A}^2 A''$ state lies 0.68(7) eV higher in energy than the $\tilde{X}^2 A'$ state of the α-furanyl radical. The excited state signal is suppressed when the laser is polarized parallel to the direction of photoelectron collection ($\theta = 0°$). We see no evidence of C-H$_\beta$ deprotonation, as Franck-Condon simulations for H$_\beta$ removal have a significantly different structure and energy from the observed photoelectron spectrum.

Using the EA of α-furanyl radical measured in this work, together with the measured gas-phase acidity of furan[32] and the well-known ionization energy of H,[84] we determine the C-H$_\alpha$ BDE of furan to be 119.8(2) kcal mol^{-1} through a thermochemical cycle.[33] This experimental value is consistent with high-level calculations[53–55] that predict an exceptionally high C-H$_\alpha$ bond dissociation energy. The high C-H$_\alpha$ bond dissociation energy—7 kcal mol^{-1} greater than that of benzene[33]—can be attributed to thermodynamic instability of the resulting radical upon H$_\alpha$ loss.

Chapter 4

Dihalomethyl Anions

4.1   Introduction

Dihalomethyl radicals CHX_2 (X = Cl, Br, I) play significant roles in atmospheric chemistry, combustion, and organic synthesis. They are potential players in the depletion of atmospheric ozone. Partially halogenated chlorofluorocarbons—commonly used in refrigerants, fire suppressants, and pesticides—are oxidized in the troposphere to form, among other species, short-lived dihalomethyl radical products.[100–102] These radicals are then photolyzed by near-UV solar radiation to produce halogen atoms,[103,104] that have been implicated in ozone loss and climate change.[105,106] Additionally, dihalomethyl radicals are byproducts of the incineration of hazardous industrial waste such as halogenated hydrocarbons, prompting research into the kinetic and thermodynamic properties of halomethyl radicals.[107] Halomethyl radicals are also of importance in several synthetic reactions, such as cyclopropanation of olefins and diiodomethylation of carbonyl compounds.[108–116]

Even though halomethyl radicals have been investigated by many groups over the past forty years, much is still unknown about the dihalomethyl anions and their corresponding radicals. There have been a considerable number of matrix-isolation infrared spectroscopy studies of dihalomethyl radicals, specifically dichloromethyl radical, where several vibrational frequencies have been determined.[117–124] However, almost all of the observed modes are asymmetric vibrations, which are generally inactive in photoelectron spectroscopy. There has been only one spectroscopic observation of the dichloromethyl anion (FTIR Ar matrix isolation spectroscopy), from which two symmetric vibrational frequencies were determined.[125]

The thermochemistry of $CHCl_2$ and $CHBr_2$ radicals has also been studied by several groups.[126–128] The most recent and extensive experimental investigation was conducted by Nibbering and coworkers,[128] who performed bracketing experiments using FTICR mass spectrometry to study the occurrence or nonoccurrence of electron transfer between a dihalomethyl radical anion and a neutral electron acceptor molecule with a known electron affinity (EA). In this way they determined the EAs of $CHCl_2$ and $CHBr_2$ to be 1.47(4) eV and 1.71(8) eV, respectively. One extensive theoretical study of halomethyl radicals and anions was performed by Li *et al.*[129] They published a computational review of the EAs, molecular structures, and thermochemistry of fluorine-, chlorine-, and bromine-substituted methyl radicals, comparing four independent density functional methods to known experimental values.

We study the dihalomethyl radicals using anion photoelectron spectroscopy. In anion photoelectron spectroscopy, a photon is used to detach an electron from a negative ion to produce a neutral radical. To a first approximation, the intensity of the neutral vibrational levels in a photoelectron spectrum is governed by the Franck-Condon overlap between the ground vibrational wavefunction of the anion with the wavefunctions of the various vibrational levels of the neutral. If there is little difference between the geometry of the anion and neutral, the best Franck-Condon overlap occurs between the ground vibrational wavefunction of the anion and the ground vibrational wavefunction of the neutral. This transition—the origin—appears as the most prominent peak in the spectrum, from which one can readily obtain the adiabatic EA. Also, the width of the photoelectron spectral envelope is minimal in the case of a small geometry change; the Franck-Condon region of the spectrum is confined to an area near the potential minimum of the neutral molecule, where vibrational modes can be well-approximated as harmonic and uncoupled. For larger but still modest geometry changes between the two electronic states, long progressions of the vibrational modes will be observed and the Franck-Condon intensity for the origin peak may be much smaller than for the higher vibrational levels of the neutral corresponding to the vertical transition. Nevertheless, as long as the origin transition can be assigned, such spectra readily yield the quantitative spectroscopic quantities we hope to obtain from photoelectron spectroscopy.[2]

If a very large geometry change occurs between the anion and the neutral, however, spectral analysis becomes more difficult. When the Franck-Condon overlap for the origin transition is insignificant, only the transitions to high vibrational levels of the neutral are observed. At these higher vibrational levels, anharmonicity and mode coupling often become significant. In order to obtain vibrational frequencies and the EA, it is necessary to rely on theory and simulations for guidance. Even if vibrational progressions are well-resolved, it may be impractical to extrapolate to the origin to find the EA.

In this work we examine the photoelectron spectra of $CHCl_2^-$, $CHBr_2^-$, CHI_2^-, and their deuterated analogs. The spectra exhibit extended, partially resolved vibrational progressions that arise from the large geometry change that takes place when an electron is detached from the pyramidal anion, producing an essentially planar neutral radical. The observed vertical detachment energy (VDE), or the binding energy at the maximum of the vibrational progression, of each dihalomethyl radical is in good agreement with the calculated values,[129] providing us with confidence that theory can be used to accurately describe the electronic energies of these species. In contrast, a standard Franck-Condon analysis using normal modes in a Cartesian displacement coordinate system is inadequate for modeling these spectra. The partially resolved vibrational progressions in the simulated spectra do not agree with those observed, and deuteration yields changes in peak spacing opposite to what is predicted with simulation. Most important, the width of the envelope in the simulation is much greater than that which is observed. This failure of the harmonic normal mode simulation to reproduce the width of the measured spectral envelope is not normally observed.

These systems represent a very challenging case for Franck-Condon simulation and analysis, both because there is no detectable Franck-Condon intensity at the origin and because of the very different nature of the vibrational motions in the neutral compared with the anion. As we look to move beyond the standard normal mode treatment, we first consider the use of an internal coordinate system as the basis for the harmonic normal mode analysis, which can be expected to provide a better description of the geometry displacements than Cartesian coordinates but still does

not adequately treat the anharmonicity of the vibrational potentials and coupling between modes. To treat those effects more accurately, we employ a multidimensional, anharmonic coupled-mode analysis for the key active modes. This investigation of dihalomethyl radicals explores the limits of conventional normal-mode analysis and illustrates the approaches required for transitions with a large geometry change and with multiple active, coupled, anharmonic vibrational modes.

4.2   Experimental Methods

The negative ion photoelectron spectrometer used in this experiment has been described in detail elsewhere.[2,34,41] The apparatus consists of four main sections: an ion source, a mass filter, an interaction region with crossed laser and ion beams, and an electrostatic electron kinetic energy analyzer. Negative ions are formed in a flowing afterglow ion source. A microwave discharge containing trace amounts of O_2 gas in He buffer gas ($\sim$0.4 Torr) generates atomic oxygen radical anion, O^-. The O^- anion abstracts an H atom from methane that is added downstream, forming hydroxide anion (OH^-), which then deprotonates the appropriate dihalomethane precursor (CH_2Cl_2, CH_2Br_2, or CH_2I_2, Sigma-Aldrich) to generate dihalomethyl anions: $OH^- + CH_2X_2 \rightarrow CHX_2^- + H_2O$. The deuterated anion CDX_2^- is produced by starting with perdeuterated dihalomethane CD_2X_2 (CD_2Cl_2, CD_2Br_2, and CD_2I_2, Sigma-Aldrich). Sufficient methane is added to ensure complete removal of O^- before CH_2X_2 is introduced, guaranteeing that CHX_2^- is produced exclusively, rather than having some CX_2^- contaminant, which would be formed by the reaction $O^- + CH_2X_2 \rightarrow CX_2^- + H_2O$.[130] Collisions with He buffer gas cool the ions to approximately 300 K. The flow tube can be further cooled with a liquid nitrogen jacket to obtain a "cold spectrum" of ions with temperatures near 150 K. The photoelectron spectra of $CHCl_2^-$ and $CDCl_2^-$ were collected at 150 K, while the spectra of $CHBr_2^-$, $CDBr_2^-$, CHI_2^-, and CDI_2^- were collected at 300 K. Anions are extracted into a differentially pumped region and are accelerated to 735 eV before entering a Wien velocity filter with a mass resolution of $m/\Delta m \sim 40$. The mass-selected ion beam (typically 100–500 pA) is decelerated to 35 eV and focused into the interaction region. Here, the $\sim$0.5 W output from a single-mode continuous-wave argon ion laser operating at 364 nm

(3.40814 eV) is built up to approximately 50 W of circulating power in an optical buildup cavity located within the vacuum system. Photoelectrons ejected in the direction orthogonal to both the laser and ion beams enter a hemispherical energy analyzer. The photoelectron signal is recorded as a function of electron kinetic energy with a position-sensitive detector. The energy analyzer has a resolution of approximately 12 meV under the conditions used for the present experiments.

The electron kinetic energy (eKE) can be converted to electron binding energy (eBE) through the relationship eBE = $h\nu$ - eKE. Absolute kinetic energies are calibrated[43] before each experiment using the well-known EA of O.[45] Additionally, the electron energy scale is corrected for a slight linear compression $(< 1\%)$[2] using the photoelectron spectrum of W^-, which provides a number of known transitions spanning the photoelectron energy range.[46] After making these corrections and accounting for the resolution of the spectrometer and rotational peak profiles, absolute electron binding energies can be determined with an accuracy of 5 meV or better.[2]

A rotatable half-wave plate positioned outside the buildup cavity controls the polarization of the photodetachment radiation. When the angle between the laser polarization and the direction of the collected electrons is 54.7°, referred to as the magic angle, the photoelectron spectrum is independent of the anisotropy parameter of the ejected electrons.[5] Therefore, spectra collected at the magic angle directly reflect the total photodetachment cross section. All spectra shown here were collected with magic angle polarization.

4.3   Theoretical Methods

4.3.1   Computational Chemistry

In this work, we perform all electronic structure calculations using the Gaussian 03 program package.[48] The geometry optimization and frequency calculations were performed with density functional theory using the B3LYP hybrid functional.[49,50] The calculations employ the 6-311++G(d,p) basis set for hydrogen, carbon, and chlorine,[51,52] and pseudopotentials for bromine and iodine that have been shown to work well for halogen-containing compounds.[131–133] Geometries were op-

timized, and harmonic vibrational frequencies and normal mode coordinates were calculated for the doublet anion and the singlet neutral states. The calculated equilibrium structures, relative energies, and frequencies of $CHCl_2$ and $CDCl_2$ are reported in Tables 4.1 and 4.2; results of analogous calculations for $CHBr_2$ and CHI_2 are provided in Tables 4.3, 4.4, 4.5, and 4.6. In addition to the non-planar minimum energy structures of the anionic and neutral $CHCl_2$ and $CDCl_2$, we also consider the low-lying saddle point on the neutral surface in which all four atoms are coplanar. This structure is calculated to be only 162 cm^{-1} above the minimum on this surface at the present level of theory. This energy is smaller than half the harmonic frequency of the CH (CD) pyramidal bend, leading us to expect that when zero-point motion is considered the ground state wavefunction will be delocalized and will have significant amplitude at the transition state geometry. The inversion barriers for $CHBr_2$ and CHI_2 (160 cm^{-1} and 1 cm^{-1}, respectively) are likewise smaller than half the harmonic frequency of the CH (CD) pyramidal bend in both of these systems (Table 4.7).

4.3.2   Franck-Condon Analysis using Cartesian Coordinates

We typically use a Franck-Condon analysis of the vibrational structure in photoelectron spectra to obtain frequencies and equilibrium geometries of the neutral species and to identify the origin transition. This method is used to simulate the photoelectron spectrum of the furanide anion ($C_4H_3O^-$), which we will use as prototype for analysis of photoelectron spectra. The intensity of a vibronic transition I_{FC} is proportional to the square of the Franck-Condon overlap integral

$$I_{FC} = \left[\int \Psi_{v'}(\mathbf{Q}')\Psi_{v''}(\mathbf{Q}'')d\mathbf{Q}' \right]^2 \tag{4.1}$$

where $\Psi_{v'}(\mathbf{Q}')$ is the full, multidimensional vibrational wavefunction of the neutral in quantum state v' as a function of the normal coordinates of the neutral $\mathbf{Q}'$, and $\Psi_{v''}(\mathbf{Q}'')$ is the corresponding vibrational wavefunction of the anion in terms of its normal coordinates $\mathbf{Q}''$. The normal modes are treated as uncoupled and harmonic.[3]

It is necessary to express the wavefunctions of both the anion and the neutral states in terms of the same set of normal coordinates in order to calculate the Franck-Condon overlap integral.

Table 4.1: Calculated, unscaled harmonic vibrational frequencies of $CHCl_2^-$, $CHCl_2$, $CDCl_2^-$, and $CDCl_2$ (B3LYP/6-311++G(d,p)), given in units of cm^{-1}. Experimental frequencies (where available) are listed in italics.

Vibrational Mode		$CHCl_2^-$	$CHCl_2$		$CDCl_2^-$	$CDCl_2$	
			Pyramidal, C_s	Planar, C_{2v}		Pyramidal, C_s	Planar, C_{2v}
A′	ClCCl bend	212.5	304.4	310.4 (A$_1$)	211.5	302.4	308.5 (A$_1$)
	ClCCl sym str	497.2, *532*[a]	748.1, *845*[b]	741.0 (A$_1$)	494.0	715.1, *814*[b]	720.2 (A$_1$)
	CH pyram bend	1029.4	469.5	352.3i (B$_1$)	768.3	384.6	285.6i (B$_1$)
	CH stretch	2917.8, *2764*[a]	3216.7	3255.8 (A$_1$)	2146.4	2368.8	2398.6 (A$_1$)
A″	ClCCl asym str	399.8	865.6, *902*[c]	897.5 (B$_2$)	396.8	805.1, *814*[c]	818.0 (B$_2$)
	CH asym wag	1172.2	1249.7, *1226*[c]	1242.5 (B$_2$)	846.5	965.0, *974*[c]	979.3 (B$_2$)

[a] Experiment, Ar matrix[125]
[b] Experiment, REMPI[134]
[c] Experiment, Ar matrix[117]

Table 4.2: Calculated equilibrium structures of $CHCl_2^-$ ($CDCl_2^-$) and $CHCl_2$ ($CDCl_2$) obtained using B3LYP/6-311++G(d,p). Bond lengths are in units of Å, and angles are in units of degrees. The geometry change upon photodetachment is defined as the difference in the values of the internal coordinates for the anion and the radical.

Internal Coordinate	$CHCl_2^-$ ($CDCl_2^-$)	Geometry Change, neutral – anion	
		Pyramidal, C_s	Planar, C_{2v}
r_{CH}	1.105	-0.025	-0.028
r_{CCl}	1.958	-0.239	-0.249
θ_{HCCl}	96.0	20.7	23.6
θ_{ClCCl}	105.2	14.1	15.6
$\tau_{ClCHCl'}$	106.0	44.2	74.0

Table 4.3: Calculated, unscaled harmonic vibrational frequencies of $CHBr_2^-$, $CHBr_2$, $CDBr_2^-$, and $CDBr_2$, given in units of cm^{-1}. Results were obtained using B3LYP/6-311++G(d,p) for C and H, and basis set and pseudopotentials for Br developed by Stoll *et al.*[131–133]

Vibrational Mode		$CHBr_2^-$	$CHBr_2$		$CDBr_2^-$	$CDBr_2$	
			Pyramidal, C_s	Planar, C_{2v}		Pyramidal, C_s	Planar, C_{2v}
A′	BrCBr *bend*	127.4	183.5	186.4 (A_1)	127.2	183.0	185.8 (A_1)
	BrCBr *sym str*	432.3	614.9	597.5 (A_1)	426.9	577.1	577.7 (A_1)
	CH *pyram bend*	957.1	410.4	*318.9i* (B_1)	710.9	337.9	*256.3i* (B_1)
	CH *stretch*	2935.1	3205.8	3235.8 (A_1)	2158.2	2359.6	2382.4 (A_1)
A″	BrCBr *asym str*	373.9	752.9	779.5 (B_2)	368.9	703.7	720.2 (B_2)
	CH *asym wag*	1110.7	1173.8	1170.8 (B_2)	801.3	894.6	902.9 (B_2)

Table 4.4: Calculated equilibrium structures of $CHBr_2^-$ ($CDBr_2^-$) and $CHBr_2$ ($CDBr_2$). Results were obtained using B3LYP/6-311++G(d,p) for C and H, and basis set and pseudopotentials for Br developed by Stoll *et al.*[131–133] Bond lengths are in units of Å, and angles are in units of degrees. The geometry change upon photodetachment is defined as the difference in the values of the internal coordinates for the anion and the radical.

Internal Coordinate	$CHBr_2^-$ ($CDBr_2^-$)	CHBr$_2$ (CDBr$_2$)		Geometry Change	
		Pyramidal, C_s	Planar, C_{2v}	Pyramidal, C_s	Planar, C_{2v}
r_{CH}	1.106	1.081	1.079	-0.025	-0.027
r_{CBr}	2.097	1.862	1.852	-0.235	-0.245
θ_{HCBr}	95.5	116.4	118.9	20.9	23.4
θ_{BrCBr}	106.4	120.6	122.1	14.2	15.7
$\tau_{BrCHBr'}$	107.1	151.7	180.00	44.6	72.9

Table 4.5: Calculated, unscaled harmonic vibrational frequencies of CHI_2^-, CHI_2, CDI_2^-, and CDI_2, given in units of cm^{-1}. Results were obtained using B3LYP/6-311++G(d,p) for C and H, and basis set and pseudopotentials for I developed by Stoll *et al.*[131–133]

Vibrational Mode		CHI_2^-	CHI$_2$		CDI_2^-	CDI$_2$	
			Pyramidal, C_s	Planar, C_{2v}		Pyramidal, C_s	Planar, C_{2v}
A′	ICI *bend*	93.7	129.1	132.0 (A$_1$)	93.6	117.7	131.7 (A$_1$)
	ICI *sym str*	377.1	508.7	506.4 (A$_1$)	372.1	489.2	489.0 (A$_1$)
	CH *pyr bend*	875.3	151.7	*88.4i* (B$_1$)	648.5	133.9	*68.2i* (B$_1$)
	CH *stretch*	2935.8	3210.0	3213.4 (A$_1$)	2157.8	2362.0	2364.6 (A$_1$)
A″	ICI *asym str*	372.6	720.7	724.0 (B$_2$)	365.9	670.9	673.1 (B$_2$)
	CH *asym wag*	1067.5	1130.8	1130.0 (B$_2$)	771.8	862.8	863.4 (B$_2$)

Table 4.6: Calculated equilibrium structures of CHI_2^- (CDI_2^-) and CHI_2 (CDI_2). Results were obtained using B3LYP/6-311++G(d,p) for C and H, and basis set and pseudopotentials for I developed by Stoll *et al.*[131–133] Bond lengths are in units of Å, and angles are in units of degrees. The geometry change upon photodetachment is defined as the difference in the values of the internal coordinates for the anion and the radical.

Internal Coordinate	CHI_2^- (CDI_2^-)	CHI$_2$ (CDI$_2$)		Geometry Change	
		Pyramidal, C_s	Planar, C_{2v}	Pyramidal, C_s	Planar, C_{2v}
r_{CH}	1.107	1.081	1.080	-0.026	-0.027
r_{CI}	2.261	2.029	2.027	-0.232	-0.234
θ_{HCI}	95.9	117.3	117.7	21.4	21.8
θ_{ICI}	108.7	124.5	124.7	15.8	16.0
$\tau_{ICHI'}$	109.6	169.6	180.0	60.0	70.4

Table 4.7: The experimental and calculated (B3LYP/6-311++G(d,p)) electron affinity (EA), vertical detachment energy (VDE), and peak spacing near the VDE for each of the dihalomethyl radicals. Basis sets and pseudopotentials for Br and I were developed by Stoll *et al.*[131–133]

		CHCl$_2$	CDCl$_2$	CHBr$_2$	CDBr$_2$	CHI$_2$	CDI$_2$
EA, eV	*Experiment*	1.3(2)^a	1.3(2)^a	1.9(2)^a	1.9(2)^a	1.9(2)^a	1.9(2)^a
		1.47(4)^b		1.71(8)^b			
	Calculation	1.430	1.433	1.744	1.747	1.820	1.826
VDE, eV	*Experiment*	2.6487	2.6815	3.0181	3.0171	2.8287	2.9057
	Calculation	2.8621	2.8630	2.8829	2.8836	2.8271	2.8271
Peak Spacing	*Experiment*	190(50)	231(6)	520(30)	170(40)	440(40)	380(60)
Near VDE, cm^{-1}	*Normal Mode*	240(10)	361(9)	205(1)	303(9)	540(10)	511(7)
	(2 + 1) − D	150(20)	240(10)	--	--	--	--
Inversion	*Calculation*	162	162	160	160	1	1
Barrier, cm^{-1}							

^{a} Estimates of EA were obtained by subtracting the calculated difference in energy between the VDE and the EA (VDE$_{calc}$ - EA$_{calc}$) from the experimentally measured VDE using Eq. 4.8.
^{b} Experiment, Fourier transform ion cyclotron resonance mass spectrometry [128]

The Duschinsky transformation[11] is applied to express the normal mode coordinates of the neutral in the basis set of the normal mode coordinates of the anion. The transformation is given by

$$\mathbf{Q}'' = \mathbf{J}''\mathbf{Q}' + \mathbf{K}''. \tag{4.2}$$

Here, $\mathbf{K}''$ is the vector that describes the difference in the nuclear equilibrium positions between the anion and neutral in terms of the normal coordinates of the anion. The Duschinsky rotation matrix $\mathbf{J}''$ accounts for mixing of normal modes resulting from the discrepancy between the normal mode coordinates of the anion and neutral.[3]

The Franck-Condon profiles of the photoelectron spectra are simulated using the PESCAL program.[21] Since none of the frequencies of the allowed vibrational modes for the dihalomethyl species are known experimentally, the simulations use theoretical geometries, normal mode vectors, and vibrational frequencies of the anion and neutral states calculated using the Gaussian 03 software package.[48] The normal mode eigenvectors ($\mathbf{Q}'$, $\mathbf{Q}''$) are expressed in terms of mass-weighted Cartesian atomic displacement coordinates, and the Duschinsky rotation $\mathbf{J}''$ matrix and displacement vector $\mathbf{K}''$ are determined using Eq. 4.2. The Franck-Condon intensities for all six modes as well as their combination bands and hot bands (at 150 K for $CHCl_2^-$ and $CDCl_2^-$; and at 300 K for $CHBr_2^-$, $CDBr_2^-$, CHI_2^-, and CDI_2^-), are computed in the harmonic oscillator approximation including Duschinsky rotation using the Sharp-Rosenstock-Chen method.[4,8,20] The normal mode simulations of $CHCl_2^-$ and $CDCl_2^-$ are computed with an EA of 1.3 eV. The individual vibronic peak contours are approximated as a Gaussian function with a 12 meV FWHM, consistent with instrumental resolution.

4.3.3   Franck-Condon Analysis using Internal Coordinates

The normal mode analysis using orthogonal Cartesian displacement coordinates is easily implemented computationally for molecules of arbitrary size and connectivity, and therefore has become the conventional method.[9] These normal modes are, to lowest order, identical to the normal modes in internal coordinates (bond lengths and angles) for infinitesimal displacements, but

become less reasonable for large geometry changes. The older **GF**–matrix techniques using internal coordinates as described by Wilson *et al.*,[10] as well as more recent formulations,[27] require calculations specific to each system. It has been shown that using curvilinear internal coordinates in the normal mode analysis is more accurate for Franck-Condon simulations of systems with large geometry changes.[13,19] Because the internal coordinates more naturally represent the vibrational potential energy surfaces, they are less likely to induce artificial couplings between modes in the mode displacements, **K**, and the Duschinsky rotation matrix.

We implement the harmonic normal mode analysis using the internal coordinates represented by the three bond stretches (CH, CX, and CX$'$) and three bond angles (HCX, HCX$'$, and XCX$'$). We start from the force constant matrix in internal coordinates from Gaussian 03,[48] and derive the Wilson **B**–, **G**–, and **F**–matrices analytically.[10] The Wilson **GF** method[10] is used to compute the normal modes and frequencies, which are verified to match those calculated using the Cartesian coordinate system. These analytical calculations were implemented using Mathematica (Wolfram Research Inc.). The resulting normal mode vectors in the internal displacement coordinate basis are then used to calculate *via* Eq. 4.2 the corresponding **K**$''$ displacements and Duschinsky **J**$''$ rotation matrix, which is now a non-orthogonal transformation.[13,19] A modified version of PESCAL[21] is used to obtain the Franck-Condon factors (FCFs), again in the harmonic oscillator approximation including Duschinsky rotation using the Sharp-Rosenstock-Chen method.[4,8,20] The spectra of CHCl$_2^-$ and CDCl$_2^-$ are simulated at 150 K, while the spectra of CHBr$_2^-$, CDBr$_2^-$, CHI$_2^-$, and CDI$_2^-$ are simulated at 300 K. As before, the simulations of CHCl$_2^-$ and CDCl$_2^-$ are computed with an EA of 1.3 eV, and the individual vibronic transitions are convoluted over the instrumental resolution function for comparison with experiment.

4.3.4   (2 + 1) − Dimensional Anharmonic Coupled-Mode Analysis

Although the harmonic normal mode analysis using the internal coordinate system is an improvement over the Cartesian coordinates for systems with large geometry changes, it does not address either the anharmonicity of the vibrational potentials or coupling between vibrational

modes within one electronic state. To address these issues, we take a multidimensional anharmonic coupled-mode approach instead. For this challenging system, we explicitly couple the two bend modes and convolute the resulting spectrum with the spectrum obtained from a one-dimensional treatment of the ClCCl stretch in an overall $(2 + 1)$ – dimensional coupled mode analysis.

First, we must choose a reduced set of vibrations to couple and solve collectively that is appropriate for the dihalomethyl system. Based on calculated geometry changes between the minimum energy structure of the anion and neutral species listed in Table 4.2, we anticipate that the three most important modes contributing to the photoelectron spectrum will be the ClCCl symmetric stretch, the HCCl (DCCl) symmetric bend, and, most importantly, the out-of-plane distortion of $CHCl_2$ ($CDCl_2$). We generate a calculated photoelectron spectrum in two parts. The first focuses on the ClCCl symmetric stretch contribution, while the second involves the HCCl symmetric bend and out-of-plane bending modes. We explicitly couple the two bending modes because we calculate a large change in the HCCl angle as the out-of-plane bend is distorted from the planar structure. This is illustrated in Fig. 4.1, in which the potential energy of $CHCl_2$ (dashed blue) and $CHCl_2^-$ (red) are plotted as a function of the out-of-plane distortion, defined as the $ClCHCl'$ improper torsion angle $\tau_{ClCHCl'}$, minimizing the energy with respect to the displacements of the remaining coordinates.[27] This improper torsion is defined as the angle between the plane containing the carbon, hydrogen, and one of the chlorine atoms and the plane that contains the carbon, hydrogen, and the other chlorine atom, as illustrated in the inset in Fig. 4.1. The minimum energy structure of the anion corresponds to a value of $\tau_{ClCHCl'}$ of 106°. Based on the plots of the other three internal coordinates along this potential cut (Fig. 4.2), we find that there are large differences in the values of the HCCl angles (green), and, to a lesser extent, the CCl distance (dashed purple) as $\tau_{ClCHCl'}$ is decreased from 180° to 106°. The changes in the CH bond length (blue) are much smaller. Because the equilibrium CH bond length is effectively independent of $\tau_{ClCHCl'}$ and its frequency is significantly higher than the other symmetry-allowed vibrational modes, we expect that the CH stretching vibrational motion will not contribute to the photoelectron spectrum or couple strongly to active modes. This expectation was further confirmed by reduced dimensional studies involving

this mode and the out-of-plane distortion.

Once the active modes have been selected, we evaluate cuts through the six-dimensional potential energy surface as functions of these coordinates. For the two-dimensional cut along the two bending coordinates, we allow the remaining two symmetric coordinates to vary in order to minimize the electronic energies. This cut is evaluated over a range from $\theta_{\text{HCCl}} = 60°$ to $140°$ (in increments of $10°$, with both HCCl angles kept equal), and from $\tau_{\text{ClCHCl}'} = 60°$ to $300°$ (in increments of $10°$). A bicubic spline interpolation scheme was used to interpolate the potential between these points. The cut along the ClCCl stretch coordinate was evaluated over a range of r_{CCl} from 1.2 Å to 2.7 Å in increments of 0.05 Å, with the two CCl distances constrained to be equal. For this cut the other coordinates are constrained to their equilibrium values on the anion surface. Two-dimensional cuts through the anion and neutral potentials are shown in Fig. 4.3.

Using these surfaces, we evaluate the vibrational energies and wavefunctions for the two subsystems. Just as the potentials are evaluated independently, two separate calculations are performed to obtain these quantities. To examine the ClCCl symmetric stretch, we define the coordinate s as the symmetric combination of the two CCl distances r_{CCl}, which are constrained by symmetry to be equal. Thus, for the ClCCl stretch, we define $s = \sqrt{2}r_{\text{CCl}}$. As such,

$$H = -\frac{\hbar^2}{2} \left[\frac{1}{m_{\text{Cl}}} + \frac{1 + \cos \theta^{(\alpha)}_{\text{CHCl},e}}{m_{\text{C}}} \right] \frac{\partial^2}{\partial s^2} + V^{(\alpha)}(s) \tag{4.3}$$

where α can represent the potential for either the anion or neutral system. As there is no dependence of the kinetic energy on the mass of the hydrogen atom, the energies and wavefunctions will be identical for $CHCl_2$ and $CDCl_2$. The Schrödinger Equation is evaluated in a discrete variable representation (sinc-DVR), as described by Colbert and Miller.[135] Specifically, 500 DVR points are used with $r_{\text{CCl}} = s/\sqrt{2}$ ranging from 1 to 2.5 Å.

In a second calculation, we evaluate the energies and wavefunctions for the two-dimensional bend problem, where the two bend coordinates are denoted $\tau_{\text{ClCHCl}'}$ for the out-of-plane distortion, and θ_s for the symmetric HCCl bend. We define the HCCl symmetric bend as the symmetric

Figure 4.1: $CHCl_2$ (dashed blue) and $CHCl_2^-$ (red) potential energy curves as a function of the out-of-plane angle ($\tau_{ClCHCl'}$).
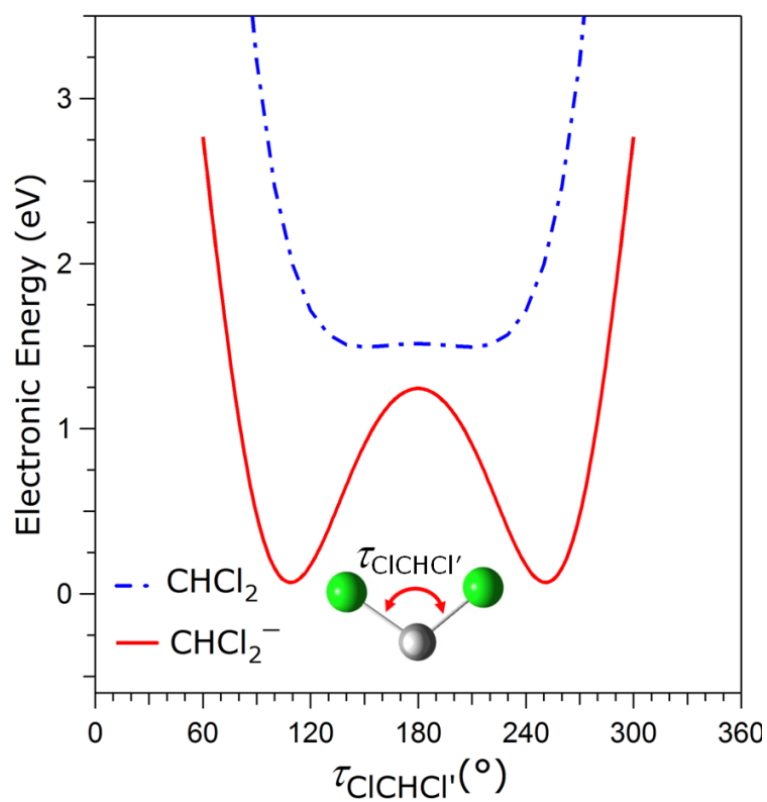
Figure 4.2: Change in the $CHCl_2$ internal coordinates θ_{HCCl} (green), r_{CCl} (dashed purple) and r_{CH} (blue) as the out-of-plane angle $\tau_{ClCHCl'}$ is varied.
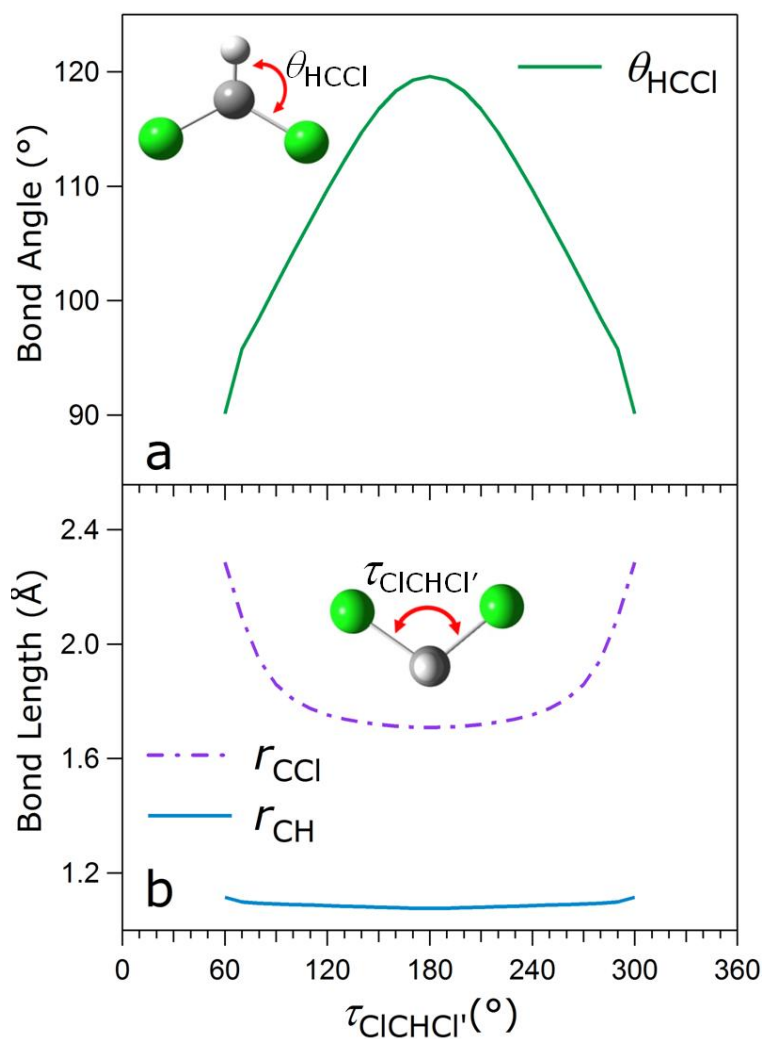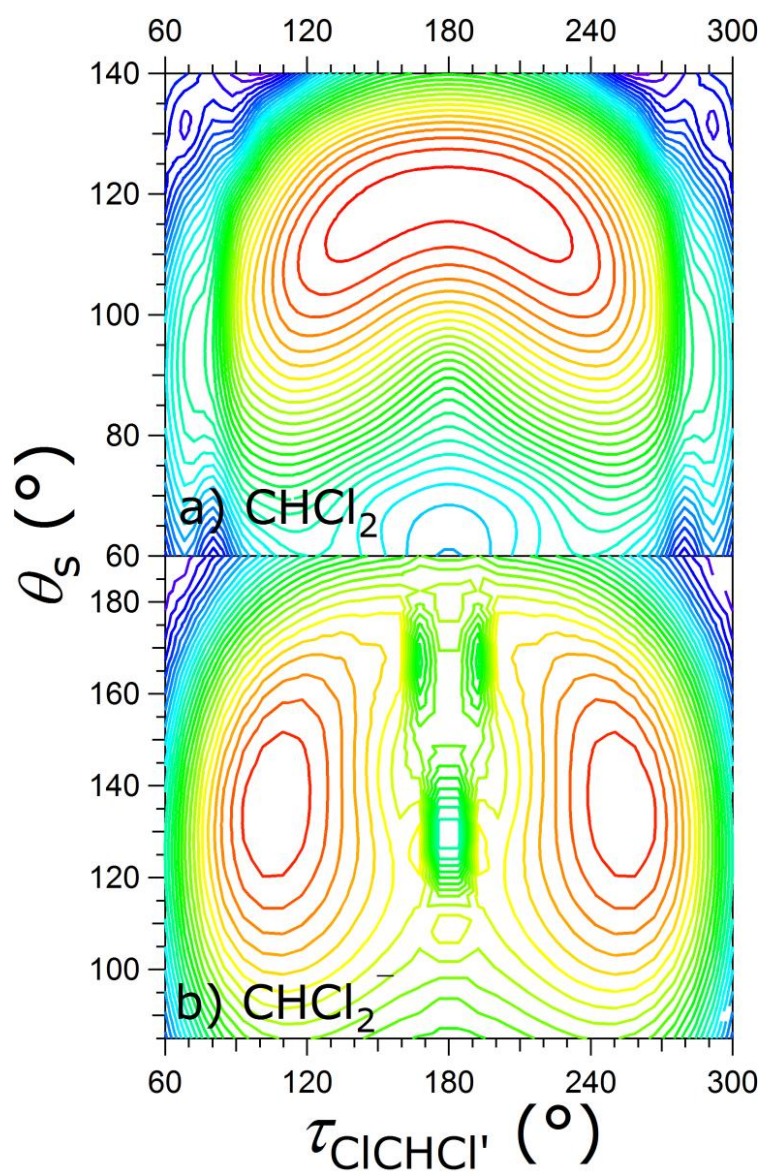
Figure 4.3: Two-dimensional cuts through the (a) CHCl$_2$ and (b) CHCl$_2^-$ potential energy surfaces.

combination of the two equivalent θ_{HCCl}. Thus, $\theta_s = \sqrt{2}\theta_{\text{HCCl}}$. Here,

$$H = \frac{1}{2}\left[p_\tau G_{\tau,\tau}p_\tau + p_\tau G_{\tau,\theta}p_\theta + p_\theta G_{\tau,\theta}p_\tau + p_\theta G_{\theta,\theta}p_\theta + V_{2d}^{(\alpha)}(\tau,\theta_s) + V'(\tau,\theta_s)\right] \qquad (4.4)$$

For this expression, the values of the $\mathbf{G}$–matrix elements and V' are obtained from the tabulation of Frederick and Woywod.[27] The $\mathbf{G}$–matrix elements depend on the two bend coordinates. The matrix representation of multiplicative operators, including the $\mathbf{G}$–matrix elements, are diagonal in the DVR whereas the momentum operators are not. As a result, in a DVR, the matrix elements have the form

$$\langle n_\tau, n_\theta|p_ip_jG_{i,j}(\tau,\theta)|m_\tau,m_\theta\rangle = \langle n_\tau, n_\theta|p_ip_j|m_\tau,m_\theta\rangle G_{i,j}(\tau_{m_\tau},\theta_{m_\theta}) \qquad (4.5)$$

and

$$\langle n_\tau, n_\theta|G_{i,j}(\tau,\theta)p_ip_j|m_\tau,m_\theta\rangle = \langle n_\tau, n_\theta|p_ip_j|m_\tau,m_\theta\rangle G_{i,j}(\tau_{n_\tau},\theta_{n_\theta}). \qquad (4.6)$$

Since analytical expressions for $\langle n_\tau, n_\theta|p_ip_j|m_\tau,m_\theta\rangle$ in a sinc-DVR are known,[135–137] expressing the terms in the kinetic energy operator in this form greatly simplifies the calculation. To ensure that the kinetic energy operator is Hermitian, we rewrite the kinetic terms in Eq. 4.4 as[136]

$$p_iG_{ij}(q_i,q_j)p_j = \frac{1}{2}\left[p_ip_jG_{i,j}(q_i,q_j) + G_{i,j}(q_i,q_j)p_ip_j - \hbar^2\frac{\partial^2 G_{ij}}{\partial q_i\partial q_j}\right] \qquad (4.7)$$

Finally, the matrix elements of p_i in a sinc-DVR have been worked out by Luckhaus.[136] In this work, we use an infinite grid limit of this expression, reported in Gardeinier *et al.*[137] For the calculations reported here, we use fifty evenly spaced grid points in each dimension and a range that spans the range of electronic energies.

Within the Franck-Condon approximation, the calculated photoelectron spectrum is obtained by first evaluating the squared overlaps of the vibrational states of the anion with energies less than 1000 cm^{-1} above the ground vibrational state with all of the calculated states on the neutral surface for each of the two potential cuts described above. To account for the increase in the frequency of the ClCCl stretch between the minimum energy geometry on the neutral surface to the region of the potential that is sampled in the spectrum (e.g., the minimum energy geometry of the anion), the

anharmonic energies of the ClCCl stretch are multiplied by 1.08. This is the ratio of the frequency of this mode when $\tau_{\mathrm{ClCHCl'}}$ and θ_s are constrained to their values in the vertical and equilibrium geometries on the neutral surface. We combine the two stick spectra, weighting the product of the overlaps by a Boltzmann factor of $\exp[-(E_{\mathrm{stretch}} + E_{\mathrm{bend}})/k_b T]$, where the energies are obtained from the one- and two-dimensional calculations and $T = 150$ K . We then convolute the resulting spectrum with Gaussian functions with FWHM of 12 meV. The calculated spectra were shifted so that the adiabatic EA is in agreement with the experimental value of 1.3 eV.

4.4   Results

4.4.1   Experimental Spectra and Qualitative Analysis

The anion photoelectron spectra of CHCl_2^-, CHBr_2^-, CHI_2^-, and their deuterated analogs are shown in Fig. 4.4. All of the spectra display extensive vibrational progressions resulting from the large geometry change that takes place upon photodetachment. The most prominent features in the spectra result from Franck-Condon overlap with high vibrational levels of the neutral. The calculated EA and calculated VDE of each dihalomethyl radical is marked with a labeled arrow in Fig. 4.4. The calculated EAs are consistent with previous experimental EA determinations of CHCl_2 and CHBr_2 (Table 4.7).[128] In each case, the origin is calculated to lie at least 1 eV below the VDE—approximately the eBE at the peak of the vibronic band—in a region of negligible signal because of poor Franck-Condon overlap. However, the calculated VDEs, computed by subtracting the energy of the anion from the energy of the neutral at the equilibrium geometry of the anion, agree reasonably well with the measured VDEs of the dihalomethyl anions, as shown in Fig. 4.4 and listed in Table 4.7. From the Franck-Condon simulations, the origin transition is calculated to have approximately 10^{-5} the intensity of the peak at the VDE. Thus, the origin will not be experimentally observable. The calculation of the difference in energy between the VDE and the EA should be fairly accurate in the case of rigid anions like the dihalomethyl anions, so we can use

the following equation to obtain an estimate of the EA:

$$\mathrm{EA}_{est} = \mathrm{VDE}_{exp} - (\mathrm{VDE}_{calc} - \mathrm{EA}_{calc}), \tag{4.8}$$

where

$$\mathrm{VDE}_{calc} = \mathrm{E}(neutral\ at\ anion\ eqm\ geom) - \mathrm{E}(anion\ at\ anion\ eqm\ geom) \tag{4.9}$$

and

$$\mathrm{EA}_{calc} = \mathrm{E}(neutral\ at\ neutral\ eqm\ geom) - \mathrm{E}(anion\ at\ anion\ eqm\ geom). \tag{4.10}$$

In this way, an estimate of the EA of each dihalomethyl radical studied is determined using the experimental VDE and the calculated difference between the energy of the anion and the energy of the neutral at the anion equilibrium geometry. These results are summarized in Table 4.7. Our estimates are consistent with the previous EA determinations of $CHCl_2$ and $CHBr_2$.[128] The estimated EA of each dihalomethyl radical obtained from Eq. 4.8 is used as the EA for the simulations and calculations of that radical.

There are several indications that the structure in the spectra does not result from a single vibrational progression and instead arises from multiple active vibrational modes with several vibronic transitions lying under each peak. First, the spacing between the peaks in the spectrum of $CDCl_2^-$ does not correspond to the calculated frequency of any of the symmetric vibrational modes. Second, isotopic substitution has an unexpected effect on the spectrum of $CHCl_2^-$. The spectrum generally becomes more congested upon deuteration, as seen in the spectra of $CHBr_2^-$ and, to a lesser extent, of CHI_2^-. However, the spectrum of $CDCl_2^-$ has more resolved structure than that of $CHCl_2^-$, implying that the observed structure is due to accidental resonance among two or more vibrational modes, rather than to a single vibrational progression. Also, the peak widths near the VDE are at least 20 meV, significantly greater than our experimental resolution of about 12 meV. Furthermore, the modulation depth of the peaks and the peak spacings change across the progression, a result of anharmonicity causing the vibronic transitions to move into and out of resonance.

Figure 4.4: Experimental spectra of the dihalomethyl anions (a) $CHCl_2^-$, (b) $CHBr_2^-$, (c) CHI_2^-, (d) $CDCl_2^-$, (e) $CDBr_2^-$, and (f) CDI_2^-. The calculated (B3LYP/6-311++G(d,p)) adiabatic electron affinity (EA) and vertical detachment energy (VDE) for each dihalomethyl radical is marked with a labeled arrow.
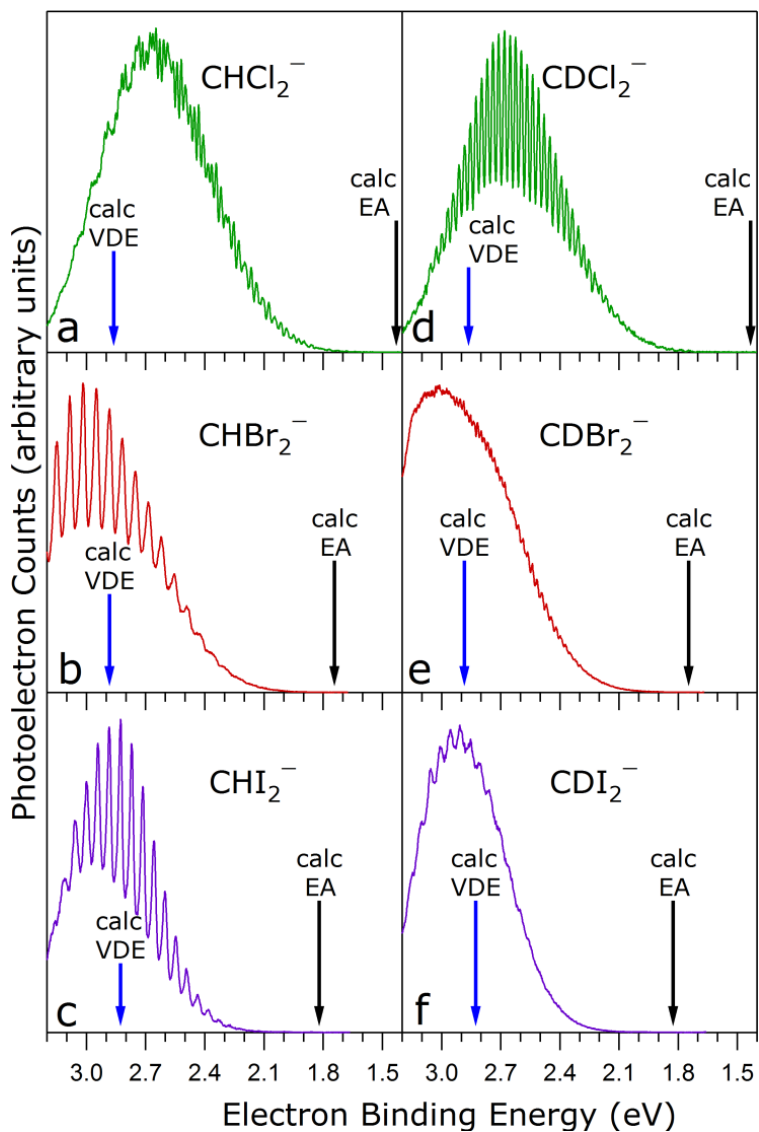
Although the spectra show that multiple active vibrational modes give rise to the observed structure, the similarity of the $CHBr_2^-$ and CHI_2^- spectra suggests that the out-of-plane bend is active, and that the spacing of the peaks roughly corresponds to the frequency of this motion in the neutral species. In $CHBr_2$ the average peak spacing is $520(30)$ cm^{-1}, and in CHI_2 it is $440(40)$ cm^{-1} near the VDE. All of these observations are summarized in Table 4.7.

Because a large geometry change takes place when an electron is removed from a dihalomethyl anion to generate the floppy radical, further quantitative analysis of the spectra is difficult. We now turn to calculations and simulations to elucidate the spectra. To illustrate the challenges involved in analyzing the photoelectron spectra of molecules that undergo large geometry changes upon photodetachment, we examine in detail the agreement between experiment and theory for $CHCl_2^-$ and $CDCl_2^-$.

4.4.2   Franck-Condon Simulation using Normal Mode Analysis in Cartesian Coordinates

We initially simulate the spectra of $CHCl_2^-$ and $CDCl_2^-$ with Franck-Condon analysis using the methods outlined in Section 4.3.2, the harmonic oscillator approximation with normal modes calculated in the mass-weighted Cartesian displacement coordinate system. The Duschinsky rotation between the normal mode vectors of the anion and neutral is fully treated. This standard approach very accurately simulates electronic spectra that involve relatively small displacements of equilibrium geometries of the neutral relative to the anion;[13,22,23,138] in those cases, the most prominent features in the spectra arise from overlap between the lowest vibrational levels of each state, where the vibrations are well-described as decoupled harmonic oscillators. Furthermore, if the equilibrium geometries and bonding of the two states are very similar, the character of their normal modes is essentially the same and the Duschinsky rotation effects may be minor.

The furanide anion illustrates such a case. The Franck-Condon simulation of the photoelectron spectrum of the furanide anion,[138] shown in Fig. 4.5(a), quantitatively reproduces the measured spectral envelope and vibrational structure. In the case of the furanide anion, the relatively

rigid ring structure constrains the molecule to a modest geometry change upon photodetachment. Thus, we observe a prominent origin peak from which we directly obtain the EA of the furanyl radical. Despite the fact that furanyl has 13 allowed symmetric vibrational modes—compared to four symmetric modes in the dihalomethyl anions—the furanide spectrum is dominated by signatures from only three of these. As one would intuitively expect, the most active vibrations are ring deformations localized around the radical center, whence the excess electron is detached. The excellent agreement between the normal-mode based simulation and experiment enables assignment of the spectral features, allowing unequivocal determination of the EA and identification of the frequencies of the most active vibrational modes. Furthermore, deviations from the predicted photoelectron spectrum occur at higher vibrational levels of the furanyl radical and can generally be corrected by simply accounting for frequency shifts of the transitions due to anharmonicity. Although the furanide anion is much larger and has many more allowed vibrational modes than the dihalomethyl anions, the fact that it undergoes a relatively small geometry change upon photodetachment means that its photoelectron spectrum is relatively straightforward to interpret, and from it we can determine a great deal of information about the furanyl radical. The Franck-Condon simulation—with vibrational parameters extracted from Gaussian output files and using the PESCAL program[21] to generate FCFs and convolute over the instrumental resolution and rotational contours—is largely an automated process in such a case.

Because the normal mode method for modeling photoelectron spectra has proven so powerful in the past, we first employ a Franck-Condon analysis using normal modes based in Cartesian coordinates to interpret the photoelectron spectra of the dihalomethyl anions. In Fig. 4.5(b), we compare the experimental spectrum of $CDCl_2^-$ to its Franck-Condon simulation using the Cartesian coordinate system. In stark contrast to the excellent agreement between simulation and experiment displayed in the furanide case (Fig. 4.5(a)), the simulation in panel (b) utterly fails to reproduce the spectral envelope of the observed $CDCl_2^-$ spectrum. Similarly broad progressions are calculated for the other dihalomethyl anions. Examination of the Franck-Condon intensities shows that the reason for the disparity in the width of the spectral envelope is due to false strong activity of the

Figure 4.5: Comparison between theory and experiment for two systems: (a) the furanide anion, $C_4H_3O^-$, and (b − d) $CDCl_2^-$. (a) The photoelectron spectrum (300 K, $\theta = 0°$) of furanide is compared to its ground state simulation using normal mode analysis in Cartesian coordinates. This is in sharp contrast to (b) the agreement between the photoelectron spectrum of $CDCl_2^-$ (150 K) and its simulation using normal mode analysis in Cartesian coordinates, which fails to reproduce the width of the spectral envelope. (c) Improvement in the agreement between experiment and the normal mode simulation is achieved by switching to an internal coordinate representation. (d) The width of the calculated spectral envelope is further reduced by using $(2 + 1)$ − dimensional anharmonic coupled-mode analysis. All $CDCl_2^-$ calculated and simulated spectra were calculated at 150 K and were shifted to match the experimental EA of 1.3 eV.
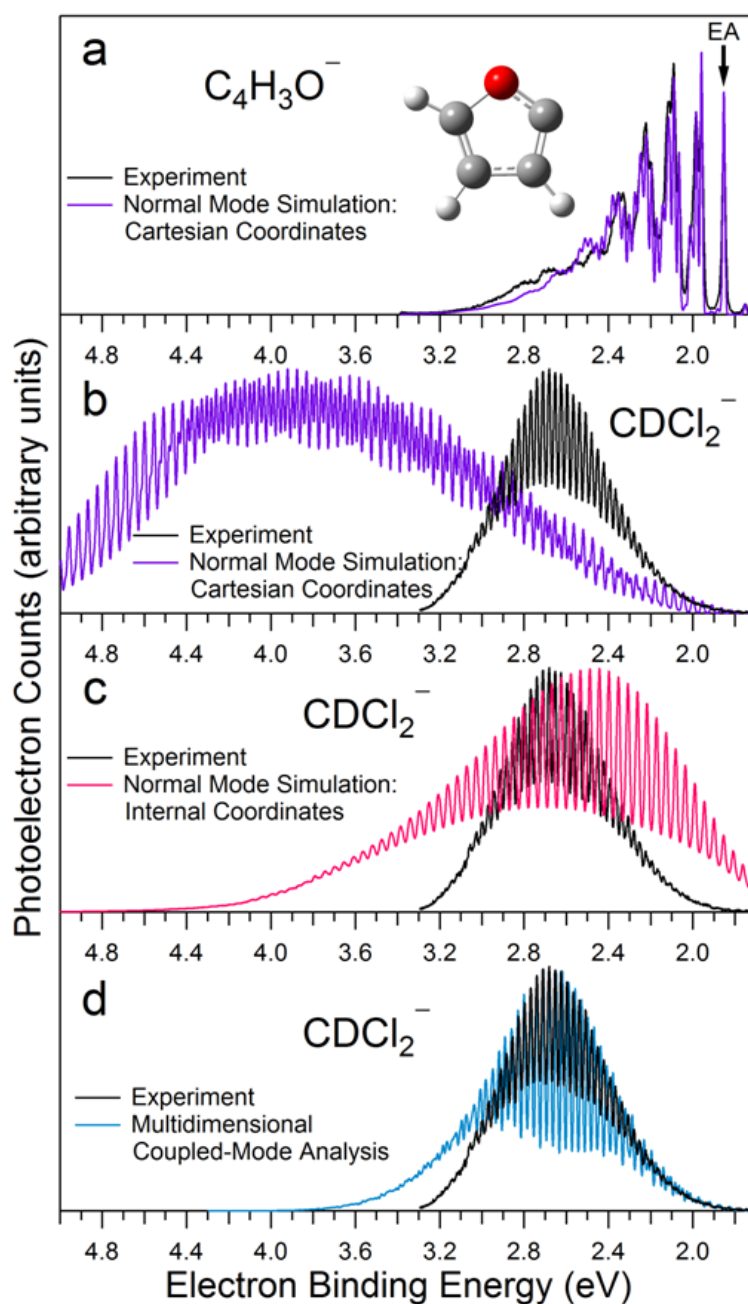
CH (CD) stretch vibrational mode. This activity is inconsistent with the calculated geometries (Table 4.2), which show only a relatively small change in the CH bond length between the anion and neutral states (an order of magnitude smaller than the CCl bond length change). Evidently, the only way the rectilinear Cartesian coordinates can reproduce the large geometry change is by inducing a spurious displacement in the CH stretch normal mode, in combination with other modes. Thus, there is a non-physical activation of the CH stretch associated with the pyramidal bend. Similar mode mixing has been observed for other molecules undergoing large geometry changes upon photodetachment,[10,13,19,25,26] where a large geometry displacement in one Cartesian coordinate is partially projected onto the others, resulting in the appearance of vibrational progressions in the computed spectrum that are not experimentally observed. For a molecule undergoing a substantial geometry change upon photodetachment, this effect is exacerbated when the Cartesian coordinate representation is used, resulting in the dramatically extended vibrational progression in Fig. 4.5(b). Such poor agreement does not enable quantitative analysis of the photoelectron spectra of the dihalomethyl anions, so we must take a more sophisticated approach to analyzing these spectra.

4.4.3   Franck-Condon Analysis using Internal Coordinates

For a better approximation of the vibrational displacement between the anion and neutral in the CHX_2 system, we next carry out the normal mode analysis using internal displacement coordinates as described in Section 4.3.3. The experimental spectrum of $CDCl_2^-$ is compared to its Franck-Condon simulation using normal modes in the internal coordinate representation in Fig. 4.5(c). The calculated spectral envelope has been dramatically reduced in better agreement with the experimental spectrum than with the simulation using Cartesian coordinates. The normal mode simulations of $CHCl_2^-$, $CHBr_2^-$, $CDBr_2^-$, CHI_2^-, and CDI_2^- using internal coordinates display a similar quality of agreement with the experimental spectra (Figs. 4.6(a), 4.7, and 4.8). Using the estimated EAs from the calculations, the band maxima of these simulations are in improved agreement with the experimental bands. However, the simulations using internal coordinates still have broader envelopes than what we observe experimentally, and the partially resolved vibrational

structure in the experiments is not reproduced in the simulations.

The normal mode analysis of molecular vibrations is valid for small displacements from the equilibrium geometry. For infinitesimal displacements, the normal coordinate vectors are identical whether represented in terms of internal coordinates (bond stretches and angles) or in terms of Cartesian atom-displacement coordinates, i.e., the displacement vectors are tangent at the equilibrium geometry. For a large change along a normal coordinate, the curvilinear internal coordinates system and the rectilinear Cartesian displacements lead to different values of the displacement (element $\mathbf{K}''$ for the normal mode, Eq. 4.2) for the same molecular geometry change. Because the vibrational potential energy surface is more naturally described in terms of internal coordinates, they tend to provide more physically accurate normal coordinate displacements. The curvilinear internal coordinates provide a much better first-order approximation to the natural nuclear motion. In particular for these systems, the Franck-Condon intensities using internal coordinates exhibit no significant contribution from the CH stretch mode.

The extended vibrational progression that is in disagreement with the experimental spectral envelope results from the method used to simulate the spectra, and not from errors in the electronic structure calculations. This fact is evidenced by the accuracy of the VDE calculation using B3LYP/6-311++G(d,p), illustrated in Fig. 4.4. Earlier DFT calculations by Li *et al.*[129] demonstrate similar agreement with our experimental results and with previous EA measurements of $CHCl_2$ and $CHBr_2$.[128] Because the VDE can be accurately calculated using DFT methods, it is clear that the harmonic normal mode simulation—and not the electronic structure calculations—is at fault for the failure to reproduce the spectral envelopes of the dihalomethyl anions. Though the agreement between simulation and experiment is too poor to determine the EA, the calculated VDEs can be employed without simulation to obtain an estimate of the EA. Using Eq. 4.8, we obtain EA estimates that are consistent with previous measurements (Table 4.7).

Although the qualitative agreement is reasonable, the simulation using internal coordinates is still not completely adequate in explaining the experimental band width or vibrational structure. The failure of this method to reproduce the experimental photoelectron spectra accurately

Figure 4.6: Comparison of the 150 K photoelectron spectrum of $CHCl_2^-$ (black) to its (a) normal mode simulation in internal coordinates calculated at 150 K (red), and to its (b) calculated spectrum using $(2 + 1)$ – dimensional analysis (blue) at 150 K.
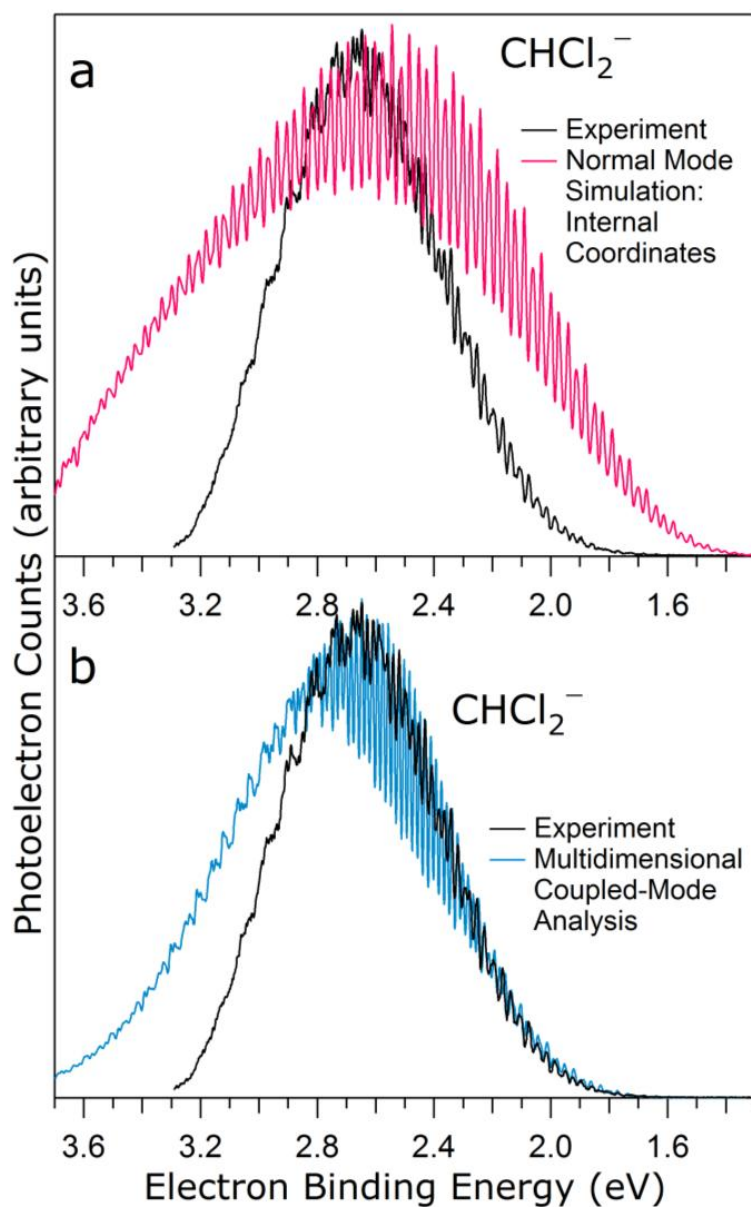
Figure 4.7: Photoelectron spectra (300 K) of (a) $CHBr_2^-$ and (b) $CDBr_2^-$ are compared to their respective normal mode simulations using internal coordinates and calculated at 300 K.
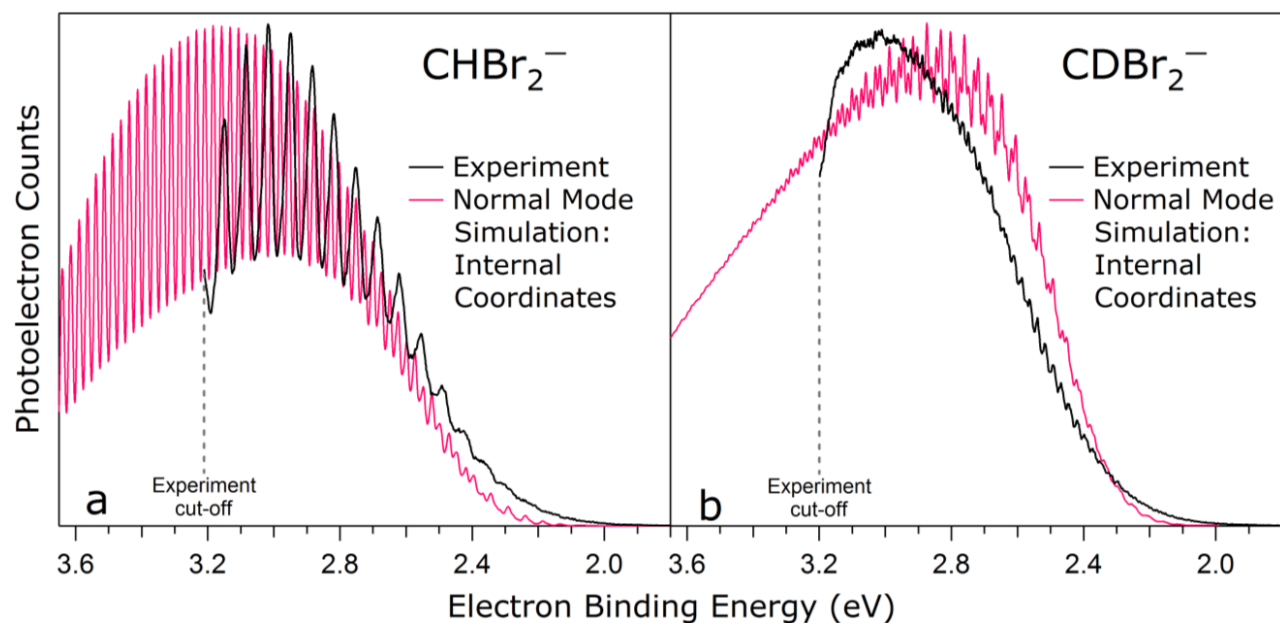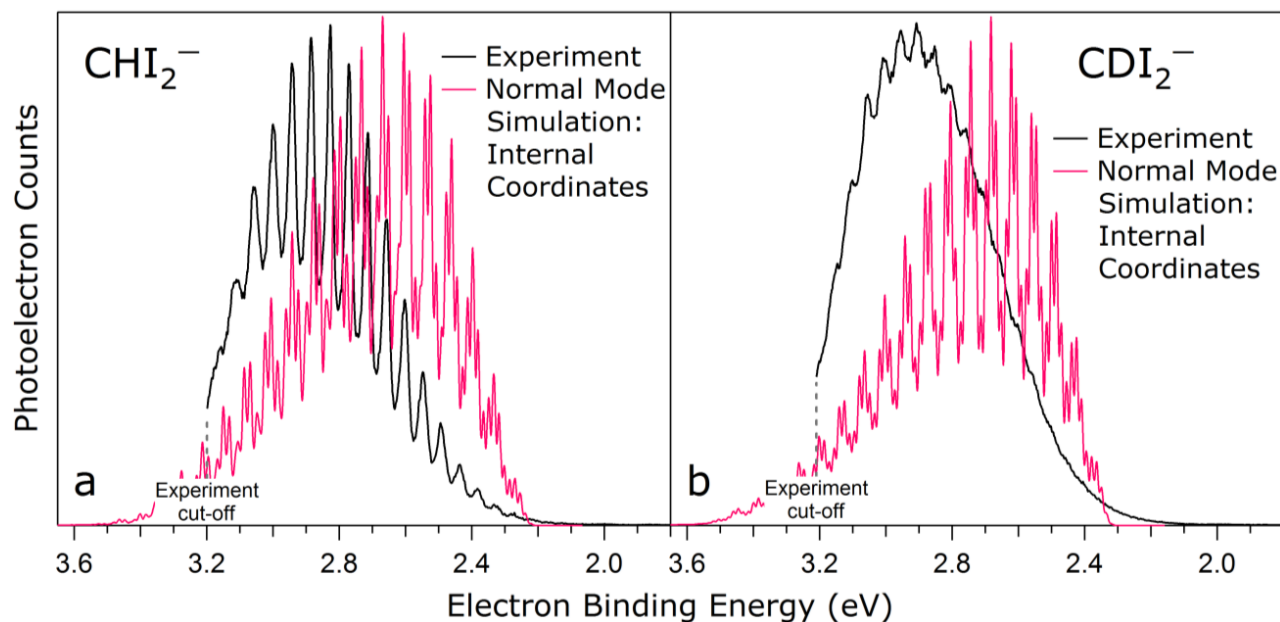

Figure 4.8: Photoelectron spectra (300 K) of (a) CHI_2^- and (b) CDI_2^- are compared to their normal mode simulations using internal coordinates and calculated at 300 K.

is a result of several factors. The large difference in equilibrium geometries and bonding between the anion and neutral cause the normal modes of the neutral to be characteristically different than those of the anion. Thus, when the normal modes of the neutral are expressed in terms of harmonic normal mode vibrations of the anion, orthogonality of the neutral normal modes is lost, resulting in mode mixing. Additionally, the neutral out-of-plane bending mode is clearly anharmonic, and representing this vibration as a harmonic oscillator is another source of discrepancy with experiment. Furthermore, the fact that we are sampling high vibrational levels of the neutral molecule for which there are multiple active vibrational modes of similar frequency, there is considerable possibility for coupling between the vibrational modes that are expected to be important. The normal mode approach to simulating the photoelectron spectra of the dihalomethyl anions has proven insufficient to elucidate the spectra, and we next take a multidimensional coupled-mode approach to computing the photoelectron spectra.

4.4.4 Multidimensional Approach for $CHCl_2$ and $CDCl_2$

The $CDCl_2^-$ photoelectron spectrum calculated using the multidimensional coupled-mode approach outlined in Section 4.3.4 is shown in Fig. 4.5(d). The calculated spectrum shown in panel (d) displays much improved agreement with experiment. Similar improvement over the normal mode approach in internal coordinates is shown for $CHCl_2^-$ (Fig. 4.6(b)). Reduced dimensional analysis shows that 98 percent of the overlap between the $CHCl_2^-$ ground vibrational state in the CH stretching coordinate ($\nu''_{CH} = 0$) occurs with $\nu'_{CH} = 0$ in $CHCl_2$. Thus, the CH (CD) stretch contributes negligible intensity above the 0-0 origin transition. Significant reduction in the width of the spectral envelope compared to the two harmonic treatments discussed above results from a combination of the inclusion of anharmonicity in each of the three modes that are considered as well as allowing for mode-mode coupling among the two bending degrees of freedom.

The extent of the coupling between the two bending vibrations $\tau_{ClCDCl'}$ and θ_s is illustrated in Fig. 4.9, which shows the development of the two-dimensional $CDCl_2$ wavefunction (color contours) with increasing energy. Wavefunctions are plotted as a function of the out-of-plane distortions

($\tau_{ClCDCl'}$) and the symmetric combination of the two DCCl bends ($\theta_s = \theta_{DCCl}$). These two internal coordinates, $\tau_{ClCDCl'}$ and θ_s, were chosen because they are a natural pair of vibrations that are coupled to each other but are reasonably decoupled from other modes, as illustrated in Fig. 4.2. The wavefunction for the lowest energy state of $CDCl_2$, shown in Fig. 4.9(a), displays the greatest probability between $\tau_{ClCDCl'} = 150°$ and $210°$ with a maximum at $180°$, indicating that in its ground vibrational state, the neutral species displays large amplitude displacements from the equilibrium geometry through the planar structure. The next higher energy state in this two-dimensional model is depicted in Fig. 4.9(b). Figures 4.9(a) and (b) show the lack of Franck-Condon overlap between the anion wavefunction (grey contours) and low vibrational levels of the neutral, resulting in our inability to experimentally observe the origin peak. From these plots, it is evident that even at low vibrational levels of the neutral, these two modes are strongly coupled, as activation of the $\tau_{ClCDCl'}$ bend is accompanied by a comparable change in θ_s.

Coupling between $\tau_{ClCDCl'}$ and θ_s becomes even more pronounced at higher vibrational levels of the neutral with energies near the VDE, where the Franck-Condon overlap with the ground vibrational wavefunction of the anion is greatest. Figure 4.9(c) shows the two-dimensional $CDCl_2$ wavefunction that has the largest Franck-Condon overlap with the ground vibrational wavefunction of $CDCl_2^-$; this transition contributes the most intensity to the calculated photoelectron spectrum. The two-dimensional wavefunction of the vibrational level shown in Fig. 4.9(c) displays the greatest probability at the turning points, which is physically manifested as a large amplitude bending motion in $\tau_{ClCDCl'}$. Also notice that the shape of the wavefunction mimics the shape of the curve in Fig. 4.2(a); i.e., the two-dimensional wavefunction follows the minimum energy curve in the $\theta_{DCCl'}$ and $\tau_{ClCDCl'}$ coordinates. In both Figs. 4.9(c) and 4.2(a), we see that the $\tau_{ClCDCl'}$ bend is accompanied by a large change in θ_s, again indicating significant coupling between these vibrational modes. Coupling of low frequency vibrations along with the highly anharmonic nature of the low frequency bend provides two sources for the breakdown of the normal mode approximation for the dihalomethyl radicals, since we can no longer treat the vibrations as products of harmonic oscillator wavefunctions. While alternative choices of the bend coordinates could reduce the coupling, these

Figure 4.9: Plots of the two-dimensional wavefunctions of $CDCl_2$ and $CDCl_2^-$. The wavefunction of the ground vibrational state of $CDCl_2^-$ is shown with gray contours, and the $CDCl_2$ wavefunctions are shown in color contours. The energy of the $CDCl_2$ wavefunction relative to the zero-point energy of the anion is given in each panel. There is negligible Franck-Condon overlap of the ground-state anion wavefunction with the ground-state neutral wavefunction (a) and with the first excited vibrational level of the neutral (b). The best overlap (c) is calculated to occur 2.424 eV above the zero-point energy of $CHCl_2^-$. (d) The next higher vibrational level of $CDCl_2$, in which one quantum of excitation in θ_s is exchanged for an additional quantum of excitation in $\tau_{ClCDCl'}$, lies only 5 meV higher in energy. This resonance leads to the highly structured $CDCl_2$ spectrum.
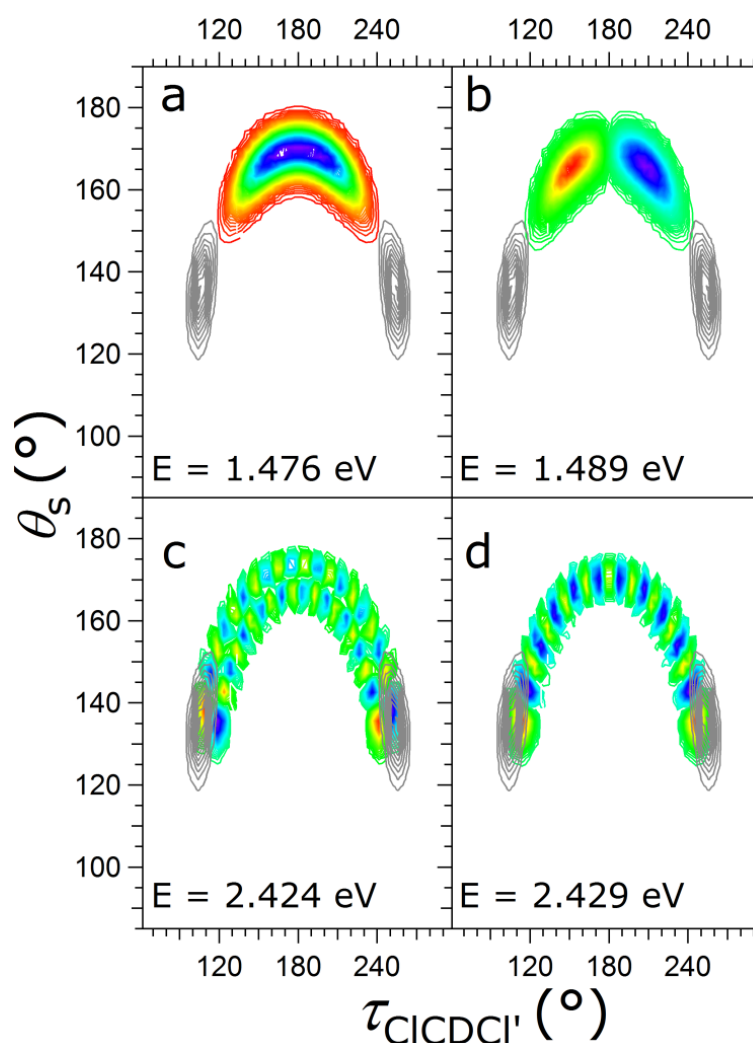
choices will also affect the separability of the ground state wavefunction on the anionic potential surface.

The structure of the spectra and the counterintuitive consequences of isotopic substitution arise from near degeneracies of the frequencies high in the potential well, where the Franck-Condon overlap is the greatest. This resonance is illustrated in panels (c) and (d) of Fig. 4.9. The vibrational state with the most intensity in the $CDCl_2^-$ photoelectron spectrum (Fig. 4.9(c)) corresponds to one quantum of excitation in θ_s and 19 quanta of excitation in the out-of-plane distortion $\tau_{ClCDCl'}$. The next highest energy state within this two-dimensional model, shown in Fig. 4.9(d), also contributes significantly to the spectrum (93 percent of the intensity of the most intense transition); this state corresponds to zero quanta of excitation in θ_s and 20 quanta of excitation in $\tau_{ClCDCl'}$. These two levels are separated by approximately 5 meV; within our instrument resolution, these two transitions appear as a single peak in the photoelectron spectrum. This is true of the coupled-bend vibrational levels of $CDCl_2$ near the VDE: "exchanging" one quantum of excitation in θ_s for an additional quantum of excitation in $\tau_{ClCDCl'}$ results in peaks separated by only 5 meV, and thus they appear as a single peak. The manifestation of this accidental degeneracy is displayed in Fig. 4.10; blue sticks correspond to the 10 most intense θ_s and $\tau_{ClCDCl'}$ transitions. The near-resonance results in a highly structured $CDCl_2^-$ photoelectron spectrum. The bend and out-of-plane distortions account for half of the observed peaks; the remaining peaks result from excitation of the ClCCl symmetric stretch.

In the case of $CHCl_2$, such a resonance of the θ_s and $\tau_{ClCHCl'}$ transitions does not occur, and the vibrational structure is significantly more congested. While exchanging one quantum of excitation in θ_s for an additional quantum of excitation in $\tau_{ClCDCl'}$ results in peaks separated by only 5 meV in $CDCl_2$, such a trade results in peaks separated by approximately 20 meV, as shown in Fig. 4.11. Figure 4.12 shows the effect of this lack of resonance on the spectrum of $CHCl_2^-$. Here again, the 10 most intense coupled bend transitions are shown in blue sticks. The 20 meV spacing between consecutive θ_s and $\tau_{ClCHCl'}$ vibrational transitions near the VDE is experimentally resolvable; when added to the ClCCl symmetric stretch contribution—which is largely unaffected

Figure 4.10: (a) The 150 K experimental photoelectron spectrum of $CDCl_2^-$ is shown in black, and the multidimensional coupled-mode calculation is overlaid in blue. Dark blue sticks correspond to the most intense transitions in the two-dimensional coupled bend coordinate. Coincidental resonances of these transitions account for the highly structured spectrum of $CDCl_2^-$. (b) The inset shows a close-up of the agreement between the experimental and calculated spectra near the vertical detachment energy.
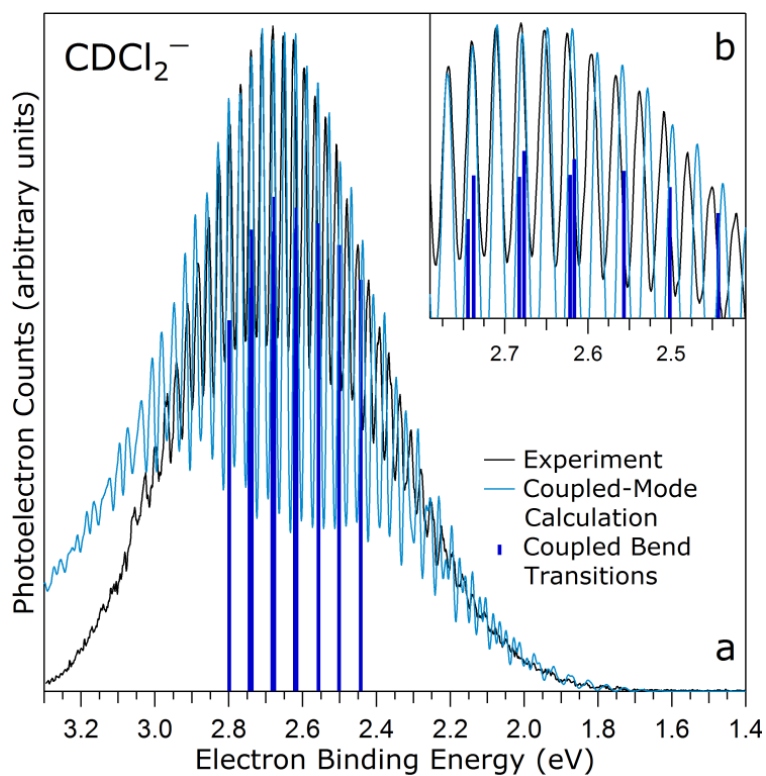
by deuteration—we observe a congested photoelectron spectrum. Thus, the counterintuitive effect of deuteration on the $CHCl_2^-$ and $CDCl_2^-$ spectra is a result of the near-resonance, or lack thereof, between the θ_s and $\tau_{ClCHCl'}$ coupled-bend vibrational transitions at the very high vibrational levels accessed.

The multidimensional coupled-mode analysis qualitatively reproduces the photoelectron spectra of $CHCl_2^-$ and $CDCl_2^-$ and yields a substantial improvement over normal-mode analysis for these molecules in terms of both the extent of the spectral envelope and peak spacing. Table 4.7 compares the average peak spacing near the VDE in the experimental spectra to peak spacing in the calculated spectra using both the harmonic normal mode and the anharmonic coupled-mode analyses. While the agreement in the width of the spectral envelope and in the peak spacing is much improved in the multidimensional approach, it is still not completely sufficient to yield reliable estimates of EAs or vibrational frequencies. Even after tackling the problem using the most sophisticated and computationally expensive multidimensional approach, our best estimates of the EAs are obtained through direct application of the calculated VDEs, *via* Eq. 4.8, without the aid of any simulations.

4.5   Conclusions

The pyramidal dihalomethyl anions become nearly planar upon photodetachment, resulting in photoelectron spectra that display extended vibrational progressions with no intensity at the origin transition. The absence of experimentally observable origins in the spectra and the inability to accurately reproduce the spectral envelopes preclude the direct determination of EAs or vibrational frequencies of the dihalomethyl anions in this study. While normal mode analysis accurately simulates the spectra of molecules that experience small displacements of equilibrium nuclear configurations upon photodetachment, false activity of the CH stretch is predicted in the dihalomethyl radicals when a Cartesian displacement coordinate system is employed. Use of internal coordinates for the normal mode analysis eliminates that problem, but the Franck-Condon simulations using independent harmonic oscillators are still inadequate. The harmonic Franck-Condon simulation using internal coordinates yields a spectral envelope that is too broad. The calculated VDE

Figure 4.11: Plots of the two-dimensional wavefunctions of $CHCl_2$ and $CHCl_2^-$. The wavefunction of the ground vibrational state of $CHCl_2^-$ is shown with gray contours, and the $CHCl_2$ wavefunctions are shown in color contours. The energy of the $CHCl_2$ wavefunction relative to the zero-point energy of the anion is given in each panel. There is negligible Franck-Condon overlap between the ground-state anion wavefunction and the ground-state neutral wavefunction (a), resulting in an unobservable origin peak in the photoelectron spectrum. Likewise, there is minimal overlap between the ground-state anion and first excited vibrational level of the neutral (b). The best overlap (c) is calculated to occur 2.382 eV above the zero-point energy of $CHCl_2^-$. The next highest energy level is shown in panel (d), in which one quantum of excitation in the θ_s is exchanged for an additional quantum of excitation in $\tau_{ClCHCl'}$. In contrast to the case of $CDCl_2$, in which such an exchange results in states separated by only 5 meV, the states shown in panels (c) and (d) are separated by 21 meV—greater than our instrument resolution.

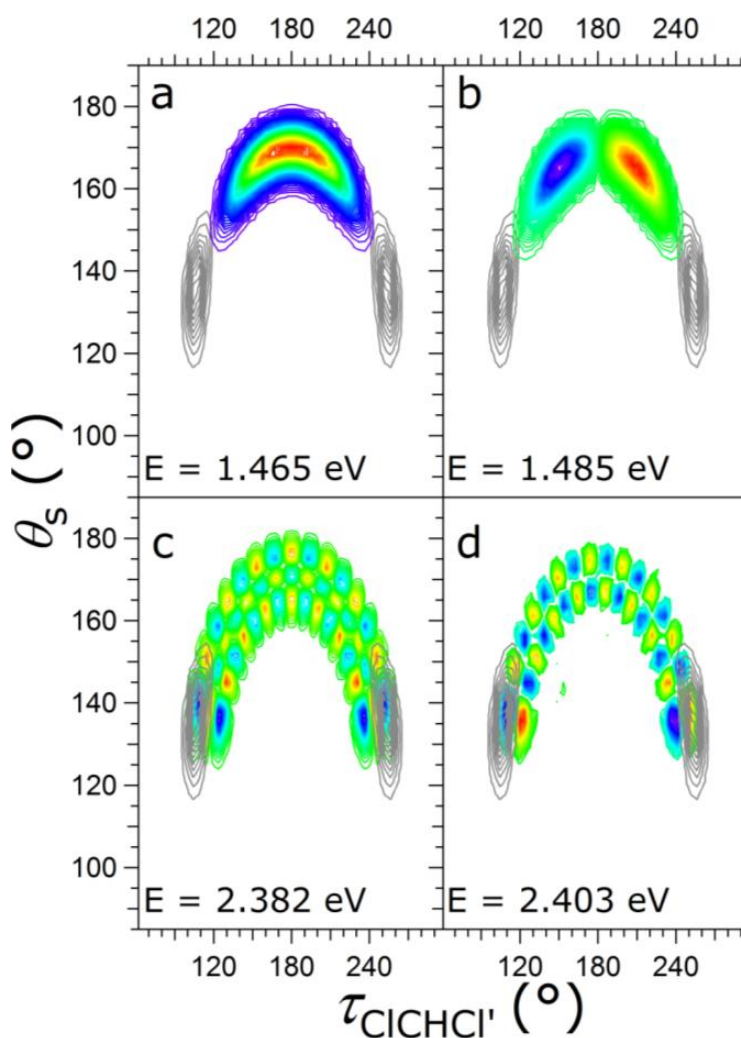Figure 4.12: (a) The 150 K experimental photoelectron spectrum of $CHCl_2^-$ is shown in black, and the multidimensional coupled-mode calculated spectrum is overlaid in blue. Dark blue sticks correspond to the most intense vibronic transitions in the two-dimensional coupled bend coordinate. (b) The inset shows a close-up of the agreement between the experimental and calculated spectra near the vertical detachment energy.
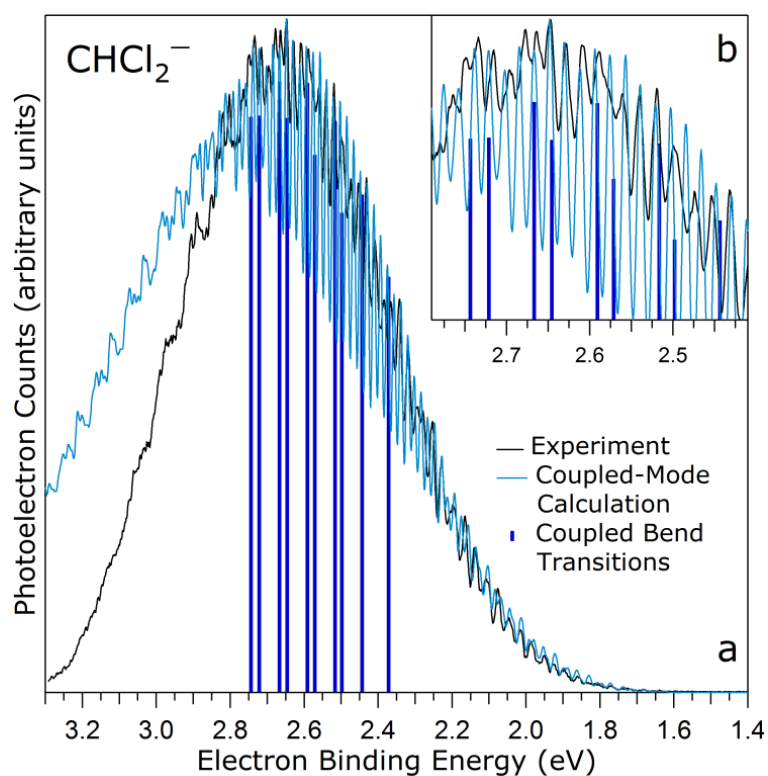
is in agreement with the measured VDE. Therefore, the inability to reproduce the shape of the vibrational progression must be an artifact of the method used to compute the FCFs.

In order to simulate the spectra of the dihalomethyl radicals with more accuracy, we take a multidimensional anharmonic coupled-mode approach. The coupling of the multiple active low-frequency bending vibrations is the source of the breakdown of the normal mode approximation for the dihalomethyl radicals; consequently, we cannot treat the vibrations as separable, nor compute FCFs as the product of harmonic oscillators. Instead, using $(2 + 1)$ – dimensional analysis we calculate negligible contribution from the CH stretch above the 0-0 transition and find that coupled $\tau_{\text{ClCHCl}'}$ and θ_s bends plus the ClCCl symmetric stretch fully account for the observed structure in the CHCl_2^- and CDCl_2^- spectra.

Unfortunately, there is no reliable, general approach to analyzing the Franck-Condon bands of transitions involving large geometry changes, such as those of the dihalomethyl anions. Normal mode analysis in an internal coordinate representation yields much better results than using rectilinear Cartesian displacement coordinates, but it requires Wilson's **GF** method to compute Duschinsky translation vectors and rotation matrices and still fails to adequately reproduce the width of the spectral envelope for these systems. Multidimensional anharmonic coupled-mode analysis achieves reasonable agreement with the observed spectra of the dihalomethyl anions; however, these simulations are computationally expensive, precluding determination of molecular parameters by direct fitting to the observed spectra, and are also specific to each molecule studied. In fact, the best experimental EA estimates of the dihalomethyl radicals are obtained by directly employing the difference in energy between the calculated VDE and calculated EA. With effort, we can understand the spectra of the dihalomethyl anions, but we are unable to obtain the quantitative information that can be determined from the photoelectron spectra of more rigid molecules.

This leaves us with the question of how one can anticipate the breakdown of harmonic treatments. In the absence of prior knowledge of the EAs, there are few clues in the measured photoelectron spectra of the dihalomethyl anions that would lead one to anticipate the need to perform anharmonic calculations. A full discussion of this issue is beyond the scope of the present study,

although this work sheds light on several of the factors that could be used to anticipate difficulties with harmonic treatments. First, there is a large structural change between the anion and the neutral, as displayed by the large change in $\tau_{\text{ClCHCl}'}$ upon photodetachment (Table 4.2). This leads to a change in the definition of the normal modes that are used to expand the wavefunctions for the anion and for the neutral. The second important factor is the low frequency and large anharmonicity in the vibrational mode associated with displacements in $\tau_{\text{ClCHCl}'}$. This leads to the sampling of very highly excited bend states on the neutral surface upon electron detachment. In the dihalomethyl radicals, the low frequency and large anharmonicity of this mode is anticipated by barriers to planarity that are lower than the harmonic zero-point energy of this mode. The high level of vibrational excitation of these anharmonic modes makes such systems challenging for approaches that are based on harmonic treatments.

Chapter 5

Cyanopolyynes

5.1   Introduction

The cyanopolyyne (HC_nN) HC_4N is a carbene (:CXY), as it contains a neutral divalent carbon atom with two electrons occupying two orbitals that lie close in energy. Carbenes are highly reactive and serve as important intermediates in chemical reactions, and their reactivity is affected by whether the carbene exists as a singlet or a triplet. The carbene's substituents determine the electronic ground state of the molecule, as well as the difference in energy between the singlet and triplet states, known as the singlet-triplet splitting (ΔE_{ST}).[139] The simplest carbene, methylene (CH_2), possesses a triplet ground state because the energy separation between the σ and π orbitals is less than the electron correlation energy.[140] The donation of π electrons, e.g., by halogen atoms, tends to increase the separation between the σ and π orbitals, leading to a singlet ground state.[130,141] Although CN is considered a "pseudohalogen," it does not donate π electrons. Previous experiments have shown that HCCN has a triplet ground state with a relatively large ΔE_{ST}.[142]

In addition to their fundamental importance as carbenes, cyanopolyynes have attracted interest because of their significance in astrophysics. These species are abundant in circumstellar environments of carbon-rich stars and dense molecular clouds; because nitrogen is a major component of interstellar dust, cyanopolyynes are also important constituents of molecular clouds.[143] Odd cyanopolyyne chains (HC_nN where n = odd) up to $HC_{11}N$ have been detected in space,[144] and microwave rotational spectra of odd cyanopolyynes up to $n = 17$ have been recorded.[145] These

studies have established that, like the isoelectronic polyacetylenes $HC_{2n}H$, odd cyanopolyynes possess a linear singlet ground state. The chain has alternating single and triple bonds, giving rise to alternating bond lengths.[146]

There have been many reports of the observation of odd cyanopolyynes in circumstellar and laboratory environments; however, the same situation does not exist for the even cyanopolyynes, implying that odd cyanopolyynes are more stable than even species.[143] In fact, McCarthy and Thaddeus report a factor of 10 – 100 lower abundance of the even cyanopolyynes HC_4N, HC_6N, and HC_8N as compared to odd cyanopolyynes of similar length.[147] They attribute this discrepancy to the greater stability of the closed shell singlet odd cyanopolyynes as compared to the reactive triplet even cyanopolyynes, and to the fact that the mechanisms of carbon chain formation[148] favor the formation of odd cyanopolyynes. Furthermore, while the geometry of odd cyanopolyynes has been characterized, the geometry of the lowest energy isomers of even cyanopolyynes is not as well understood.

HC_4N is of particular interest to experimental and theoretical groups alike because it is one of the smallest systems calculated to possess multiple low-lying, highly polar carbene isomers.[149] McCarthy *et al.* generated two singlet isomers of HC_4N in a supersonic molecular beam and detected them with Fourier transform microwave (FTM) spectroscopy: a cyanovinylidene carbene structure, $NC(H)C=C=C:$,[150] and a ring-chain structure.[151] A number of theoretical works have been aimed at understanding the relative stability of various isomers and electronic states;[143,149,152–155] for the most part, these studies found that the ring-chain (cyclopropenylidene) singlet isomer of HC_4N is lower in energy than the linear chain triplet isomer, but the results were dependent upon the method employed.

There is also question as to whether the structure of the triplet ground state of the chain isomer of HC_4N is linear or bent; it is useful to compare HCC-C-CN with several other triplet carbenes (Scheme 5.1).

Scheme 5.1

$$H-C\equiv C-\overset{\cdot\cdot}{C}-C\equiv C-H$$
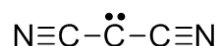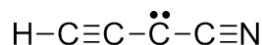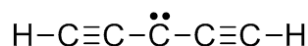
$$H-C\equiv C-\overset{\cdot\cdot}{C}-C\equiv N$$

$$N\equiv C-\overset{\cdot\cdot}{C}-C\equiv N$$

In the case of triplet HCC-C-CCH, experiment and theory agree that the triplet is axially symmetric.[156] Sanov and coworkers concluded that triplet NC-C-CN is linear or quasilinear.[157] Tang *et al.* reported the first observation of the triplet ground state of the chain isomer of HCC-C-CN in the laboratory using FTM spectroscopy; with the aid of calculations, they concluded that triplet HC_4N has a very small barrier to linearity ($25\,cm^{-1}$ at CCSD(T)/6-311G(d,p)) and thus can be considered a linear molecule.[158] Aoki and coworkers, also using CCSD(T), predict a linear triplet.[153] Later, Cernicharo *et al.* reported the observation of the linear triplet form of HC_4N in the carbon-rich IRC +10216 envelope.[159]

Here we present a photoelectron spectroscopy study of the HC_4N^- anion. From the 364-nm photoelectron spectrum of HC_4N^-, we obtain the first experimental measurement of the electron affinity (EA) and ΔE_{ST} of the chain isomer of HC_4N. For comparison and to aid in our understanding of the HC_4N^- spectrum, we also report the 364-nm photoelectron spectra of $HCCN^-$ and $DCCN^-$ with improved signal-to-noise over the previously published spectrum.[142] The improvement in the $HCCN^-$ and $DCCN^-$ photoelectron spectra allows for better resolution of the vibrational progressions and a more precise determination of the EAs and ΔE_{ST}s of HCCN and DCCN. We compare the HC_4N^- and $HCCN^-$ ($DCCN^-$) spectra and consider them in the context of a broader set of carbene carbon chains.

5.2   Experimental Methods

The negative ion photoelectron spectrometer used in this experiment has been described in detail elsewhere.[2,34,41] The apparatus consists of four main sections: an ion source, a mass filter,

an interaction region with crossed laser and ion beams, and an electrostatic electron kinetic energy analyzer. Negative ions are formed in a flowing afterglow ion source. A microwave discharge containing trace amounts of O_2 gas in He buffer gas ($\sim$0.4 Torr) generates atomic oxygen radical anion, O^-. To generate HC_4N^- anions, tetrolonitrile (H_3C_4N), prepared in the McMahon lab at the University of Wisconsin-Madison,[160] is added downstream of O^- (Scheme 5.2).

Scheme 5.2
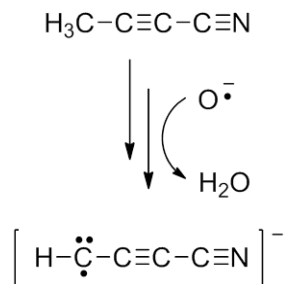
To make $HCCN^-$ anions, acetonitrile (H_3CCN) is added downstream of O^-: O^- + $H_3CCN \rightarrow$ $HCCN^-$ + H_2O. We produce $DCCN^-$ using the analogous reaction and beginning with D_3CCN. Collisions with He buffer gas cool the ions to approximately 300 K. The flow tube can be further cooled with a liquid nitrogen jacket to obtain a "cold spectrum" of ions with temperatures near 150 K. Anions are extracted into a differentially pumped region and are accelerated to 735 eV before entering a Wien velocity filter with a mass resolution of $m/\Delta m \sim 60$.[38,161] With this resolution, we cannot cleanly resolve HC_4N^- and $H_2C_4N^-$, both of which are produced in the flowing afterglow ion source; however, we select the low-mass side of the $m/z \sim 63 - 64$ peak to obtain the spectrum of HC_4N^-. We also obtained the photoelectron spectrum of neat $H_2C_4N^-$ (generated by first reacting O^- with CH_4 to produce OH^-, which then reacts with H_3C_4N to produce $H_2C_4N^-$) to ensure that there was no contribution from $H_2C_4N^-$ in the HC_4N^- spectra. The photoelectron spectrum of $H_2C_4N^-$ is a broad, featureless progression that appears at lower binding energy than HC_4N^-, as shown in Fig. 5.1.

The mass-selected ion beam (typically 70 pA) is decelerated to 35 eV and focused into the laser interaction region. Here, the 1-W output from a single-mode continuous-wave argon ion laser operating at 364 nm (3.40814 eV) is built up to approximately 100 W of circulating power in an

Figure 5.1: Photoelectron spectrum (364 nm) of $H_2C_4N^-$, collected at the magic angle at 150 K.
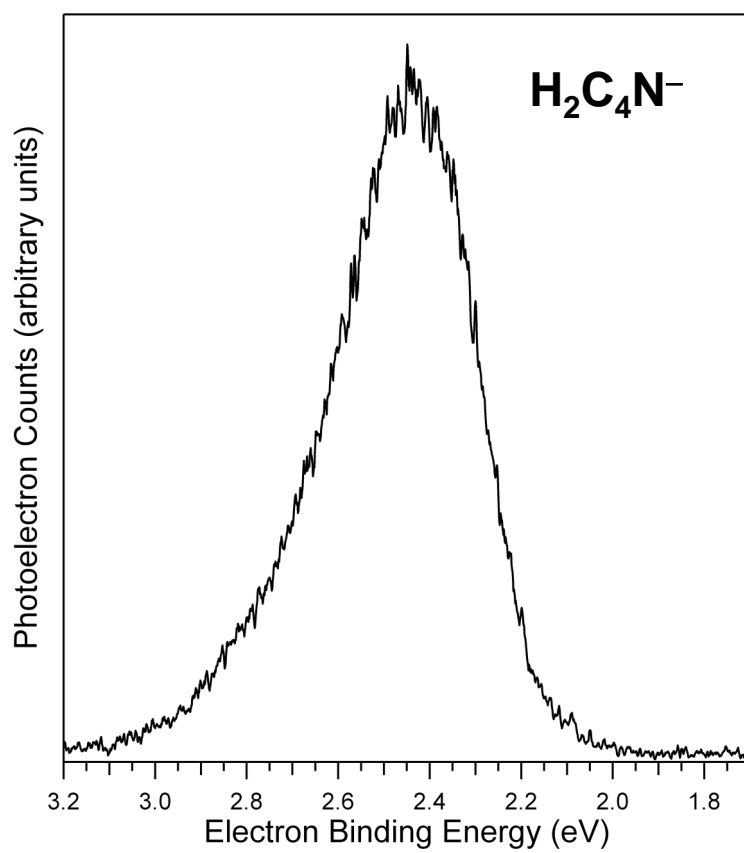
optical buildup cavity located within the vacuum system. Photodetachment of an electron yields the neutral species, as depicted for HC_4N^- photodetachment in Scheme 5.3.

Scheme 5.3

Photoelectrons ejected in the direction orthogonal to both the laser and ion beams enter a hemispherical energy analyzer. The photoelectron signal is recorded as a function of electron kinetic energy with a position-sensitive detector. The energy analyzer has a resolution of approximately 11 meV under the conditions used for the present experiments.

The electron kinetic energy (eKE) can be converted to electron binding energy (eBE) through the relationship eBE = $h\nu$ - eKE. The absolute kinetic energy scale is calibrated[2,34,43] before and after each experiment using the well-known EA of atomic oxygen.[45] Additionally, the energy scale is corrected for a slight linear compression $(<1\%)^2$ using the photoelectron spectrum of O_2^-, which provides a number of known transitions spanning the photoelectron energy range.[21,47] After making these corrections and accounting for the resolution of the spectrometer and rotational peak profiles, absolute electron binding energies can be determined with an accuracy of better than 5 meV.

A rotatable half-wave plate positioned outside the buildup cavity varies the polarization of the photodetachment radiation in order to control the angle θ between the electric field vector of the laser beam and the photoelectron collection axis. The photoelectron angular distribution is described by the equation[5]

$$I(\theta) = \frac{\sigma_0}{4\pi}(1 + \beta P_2(\cos \theta))$$

(5.1)

where σ_0 is the total photodetachment cross section, β is the anisotropy parameter, and $P_2(\cos \theta)$ is the second Legendre polynomial. We measure the anisotropy parameter explicitly by recording

the photoelectron signal at the kinetic energy of one suitable intense peak in the photoelectron spectrum as a function of θ (between $\theta = 0°$ and $\theta = 360°$ in steps of $10°$). The photoelectron angular distribution is fit with Eq. 5.1, and full spectra collected at $\theta = 0°$ and $\theta = 90°$ are scaled to match β at the energy at which it was measured. Separately, we collect a photoelectron spectrum at $\theta = 54.7°$ (the so-called magic angle), where the photoelectron intensity is independent of β and directly reflects the relative photodetachment cross section.

5.3   Theoretical Methods

All electronic structure calculations were performed using the Gaussian 03 program package.[48] Optimized geometries, harmonic vibrational frequencies, and normal mode coordinates were calculated at the ROMP2 level of theory[162] with the 6-311++G(d,p) basis set[52] for the $\tilde{X}^2 A''$ states of HC_4N^- and $HCCN^-$ ($DCCN^-$) as well as for the $\tilde{X}^3 A''$ and $\tilde{a}^1 A'$ states of the neutrals HC_4N and $HCCN$ ($DCCN$). All molecules were constrained to C_s symmetry. For the reported scans along the CCC (HC_4N) or HCC ($HCCN$) angle (Figs. 5.5 and 5.8), the geometries were further constrained so that all but the scanned angles were $180°$, and the bond lengths were constrained to their optimized values on the anion surface when all but one of the angles was $180°$.

We employ a Franck-Condon analysis of the vibrational structure in the photoelectron spectra to identify the active vibrational modes and the geometry change upon photodetachment. The Franck-Condon profiles of the photoelectron spectra are simulated with the PESCAL program,[21] using the calculated geometries, normal mode vectors, and vibrational frequencies of the anion and neutral states. The normal modes and the Duschinsky $\mathbf{J}''$ matrix and $\mathbf{K}''$ displacements are calculated. The Franck-Condon factors are computed in the harmonic oscillator approximation including Duschinsky rotation using the Sharp-Rosenstock-Chen method.[4] The individual vibronic peak contours are simulated by a Gaussian function with a full-width half-maximum of 11 meV, consistent with instrumental resolution.

Activity of a large-amplitude bending vibration upon photodetachment of the bent HC_4N^- anion to the quasilinear $\tilde{X}^3 A''$ state of HC_4N renders our standard independent harmonic oscilla-

tor approximation unsuitable for simulating $\tilde{X}^3A'' \leftarrow \tilde{X}^2A''$ photodetachment of HC_4N^-. A more appropriate treatment of $\tilde{X}^3A'' \leftarrow \tilde{X}^2A''$ photodetachment would utilize a curvilinear HCC-C-CN bending coordinate and a vibration-rotation Hamiltonian that allows for large displacements of the bending coordinate.[163] However, this more sophisticated treatment is beyond the scope of this work. In our standard Franck-Condon analysis using the Sharp-Rosenstock-Chen method, non-physical $\mathbf{K}''$ displacements are computed that result in an inadequate simulation of $\tilde{X}^3A'' \leftarrow \tilde{X}^2A''$ photodetachment. For this reason, we will only rely on partial simulations of the HC_4N^- and $HCCN^-$ ($DCCN^-$) photoelectron spectra in our analysis; full simulations are shown in Fig. 5.6.

5.4   Results

5.4.1 HC_4N^-

5.4.1.1   Photoelectron Spectra of HC_4N^-

It is instructive to first consider the valence electronic structure of HC_4N (Fig. 5.2) and its implications for the photoelectron spectrum of HC_4N^-. Like $HCCN^-$,[142] the ground state of HC_4N^- is $\tilde{X}^2A''$. The excess charge resides primarily on the third carbon atom, and the anion is bent. If an electron is photodetached from the in-plane σ orbital to form the $\tilde{X}^2A''$ ground state of HC_4N, the molecule straightens to become quasilinear. However, if an electron is removed from the out-of-plane π orbital to form the $\tilde{a}^1A'$ excited state of HC_4N, the molecule remains bent in much the same geometry as the anion. Intuitively, we expect the large geometry change upon photodetachment of the bent anion to the quasilinear triplet ground state to result in an extended vibrational progression at low binding energy in the photoelectron spectrum of HC_4N^-. We expect multiple vibrational modes—especially bending modes involving the carbene center—to be active upon photodetachment and to contribute intensity to the triplet manifold. Since both the anion and the neutral singlet are bent, we expect significant Franck-Condon overlap between the ground vibrational state of HC_4N^- and the singlet state of HC_4N. This will result in an intense "origin" peak corresponding to the 0-0 transition, and it will appear higher in energy than the triplet state.

Figure 5.2: Generalized valence bond diagrams of the $\tilde{X}^2A''$ state of HCCN$^-$, the $\tilde{X}^3A''$ and $\tilde{a}^1A'$ states of HCCN,[142] as well as the $\tilde{X}^2A''$ state of HC$_4$N$^-$ and the $\tilde{X}^3A''$ and $\tilde{a}^1A'$ states of HC$_4$N.
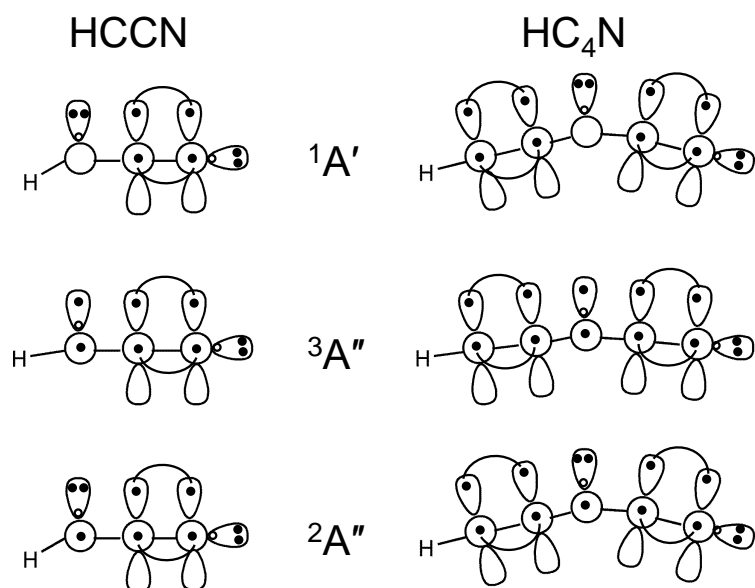
The 364-nm, magic angle photoelectron spectrum of HC_4N^- is shown in Fig. 5.3. The spectrum was collected at both room temperature (300 K, blue trace) and at 150 K (black trace). As anticipated, we observe a broad progression at low binding energy, corresponding to photodetachment to the $\tilde{X}^3A''$ ground state of HC_4N. The large geometry change that occurs upon $\tilde{X}^3A'' \leftarrow \tilde{X}^2A''$ photodetachment precludes the observation of the origin peak. Additionally, because there are multiple active modes upon photodetachment—particularly the low frequency HCC-C-CN bend—we observe a congested spectrum and are unable to resolve individual vibronic peaks in the triplet envelope. Therefore, we cannot measure vibrational frequencies of the $\tilde{X}^3A''$ ground state of HC_4N. Though we do not resolve an origin peak from which we can determine the EA, comparison of the 300 K and 150 K spectra shows that the EA of HC_4N is 2.05(8) eV (Table 5.1). The 300 K spectrum displays a sharp onset at 2.00 eV; in the 150 K spectrum, the intensity between 2.00 and 2.05 eV is suppressed. This indicates that the intensity observed between 2.00 and 2.05 eV in the 300 K spectrum results from hot bands, or vibronic transitions arising from vibrationally excited anions. In the 150 K spectrum, we observe intensity above the baseline beginning at approximately 2.05 eV, and we begin to resolve two features between 2.00 and 2.15 eV (see inset of Fig. 5.3). Unfortunately, the substantial geometry change in coupled modes means that the independent mode Franck-Condon simulation is not even qualitatively reliable[24,130] and cannot help in estimating a lower bound for the origin (EA) of the triplet state. Because the features in the origin region are not well resolved, we assign the EA of HC_4N to be 2.05 eV—where we see appreciable intensity above the baseline in the cooled spectrum—with an uncertainty that encompasses both the shelf in the 300 K spectrum and the two small features in the 150 K spectrum. Thus, the EA of HC_4N is measured to be 2.05(8) eV.

At higher binding energy, a sharp feature appears at eBE = 2.809(4) eV. The polarization dependence of the photoelectron spectrum of HC_4N^- is given in Table 5.1 and is shown in Fig. 5.4; the difference in the β anisotropy parameters between the broad progression beginning at 2.05(8) eV and the sharp feature at eBE = 2.809(4) eV indicates that these features result from two different electronic states of HC_4N. The peak at eBE = 2.809(4) eV corresponds to the origin of the $\tilde{a}^1A'$

Figure 5.3: Photoelectron Spectra of HC_4N^-. The 364-nm spectra were collected at the magic angle at 150 K (black trace) and 300 K (blue trace). The partial Franck-Condon simulation of the 150 K HC_4N^- photoelectron spectrum is shown in purple, with gray sticks representing individual vibronic transitions. The calculated geometries, frequencies, and $\mathbf{K}''$ displacements used in the $\tilde{a}^1A' \leftarrow \tilde{X}^2A''$ photodetachment simulation are listed in Tables 5.2 – 5.3. The simulation uses the experimental binding energy of the $\tilde{a}^1A'$ state of HC_4N. The equilibrium structures of the $\tilde{X}^3A''$ and $\tilde{a}^1A'$ states of HC_4N are also shown.
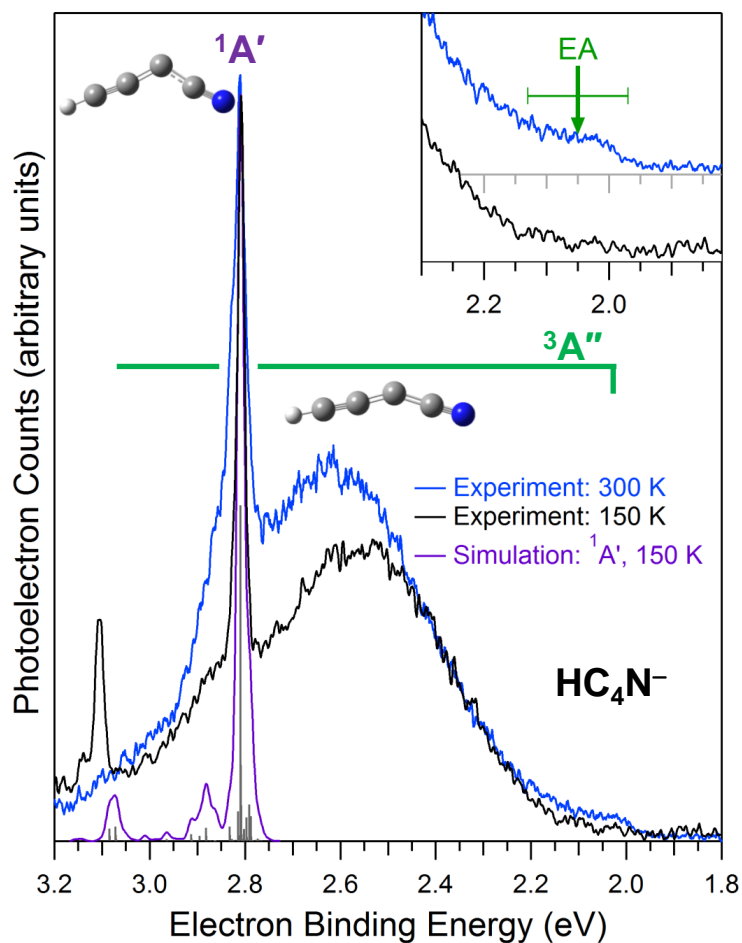
Table 5.1: Experimental and calculated electron affinities (EA), vertical detachment energies (VDE), and singlet-triplet splittings (ΔE_{ST}) of HCCN and HC$_4$N given in eV.

		$\widetilde{X}\,^3A'' \leftarrow \widetilde{X}\,^2A''$			$\tilde{a}\,^1A' \leftarrow \widetilde{X}\,^2A''$			
		EA	VDE	β	(0-0)	VDE	β	ΔE_{ST}
HC$_4$N	*Experiment*[a]	2.05(8)	2.57(3)	+0.2	2.809(4)	2.809(4)	-0.3	0.76(8)
	Calculated[b]	2.229	2.533		2.771	2.784		0.542
HCCN	*Experiment*[a]	2.001(15)	2.36(2)	-0.25	2.511(4)	2.512(4)	-0.62	0.510(15)
	Experiment[c]	2.003(14)		-0.37[d]	2.518(8)		-0.77	0.515(16)
	Calculated[b]	1.746	2.185		2.512	2.562		0.765
DCCN	*Experiment*[a]	1.998(15)	2.37(2)	-0.28	2.506(4)	2.506(4)	-0.63	0.508(15)
	Experiment[c]	2.009(20)		-0.33[d]	2.527(18)		-0.78	0.518(27)
	Calculated[b]	1.749	2.184		2.509	2.560		0.761

[a] Experiment, this work
[b] ROMP2/6-311++G(d,p)
[c] Experiment, Nimlos *et al.*[142]
[d] β value listed is the average of the β values of the peaks in the triplet progression

Table 5.2: Calculated (ROMP2/6-311++G(d,p)) equilibrium geometry of $\tilde{X}^2A''$ HC$_4$N$^-$ and the calculated net geometry change upon photodetachment to the $\tilde{X}^3A''$ and $\tilde{a}^1A'$ states of HC$_4$N. Bond lengths are given in units of angstrom (Å), and bond angles are given in units of degree (°). Boldfaced entries highlight the internal coordinates that undergo significant change upon photodetachment.
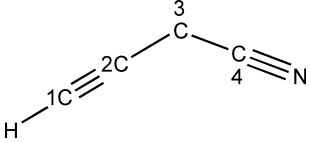
| | HC$_4$N$^-$ | Geometry Change | |
Internal Coordinate	$\tilde{X}\,^2A''$	$\tilde{X}\,^3A'' \leftarrow \tilde{X}\,^2A''$	$\tilde{a}\,^1A' \leftarrow \tilde{X}\,^2A''$
H-C1	1.062	+0.003	+0.005
C1-C2	1.223	-0.003	+0.011
C2-C3	1.377	**-0.059**	-0.008
C3-C4	1.402	-0.023	+0.004
C4-N	1.167	-0.027	+0.017
∠H-C1-C2	178.6	+0.4	-1.9
∠C1-C2-C3	173.9	+1.5	-2.8
∠C2-C3-C4	119.6	**+28.2**	-1.7
∠C3-C4-N	173.6	+4.5	-1.6

Table 5.3: Calculated (ROMP2/6-311++G(d,p)) unscaled, harmonic frequencies of $\tilde{X}^2A''$ HC_4N^- and the $\tilde{X}^3A''$ and $\tilde{a}^1A'$ states of HC_4N. The measured CN stretch frequency is listed in italics below the calculated value. Computed $\mathbf{K}''$ displacements (PESCAL) are also listed. The computed $\tilde{X}^3A'' \leftarrow \tilde{X}^2A''$ $\mathbf{K}''$ displacements do not accurately represent the geometry change that takes place upon photodetachment and result in a Franck-Condon simulation that does not reproduce the observed triplet progression (Fig. 5.6(a)).

| Mode		Description	HC_4N^- $^2A''$, cm^{-1}	$\tilde{X}\,^3A'' \leftarrow \tilde{X}\,^2A''$ $\Delta\mathbf{K}''$	$^3A''$, cm^{-1}	$\tilde{a}\,^1A' \leftarrow \tilde{X}\,^2A''$ $\Delta\mathbf{K}''$	$^1A'$, cm^{-1}
A'	ν_1	CH stretch	3521.5	-0.0093727	3494.4	0.0025897	3486.5
	ν_2	CN stretch	2159.8	-0.12460	2309.5	0.045273	2217.6
							2395(40)^a
	ν_3	CCC asym stretch	1937.7	-0.052916	1714.3	0.021984	2111.4
	ν_4	CCC asym stretch	1215.3	-0.044035	1308.1	-0.027163	1247.1
	ν_5	CCC sym stretch	812.1	-0.48678	651.6	0.033921	831.3
	ν_6	HCC-C-CN bend	580.3	0.48465	353.7	-0.065517	579.5
	ν_7	HCC-C-CN rocking	407.6	0.23376	214.0	0.0093059	409.5
	ν_8	H wag	283.2	0.29055	589.1	-0.027086	507.8
	ν_9	HCCC-C-N bend	153.6i	1.7090	286.0i	0.073406	142.4
A''	ν_{10}	H wag	403.4	0	491.8	0	808.2
	ν_{11}	N-C-C bend	336.3	0	177.7	0	346.4
	ν_{12}	NCC-C-CH bend	155.7	0	297.2	0	291.9

^{a} Experiment, this work

excited state of HC_4N. Because the geometry of the $\tilde{X}^2A''$ state of HC_4N^- and the $\tilde{a}^1A'$ excited state of HC_4N are both bent, we observe a very prominent $\tilde{a}^1A'$ origin peak. We measure the singlet-triplet splitting (ΔE_{ST}) of HC_4N to be 0.76(8) eV (Table 5.1).

The most striking—and most curious—difference between the 300 K and 150 K HC_4N spectra shown in Fig. 5.3 is the appearance of an additional sharp feature at 3.106(4) eV in the 150 K spectrum. The intensity of this peak, which is separated from the $\tilde{a}^1A'$ origin by 2395 cm^{-1}, fluctuated with respect to the $\tilde{X}^3A''$ and $\tilde{a}^1A'$ features throughout the day and from day to day, and it was never observed at room temperature. The eBE of this feature suggests that it is a CN stretch of the singlet state, but such a temperature dependence of a combination band is not typically seen in photoelectron spectra. A measurement of the β of this peak would lend insight into the source of this feature, but unfortunately the intensity fluctuations of this peak made it difficult to obtain a reliable β measurement of the peak (we measure β(3.106 eV) ~ 0.3). As discussed in the following section (5.4.1.2), we employ calculations and simulations to confirm that this feature does indeed correspond to activation of CN stretch in the $\tilde{a}^1A'$ state of HC_4N.

5.4.1.2   Electronic Structure Calculations for HC_4N^-

As discussed in Section 5.3, our standard Franck-Condon analysis of the HC_4N^- photoelectron spectrum is inadequate for modeling $\tilde{X}^3A'' \leftarrow \tilde{X}^2A''$ photodetachment. Using ROMP2/6-311++G(d,p), we calculate the EA(HC_4N) to be significantly greater than the measured EA of 2.05(8) eV (Table 5.1); Kalchers ACPF/aug-cc-pVTZ calculation also overestimates the EA by approximately 250 meV.[154] The calculated geometry change upon photodetachment is illustrated in Table 5.2, and the calculated vibrational frequencies are listed in Table 5.3. As expected, a large geometry change is calculated to occur upon $\tilde{X}^3A'' \leftarrow \tilde{X}^2A''$ photodetachment, which results in the observed extended vibrational progression. Specifically, the C2-C3 bond length decreases by 0.059 Å, while the $\angle$C2-C3-C4 increases by 28.2° as the molecule becomes nearly linear. Previous studies seem to favor a linear $\tilde{X}^3A''$ structure,[153,158,159] while our calculations predict a slightly bent equilibrium geometry. Though we calculate the minimum to occur at a $\angle$C2-C3-C4 of 147.8°

Figure 5.4: Polarization Dependence of the Photoelectron Spectrum of HC_4N^-. Photoelectron spectra were collected at 300 K at $\theta = 0°$ (cyan trace) and $\theta = 90°$ (gray trace) and scaled for the measured β anisotropy at eBE = 2.8 eV.
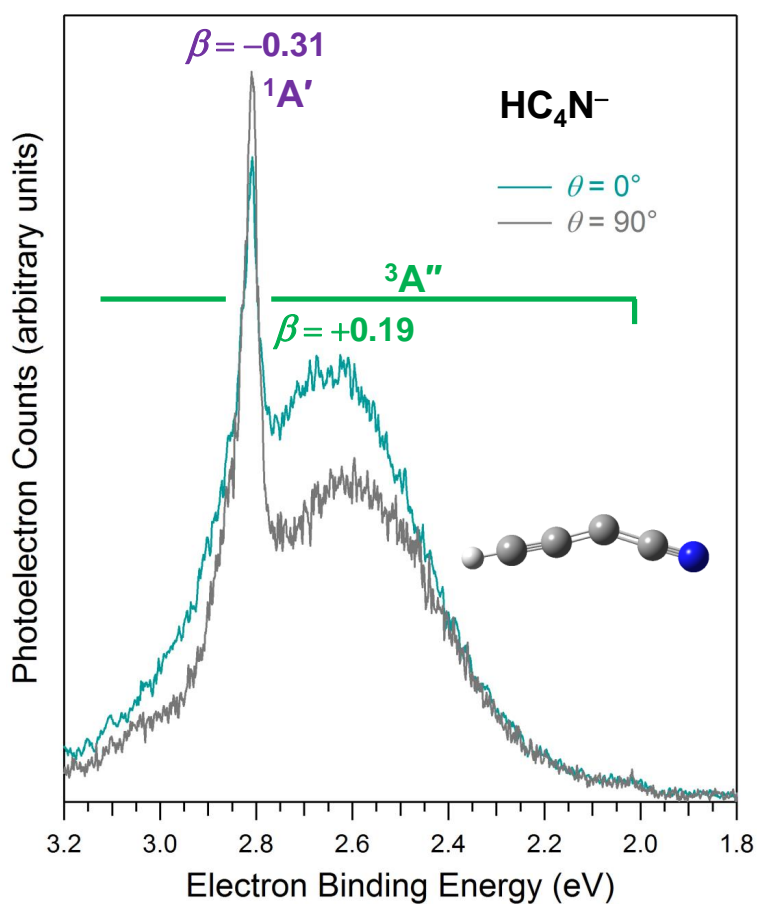
(Table 5.2), a one-dimensional potential cut along the $\angle$C2-C3-C4 bending coordinate (Fig. 5.5) reveals that the $\tilde{X}^3\mathrm{A}''$ state of HC_4N is extremely floppy with a barrier to linearity of only $\sim$24 meV. The one-dimensional cuts also reveal that as C2-C3-C4 becomes more bent, the triplet and singlet states cross. The unresolved nature of the triplet vibrational progression prevents us from determining the geometry of the $\tilde{X}^3\mathrm{A}''$ state from the photoelectron spectrum. Activity of this large-amplitude bending motion is the source of the breakdown of the independent harmonic oscillator analysis (see Fig. 5.6(a) for the $\tilde{X}^3\mathrm{A}'' \leftarrow \tilde{X}^2\mathrm{A}''$ photodetachment spectrum). Such failure of the harmonic, normal mode analysis has been observed in other floppy systems undergoing large amplitude geometry changes upon photodetachment.[13,19,24,142]

The partial simulated HC_4N^- spectrum, which shows only those features arising from $\tilde{a}^1\mathrm{A}' \leftarrow \tilde{X}^2\mathrm{A}''$ photodetachment, is shown in Fig. 5.3 in purple, with gray sticks representing individual calculated vibronic transitions. The simulation uses the calculated geometries, $\mathbf{K}''$ displacements, and vibrational frequencies (Tables 5.2 – 5.3). The calculated $\tilde{a}^1\mathrm{A}'$ origin, using either ROMP2 or ACPF,[154] is lower than the measured value of 2.809(4) eV (Table 5.1); therefore, we use the observed $\tilde{a}^1\mathrm{A}'$ origin in the simulation. The simulation of $\tilde{a}^1\mathrm{A}' \leftarrow \tilde{X}^2\mathrm{A}''$ photodetachment is very successful. Both the HC_4N^- anion and the $\tilde{a}^1\mathrm{A}'$ excited state of HC_4N are bent ($\angle$C2-C3-C4 $\sim$ 120°). None of the internal coordinates of HC_4N^- undergo a significant change upon photodetachment to the $\tilde{a}^1\mathrm{A}'$ state, resulting in a very prominent origin peak and a modest vibrational progression. The simulation reproduces the temperature-dependent peak that appears at 3.106(4) eV. The simulation confirms that this feature is a combination band arising primarily from activation of the ν_2 CN stretch, as well as activity of ν_3 (C1-C2-C3 asymmetric stretch).

We find no evidence of an open-shell singlet state in our spectra. In the case of NCCCN, Sanov and coworkers calculate the open-shell $^1\Delta_g$ to lie 0.1 – 0.3 eV higher in energy than the closed-shell $^1\mathrm{A}_1$, depending on the level of theory.[157] The two singlet states are degenerate at the linear NCCCN geometry, but upon distortion Renner-Teller coupling results in energy splitting to make the closed-shell singlet more stable. In the case of the oxyallyl diradical, the open-shell $^1\mathrm{B}_2$ is calculated to lie 1.346 eV higher in adiabatic energy than the closed-shell $\tilde{X}^1\mathrm{A}_1$.[139,164] To

Figure 5.5: One-Dimensional Potential Cut along the HCC-C-CN Bend Coordinate. Energies are relative to the minimum on the anion surface. All internal angles except $\angle$C2-C3-C4 are constrained to be linear, while the remaining internal coordinates are set to the values that minimize the energy of the anion under these constraints. All curves were calculated using ROMP2/6-311++G(d,p) level of theory/basis set.
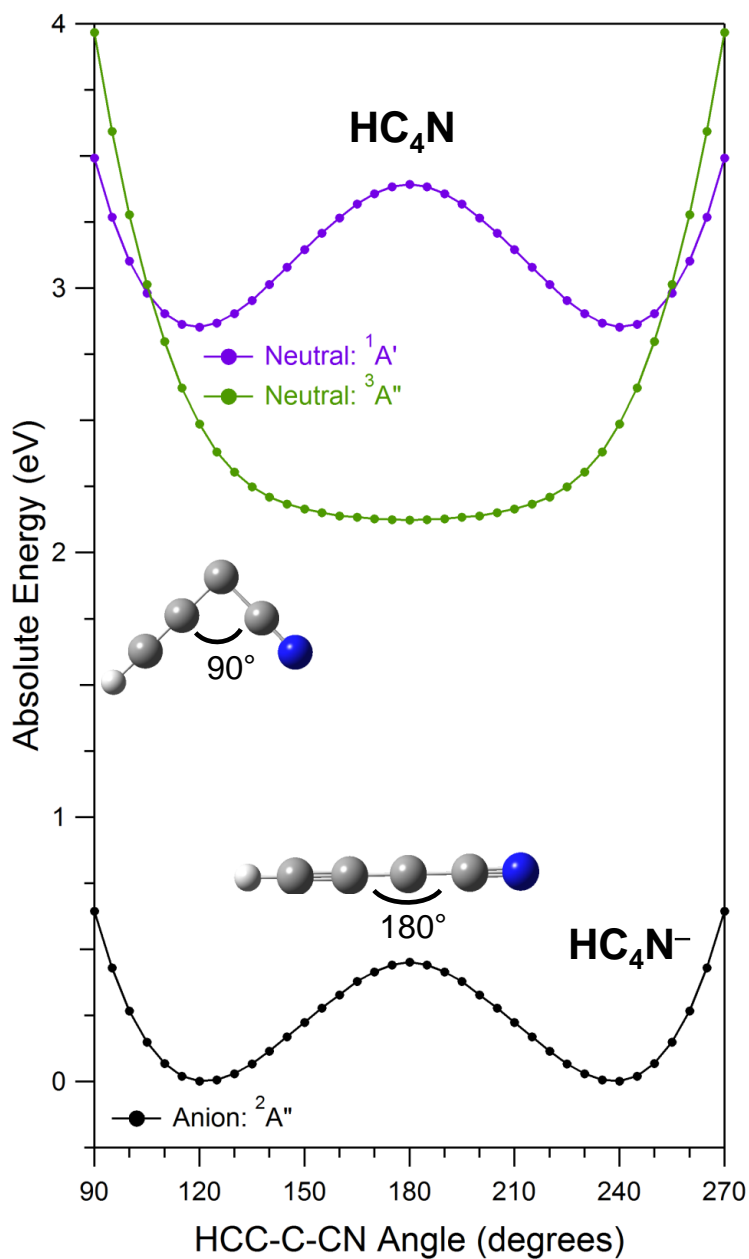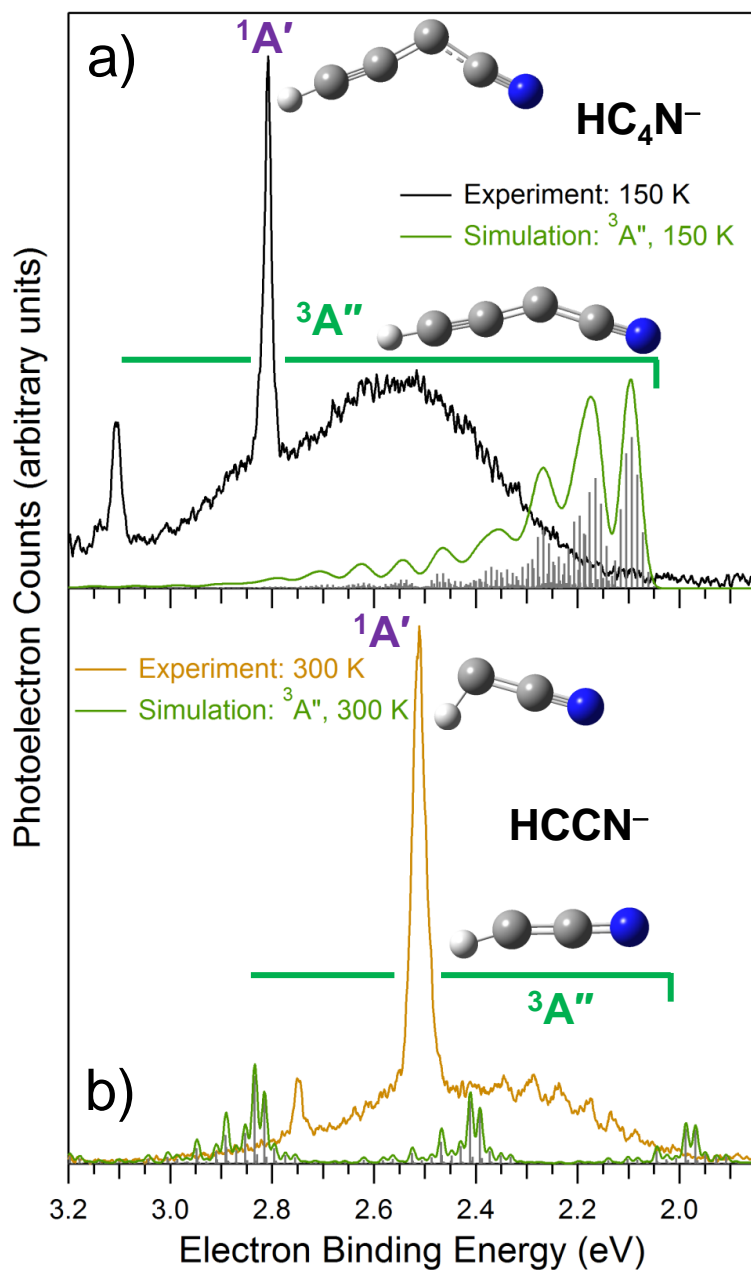
Figure 5.6: Franck-Condon Simulations of the Photoelectron Spectra of $\tilde{X}^3A''$ (a) HC_4N^- and (b) $HCCN^-$. Geometries, frequencies, and $\mathbf{K}''$ displacements used in the simulation are listed in Tables 5.2, 5.3, 5.4, and 5.5. The simulation uses the experimental electron affinities and term energies of the $\tilde{X}^3A''$ states of HC_4N and $HCCN$.

our knowledge, the energy of the open-shell singlet of HC_4N has not been computed. There is no indication of the open-shell singlet state in our spectra, though it is possible that it lies close in energy to the closed shell $^1A'$.

5.4.2 $HCCN^-$ and $DCCN^-$

The new 364-nm, magic angle photoelectron spectra of $HCCN^-$ and $DCCN^-$ are shown in Fig. 5.7. The data shown in Fig. 5.7 display significantly improved signal-to-noise over the previous data.[142] As a result, we more clearly resolve transitions within the vibrational progressions. As briefly mentioned in connection with HC_4N^-, it is extremely difficult to obtain a precise, reliable measurement of the EA of a molecule exhibiting an extended vibrational progression. In such cases, the intensity of the origin peak is weak, or even unobservable. Furthermore, normal mode analysis often fails to accurately represent the photoelectron spectrum, and we therefore cannot use calculated Franck-Condon factors to help assign the origin or to anticipate its relative intensity. Like HC_4N^-, the photoelectron spectra of $HCCN^-$ and $DCCN^-$ display extended vibrational progressions in the ground state. Through comparison of the $HCCN^-$ and $DCCN^-$ spectra, we assign the origins of $HCCN^-$ and $DCCN^-$ to the peaks marked with arrows in Fig. 5.7. We measure the EA of HCCN to be 2.001(15) eV and of DCCN to be 1.998(15) eV, in accord with the measurements of the previous work (Table 5.1). We measure the ΔE_{ST} of HCCN as 0.510(15) eV and the ΔE_{ST} of DCCN to be 0.508(15) eV. The stated uncertainties assume that the origin peaks have been assigned correctly. However, it is notoriously difficult to assign the origin of an extended progression, and the uncertainties given in the previous study[142] were definitely optimistic.

The photoelectron spectra of $HCCN^-$ and $DCCN^-$ exhibit several similarities to the HC_4N^- spectrum. Both HC_4N and HCCN (DCCN) possess a $\tilde{X}^3A''$ ground state that is significantly less bent than the anion. Upon $\tilde{X}^3A'' \leftarrow \tilde{X}^2A''$ photodetachment, the $\angle$H-C1-C2 increases by $35.0°$, and the C1-C2 bond decreases by 0.050 Å(Table 5.4). The large geometry change from the bent anion to the quasilinear triplet[165] results in an extended vibrational progression beginning at 2.0 eV (Table 5.1). The peaks in the $\tilde{X}^3A''$ HCCN progression are spaced by roughly 400 cm^{-1},

Figure 5.7: Partial Franck-Condon Simulations of the Photoelectron Spectra of HCCN$^-$ and DCCN$^-$. Green arrows mark the origin peaks, and insets of the origin regions show the measured EAs and uncertainties. The equilibrium structures of the $\tilde{X}^3A''$ and $\tilde{a}^1A'$ states of HCCN (DCCN) are also shown. The new photoelectron spectra collected in the present work display improved signal-to-noise, enabling us to resolve additional peaks. Geometries, frequencies, and $\mathbf{K}''$ displacements used in the simulation are listed in Tables 5.4 – 5.6. The simulations use the measured electron affinity and term energy of the $\tilde{X}^3A''$ and $\tilde{a}^1A'$ states of HCCN and of DCCN.
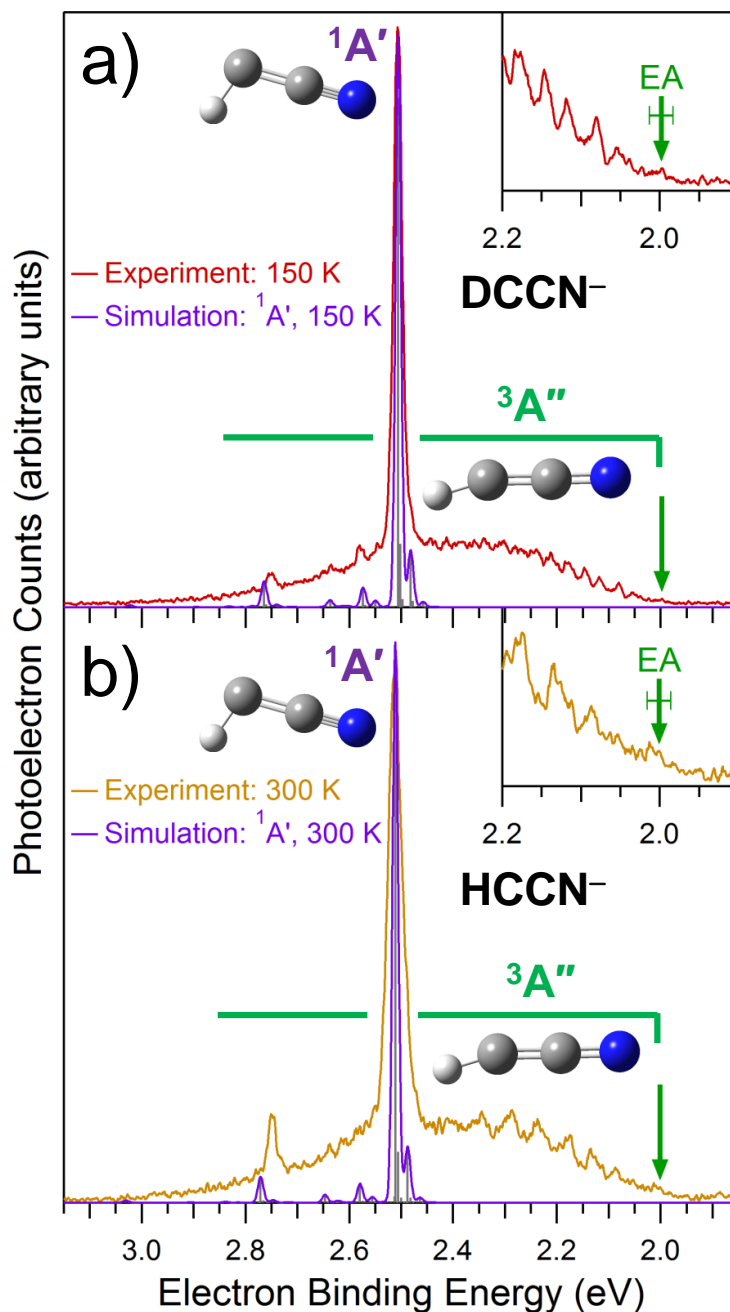
corresponding to activity of the ν_5 HCC bending mode.[142]

As in the case of HC_4N^-, the large geometry change leads to the failure of the harmonic normal mode analysis to adequately model the $\tilde{X}^3A'' \leftarrow \tilde{X}^2A''$ photodetachment photoelectron spectrum. One-dimensional potential cuts along the H-C-CN bend coordinate are presented in Fig. 5.8. The simulated $\tilde{X}^3A'' \leftarrow \tilde{X}^2A''$ spectrum of $HCCN^-$ is shown in Fig. 5.6(b); the calculated geometries, $\mathbf{K}''$ displacements, and vibrational frequencies are given in Tables 5.4 – 5.6. In the $HCCN^-$ ($DCCN^-$) case, the large change in the ∠H-C1-C2 is represented in the harmonic normal mode analysis in Cartesian coordinates by a nonphysical change in the H-C1 bond length.[24] This is manifested in the appearance of a CH (CD) stretch progression in the predicted spectrum.

Like HC_4N, the origin of the excited $\tilde{a}^1A'$ state is the most prominent feature in the spectrum of HCCN. The ∠H-C1-C2 of both $HCCN^-$ and the $\tilde{a}^1A'$ state of HCCN are strongly bent ($\sim110°$), resulting in an intense origin peak and a short vibrational progression. At higher binding energy, we observe an additional sharp feature at eBE = 2.747 eV, or 1903 cm^{-1} higher in energy than the $\tilde{a}^1A'$ HCCN origin. As in the case of HC_4N^-, the eBE of this peak suggests it is a CN stretch of the $\tilde{a}^1A'$ state. In the $HCCN^-$ and $DCCN^-$ spectra, this feature does not display the same strong temperature dependence as the analogous peak in the HC_4N^- 150 K spectrum; however, the intensity of the peak does vary with time with respect to the $\tilde{a}^1A'$ origin peak and the $\tilde{X}^3A''$ progression. The photoelectron spectra shown in Fig. 5.7 indicate the average intensity of the eBE $\sim$ 2.75 eV peak over the data sets collected.

In the previous anion photoelectron spectroscopy study of $HCCN^-$ and $DCCN^-$, Nimlos *et al.* also report the appearance of a peak at eBE $\sim$ 2.75 eV.[142] In contrast to our findings, however, they observe this peak in the cold $HCCN^-$ spectrum but not at room temperature. Furthermore, they do not report the appearance of this peak in either the cold or room temperature $DCCN^-$ spectra. The photoelectron spectrum of the isomer $HCNC^-$ is also shown in the 2002 work. There is no indication of a peak at eBE $\sim$ 2.75 eV due to the $HCNC^-$ isomer, confirming that the eBE $\sim$ 2.75 eV peak is indeed due to $HCCN^-$ ($DCCN^-$). In the 2002 study, the peak is not assigned.

Table 5.4: Calculated (ROMP2/6-311++G(d,p)) equilibrium geometry of $\tilde{X}^2A''$ HCCN$^-$ (DCCN$^-$) and the calculated net geometry change upon photodetachment to the $\tilde{X}^3A''$ and $\tilde{a}^1A'$ states of HCCN (DCCN). Bond lengths are given in units of angstrom (Å), and bond angles are given in units of degree (°). Boldfaced entries highlight the internal coordinates that undergo significant change upon photodetachment.

| | HCCN$^-$ | Geometry Change | |
Internal Coordinate	$\tilde{X}^2A''$	$\tilde{X}^3A'' \leftarrow \tilde{X}^2A''$	$\tilde{a}^1A' \leftarrow \tilde{X}^2A''$
H-C1	1.104	−0.030	−0.001
C1-C2	1.382	**−0.050**	+0.026
C2-N	1.210	−0.006	−0.026
∠H-C1-C2	109.6	**+35.0**	−1.69
∠C1-C2-N	172.3	+3.0	−1.14

Table 5.5: Calculated (ROMP2/6-311++G(d,p)) unscaled, harmonic frequencies of $\tilde{X}^2A''$ HCCN$^-$ and the $\tilde{X}^3A''$ and $\tilde{a}^1A'$ states of HCCN. The measured CN stretch frequency is listed in italics below the calculated value. Computed $\mathbf{K}''$ displacements (PESCAL) are also listed. The computed $\tilde{X}^3A'' \leftarrow \tilde{X}^2A''$ $\mathbf{K}''$ displacements do not accurately represent the geometry change that takes place upon photodetachment and result in a Franck-Condon simulation that does not reproduce the observed triplet progression (Fig. 5.6(b)).

| | | | HCCN$^-$ | $\tilde{X}^3A'' \leftarrow \tilde{X}^2A''$ | | $\tilde{a}^1A' \leftarrow \tilde{X}^2A''$ | |
Mode		Description	$^2A''$, cm^{-1}	$\Delta\mathbf{K}''$	$^3A''$, cm^{-1}	$\Delta\mathbf{K}''$	$^1A'$, cm^{-1}
A′	ν_1	CH stretch	3031.6	−0.15904	3379.8	−0.0035737	3093.3
	ν_2	CN stretch	1764.1	−0.061446	1631.5	−0.066178	2227.7
							1903(40)^a
	ν_3	HCC bend	1032.7	0.16846	260.3	5.1113x10^{-6}	1065.9
	ν_4	CC stretch	936.5	−0.51123	1071.0	0.047076	979.6
	ν_5	CCN bend	458.7	0.18347	470.3	0.025295	404.2
A″	ν_6	CCN bend	457.2	0	416.5	0	334.8

^{a} Experiment, this work

Figure 5.8: One-Dimensional Potential Cut along the H-C-CN Bend Coordinate. Energies are relative to the minimum on the anion surface. All internal angles except $\angle$H-C-C are linear, and bond lengths are set to the values that minimize the energy of the anion. The $\angle$C-C-N angle is constrained to be linear in this scan, while the remaining internal coordinates are set to the values that minimize the energy of the anion when the C-C-N angle was 180°. All potential curves were calculated using ROMP2/6-311++G(d,p).
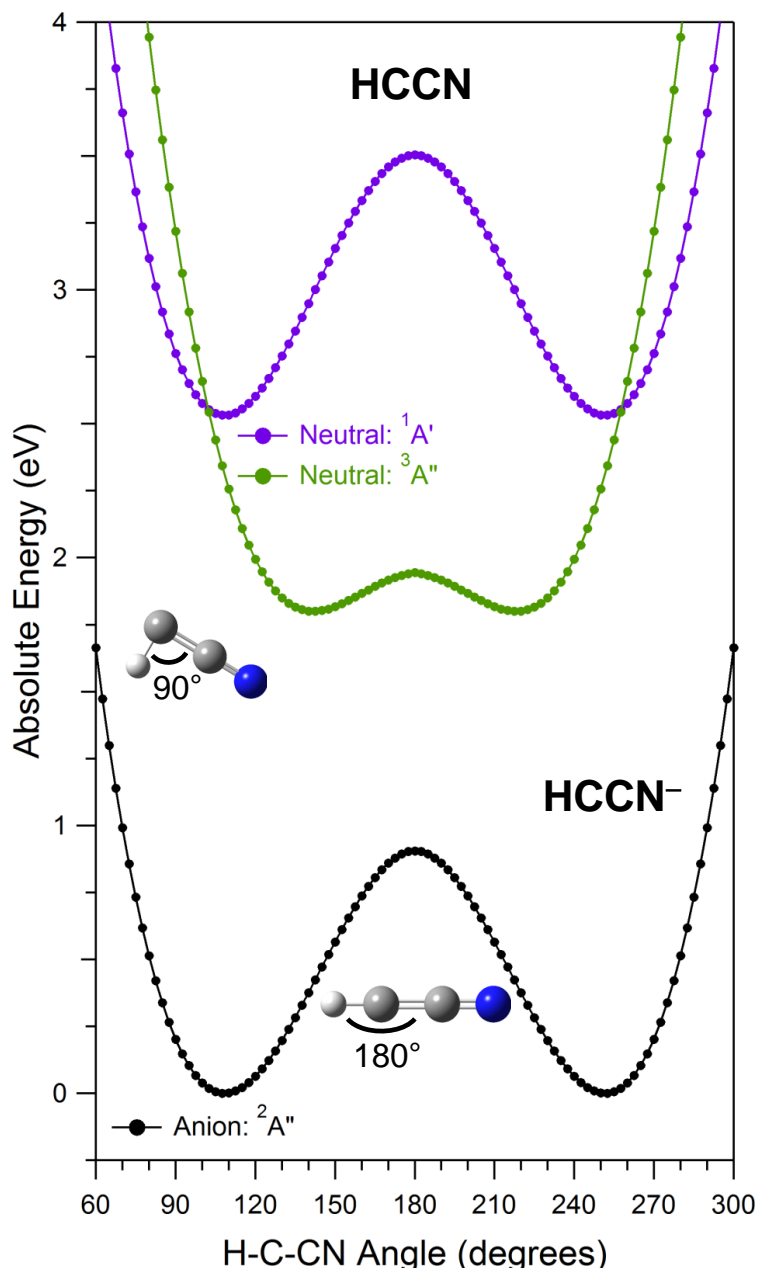
Table 5.6: Calculated (ROMP2/6-311++G(d,p)) unscaled, harmonic frequencies of $\tilde{X}^2A''$ DCCN$^-$ and the $\tilde{X}^3A''$ and $\tilde{a}^1A'$ states of DCCN. The measured CN stretch frequency is listed in italics below the calculated value. Computed $\mathbf{K}''$ displacements (PESCAL) are also listed. The computed $\tilde{X}^3A'' \leftarrow \tilde{X}^2A''$ $\mathbf{K}''$ displacements do not accurately represent the geometry change that takes place upon photodetachment and result in a Franck-Condon simulation that does not reproduce the observed triplet progression.

			DCCN$^-$	$\widetilde{X}\,^3A'' \leftarrow \widetilde{X}\,^2A''$		$\tilde{a}\,^1A' \leftarrow \widetilde{X}\,^2A''$	
Mode		Description	$^2A''$, cm^{-1}	$\Delta\mathbf{K}''$	$^3A''$, cm^{-1}	$\Delta\mathbf{K}''$	$^1A'$, cm^{-1}
A'	ν_1	CD stretch	2226.0	−0.20592	2498.0	−0.0062980	2280.4
	ν_2	CN stretch	1759.4	−0.046471	1620.9	−0.066722	2216.5
							1936(40)[a]
	ν_3	DCC bend	998.4	−0.089994	204.5	0.020164	984.4
	ν_4	CC stretch	776.0	0.61268	1011.3	−0.046367	825.2
	ν_5	CCN bend	418.0	0.43067	466.1	0.012876	378.4
A''	ν_6	CCN bend	450.4	0	410.0	0	328.2

[a] Experiment, this work

One important outcome of our reexamination of the $HCCN^-$ and $DCCN^-$ spectra is the identification of the eBE ~ 2.75 eV peak, which was previously left unassigned. The harmonic normal mode analysis successfully predicts the $\tilde{a}^1A' \leftarrow \tilde{X}^2A''$ photodetachment photoelectron spectra of $HCCN^-$ and $DCCN^-$ (Fig. 5.7) to verify the identity of the eBE ~ 2.75 eV peak. The simulation shows a peak at eBE $= 2.77$ eV resulting from excitation of CN stretch in the $\tilde{a}^1A'$ state of HCCN. We resolve additional features in the $DCCN^-$ 150 K spectrum (Fig. 5.7(a)) between 2.55 and 2.65 eV that are reproduced in the simulation, giving us further confidence in the Franck-Condon simulations of the $\tilde{a}^1A' \leftarrow \tilde{X}^2A''$ photoelectron spectra of these species.

The fact that this condition-dependent peak appears at a similar energy relative to the $\tilde{a}^1A'$ origin in both the HC_4N^- and $HCCN^-$ ($DCCN^-$) spectra (2395 and $\sim$1920 cm^{-1}, respectively) and that there is no significant isotope shift upon deuteration of $HCCN^-$, confirms that these peaks result from CN stretch excitation of the $\tilde{a}^1A'$ state of the neutral.

5.5   Discussion

We observe several similarities between the HC_4N and HCCN (DCCN) systems, but it is useful to also examine them in the context of a broader series of molecules.

First, we observe that the EAs of HCCN and HC_4N are similar, but they are very different from the EA of HC_3N. The EAs of HCCN and HC_4N are both approximately 2.0 eV, whereas the EA of HC_3N is considerably lower: ~ 0.5 eV.[166] This is perhaps not surprising, as trends in abundance, structure, and reactivity that depend on whether n is even or odd have been noted among HC_nN cyanopolyynes. This difference may be due in part to the carbene nature of the even cyanopolyynes, as compared to the closed-shell singlet odd cyanopolyynes. The neutral $n =$ odd cyanopolyyne molecules are considered to be more stable than the even ones; thus, the greater EA of the even cyanopolyynes implies that—unlike their neutral counterparts—the odd cyanopolyyne anions are not more stable than the even cyanopolyyne anions.

We also observe that exchanging an alkyne group for a nitrile raises the vertical detachment energy (VDE) by approximately 1 eV, which is clearly a result of the CN group shifting the spectrum

to higher eBE. The VDE is the energy at which the greatest Franck-Condon overlap occurs, and it appears as the maximum of the vibrational progression. The VDE of the triplet ground state of HCCCH is 1.714 eV,[?] of HCCN is 2.36 eV, and of NCCCN[157] is 3.53 eV. As a pseudohalogen, the CN group acts to stabilize negative ions.[157,166–168] Because the CN group stabilizes the negative charge of the anion more than it stabilizes the corresponding neutral, the addition of CN groups has the effect of increasing the VDE.

5.6   Conclusions

We report the 364-nm photoelectron spectrum of HC_4N. At lower binding energy, we observe a broad progression corresponding to photodetachment from the $\tilde{X}^2A''$ HC_4N^- anion to the $\tilde{X}^3A''$ ground state of HC_4N. The large geometry change upon photodetachment—specifically, an increase of 28.2° in the $\angle$C2-C3-C4—precludes the observation of an origin peak. The adiabatic EA of HC_4N is measured to be 2.05(8) eV. At 2.809(4) eV, we observe the $\tilde{a}^1A'$ origin of HC_4N. The ΔE_{ST} of HC_4N is measured to be 0.76(8) eV, with an uncertainty primarily due to our inability to resolve the origin of the triplet state.

For comparison, we also report the photoelectron spectra of $HCCN^-$ and $DCCN^-$. The photoelectron spectra of $HCCN^-$ and $DCCN^-$ also exhibit an extended progression corresponding to $\tilde{X}^3A'' \leftarrow \tilde{X}^2A''$ photodetachment. In this case, however, the origin transition can be resolved, giving EA(HCCN) = 2.001(15) eV, which is very similar but more accurate than the EA(HC_4N). The $\tilde{a}^1A'$ origin of HCCN appears at 2.511(4) eV, yielding a ΔE_{ST} of HCCN of 0.510(15) eV. Like HC_4N^-, the photoelectron spectra of $HCCN^-$ and $DCCN^-$ reveal peaks $\sim$ 2000 cm^{-1} higher in energy than the singlet origin that vary in intensity depending on experimental conditions. In each case, these peaks result from CN stretch excitation of the $\tilde{a}^1A'$ state of the neutral.

The HC_4N and HCCN (DCCN) systems display several similarities, but through comparison with other organic chains, we gain insight into how they relate to a broader series of molecules. While the EA of HC_4N is essentially the same as that of HCCN, the EA of HC_3N is much lower. In addition, exchanging an alkyne group for a nitrile raises the VDE by approximately 1 eV.

Chapter 6

Propadienylidene

6.1 Introduction

Not only is the carbene propadienylidene (:C=C=CH$_2$) interesting from a fundamental point of view, it also has astrophysical relevance. It is abundant in the interstellar medium[169] and has been detected in multiple astronomical sources.[170,171] Early laboratory studies produced rotational spectra of gas-phase H$_2$CCC.[172–174] In conjunction with calculations,[175] these experiments indicated the ground state geometry of H$_2$CCC to be a near-prolate top with C_{2v} symmetry. Electronic spectra of H$_2$CCC in Ar and Ne matrices have been collected by McMahon and coworkers.[176,177] Using cavity ring-down spectroscopy, Maier and coworkers collected electronic spectra of gas-phase H$_2$CCC.[178,179] The interesting electronic properties of propadienylidene were evidenced in these studies,[176–179] as the symmetry-forbidden $\tilde{A}^1A_2 \leftarrow \tilde{X}^1A_1$ transition was observed as a result of vibronic coupling.

Oakes and Ellison were the first to publish the photoelectron spectrum of H$_2$C$_3^-$ (m/z 38).[180] In their experiment, H$_2$C$_3^-$ was prepared in a high pressure, direct current, electrical discharge containing propene (C$_3$H$_6$) and oxygen; the 488 nm photoelectron spectrum of m/z 38 was collected. They did not observe much vibrational structure in the H$_2$C$_3^-$ spectrum, indicating that the anion and the neutral formed upon photodetachment had similar geometries; thus, they concluded that they had prepared and collected the photoelectron spectrum of the propadienylidene isomer. Had signal from another H$_2$C$_3^-$ isomer, propargylene (HCCCH), been present in the spectrum, one would expect to see a vibrational progression corresponding to the C-C-H bend, which is antici-

pated to be active when an electron is removed from the bent HCCCH$^-$ anion to become a more planar neutral. They measured EA(H$_2$CCC) to be 1.794(25) eV; they were unable to resolve any vibrational frequencies, nor did they observe excited states.

Propadienylidene was revisited in 1995 by Robinson *et al.*[181] H$_2$CCC$^-$ anions were generated using a flowing afterglow ion source by reacting O$^-$ with allene, H$_2$CCH$_2$. In their 351-nm photoelectron spectrum, they observe transitions to both the $\tilde{X}^1A_1$ and $\tilde{a}^3B_1$ states of H$_2$CCC. They measure the EA (1.794(8) eV) and the singlet-triplet splitting, ΔE_{ST} (29.7(2) kcal mol^{-1}). Further analysis of the spectrum is not performed.

Here, we reexamine the photoelectron spectrum of H$_2$CCC$^-$. As in the previous study, we form H$_2$CCC$^-$ in a flowing afterglow by reacting O$^-$ with allene. We collect the 364-nm photoelectron spectrum of H$_2$CCC$^-$. The data presented here display improved vibrational resolution, a result of vibrational cooling of the ions. We also present the photoelectron spectrum of D$_2$CCC$^-$ for the first time. Detailed analysis of these spectra is reported herein.

6.2   Experimental Methods

The negative ion photoelectron spectrometer used in this experiment has been described in detail elsewhere.[2,34,41] The apparatus consists of four main sections: an ion source, a mass filter, an interaction region with crossed laser and ion beams, and an electrostatic electron kinetic energy analyzer.

Negative ions are formed in a flowing afterglow ion source. A microwave discharge containing trace amounts of O$_2$ gas in He buffer gas ($\sim$0.4 Torr) generates atomic oxygen radical anion, O$^-$. Allene (H$_2$CCCH$_2$) is added downstream of O$^-$ to generate propadienylidene (H$_2$CCC$^-$) anions: O$^-$ + H$_2$CCCH$_2$ $\rightarrow$ H$_2$CCC$^-$ + H$_2$O.[180,181] Similarly, D$_2$CCC$^-$ is produced by reacting O$^-$ with allene-d_4 (D$_2$CCCD$_2$). Collisions with He buffer gas cool the ions to approximately 300 K. The flow tube can be further cooled with a liquid nitrogen jacket to obtain a "cold spectrum" of ions with temperatures near 150 K.

Anions are extracted into a differentially pumped region and are accelerated to 735 eV before entering a Wien velocity filter for mass selection. The recently rebuilt Wien filter has a mass resolution of $m/\Delta m \sim 60$.[38,161] Great care is taken to ensure that there is no contribution from propargyl or 1-propynyl anions (H_2CCCH^- and H_3CCC^-, respectively; m/z 39) in the photoelectron spectra of propadienylidene (m/z 38).

The mass-selected ion beam (typically 70 pA) is decelerated to 35 eV and focused into the laser interaction region. Here, the 1-W output from a single-mode continuous-wave argon ion laser operating at 364 nm (3.40814 eV) is built up to approximately 100 W of circulating power in an optical buildup cavity located within the vacuum system. Photoelectrons ejected in the direction orthogonal to both the laser and ion beams enter a hemispherical energy analyzer. The photoelectron signal is recorded as a function of electron kinetic energy (eKE) with a position-sensitive detector. The energy analyzer has a resolution of approximately 11 meV under the conditions used for the present experiments.

The eKE is then converted to electron binding energy (eBE), which is independent of photon energy: eBE = $h\nu$ - eKE. The absolute kinetic energy scale is calibrated[2,34,43] before and after each data set using the well-known electron affinity of atomic oxygen.[45] Additionally, the energy scale is corrected for a slight linear compression $(<1\%)$[2] using the photoelectron spectrum of O_2^-, which provides a number of known transitions spanning the photoelectron energy range.[21,47] After making these corrections and accounting for the resolution of the spectrometer and rotational peak profiles, absolute eBEs can be determined with an accuracy of better than 5 meV.

A rotatable half-wave plate positioned outside the buildup cavity varies the polarization of the photodetachment radiation in order to control the angle θ between the electric field vector of the laser beam and the photoelectron collection axis. The photoelectron angular distribution is described by the equation[5]

$$I(\theta) = \frac{\sigma_0}{4\pi}(1 + \beta P_2(\cos \theta))$$

$$(6.1)$$

where σ_0 is the total photodetachment cross section, β is the anisotropy parameter, and $P_2(\cos \theta)$

is the second Legendre polynomial. We measure the anisotropy parameter explicitly by recording the photoelectron signal at the kinetic energy of one suitable intense peak in the photoelectron spectrum as a function of θ (between $\theta = 0°$ and $\theta = 360°$ in steps of $10°$). The photoelectron angular distribution is fit with Eq. 6.1, and full spectra collected at $\theta = 0°$ and $\theta = 90°$ are scaled to match β at the energy at which it was measured. Separately, we collect a photoelectron spectrum at $\theta = 54.7°$ (the "magic angle"), where the photoelectron intensity is independent of β and directly reflects the relative photodetachment cross section.

6.3   Theoretical Methods

All electronic structure calculations were performed using the Gaussian 03 program package.[48] Optimized geometries, harmonic vibrational frequencies, and normal mode coordinates were calculated at the B3LYP level of theory[49,50] with the 6-311++G(d,p) basis set[52] for the $\tilde{X}^2B_1$ state of H_2CCC^- as well as for the $\tilde{X}^1A_1$ and $\tilde{a}^3B_1$ states of the neutral H_2CCC. All molecules were constrained to C_{2v} symmetry.

We employ a Franck-Condon analysis of the vibrational structure in the photoelectron spectra to identify the active vibrational modes and the geometry change upon photodetachment. The Franck-Condon profiles of the photoelectron spectra are simulated with the PESCAL program,[21] using the calculated geometries, normal mode vectors, and vibrational frequencies of the anion and neutral states. The normal modes and the Duschinsky $\mathbf{J}''$ matrix and $\mathbf{K}''$ displacements are calculated. The Franck-Condon factors are computed in the harmonic oscillator approximation including Duschinsky rotation using the Sharp-Rosenstock-Chen method.[4] The individual vibronic peak contours are simulated by a Gaussian function with a full-width half-maximum of 11 meV, consistent with instrumental resolution.

Figure 6.1: Generalized Valence Bond Diagrams of the $\tilde{X}^2B_1$ state of H_2CCC^- and the $\tilde{X}^1A_1$ and $\tilde{a}^3B_1$ states of H_2CCC.
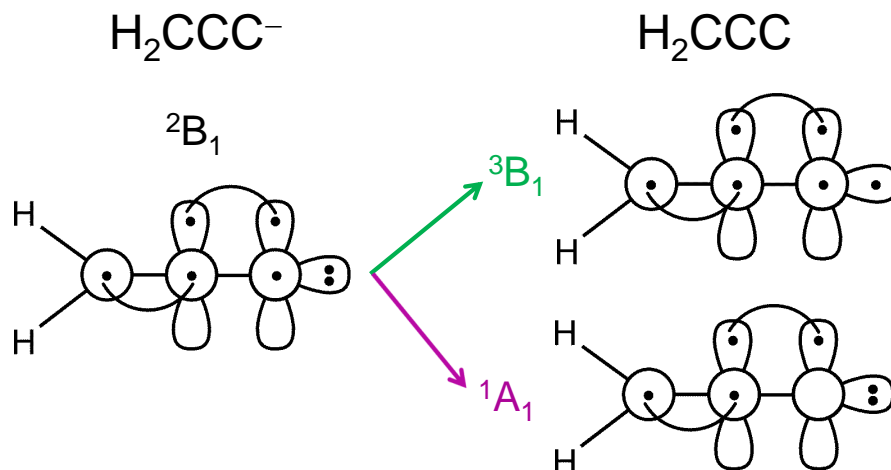
6.4   Results

6.4.1   Photoelectron Spectroscopy of H_2CCC^- and D_2CCC^-

The geometry change that takes place upon photodetachment dictates the vibrational structure of the photoelectron spectrum. As depicted in the generalized valence bond diagrams of the ground $\tilde{X}^2B_1$ state of H_2CCC^- and the ground $\tilde{X}^1A_1$ and excited $\tilde{a}^3B_1$ states of H_2CCC in Fig. 6.1, the excess electron of the anion resides primarily on the terminal C, and all three states have C_{2v} symmetry with a linear C-C-C backbone. If an electron is removed from the out-of-plane π orbital, the ground $\tilde{X}^1A_1$ state is formed. The excited $\tilde{a}^3B_1$ state is generated when an electron is photodetached from the in-plane σ orbital. Upon either $\tilde{X}^1A_1 \leftarrow \tilde{X}^2B_1$ or $\tilde{a}^3B_1 \leftarrow \tilde{X}^2B_1$ photodetachment, we expect the primary geometry changes to involve the C-C bond lengths and the H-C-H bond angle. Thus, we anticipate the C-C stretching modes and H-C-H bending modes to be active in the photoelectron spectrum. Furthermore, we predict that the modest geometry change will result in a short, resolved vibrational progression for each state of the neutral H_2CCC.

The 364-nm, 150 K photoelectron spectra of H_2CCC^- are shown in Fig. 6.2. The $\theta = 0°$ (blue) and $\theta = 90°$ (red) spectra are shown, with the measured β values plotted above the major

Table 6.1: Experimental and calculated electron affinity, singlet-triplet splitting, and vertical detachment energies of H_2CCC (B3LYP/6-311++G(d,p)) given in eV.

		$\tilde{X}\,^1A_1 \leftarrow \tilde{X}\,^2B_1$			$\tilde{a}\,^3B_1 \leftarrow \tilde{X}\,^2B_1$			
		(0-0)	VDE	β	(0-0)	VDE	β	ΔE_{ST}
H_2CCC	*Experiment*	1.794(4)	1.794(4)	–0.86	3.076(4)	3.078(4)	0.61	1.282(4)
	Calculated	1.945	2.011		3.224	3.334		1.279
D_2CCC	*Experiment*	1.786(4)	1.786(4)	––	3.072(4)	3.072(4)	––	1.286(4)
	Calculated	1.937	2.001		3.219	3.333		1.282

peaks. As anticipated, we observe well-resolved, relatively short vibrational progressions. The difference between the $\theta = 0°$ and $\theta = 90°$ spectra, as quantified by the drastic shift in β values of peaks with eBE greater than 3 eV, clearly indicates that there are two electronic states detected in the 364-nm spectra. In accord with the previous study,[181] we assign the lower energy progression to the $\tilde{X}^1A_1$ ground state of H_2CCC. The cooled spectra obtained in this work display improved energy resolution, enabling a more precise determination of the EA: 1.794(4) eV (Table 6.1).

At higher binding energy, we observe a short vibrational progression corresponding to photodetachment to the $\tilde{a}^3B_1$ excited state of H_2CCC. The origin of the $\tilde{a}^3B_1$ state appears at 3.076(4) eV, and we obtain the ΔE_{ST} of 1.282(4) eV (Table 6.1). Using this photon energy, we are able to see the origin of the triplet manifold as well as the fundamentals of the lowest-frequency active modes.

The 364-nm, magic angle photoelectron spectrum of D_2CCC^- is shown in Fig. 6.3(b). Comparison of the D_2CCC^- (purple, panel (b)) and H_2CCC^- (black, panel (a)) spectra confirm our spectral assignments and lend additional insight into the photodetachment process. The EA of D_2CCC is measured to be 1.786(4) eV, and the ΔE_{ST} is measured to be 1.286(4) eV. The energies of the observed vibronic transitions indicate that stretching modes of the C-C-C backbone and the D-C-D bend are active upon photodetachment. Deuteration lowers the frequency of the vibrations,

Figure 6.2: Photoelectron spectra of H_2CCC^- taken at $\theta = 0°$ and $\theta = 90°$ and scaled for β anisotropy.
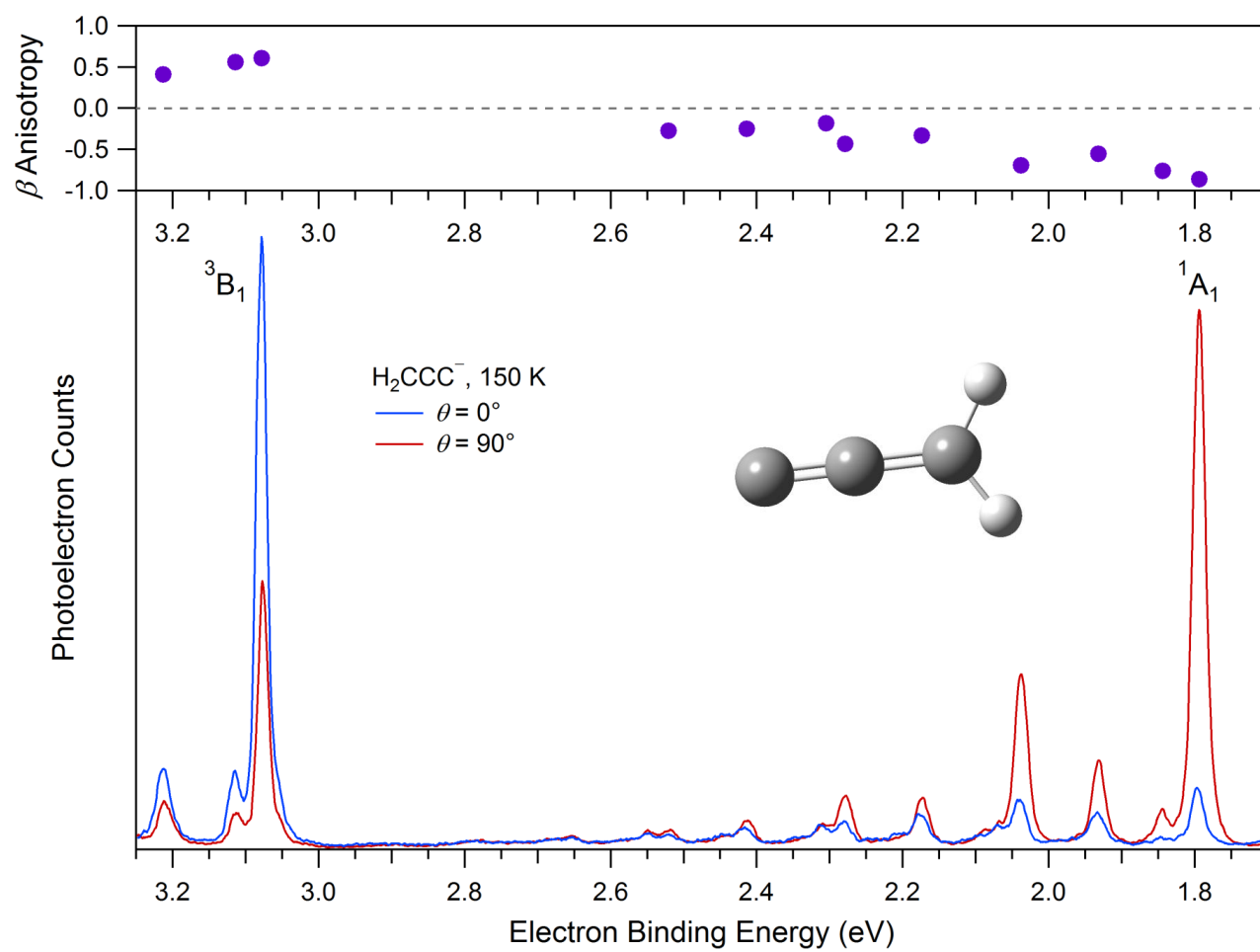
especially those involving significant H (D) displacements. With the aid of simulations, detailed in the following section (Section 6.5), we identify the individual vibronic transitions underlying the peaks in the spectrum and determine experimental frequencies for the most active vibrational modes.

6.5 Electronic Structure Calculations of H_2CCC (D_2CCC) and H_2CCC^- (D_2CCC^-)

As indicated by the short, resolved vibrational progression observed in the photoelectron spectra of H_2CCC^- and D_2CCC^-, we calculate only a modest geometry change upon photodetachment (Table 6.2). Unlike many of the molecules presented in this thesis, the rigidity of propadienylidene makes it well-suited for our standard Franck-Condon analysis, which assumes vibrational modes are uncoupled and harmonic. Such assumptions are valid near the bottom of the potential energy well; in the case of a molecule that does not undergo a substantial geometry change upon photodetachment—like propadienylidene—the most intense vibronic transitions access the bottom of the potential well. Thus, treating the vibrational modes as uncoupled and harmonic is a reasonable approximation.

The simulated photoelectron spectra of H_2CCC^- and D_2CCC^- are presented in Figs. 6.4(a) and (b), respectively. Like another rigid molecule furanide,[138] the Franck-Condon simulation using Cartesian coordinates reproduces the observed spectrum very well. In the simulations shown in Fig. 6.4, the $\mathbf{K}''$ displacements and vibrational frequencies have been optimized to obtain the best agreement between simulation and experiment. With minor adjustments to the *ab initio* $\mathbf{K}''$ displacements and vibrational frequencies, we achieve excellent agreement between theory and experiment (Tables 6.3 and 6.4). The agreement between the simulation and the observed photoelectron spectrum enables assignment of the major peaks, labeled in Fig. 6.4. In the H_2CCC^- spectrum, we primarily observe activity of the ν_2 symmetric and ν_4 asymmetric C-C-C stretching modes upon $\tilde{X}^1A_1 \leftarrow \tilde{X}^2B_1$ photodetachment; in the D_2CCC^- spectrum, we also resolve vibronic transitions involving excitation of the ν_1 D-C-D bending mode. Below 3.25 eV, we observe only the

Figure 6.3: Comparison of the 364-nm, magic angle photoelectron spectra of (a) H_2CCC^- and (b) D_2CCC^-.
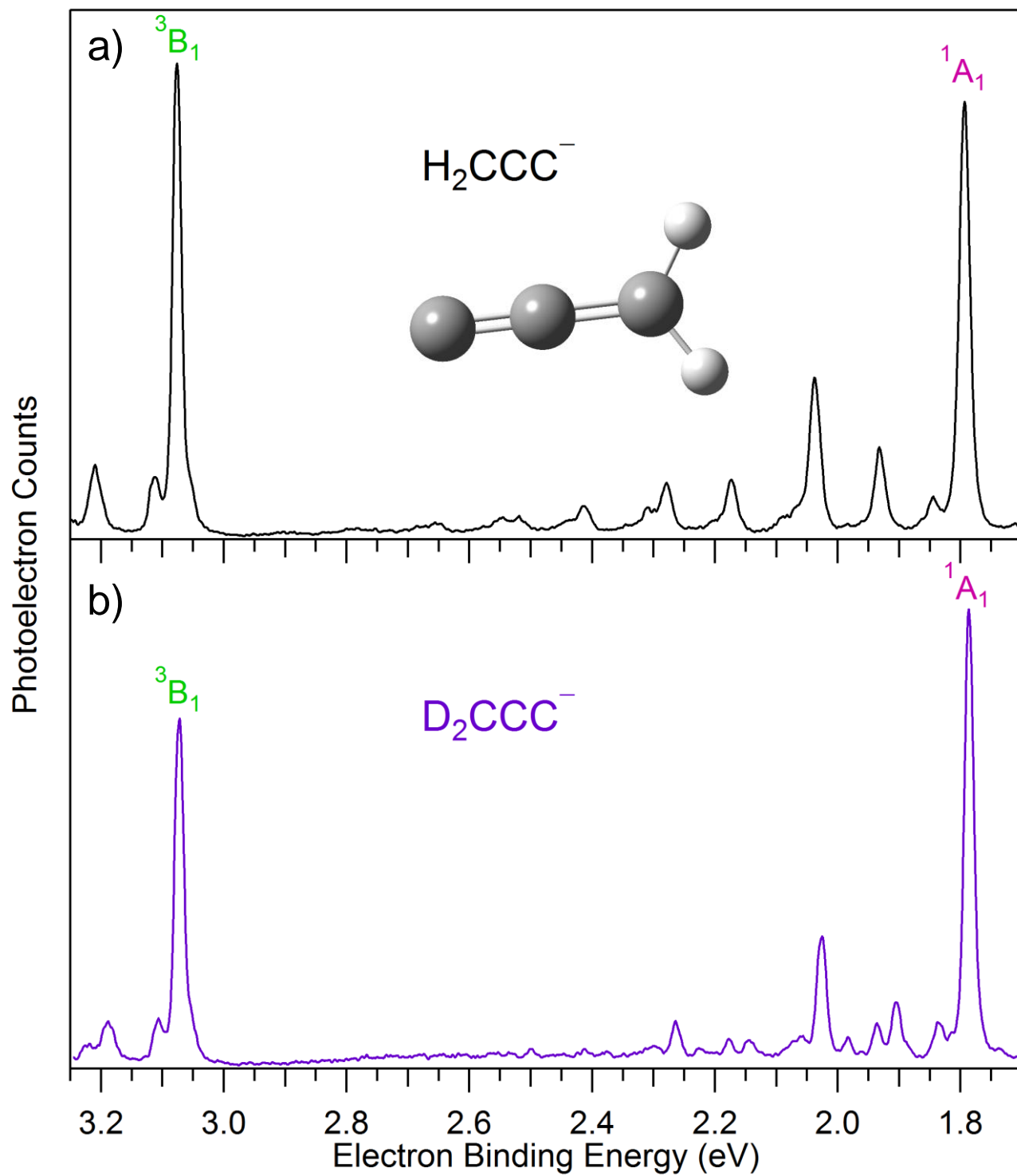
Table 6.2: Calculated (B3LYP/6-311++G(d,p)) equilibrium geometry of $\tilde{X}^2B_1$ H_2CCC^- and the calculated and experimental net geometry change upon photodetachment to the $\tilde{X}^1A_1$ and $\tilde{a}^3B_1$ states of H_2CCC. The experimental geometry change upon detachment to the $\tilde{X}^1A_1$ state is obtained from the experimental $\mathbf{K}''$ displacements (Table 6.3). Bond lengths are given in units of angstrom (Å), and bond angles are given in units of degree (°). Boldfaced entries highlight the internal coordinates that undergo significant change upon photodetachment.

H $\diagdown$ $\diagup$ 1C=C2=C3 H Internal Coordinate	H_2CCC^- $\tilde{X}^2B_1$ _Calculated_	Geometry Change		$\tilde{a}\,^3B_1 \leftarrow \tilde{X}^2B_1$ _Calculated_
		$\tilde{X}^1A_1 \leftarrow \tilde{X}^2B_1$		
		Calculated	_Experiment_	
H-C1	1.090	-0.001	−0.002	-0.007
C1-C2	1.371	**-0.047**	**−0.072**	-0.010
C2-C3	1.269	+0.015	+0.031	**-0.036**
∠H-C1-H	115.9	+0.8	+3.4	+2.7
∠H-C1-C2	122.0	-0.4	−1.7	-1.3
∠C1-C2-C3	180.0	+0	+0	+0

origin and the ν_4 fundamental of the $\tilde{a}^3B_1$ excited state of H_2CCC. Upon deuteration the frequency of ν_3 is lowered such that we can detect the origin and the ν_4 and ν_3 fundamentals of the $\tilde{a}^3B_1$ excited state of D_2CCC. The Franck-Condon simulation is unable to reproduce the peaks approximately 300 cm^{-1} higher in energy than the $\tilde{a}^3B_1$ origin in the H_2CCC^- and D_2CCC^- spectra. These peaks are assigned to the first overtone of ν_9; vibronic coupling with the higher-lying $\tilde{b}^3A_2$ state lends intensity to this transition.[182]

From the least-squares optimization of the Franck-Condon simulation, we determine the experimental frequencies of the most active modes upon $\tilde{X}^1A_1 \leftarrow \tilde{X}^2B_1$ photodetachment. Tables 6.3 and 6.4 list the *ab initio* calculated $\mathbf{K}''$ displacements and vibrational frequencies (B3LYP/6-311++G(d,p)), along with the experimental values (in italics) obtained through least-squares optimization of the simulation to experiment. In the $\tilde{X}^1A_1$ state of H_2CCC, $\nu_2 = 1957$ cm^{-1} and $\nu_4 = 1103$ cm^{-1}. The ν_2 frequency determined in this work is in excellent agreement with the ν_2 frequency of H_2CCC in an Ar matrix measured by Seburg *et al.*: 1960 cm^{-1}.[183,184] We measure the frequency of ν_4 in the $\tilde{a}^3B_1$ excited state of H_2CCC to be 1075 cm^{-1}. In the $\tilde{X}^1A_1$ state of D_2CCC, $\nu_2 = 1940$ cm^{-1}, $\nu_3 = 1202$ cm^{-1}, and $\nu_4 = 944$ cm^{-1}. In the $\tilde{a}^3B_1$ state of D_2CCC, we measure the harmonic frequency of ν_3 to be 1186 cm^{-1} and of ν_4 to be 941 cm^{-1}.

6.6   Discussion

These experiments were conducted in conjunction with Velocity-map Imaging (VMI – JILA) and Slow-Electron Velocity-map Imaging (SEVI – Berkeley) to gain additional insight into the rich electronic structure of the propadienylidene radical.[182] The composite H_2CCC^- photoelectron spectrum containing data obtained from all three experiments is shown in Fig. 6.5. In accord with our measured values, the EA and ΔE_{ST} of H_2CCC are measured with SEVI to be 1.7957(10) eV and 1.2837(14) eV, respectively. The two lowest lying excited states of H_2CCC are the $\tilde{a}^3B_1$ and $\tilde{b}^3A_2$ triplet states. As noted in the discussion of the peak assignments of the $\tilde{a}^3B_1$ state of H_2CCC (Section 6.4.1), vibronic coupling between $\tilde{a}^3B_1$ and $\tilde{b}^3A_2$ lends intensity to the ν_9 fundamental in our spectra. Above our experimental cut-off of 3.25 eV, strong vibronic coupling between the $\tilde{a}^3B_1$

Figure 6.4: Comparison of the magic angle, 150 K photoelectron spectra of (a) H_2CCC^- and (b) D_2CCC^- with their respective Franck-Condon simulations.
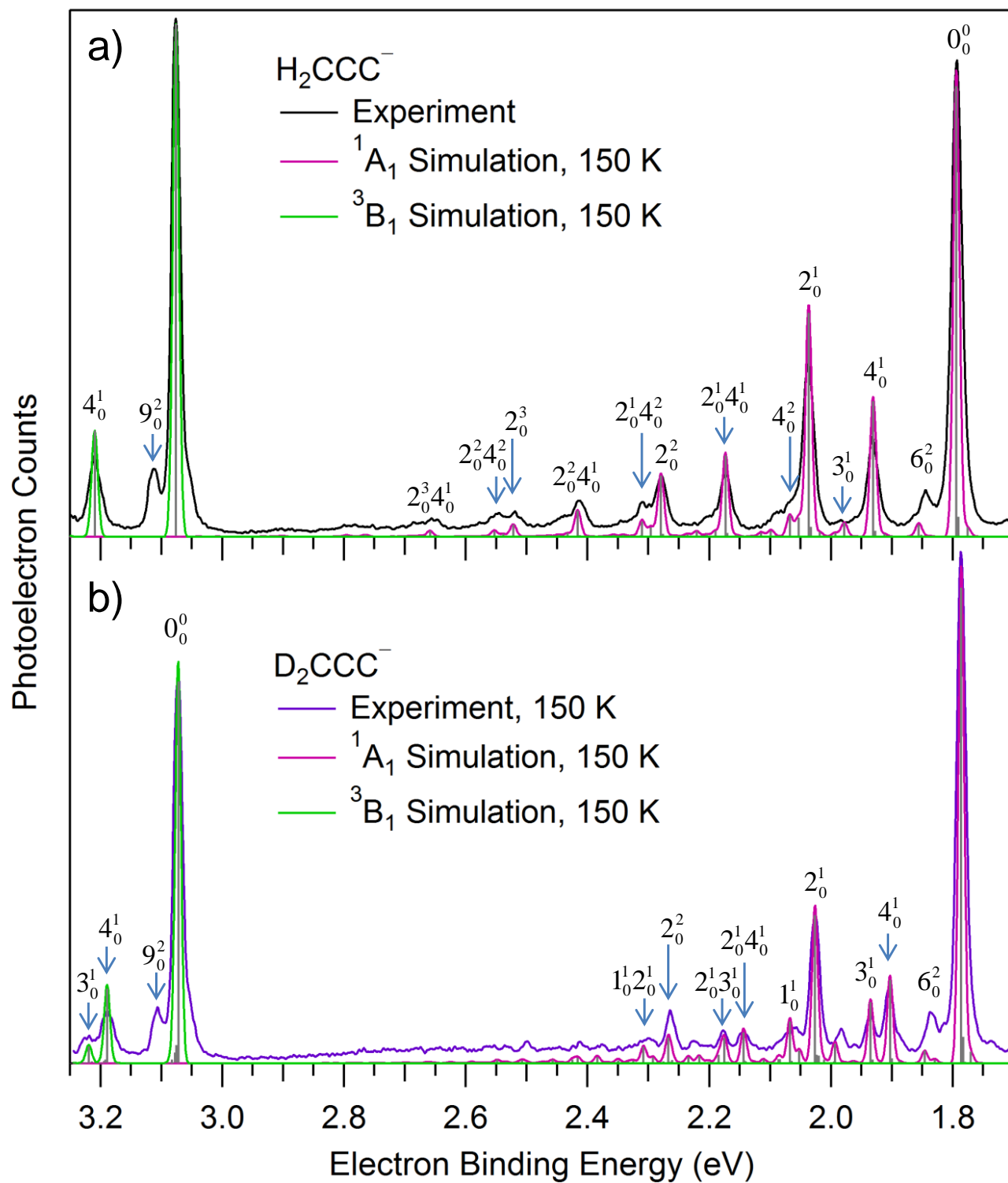
Table 6.3: Calculated (B3LYP/6-311++G(d,p)) unscaled, harmonic frequencies of $\tilde{X}^2B_1$ H_2CCC^- and the $\tilde{X}^1A_1$ and $\tilde{a}^3B_1$ states of H_2CCC. Computed $\mathbf{K''}$ displacements (PESCAL) are also listed. Experimental harmonic frequencies and displacements are listed in italics below the calculated value.

Mode		Description	Frequencies	$\tilde{X}^1A_1 \leftarrow \tilde{X}^2B_1$		$\tilde{a}\,^3B_1 \leftarrow \tilde{X}^2B_1$	
			H_2CCC^-, cm^{-1}	$\Delta\mathbf{K''}$	$^1A_1$, cm^{-1}	$\Delta\mathbf{K''}$	$^3B_1$, cm^{-1}
A_1	ν_1	CH sym stretch	3054.4	-2.125E-4	3093.8	-0.007153	3138.8
	ν_2	CCC asym stretch	1891.6	0.06896	2041.3	-0.06014	1982. 9
				0.1204[a]	*1957*[a]		
	ν_3	HCH bend	1457.3	0.001219	1484.1	0.01479	1450.5
				0.03123[a]			
	ν_4	CCC sym stretch	1077.0	-0.1092	1145.3	-0.1206	1110.9
				-0.1586[a]	*1103*[a]		*1075*[a]
B_1	ν_5	OOP CH flap	578.4	0.0	1045.0	0.0	710.5
	ν_6	OOP CCC bend	398.7	0.0	250.6	0.0	429.6
B_2	ν_7	CH asym stretch	3105.8	0.0	3172.0	0.0	3230.5
	ν_8	CCC bend + CH wag	1033.1	0.0	1051.0	0.0	903.9
	ν_9	CCC bend + CH wag	327.1	0.0	298.8	0.0	336.1i

[a] Experiment, this work

Table 6.4: Calculated (B3LYP/6-311++G(d,p)) unscaled, harmonic frequencies of $\tilde{X}^2B_1$ D_2CCC^- and the $\tilde{X}^1A_1$ and $\tilde{a}^3B_1$ states of D_2CCC. Computed $\mathbf{K}''$ displacements (PESCAL) are also listed. Experimental harmonic frequencies and displacements are listed in italics below the calculated value.

Mode		Description	Frequencies	$\tilde{X}^1A_1 \leftarrow \tilde{X}^2B_1$		$\tilde{a}\,^3B_1 \leftarrow \tilde{X}^2B_1$	
			D_2CCC^-, cm^{-1}	$\Delta\mathbf{K}''$	$^1A_1$, cm^{-1}	$\Delta\mathbf{K}''$	$^3B_1$, cm^{-1}
A_1	ν_1	CD sym stretch	2215.5	0.008722	2270.5	-0.01173	2277.3
				0.02728[a]	*2270[a]*		
	ν_2	CCC asym stretch	1887.2	0.06795	2013.1	-0.05960	1980.1
				0.09963[a]	*1940[a]*		
	ν_3	DCD bend	1183.7	-0.05568	1242.7	-0.04755	1199.5
				-0.09362[a]	*1202[a]*		*1186[a]*
	ν_4	CCC sym stretch	940.7	-0.1047	970.4	-0.1264	952.0
				-0.1335[a]	*944[a]*		*941[a]*
B_1	ν_5	OOP CD flap	486.7	0.0	836.6	0.0	572.7
	ν_6	OOP CCC bend	365.5	0.0	241.3	0.0	410.8
B_2	ν_7	CD asym stretch	2310.8	0.0	2362.4	0.0	2403.7
	ν_8	CCC bend + CD wag	834.1	0.0	848.7	0.0	688.6
	ν_9	CCC bend + CD wag	300.9	0.0	274.5	0.0	327.5i

[a] Experiment, this work

and $\tilde{b}^3A_2$ states results in a congested spectrum characterized by significant activity of the ν_4, ν_8, and ν_9 vibrational modes of $\tilde{a}^3B_1$, as well as ν_2 of $\tilde{b}^3A_2$.

Higher in energy are the coupled singlet states, $\tilde{A}^1A_2$ and $\tilde{B}^1B_1$. These states are particularly interesting to the chemical physics and astrophysics communities. The strong vibronic coupling between these states has been recognized for over a decade.[176,178,179,183–185] Furthermore, absorptions from these states of H_2CCC have been identified in diffuse interstellar bands (DIBs).[176,186] The prominent origin of the $\tilde{A}^1A_2$ state is observed at 3.4916(10) eV. The position of the ν_2 band of $\tilde{A}^1A_2$ is consistent with the assertion that the absorption observed at 5450 Å in acetylene discharges and in DIBs is due to H_2CCC. Further analysis of the band is complicated by vibronic coupling and low signal. The significant vibronic coupling between the $\tilde{A}^1A_2$ and $\tilde{B}^1B_1$ states diminishes the intensity of the $\tilde{B}^1B_1$ state. A weak feature just below 4.1 eV is assigned to the $\tilde{B}^1B_1$ state, but the origin is unobservable.

The highest energy excited state observed in these spectra is the $\tilde{c}^3A_1$ state, appearing at a term energy of 2.5968(14) eV. This state is not significantly coupled to any other electronic state. Therefore, the vibrational structure of the $\tilde{c}^3A_1 \leftarrow \tilde{X}^2B_1$ photoelectron spectrum is straightforward to interpret. The dominant vibrational progression is the ν_4 C-C stretch, as the C-C bonds are calculated to lengthen upon photodetachment to the $\tilde{c}^3A_1$ state of H_2CCC.

6.7   Conclusions

In this work, we have collected the 364-nm photoelectron spectra of H_2CCC^- and D_2CCC^-. We observe photodetachment from $\tilde{X}^2B_1$ H_2CCC^- (D_2CCC^-) to the $\tilde{X}^1A_1$ and $\tilde{a}^3B_1$ states of H_2CCC (D_2CCC). The photoelectron spectrum of H_2CCC^- presented here displays improved resolution over earlier studies,[180,181] enabling a more precise measurement of the EA and ΔE_{ST} of H_2CCC: 1.794(4) eV and 1.282(4) eV, respectively. From the photoelectron spectrum of D_2CCC^-, reported for the first time here, we measure EA(D_2CCC) = 1.786(4) eV and $\Delta E_{ST}(D_2CCC)$ = 1.286(4) eV.

Figure 6.5: Composite photoelectron spectrum of H_2CCC^- using PES, VMI, and SEVI. Labels indicate the origins of the electronic states of H_2CCC.
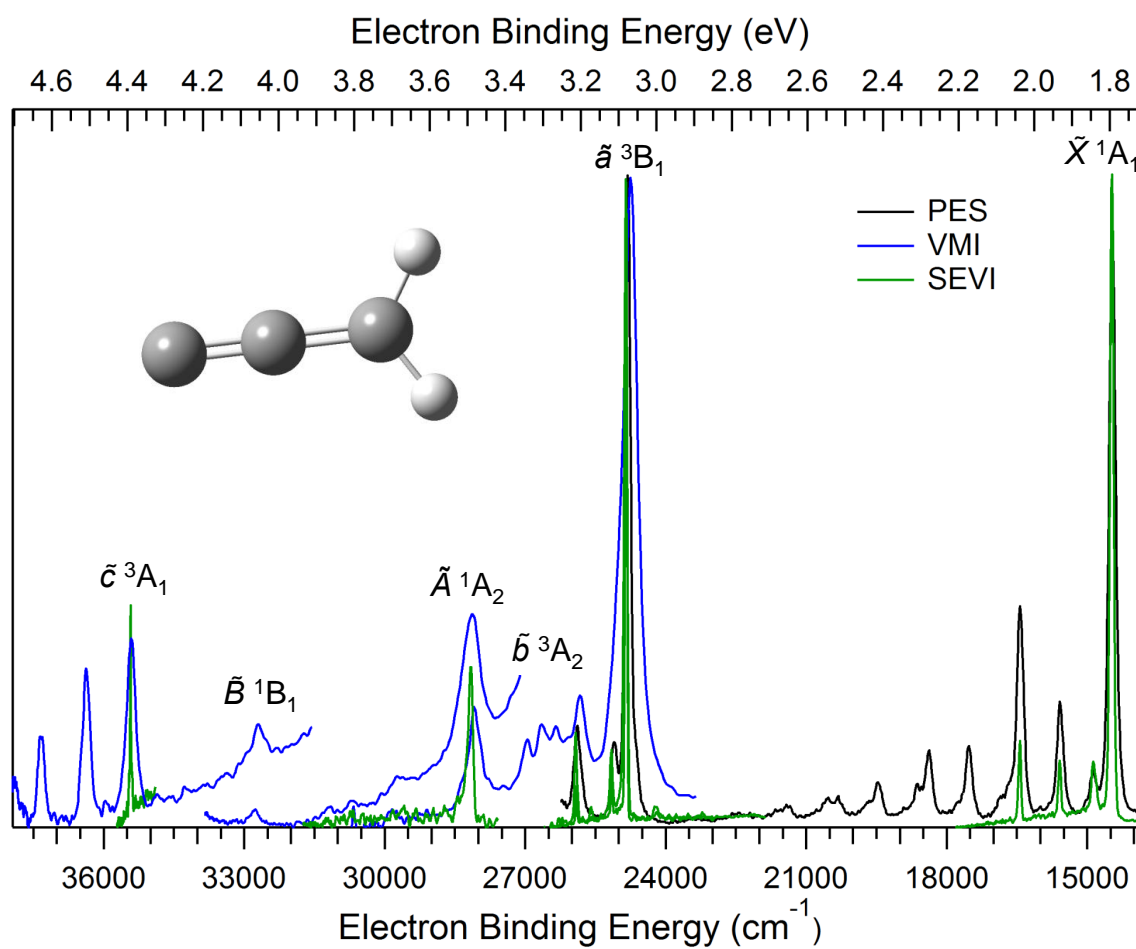
Because there is only a modest geometry change upon photodetachment—primarily shortening of C-C bonds—we observe a readily analyzable photoelectron spectrum. The origin peaks of the ground and excited states are prominent, and we observe a resolved vibrational progression corresponding to C-C stretching. The observed photoelectron spectrum can be reproduced using the standard Franck-Condon analysis, assuming harmonic and uncoupled vibrational modes. As a result of the good agreement between simulation and experiment, we determine several harmonic vibrational frequencies of H_2CCC and D_2CCC. Such problems are well-suited for photoelectron spectroscopy!

Though the photoelectron spectrum of the ground state is straightforward to analyze, the higher-lying excited states of H_2CCC, accessed using the more energetic photons available in VMI and SEVI, present more of a challenge.[182] Strong vibronic coupling between the $\tilde{a}^3B_1$ and $\tilde{b}^3A_2$ states and between the $\tilde{A}^1A_2$ and $\tilde{B}^1B_1$ states yields complex spectra. The $\tilde{A}^1A_2$ and $\tilde{B}^1B_1$ states are of particular interest to the astrophysical community, as DIBs profiles have been suggested as due to absorptions in these states. The energy of the ν_2 fundamental of $\tilde{A}^1A_2$ is consistent with DIB absorptions that have previously been ascribed to H_2CCC.

Chapter 7

Propargylene

7.1   Introduction

Carbenes, hydrocarbons in which one carbon atom has two electrons not involved in bonding, are a ubiquitous and fascinating class of compounds that play central roles in organic chemistry, combustion chemistry, and astrochemistry. The simplest carbene, methylene (H_2C:), has only one isomer, whereas carbenes containing two carbons, vinylidene ($H_2C=C$:) and ethylidene ($H_3C\ddot{C}H$), have only one carbene isomer in addition to their more stable forms ($HC\equiv CH$ and $H_2C=CH_2$). The addition of a third carbon atom dramatically broadens the carbene landscape, with C_3H_2 the best prototype of this expanded complexity. In addition to many structural isomers that now become plausible, more than one carbon atom may act as the carbene center, and conjugation among π orbitals is possible. Propargylene **1**, propadienylidene **2**, and cyclopropenylidene **3**, represent three of the possible structures of C_3H_2 (Schemes 7.1 and 7.2). For these reasons the C_3H_2 system has been the subject of many investigations to determine molecular and electronic structures, both for fundamental understanding and for the clues this knowledge provides in elucidating reaction mechanisms.

In this work we use negative ion photoelectron spectroscopy in the gas phase to investigate the HCCCH isomer, known as propargylene or propynylidene, and its fully deuterated isotopologue DCCCD.[187] We measure the electron affinity (EA) of propargylene and observe vibrational progressions in four electronic states of this molecule. We compare these results with high level electronic structure calculations for additional insight. Together, our photoelectron spectra, their angular

dependence, and the calculations characterize the molecular structure of propargylene anion and neutral and the quasilinear nature of the ground state of HCCCH.

7.2 Background

Propargylene **1** is the simplest acetylenic carbene and has several plausible electronic structures (1a – 1c), as shown in Scheme 7.1.

Scheme 7.1, Possible valence bond structures of propargylene.

1a

1b

1c
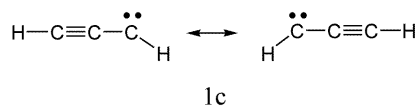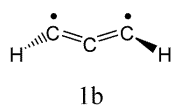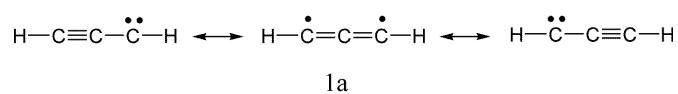
Scheme 7.2 shows two additional C_3H_2 isomers; propadienylidene **2** is the simplest vinylidene carbene, while cyclopropenylidene **3** is the smallest aromatic carbene.[184]

Scheme 7.2, Two additional isomers of C_3H_2: propadienylidene **2** and cyclopropenylidene **3**.

Automerization processes have been observed that connect these C_3H_2 isomers. The lowest energy isomer is cyclopropenylidene (c-C_3H_2) **3**, one of the most abundant carbenes in the interstellar medium (ISM), where carbon chains derived from c-C_3H_2 have been also been detected by radio astronomy. In the laboratory, c-C_3H_2 was first studied using matrix isolation and later *via* photoelectron spectroscopy and microwave spectroscopy.[188] It has a singlet ground state with a rigid structure in C_{2v} symmetry.

Propadienylidene **2**, the focus of Chapter 6, is also abundant in the ISM[169] and is a carrier of the diffuse interstellar bands (DIBs).[185] It has been detected in both dense clouds (IRC+10216 and TMC-1)[170,171] and the diffuse ISM.[189] Microwave spectroscopy[172–174] in combination with theory[175] indicate the equilibrium geometry of H_2CCC is a near prolate top in C_{2v} symmetry, with a singlet ground state and a large dipole moment. Propadienylidene has been studied extensively in the laboratory using photoelectron spectroscopy,[190] negative ion photoelectron spectroscopy,[180–182] and absorption spectroscopy.[191]

Returning to the focus of this study, propargylene **1** was first observed by Bernheim and Skell in 1965 by electron spin resonance (ESR) spectroscopy following photolysis of diazopropyne in a solid matrix at 77 K.[192] They assigned a triplet ground state of HCCCH with a linear geometry. Vibrational fundamentals of HCCCH were first measured via matrix isolation infrared spectroscopy by Chi in 1972,[193] and later by Jacox and Milligan in 1974.[194] Seburg, McMahon, and co-workers, in a series of elegant site-specific ^{13}C and ^{2}H isotopic labeling experiments, used both matrix isolation infrared spectroscopy and ESR spectroscopy to provide substantial evidence that despite the small barriers to linearity in all bending coordinates, the ground electronic state of HCCCH is a triplet diradical with a bent geometry in the C_2 point group; i.e., it most resembles the structure **1b**.[183,184,195]

Isomers of C_3H_2—particularly HCCCH—are important to combustion chemistry and have been implicated in the formation of polycyclic aromatics and soot.[196,197] C_3H_2 has been detected in C_2H_4/O_2 flames[198] and identified as an intermediate in the formation of C_2H from $C_2H_2/O/H$ flames.[199] In a photoionization efficiency study of C_3H_2 in a rich cyclopentene flame, Taatjes *et al.* measured the ionization energy (IE) of ^{3}HCCCH and found evidence for the presence of both HCCCH and cyclopropenylidene in a cyclopentene flame.[200] C_3H_2 isomers have been observed as products of the crossed molecular beam reaction of CH and C_2H_2.[201] *Ab initio* calculations and RRKM analysis show ^{3}HCCCH is a primary product of the reaction of C_2H_2 with CH and other hydrocarbons.[202–205] In contrast, c-C_3H_2 is detected as the main product of the CH + C_2H_2 reaction, studied using VUV photoionization and time-resolved mass spectrometry.[206]

Aside from its relevance to combustion chemistry and its fundamental importance as the smallest acetylenic carbene, substituted propargylene derivatives are used as ligands in organometallic chemistry,[207,208] and their interesting reactivity has been applied to organic synthesis.[209,210]

The technique of gas-phase negative ion photoelectron spectrometry is a powerful complement to the matrix IR and ESR approaches. Whereas these latter techniques provide fundamental frequencies of the IR active vibrations, and information on the locations and couplings of unpaired electrons in the molecule, they have been conducted in a low temperature solid state environment. Gas-phase negative ion photoelectron spectroscopy accesses higher lying vibrational and electronic states of the isolated molecule, providing valuable information on the shape of the potential energy surface without the potential perturbations of a solid matrix. This technique also measures the electron affinity (EA) and singlet-triplet splitting (ΔE_{ST}) of HCCCH, both fundamentally important values. The configuration of the anion, both nuclear and electronic, provides a single reference to which all neutral electronic states may be compared. Finally, the angular distribution of the electrons relative to the electric field of the detachment laser provides important clues to the nature of the molecular orbitals and hence the molecular structure of HCCCH.

7.3   Experimental Methods

The negative ion photoelectron spectrometer (NIPES) used in this experiment has been described in detail elsewhere.[2,34,41] The apparatus consists of four main sections: an ion source, a mass filter, an interaction region with crossed laser and ion beams, and an electrostatic electron kinetic energy analyzer.

Negative ions are formed in a flowing afterglow ion source. A microwave discharge containing trace amounts of O_2 gas in He buffer gas (~ 0.4 Torr) generates atomic oxygen radical anion, O^-. Propyne ($H_3CC{\equiv}CH$) is added downstream of O^- to generate both propargylenide (HCCCH$^-$) and propadienylidenide (H_2CCC^-) anions:

Scheme 7.3

$$O^- + H_3CCCH \diagup\diagdown \begin{array}{l} HCCCH^- + H_2O \\ H_2CCC^- + H_2O \end{array}$$
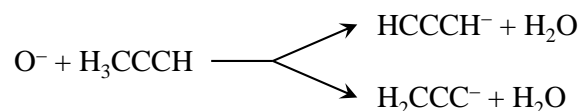
In a separate experiment we react O^- with allene ($H_2C{=}C{=}CH_2$), a reaction that generates predominantly propadienylidenide: $O^- + H_2C{=}C{=}CH_2 \rightarrow H_2CCC^- + H_2O$.[180,181] Subtraction of the latter spectra (appropriately scaled) from the former spectra yields photoelectron spectra of the propargylenide isomer. Similarly, propyne-d_4 ($D_3CC{\equiv}CD$) and allene-d_4 ($D_2C{=}C{=}CD_2$) are used to produce DCCCD$^-$ and D_2CCC^-. Collisions with He buffer gas cool the ions to approximately 300 K. The flow tube can be further cooled with a liquid nitrogen jacket to obtain a "cold spectrum" of ions with temperatures near 150 K. In the case of propargylene, vibrational quenching of the anions with liquid nitrogen dramatically improves our ability to resolve vibrational structure; thus, with one exception to demonstrate this effect, all the photoelectron spectra shown in this work were collected at 150 K.

In addition to formation of $C_3H_2^-$ isomers, we also observe formation of the allenyl anion ($H_2C{=}C{=}CH^-$) at $m/z = 39$. Beginning with very low propyne flows, increasing propyne concentration in the flowing afterglow source significantly increases production of the allenyl anion until all O^- anions are consumed. By contrast, the concentration of $C_3H_2^-$ isomers first increases modestly,

and then decreases. The optimal propyne concentration for production of $C_3H_2^-$ isomers is small and is achieved when a significant proportion of the O^- anions do not react. This observation is evidence that the reaction proceeds by hydrogen atom abstraction (not proton abstraction)

$$O^- + H_3CCCH \rightarrow OH^- + H_2CCCH \qquad \Delta H_0 = -21.0 \text{kcal mol}^{-1} \qquad (7.1)$$

where the exothermicity is sufficient that the OH^- product escapes from the $[OH^- \bullet H_2CCCH]$ Langevin complex. If propyne were in great excess of O^-, the OH^- would react primarily with propyne, forming $H_2C=C=CH^- + H_2O$, rather than reacting with the H_2CCCH radical from Eq. 7.1, which would give the desired $C_3H_2^-$ product. The need to keep the propyne concentration low restricts the quantity of $C_3H_2^-$ ions that can be produced.

Anions are extracted into a differentially pumped region and are accelerated to 735 eV before entering a Wien velocity filter for mass selection. The recently rebuilt Wien filter has a mass resolution of $m/\Delta m \sim 60$.[38,161] Great care is taken to ensure that there is no contribution from propargyl or 1-propynyl anions (H_2CCCH^- and H_3CCC^-, respectively; $m/z = 39$) in the photoelectron spectra of either propargylenide or propadienylidenide ($m/z = 38$).

The mass-selected ion beam (typically 70 pA) is decelerated to 35 eV and focused into the laser interaction region. Here, the 1-W output from a single-mode continuous-wave argon ion laser operating at 364 nm (3.40814 eV) is built up to approximately 100 W of circulating power in an optical buildup cavity located within the vacuum system. Photoelectrons ejected in the direction orthogonal to both the laser and ion beams enter a hemispherical energy analyzer. The photoelectron signal is recorded as a function of electron kinetic energy (eKE) with a position-sensitive detector. The energy analyzer has a resolution of approximately 11 meV under the conditions used in the present experiments.

The eKE is then converted to electron binding energy (eBE), which is independent of photon energy: eBE = $h\nu$ - eKE. The absolute kinetic energy scale is calibrated[2,34,43] before and after each data set using photoelectron spectra of atomic oxygen anion because the EA of oxygen atom is known accurately.[45] Additionally, the energy scale is corrected for a slight linear compression

$(<1\%)^2$ using the photoelectron spectrum of O_2^-, which provides many known transitions spanning the photoelectron energy range.[21,47] After making these corrections and accounting for the resolution of the spectrometer and rotational peak profiles, absolute eBEs can be determined with an accuracy of better than 5 meV.

A rotatable half-wave plate positioned outside the buildup cavity varies the polarization of the photodetachment radiation in order to control the angle θ between the electric field vector of the laser beam and the photoelectron collection axis. The photoelectron angular distribution (the relative differential photodetachment cross section) is described by the equation[5]

$$I(\theta) = \frac{\sigma_0}{4\pi}(1 + \beta P_2(\cos \theta)) \tag{7.2}$$

where σ_0 is the total photodetachment cross section, β is the anisotropy parameter, and $P_2(\cos \theta)$ is the second Legendre polynomial. We measure the anisotropy parameter explicitly by recording the photoelectron signal at the kinetic energy of a few intense peaks in the photoelectron spectrum as a function of θ (between $\theta = 0°$ and $\theta = 360°$ in steps of $10°$). The photoelectron angular distribution is fit with Eq. 7.2, and full spectra collected at $\theta = 0°$ and $\theta = 90°$ are scaled to match β at the energy at which it was measured. Separately, we collect a photoelectron spectrum at $\theta = 54.7°$ (the "magic angle"), where the photoelectron intensity is independent of β and directly reflects the relative photodetachment cross section.

To access higher lying electronic excited states, we employ a negative ion velocity-map imaging[211,212] (VMI) photoelectron spectrometer.[213] This experimental apparatus uses a pulsed anion beam that is mass selected *via* a Wiley-McLaren time-of-flight mass spectrometer (TOF MS).[214] Anions are excited by a tunable laser, allowing broad control of the kinetic energies of the detached electrons. The following description details the major differences of the VMI and NIPES instruments.

For anion preparation, we follow the same ion-molecule reaction[180,181,215] as above and form $HCCCH^-$ in a pulsed supersonic entrainment reactor.[216] Photoelectron spectra of the $m/z = 38$ anions arising from both reactions (O^- + propyne and O^- + allene) are taken under the same

experimental conditions in the present experiment. The entrainment reactor consists of a central and two side pulsed General Valves operating at a repetition rate of 80 Hz with separate timings and pulse widths. The middle valve provides the main expansion using 1% propyne or 1% allene seeded in Ar at a stagnation pressure of 45 psig. One of the side valves entrains neat N_2O into the main expansion. Collisions of the gas expansion with a guided 1-keV electron beam yield slow secondary electrons that form the O^- reactant through dissociative electron attachment of N_2O. Subsequently, the O^- reacts with propyne or allene to form the $m/z = 38$ anion. If the N_2O entrainment valve is turned off, the $m/z = 38$ signal disappears.

The anions are perpendicularly extracted and mass-selected using a Wiley-McLaren TOF MS. Anions of $m/z = 38$ are photodetached by spatially and temporally overlapping them with a tunable-light pulse (240 or 527 nm) from the frequency-doubled or fundamental signal output of a 355-nm pumped optical parametric oscillator. The kinetic energy distribution of the ejected electrons is then acquired by the VMI photoelectron spectrometer. The energy scale for the reported images is calibrated using the well-known photoelectron spectrum of I^-.[217] The spectra reported here cover an eKE range from 0 to 1.2 eV, with a declining energy resolution of 10 to 60 meV across this range.

7.4   Theoretical Methods

We use two electronic structure methods to calculate geometries, harmonic vibrational frequencies, and energies extrapolated to the complete basis set limit for anions and neutrals. We calculate the lowest electronic state of each symmetry using coupled cluster (CCSD(T)) theory. Geometries and frequencies are calculated at the CCSD(T)/aug-cc-pVTZ level, with energies calculated up to the aug-cc-pV5Z basis set, extrapolated to the complete basis set limit. These states and higher lying electronic states are also calculated using multi-reference configuration interaction (MRCI) theory, with geometries and frequencies at the (6e,6o)-CAS+1+2+QC/aug-cc-pVTZ level of theory, and energies up to the aug-cc-pV5Z basis set extrapolated to the complete basis set limit. We utilized the Gaussian09 package[218] with unrestricted wavefunctions to calculate the

ground electronic states of the anions and neutrals. For all other electronic states, and all MRCI calculations, we employed restricted wavefunctions using the MolPro package.[219] If one considers HCCCH as a linear molecule, with its symmetry axis along the z-axis, the 6-electron/6-orbital active space is composed of three p_x and three p_y atomic orbitals that together form three π_x and three π_y molecular orbitals, with zero, one, and two nodes perpendicular to the z-axis, respectively.

We calculate the Franck-Condon factors for detachment of HCCCH$^-$ with *ab initio* geometries and force constants for the anion and the neutral ground state using the PESCAL program.[21] To compare with the experimental photoelectron spectrum, we simulate the spectrum of HCCCH$^-$ within the normal mode approximation in Cartesian coordinates, including Duschinsky rotation.[4] Optimized geometries, vibrational frequencies, and normal mode vectors used in the simulations were calculated at the B3LYP level of theory[49,50] with the 6-311++G(d,p) basis set.[52] Simulations use the experimental values for the EA and $\tilde{a}(^1A)$ origin transition. Vibrational stick spectra are convolved with a Gaussian of 11 meV FWHM to account for the instrumental resolution.

7.5   Results

7.5.1   Isomer-specific Chemistry

When O$^-$ reacts with a hydrocarbon, it usually removes a hydrogen atom and a proton, forming neutral H$_2$O and a hydrocarbon anion. In the case of the O$^-$ + C$_3$H$_4$ reaction, we observe that the isomer distribution of the C$_3$H$_2^-$ anion depends on the isomeric form of the C$_3$H$_4$ reactant. Upon reaction with allene (H$_2$C=C=CH$_2$), we observe, using the NIPES apparatus, the relatively simple photoelectron spectra in Fig. 7.1(a), which arise almost exclusively from electron detachment of the propadienylidene anion, H$_2$CCC:$^-$, in agreement with previous results.[177,181] By contrast, when O$^-$ reacts with propyne (HC≡CCH$_3$), the resulting spectra in Fig. 7.1(b) show many new features in addition to all the peaks observed in Fig. 7.1(a). This observation is strong evidence that the reaction of O$^-$ with propyne forms at least one additional isomer of C$_3$H$_2^-$ in significant yield in addition to H$_2$CCC:$^-$. We will show below that all the new features in Fig. 7.1(b) can be

conclusively assigned to production of the propargylene anion, $HCCCH^-$.

A close inspection of the peak widths as a function of anion temperature in the magic angle spectra in Fig. 7.1(b) provides further evidence for the presence of two different isomers of $C_3H_2^-$. With decreasing anion temperature, the peak at eBE = 1.796 eV, assigned to the ground electronic state of H_2CCC, shows only modest narrowing, in contrast to the dramatic narrowing of the peak at 1.656 eV. This behavior is evidence that the latter feature cannot arise from H_2CCC but is instead consistent with the quasilinear, "floppy" nature of the HCCCH isomer. Corresponding photoelectron spectra from the reactions of O^- with allene-d_4 and propyne-d_4 are shown in Fig. 7.2.

These results pose the intriguing question of why, when O^- reacts with allene, the hydrogen atom and proton are almost always taken from the same end of the molecule, yielding $H_2CCC:^-$, whereas reaction with propyne demonstrates the ability of O^- to react at both ends of this C_3H_4 isomer. The distance between hydrogen atoms on opposite ends of allene is essentially identical to that in propyne, hinting that the difference in electronic structure (two double bonds vs. one single and one triple bond) may control the reactivity. The answer to this question is outside the scope of this work.

Figure 7.3 shows spectra from the VMI photoelectron spectrometer, which provides higher photon energies compared to the NIPES spectrometer, allowing access to higher-lying electronic states of HCCCH. The right portion of Fig. 7.3, acquired at a photon energy of 2.335 eV, provides a direct comparison with the NIPES spectra in Fig. 7.1. Although the anion source in the VMI instrument is quite different from that in the NIPES instrument, comparing features from 1.4 to 2.1 eV binding energy between the two instruments shows the same isomer-specific chemistry in both sources. Therefore we assume, at all binding energies, that the black spectra in Fig. 7.3 arise primarily from detachment of H_2CCC^-, whereas features in the red spectra that were not present in the black spectra arise from $HCCCH^-$. Using a higher photon energy of 5.165 eV, we observe the photoelectron spectra in the left portion of Fig. 7.3, which could not be acquired on the NIPES instrument. We attribute the peaks in the red spectrum (propyne reactant) that are not present in the black spectrum (allene reactant) to higher electronic states of HCCCH.

Figure 7.1: Photoelectron spectra of the product anions from (a) O^- + allene and (b) O^- + propyne. θ is the angle between the electric field polarization vector and the axis of electron detection. Structural assignments shown here are justified in the text.

Figure 7.2: Photoelectron spectra of the product anions from (a) O^- + allene-d_4 and (b) O^- + propyne-d_4. θ is the angle between the electric field polarization vector and the axis of electron detection. Structural assignments shown here are justified in the main text.
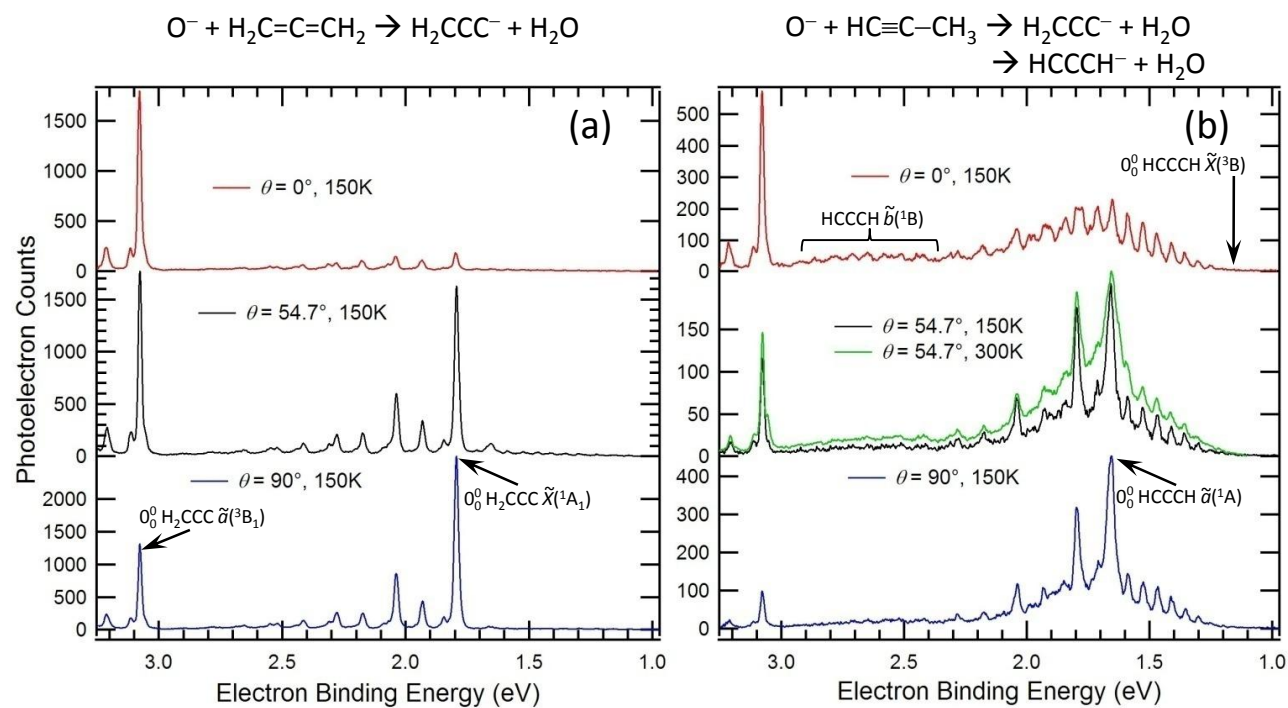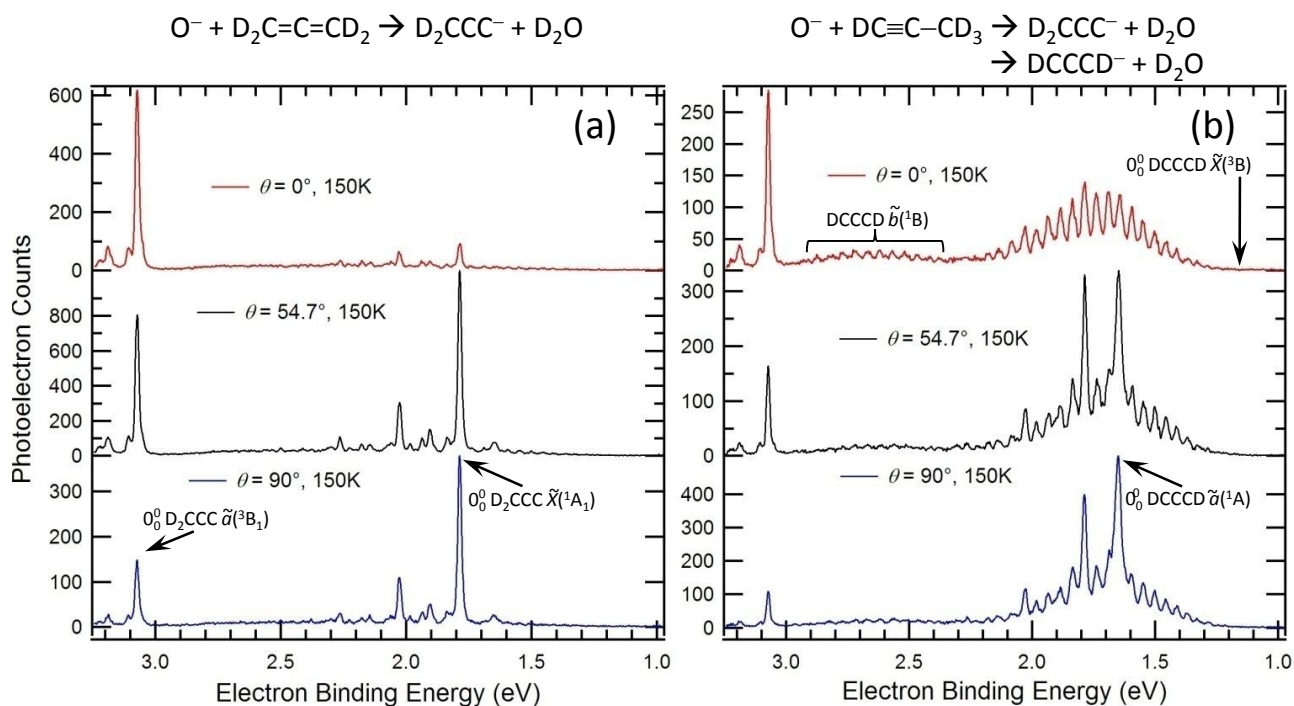
Figure 7.3: Photoelectron spectra of the product anions from O^- + allene (black), and O^- + propyne (red) acquired with the velocity-mapped imaging photoelectron spectrometer. Spectra on the right side were acquired with $h\nu = 2.335$ eV, and on the left side with $h\nu = 5.165$ eV. The low binding energy spectra(right) provide strong evidence that the isomer distributions of product anions using this ion source are similar to the distributions obtained from O^- + allene and O^- + propyne in the flowing afterglow source.
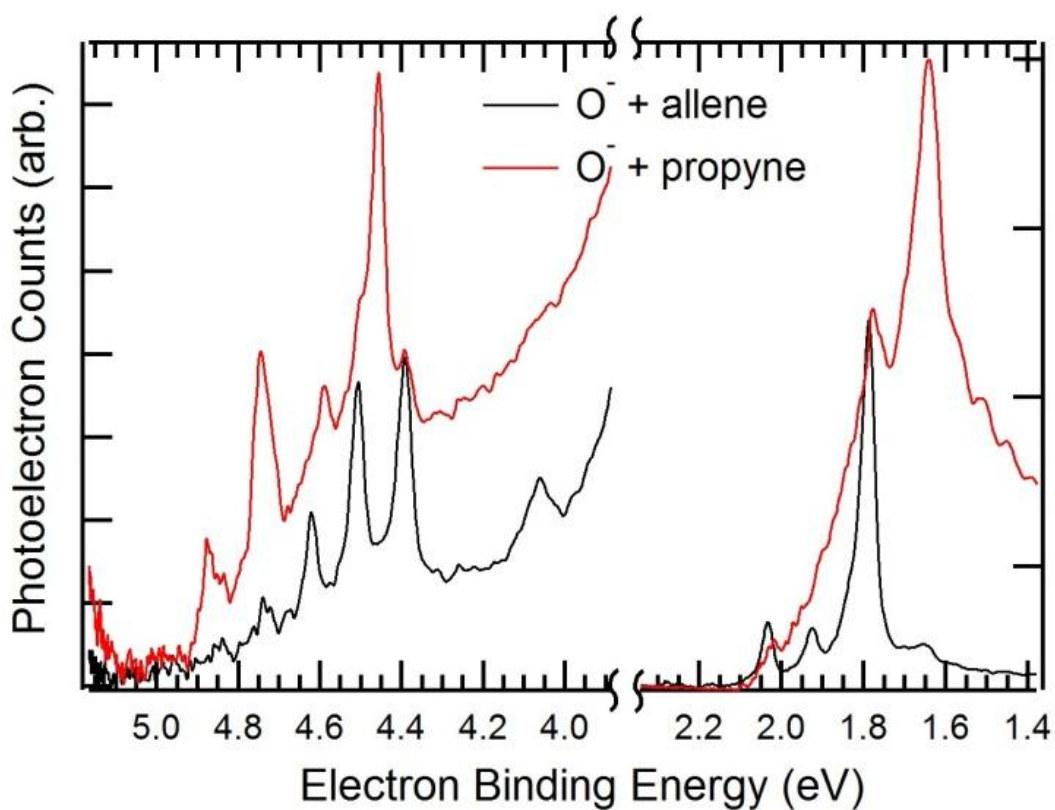
7.5.2   Photoelectron Angular Distributions

Figures 7.1 and 7.2 show the change in peak intensities with respect to the angle between the electric field of the detachment laser and the axis of electron collection. The angular distribution of photoelectrons enables two aspects of our analysis. First, the groups of vibrational peaks arising from each electronic state of the neutral generally have distinct angular distributions, allowing a purely experimental method for delineating different electronic states of the neutral even if their spectra overlap in electron binding energy. Second, because the reaction of O^- with allene happens to produce mostly the $H_2CCC:^-$ isomer of $C_3H_2^-$, whereas the reaction with propyne shows contributions from both $H_2CCC:^-$ and $HCCCH^-$, we can subtract the allene spectra from the propyne spectra to isolate the contributions of $HCCCH^-$.

However, because some electronic states of H_2CCC and $HCCCH$ produce overlapping photoelectron spectra, we must first scale the allene-derived spectra to the propyne-derived spectra using a spectral peak of H_2CCC that does not overlap any peaks arising from $HCCCH$. This practice will ensure that we complete subtraction of H_2CCC contributions even at electron binding energies where the isomers' spectra do overlap. Fortunately, the relative spectral intensities in Figs. 7.1(a) and 7.1(b) are identical from eBE = 3.0 – 3.25 eV, implying that only H_2CCC contributes to this section of the spectra. The strong peak at eBE = 3.076 eV was assigned to the origin transition of H_2CCC $\tilde{a}(^3B_1)$ by Robinson et al.,[181] and we use its angle-dependent intensity to scale the spectra in Fig. 7.1(a) to corresponding spectra in Fig. 7.1(b) in order to quantitatively subtract contributions of H_2CCC from the propyne-derived spectra. We note that the capability of the NIPES spectrometer to provide photoelectron spectra over wide eBE ranges (> 2 eV) with constant collection efficiency and excitation energy is critical to this isomer separation approach.

Figure 7.4(b) shows the differential detachment cross sections obtained from product anions of the O^- + propyne reaction in 150 meV-wide windows centered at eBE = 3.076 eV (the origin of the H_2CCC $\tilde{a}(^3B_1)$ state) and at eBE = 1.671 eV, where the signal arises primarily from the $\tilde{a}(^1A)$ state of HCCCH. We extract anisotropy parameters $\beta[H_2CCC\ \tilde{a}(^3B_1)] = +0.60 \pm 0.04$ and

β[HCCCH $\tilde{a}(^1A)$] = -0.69 $\pm$ 0.02 by fitting Eq. 7.2 to the data in Fig. 7.4(b). Such measurements, at many different electron ejection angles, are the most robust method for obtaining β but are too time consuming for measurements of the energy dependent anisotropy parameter β(E).

Figure 7.5(a) shows photoelectron spectra from the O^- + propyne reaction normalized to the differential cross section for electron detachment from H_2CCC^- at 3.076 eV using the value of β from the previous paragraph. These three spectra allow a three-point fit to Eq. 7.2 at each electron binding energy, providing β(E), which is plotted above the spectra.

7.5.3   Pure Spectra of HCCCH and DCCCD

Subtracting the contributions of H_2CCC from the O^- + propyne (and O^- + propyne-d_4) data provides the photoelectron spectra that arise from HCCCH$^-$ and DCCCD$^-$ in Figs. 7.6(a) and 7.6(b). (Note that Ikuta calculates a negative EA for cyclopropenylidene,[220] precluding its presence in negative ion photoelectron spectroscopy. Nothing in our results contradicts this conclusion.) The energy-dependent anisotropy parameter, β(E), is also shown in Fig. 7.6 and is only available for the HCCCH isotopologue. The same photoelectron spectra for HCCCH can be seen in Fig. 7.5(b), normalized to the differential cross section. This presentation of the data emphasizes that at all but the highest electron binding energies, the detachment cross section of HCCCH$^-$ is largest at $\theta =$ 90°, i.e., at negative values of β(E). Such negative values correspond to detachment from a p orbital in an atomic anion, resulting in s and d partial waves of the outgoing electron. In a molecule the correspondence is more complicated, but negative anisotropy parameters generally correspond to detachment from a π orbital, whereas positive values are consistent with detachment from orbitals with σ character. In addition, the abrupt changes in β as a function of binding energy (e.g., at 1.803 eV vs. 1.773 eV) are evidence that multiple electronic states of the neutral contribute to the spectra for eBE above 1.65 eV.

Returning to Fig. 7.6(a), we can make some initial observations about electronic states of HCCCH that are populated when different electrons are removed from the anion. The angular distributions are critical to this endeavor. The red spectrum at $\theta = 0°$ shows a long progression

Figure 7.4: Photoelectron spectrum (a) and differential cross sections (b) from product anions of the O^- + propyne reaction. The red data at electron binding energy of 3.076 eV arise from the origin of the H_2CCC $\tilde{a}(^3B_1)$ state. The blue data at electron binding energy of 1.671 eV arise primarily from the origin of the HCCCH $\tilde{a}(^1A)$ state.

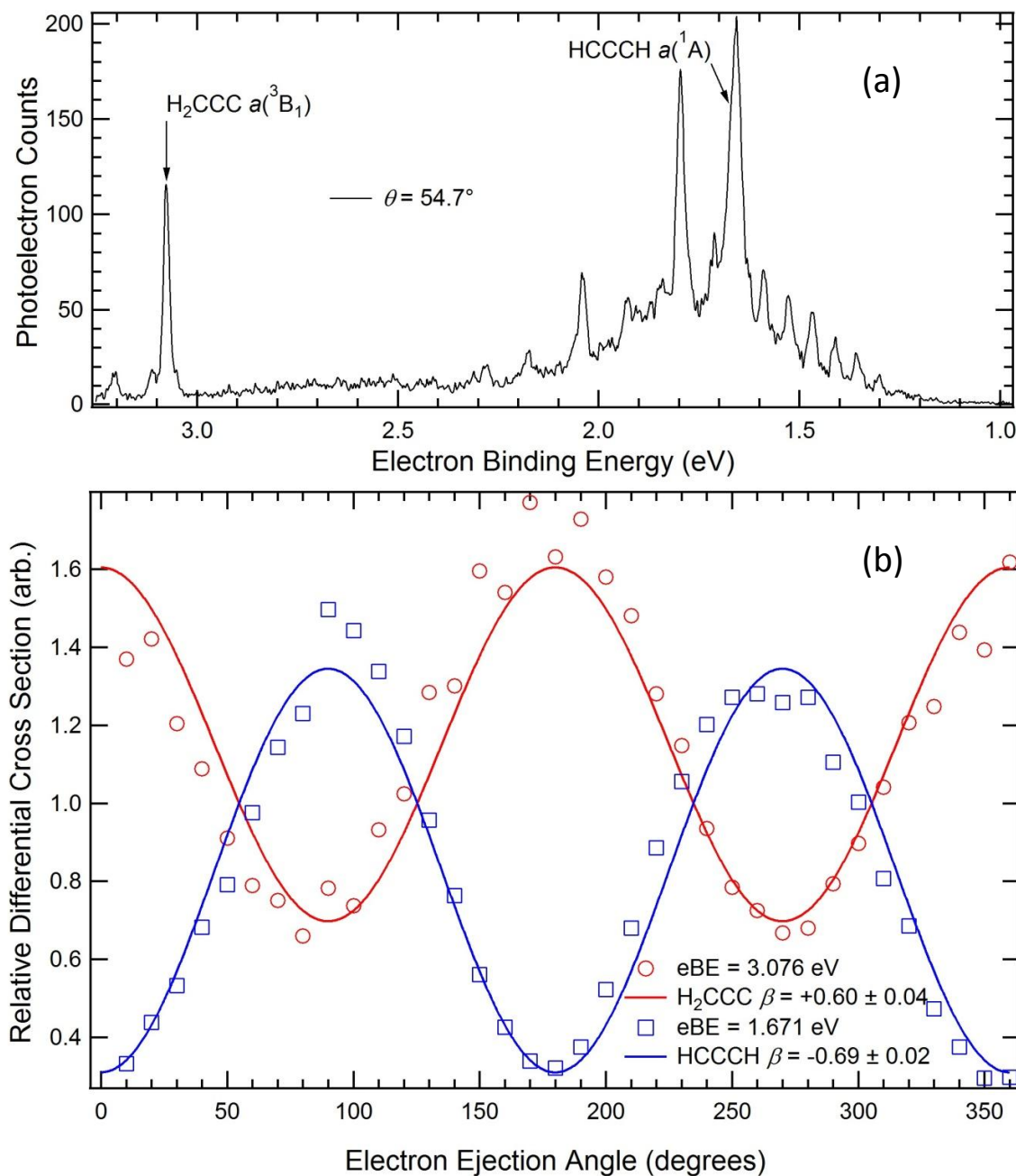Figure 7.5: Photoelectron spectra normalized to the differential cross section of H_2CCC^- at eBE = 3.076 eV for (a) $HCCCH^-$ and H_2CCC^- produced from the O^- + propyne reaction, and (b) $HCCCH^-$ with the contributions from H_2CCC^- subtracted. θ is the angle between the electric field polarization vector and the axis of electron detection. Ion temperature is $\sim$ 150 K. The energy-resolved anisotropy parameter $\beta(E)$ is shown above each set of spectra.

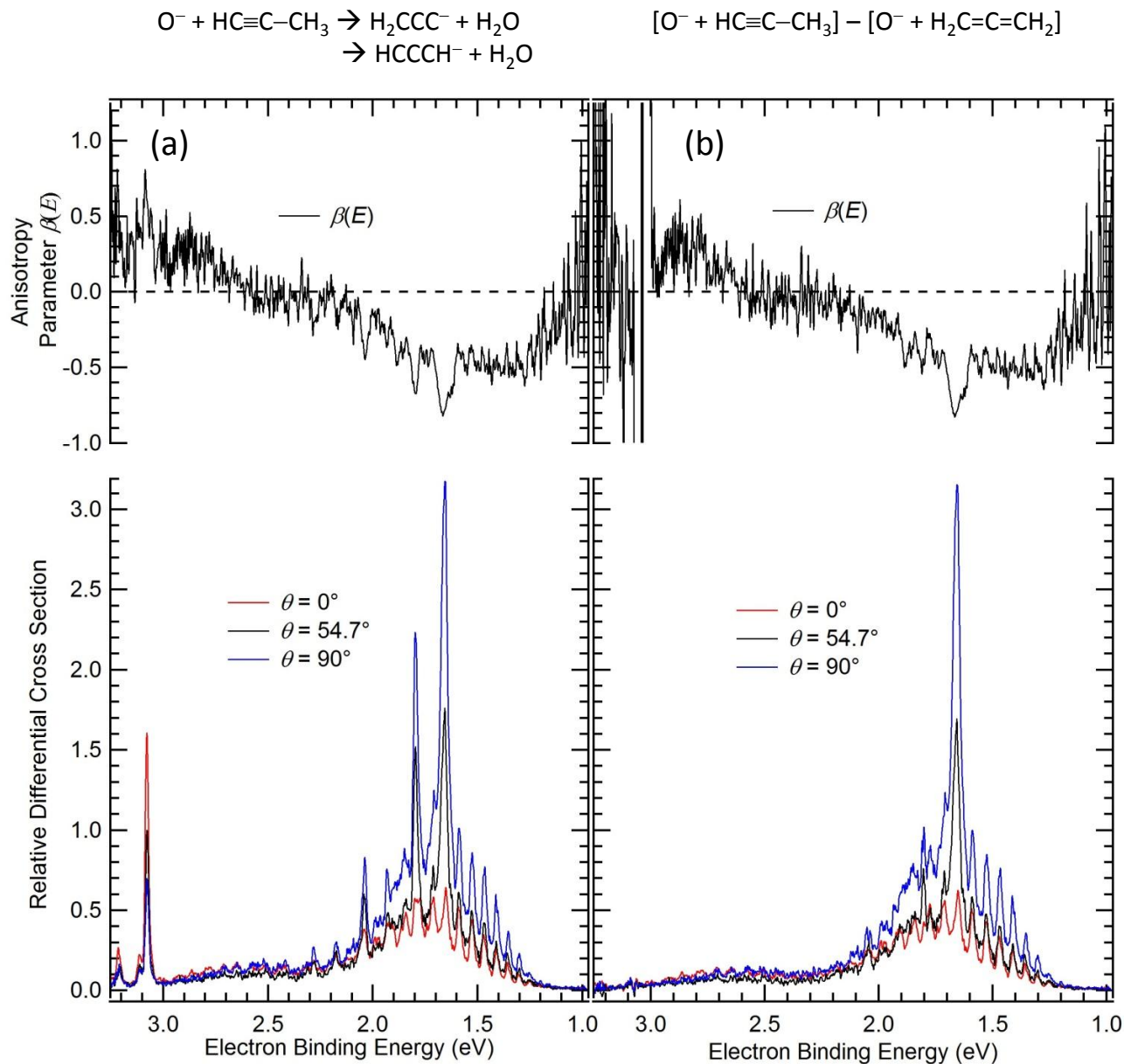$O^- + HC{\equiv}C{-}CH_3 \rightarrow H_2CCC^- + H_2O$
$\rightarrow HCCCH^- + H_2O$

$[O^- + HC{\equiv}C{-}CH_3] - [O^- + H_2C{=}C{=}CH_2]$

Figure 7.6: Photoelectron spectra of (a) HCCCH$^-$, and (b) DCCCD$^-$ with contributions from H$_2$CCC$^-$ and D$_2$CCC$^-$ subtracted. θ is the angle between the electric field polarization vector and the axis of electron detection. Ion temperature is ~ 150 K. The artifacts at 3.076 eV arise from imperfect subtraction of the propadienylidene contributions. The energy-resolved anisotropy parameter β(E) is shown for HCCCH$^-$.
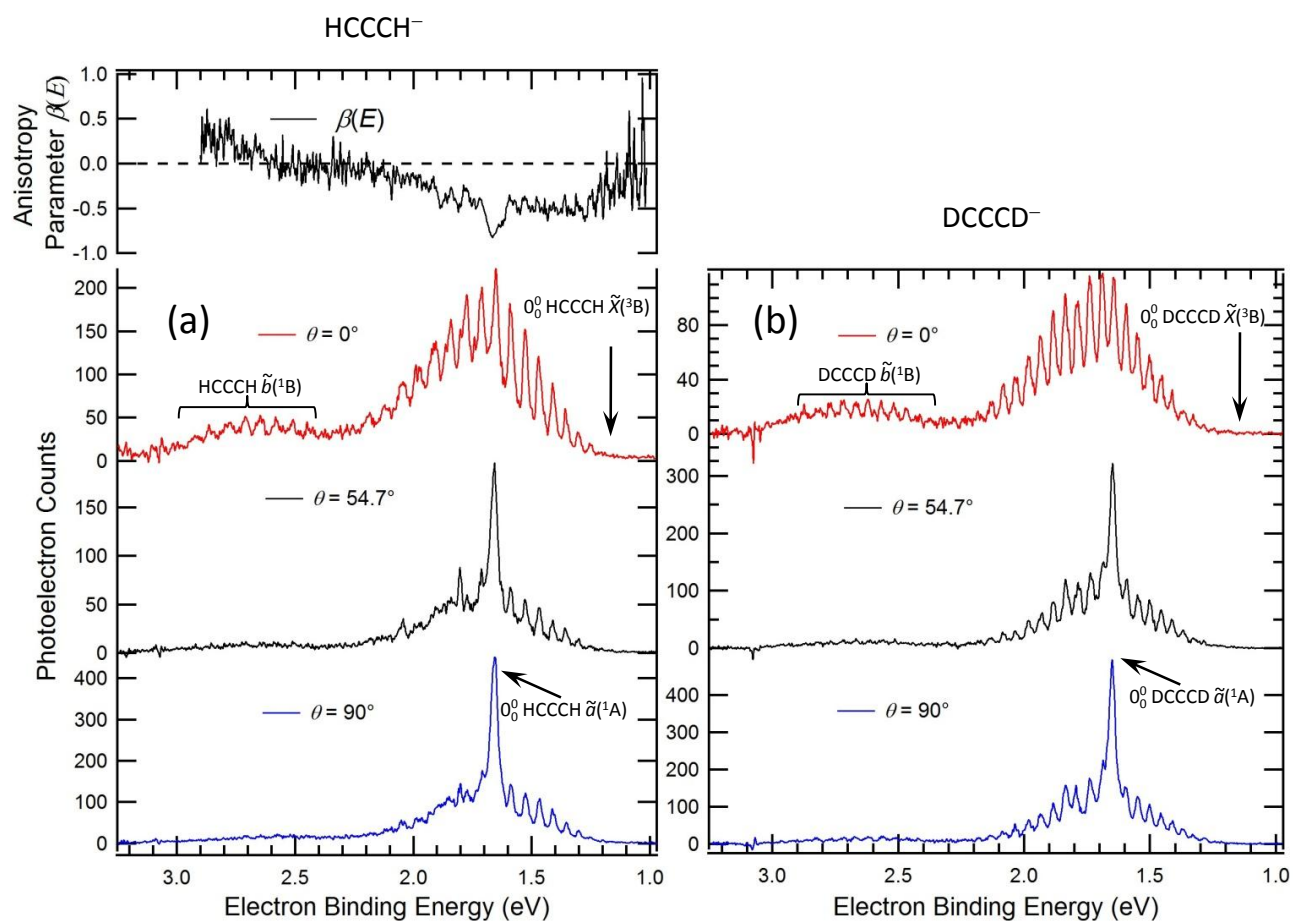
with a smooth envelope apparently beginning at 1.249 eV, reaching a maximum near 1.7 eV, and tapering back to baseline at $\sim$ 2.3 eV. Strikingly, this progression is dwarfed in the black magic angle spectrum by a strong peak at 1.656 eV. The anisotropy parameter has an average value of -0.45 from 1.25 – 1.59 eV but becomes more energy dependent for eBE $\geq$ 1.65 eV. Based on these observations it seems reasonable to assign the ground electronic state of HCCCH $\tilde{X}(^3B)$ to the long progression prominent in the red spectrum, and the sharp peak at 1.656 eV to the origin of the first excited state $\tilde{a}(^1A)$. Evidently, the geometry of the ground state neutral is quite different from that of the anion, whereas the geometry of the excited $\tilde{a}(^1A)$ state is similar to the anion. The term symbols will be justified in Section 7.6.1, and the experimental determination of the $\tilde{X}(^3B)$ origin in Section 7.5.4. Finally, we assign a third electronic state, the $\tilde{b}(^1B)$ state, to the series of peaks from $\sim$ 2.4 – 2.95 eV, which are most prominent in the $\theta = 0°$ spectra, and for which a large geometry change from the anion seems clear due to the long vibrational progression. Note that this state shows an energy-dependent anisotropy parameter that rises from -0.1 to +0.2 with increasing eBE. Based on the intensities of the features in this progression there is little hope of locating the origin transition of the $\tilde{b}(^1B)$ state, but we assign the vertical detachment energy (VDE) of this state, determined at the peak of the progression envelope, as 2.648 $\pm$ 0.020 eV.

Comparing the spectra of HCCCH$^-$ to DCCCD$^-$ supports these assignments of electronic states. Although the peak spacing in vibrational progressions attributed to each electronic state becomes smaller upon deuteration, the sharp peak assigned to the $\tilde{a}(^1A)$ origin does not shift, as expected if it represents the origin of a higher-lying electronic state. The HCCCH $\tilde{X}(^3B)$ state appears to support at least two vibrational progressions, as shown by the peak splittings for eBE > 1.7 eV, whereas in DCCCD the second progression is less obvious.

It is more difficult to draw conclusions purely from experiment about the spectra in Fig. 7.3 that probe higher-lying electronic states of HCCCH. Focusing on the peaks in the propyne-derived (red) spectra that are not present in the allene-derived (black) spectra, there appear to be four peaks that arise from HCCCH at eBE = 4.456, 4.589, 4.743, and 4.877 eV.

7.5.4   Experimental Assignment of the HCCCH $\tilde{X}(^3B)$ Origin

It is challenging to experimentally assign the origin of an electronic transition with a large geometry change from anion to neutral. We adopt the approach taken by Robinson *et al.*[181] in determining the EA of the propargyl radical ($HCCCH_2$), where NIPES spectra from the allenyl ($HCCCH_2^-$) and the allenyl-d_3 ($DCCCD_2^-$) anions were compared. The binding energy of the origin transition should be essentially independent of deuterium substitution because, upon deuteration, the electronic part of the transition energy is unchanged, while the lowering of zero point energy (ZPE) in the neutral is almost exactly matched by the lowering of ZPE in the anion, leaving the overall transition energy essentially unchanged. The same cancellation will not occur when transitions from the zero point level of the anion terminate in excited vibrational levels of the neutral, in which case the peak positions of a deuterated isotopologue, for identical vibrational quantum numbers, will occur at lower transition energies compared to the undeuterated molecule. One therefore needs to compare spectra of $HCCCH^-$ to $DCCCD^-$ in the expected region of the origin transition. Peaks of the two isotopologues that have nearly identical energies are candidates for the origin transition.

With this approach in mind, Fig. 7.7 shows photoelectron spectra of $HCCCH^-$ and $DCCCD^-$ in the region of the expected $\tilde{X}(^3B)$ origin transition, with a shorter scan range allowing greater signal averaging. Cooling of the anions to ~ 150 K should diminish the intensity of hot band transitions from vibrationally excited anions. Peak positions for the two isotopomers, taken from Figs. 7.6 and 7.7, are shown in Table 7.1. Near matches of peak positions between the two isotopologues occur at 1.409 and 1.249 eV. The choice of 1.409 eV as the origin would require assignment of all peaks at lower binding energies as hot bands: an unlikely scenario for anions at 150 K. The peaks near 1.249 eV are much better candidates for the origin transition, yet in the HCCCH spectrum there are two peaks at even lower binding energies. Figure 7.8 shows a graph of peak spacings for the data in Fig. 7.7. The peak spacings increase smoothly from 360 to 500 cm^{-1} for HCCCH (310 – 400 cm^{-1} for DCCCD) with increasing quantum number, indicating a negative

anharmonicity in this progression. We observe no abrupt change in spacing for the peaks below 1.249 eV (peak $n = 2$ of HCCCH). An abrupt change in peak spacing might be expected if peaks $n = 0, 1$ were hot bands, with spacings determined by the energy levels of the anion, instead of the neutral. Furthermore, while one hot band might have noticeable intensity at $T \sim 150$ K, it is hard to justify a second hot band with sufficient intensity to be observed.

Therefore we assign the origin transition in HCCCH to the peak with the lowest observed binding energy and assign the experimental EA(HCCCH) $= 1.156 \pm \binom{0.010}{0.050}$ eV. The asymmetric error bar acknowledges the possibility that our assignment may be in error by one quantum of the active vibrational mode. The peak with the lowest binding energy for DCCCD occurs at 1.208 eV. It is unlikely that this peak represents the origin transition for the reasons explained above of the changes in detachment energies expected upon deuteration. Assuming a very small isotope shift in the origin transition, we assign the first peak observed in DCCCD to two quanta of the main vibrational progression. The ramifications of this assignment will be discussed in Section 7.6.4. Based on this assignment, the singlet-triplet splitting between the $\tilde{a}(^1A)$ and the $\tilde{X}(^3B)$ state is determined to be $\Delta E_{TS} = 1.656 \ 1.156 = 0.50 \pm \binom{0.050}{0.011}$ eV.

7.5.5 Theoretical Results

Given our experimental determination that the lowest three electronic states of HCCCH span a range of only ~ 1 eV, and the multiple valence bond structures shown in Scheme 7.1, it is not surprising that the electronic structure of HCCCH has significant multi-reference character. Adiabatic and vertical detachment energies (ADE, VDE) resulting from our CCSD(T) and MRCI calculations, extrapolated to the complete basis set limits, are shown in Table 7.2, along with comparisons to our experimentally derived transition energies. To evaluate the accuracy of these calculations, we have calculated other 21-electron anions and 20-electron neutral systems at the same levels of theory, specifically for H_2CCC, HCCN,[160] and NCN[221] (the latter two being isoelectronic with HCCCH), and compared the calculated values with experimental detachment energies when possible. Geometries and frequencies for the propargylene anion and lowest three electronic states of

Figure 7.7: Photoelectron spectra of HCCCH$^-$ and DCCCD$^-$ with $\theta = 90°$ laser polarization and anion temperature of ~ 150 K. Near matches of peak positions between the two isotopologues occur at eBE ~ 1.409 and 1.249 eV.
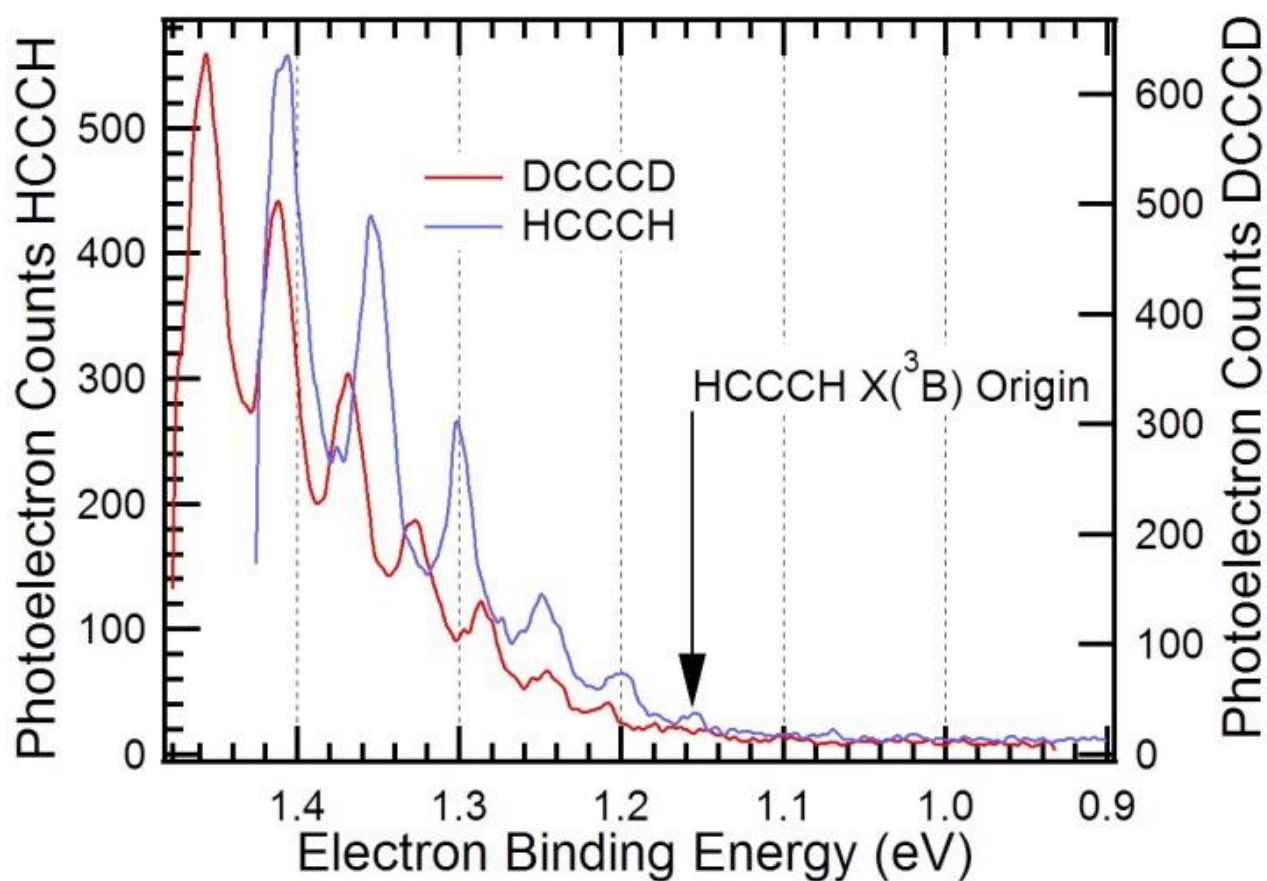
Table 7.1: Peak assignments, electron binding energies, and anisotropy parameters $[\beta]$ in the photoelectron spectra of HCCCH$^-$ and DCCCD$^-$.

Electronic State	Mode assignment	HCCCH$^-$ (eV) $[\beta]$	DCCCD$^-$ (eV)
$\tilde{X}$ (^{3}B)	$\nu_5 = 0$	1.156	
	$\nu_5 = 1$	1.201	
	$\nu_5 = 2$	1.249 [-0.36]	1.208
	$\nu_5 = 3$	1.300 [-0.51]	1.246
	$\nu_5 = 4$	1.353 [-0.53]	1.286
	$\nu_5 = 5$	1.410 [-0.46]	1.327
	$\nu_5 = 6$	1.467 [-0.49]	1.368
	$\nu_5 = 7$	1.526 [-0.39]	1.412
	$\nu_5 = 8$	1.588 [-0.42]	1.456
	$\nu_5 = 9$		1.502
	$\nu_5 = 10$		1.549
	$\nu_5 = 11$		1.599
$\tilde{a}$ (^{1}A$_1$)	$\nu_6 = 0$	1.656 [-0.79]	
	$\nu_6 = 1$	1.803 [-0.46]	

Figure 7.8: Vibrational peak spacings in the HCCCH and DCCCD $\tilde{X}(^3B)$ state. The positive slope indicates a negative anharmonicity in this vibrational mode. For HCCCH, peak $n = 0$ denotes the origin transition at 1.156 eV eBE. The frequency of the $\nu_5 = 1 \leftarrow \nu_5 = 0$ vibrational transition of HCCCH is 361 cm^{-1}.
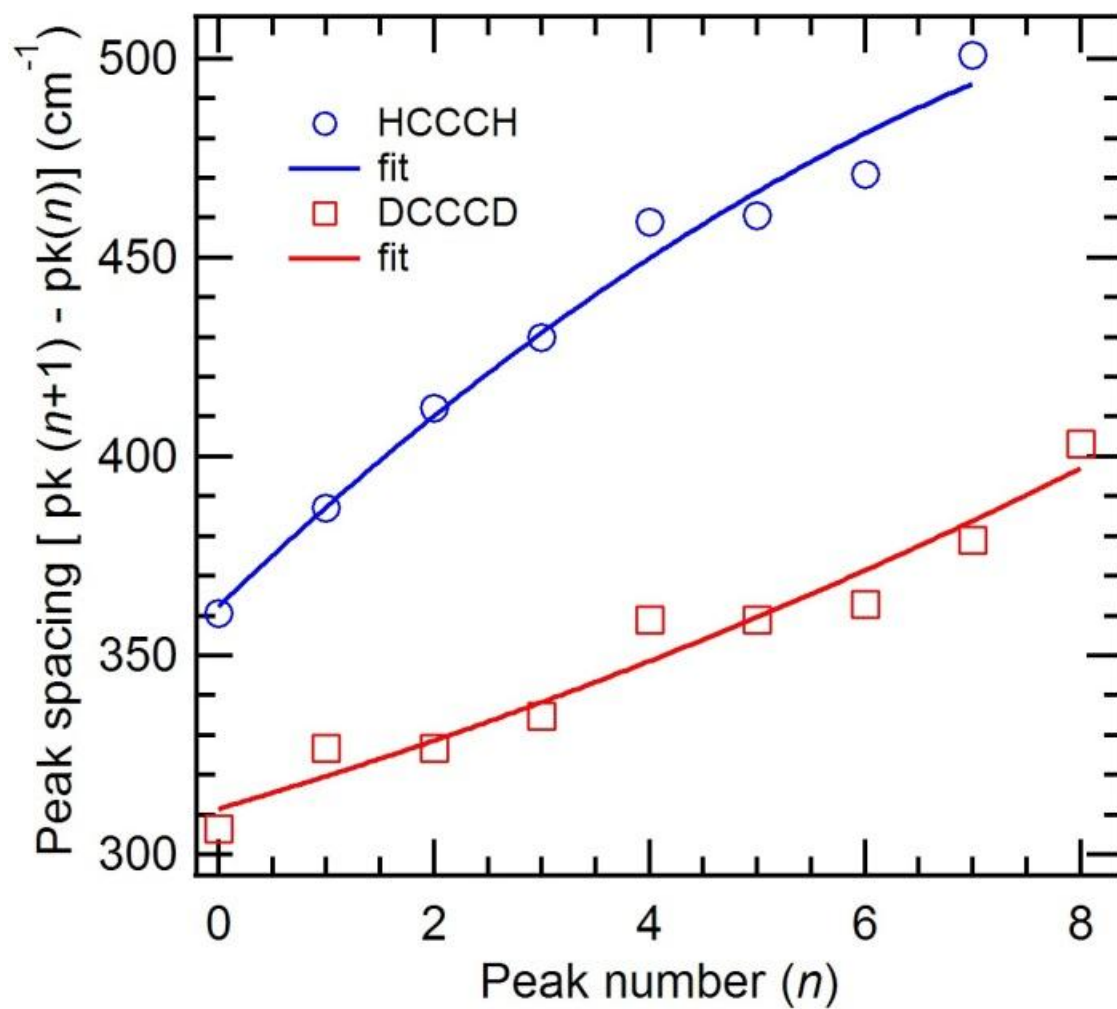
the neutral are given in Table 7.3, with representations of the geometries in Figs. 7.9. The ratio of vibrational frequencies for HCCCH : DCCCD are also given in Table 7.3.

The adiabatic detachment energies of H_2CCC, HCCN, and NCN, calculated at the CCSD(T)/CBS level, deviate at most by 19 meV from experiment, even when excited electronic states of the neutral are included. Although the T1 diagnostic values for these calculations (a measure of the multireference character of the electronic wavefunction) provide reason for caution, the very favorable comparison to experiments provides confidence in the CCSD(T) calculations. Whereas CCSD(T) as implemented here is only valid for the lowest electronic state of a given symmetry, MRCI calculations can provide adiabatic and vertical detachment energies for all electronic states. Our results show that the MRCI calculations are on average ~ 0.14 eV lower than the CCSD(T) calculations. Adding this offset to the MRCI value for the HCCCH $\tilde{X}(^3B)$ state (1.01 eV) brings it into excellent agreement (1.15 eV) with the CCSD(T) value of 1.146 eV. The VDEs compare favorably with the peaks of the Franck-Condon envelopes from the experimental NIPES spectra when the same offset is applied to these MRCI values. We therefore conclude that the MRCI state energies, when increased by 0.14 eV, should provide accurate estimates of the electronic state energies of HCCCH.

Figure 7.10 plots the unrestricted Hartree Fock frontier orbitals of $\tilde{X}(^2B)$ HCCCH$^-$, together with an energy level diagram that qualitatively explains the origin and ordering of the neutral states of HCCCH; corresponding plots for $\tilde{A}(^2A)$ HCCCH$^-$ are given in Fig. 7.11. Finally, Fig. 7.12 shows unrelaxed scans of the potential energy surface along all three bending coordinates ($\angle$CCC, $\angle$CCH, and $\angle$HCCC) in C_2 symmetry of the HCCCH$^-$ $\tilde{A}(^2A)$ and the HCCCH $\tilde{X}(^3B)$ states. The potentials are upper limits to the potentials that would be obtained if fully optimized in the eight orthogonal coordinates. Nevertheless, they provide a qualitative picture of the dramatically different potential surfaces along these bending coordinates.

In the $\angle$CCC coordinate, the barriers to linearity are only 1081 and 142 cm^{-1} in the anion and neutral states, respectively, with a modest increase in $\angle$CCC by 8° upon detachment. Differences between anion and neutral are more pronounced in the $\angle$CCH coordinate, where the barriers to linearity are 7125 and 239 cm^{-1}, with $\angle$CCH increasing 36° upon detachment. The much deeper

Table 7.2: Geometric parameters and detachment energies of 21-electron anions and their corresponding neutrals.

Species	State	∠CCC (°)	∠HCC (°)	Detachment Energy (eV)			Term Energy (eV)
				CCSD(T)/CBS $Adiabatic^a$ (Vertical)	MRCI/CBS Adiabatic (Vertical)	Experiment Adiabatic	Experiment
$HCCCH^-$	$\tilde{X}\,(^2B)$	179	126	0.00 (0.00)	0.00 (0.00)		
	$\tilde{A}\,(^2A)$	163	123	0.026	0.026		
HCCCH	$\tilde{X}\,(^3B)$	173	161	1.146	1.00^a (1.54)	$1.156\pm^{0.010}_{0.050}$	0.0
	$\tilde{a}\,(^1A)\,(^1A_1)$	159	125	(1.66)	1.49^a (1.45)	1.656 ± 0.005	$0.50\pm^{0.050}_{0.011}$
	$\tilde{b}\,(^1B)\,(^1\Delta)$	180	180		1.80^a (2.54)	$2.648^d\pm0.02$	0.94 ± 0.08
	$\tilde{c}\,(^1A)\,(^1\Sigma^+)$	180	180		2.45^a (4.15)		
	$\tilde{A}\,(^3B)\,(^3B_2)$	108	131		4.24^a (4.63)		
	$\tilde{d}\,(^1A)\,(^1A_2)^e$	160	135		4.27^c (4.38)		
	$\tilde{B}\,(^3A)\,(^3A_2)$	161	132	(4.79)	4.46^c (4.51)	4.456 ± 0.02	$3.30\pm^{0.054}_{0.022}$
H_2CCC	$\tilde{X}\,(^1A_1)$			1.80 (1.83)	$1.62^{a,b}\,(1.65)^b$	1.793 ± 0.005	
	$\tilde{a}\,(^3B_1)$			3.08 (3.16)	$2.95^{a,b}\,(3.02)^b$	3.076 ± 0.005	
HCCN	$\tilde{X}\,(^3A'')$			2.02 (2.46)	$1.89^{a,b}\,(2.34)^b$	$2.001^f\pm0.015$	
	$\tilde{a}\,(^1A')$			2.521 (2.533)	$2.53^b\,(2.55)^b$	$2.511^f\pm0.004$	
NCN	$\tilde{X}\,(^3\Sigma_g^-)$			2.47 (2.51)	$2.36^{a,b}\,(2.40)^b$	$2.484^g\pm0.006$	
	$\tilde{a}\,(^1\Delta_g)$				$(3.34)^b$	$3.491^g\pm0.013$	
	$\tilde{b}\,(^1\Sigma_g^-)$				$(3.90)^b$	$4.110^g\pm0.013$	

[a] Includes zero point energy
[b] Energy extrapolated to the complete basis set limit
[c] Does not include zero point energy
[d] Vertical detachment energy
[e] The dominant configuration of this state is only accessible by a two-electron transition
[f] Negative ion photoelectron spectroscopy[160]
[g] Negative ion photoelectron spectroscopy[221]

Table 7.3: Calculated geometries and vibrational frequencies of HCCCH⁻, HCCCH, and their deuterated isotopologues.

Vibrational Frequencies (cm⁻¹)	UCCSD(T)/ aug-pVTZ	UCCSD(T)/ aug-pVTZ	UCCSD(T)/ aug-pVTZ	MRCI/ aug-pVTZ	MRCI/ aug-pVTZ
Mode	HCCCH⁻ $\tilde{X}$ (^{2}B)	HCCCH⁻ $\tilde{A}$ (^{2}A) (DCCCD⁻) [D/H]	HCCCH $\tilde{X}$ (^{3}B) (DCCCD⁻) [D/H]	HCCCH $\tilde{a}$ (^{1}A)	HCCCH $\tilde{b}$ (^{1}B)
1A (out-of-plane CCH bend)	173	154 (121) [.78][1]	237 (186) [.78]	290	113
2B (in-plane asym. CCH bend)	298	349 (271) [.78]	114 (89) [.78]	310	113
3A[2] (out-of-plane CCC bend)	437	452 (433) [.96]	402 (370) [.92]	453	234
4B[3] (in-plane CCC bend)	554	468 (383) [.82]	407 (389) [.96]	799	234
5A (in-plane sym. CCH bend)	741	818 (709) [.87]	351 (265) [.75]	933	413[4]
6A (symmetric CCC stretch)	1149	1157 (1129) [.98]	1257 (1191)[.95]	1202	1276
7B (asymmetric CCC stretch)	1650	1612 (1561) [.97]	1623 (1570)[.97]	1814	1842
8B (asymmetric CH stretch)	3160	3162 (2343) [.74]	3399 (2532)[.74]	3249	3459
9A (symmetric CH stretch)	3160	3166 (2338) [.74]	3408 (2550)[.75]	3253	3468
Geometry					
CC (Å)	1.313	1.316	1.279	1.300	1.273
CH (Å)	1.085	1.086	1.066	1.081	1.062
∠CCC (°)	179.0	165.2	173.3	161.7	180.0
∠HCC (°)	126.1	124.4	160.7	127.6	180.0
∠HCCC dihedral (°)	97.1	174.1	145.6	180.0	180.0

[1] Numbers in brackets are the ratios of DCCCD : HCCCH frequencies.
[2] In all states other than the ground state of the anion, the symmetry for mode 3 is B.
[3] In all states other than the ground state of the anion, the symmetry for mode 4 is A.
[4] Mode 5 is doubly degenerate in the $\tilde{b}$(^{1}B) state, which has a linear geometry and 10 vibrational modes.

Figure 7.9: Side-on and end-on views of equilibrium geometries calculated at the MRCI(6e,6o)/aug-cc-pVTZ level for the $\tilde{X}(^2B)$ and $\tilde{A}(^2A)$ states of HCCCH$^-$, and for the $\tilde{X}(^3B)$, $\tilde{a}(^1A)$, and $\tilde{b}(^1B)$ states of HCCCH.
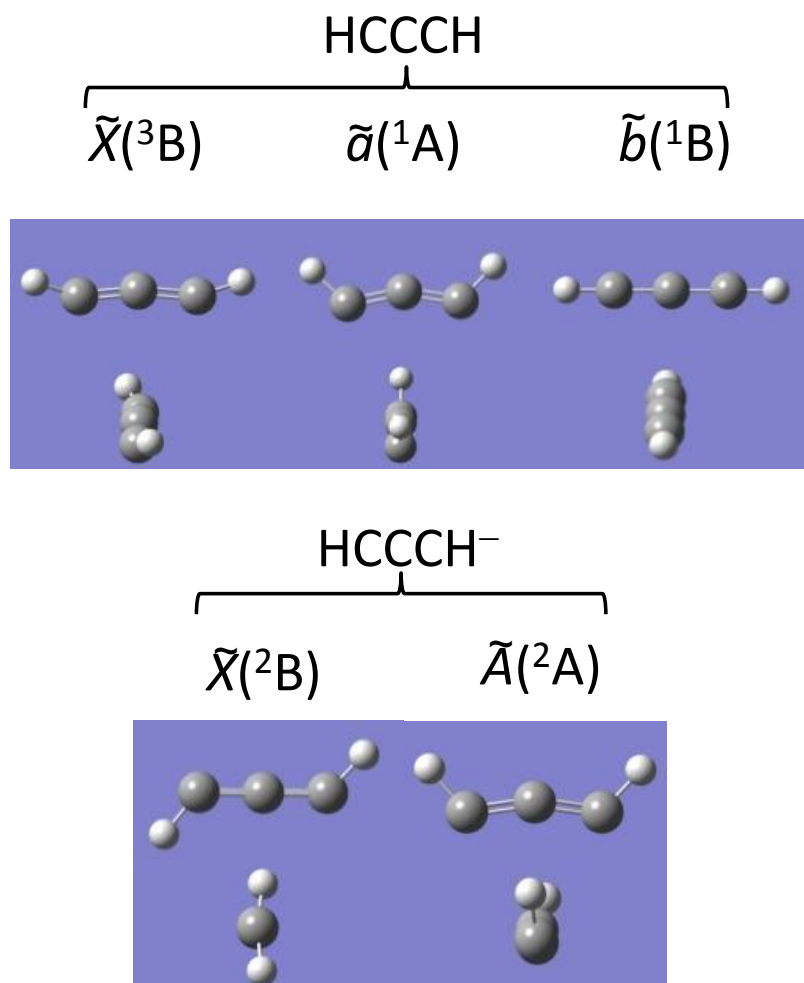
Figure 7.10: Unrestricted Hartree-Fock frontier orbitals of $\tilde{X}(^2B)$ HCCCH$^-$ at its CCSD(T)/aug-cc-pVTZ equilibrium geometry. The C_2 axis is oriented vertically and tilted 20° out of the plane of the figure. Orbital energies and symmetries are shown below each panel. The right side of the figure shows the electronic states produced upon removal of different electrons from the anion in a Koopmans theorem approach.

Figure 7.11: Unrestricted Hartree-Fock frontier orbitals of $\tilde{A}(^2A)$ HCCCH$^-$ at its CCSD(T)/aug-cc-pVTZ equilibrium geometry. This state lies 0.026 eV above the HCCCH$^-$ $\tilde{X}(^2B)$ state at the CCSD(T)/CBS limit. The C_2 axis is oriented vertically and tilted 20° out of the plane of the figure. Orbital energies and symmetries are shown below each panel. The right side of the figure shows the electronic states produced upon removal of different electrons from the anion in a Koopmans theorem approach.
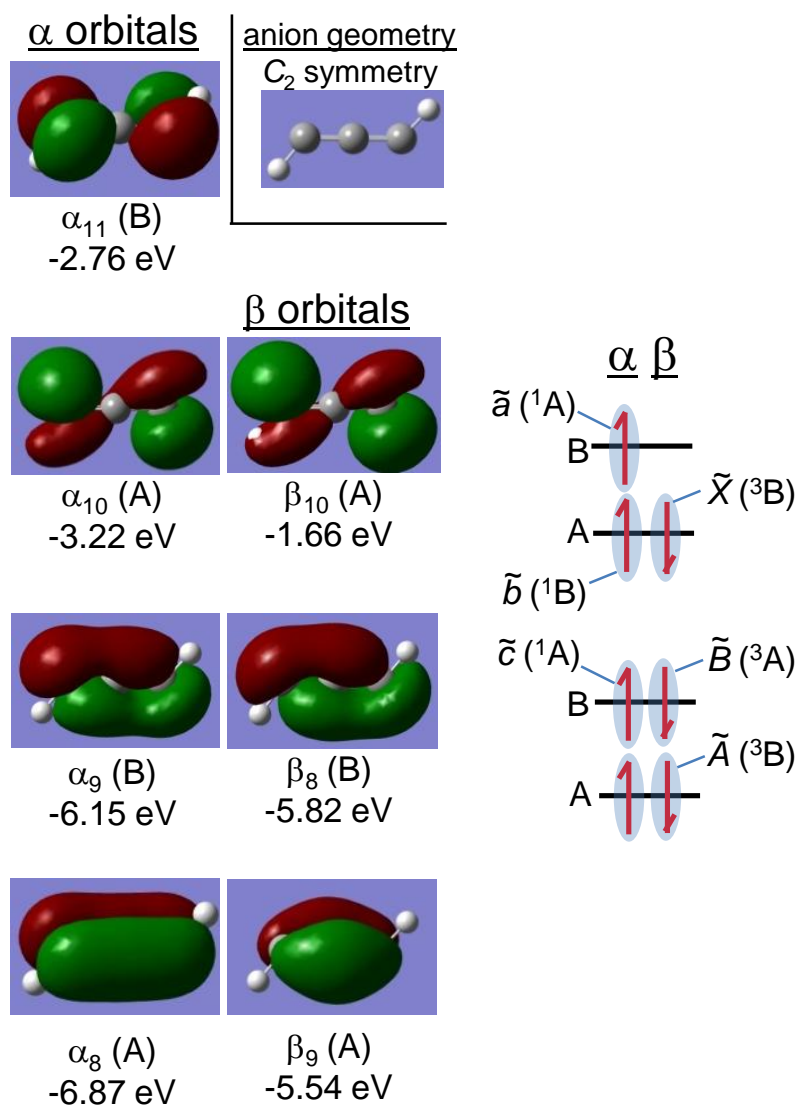
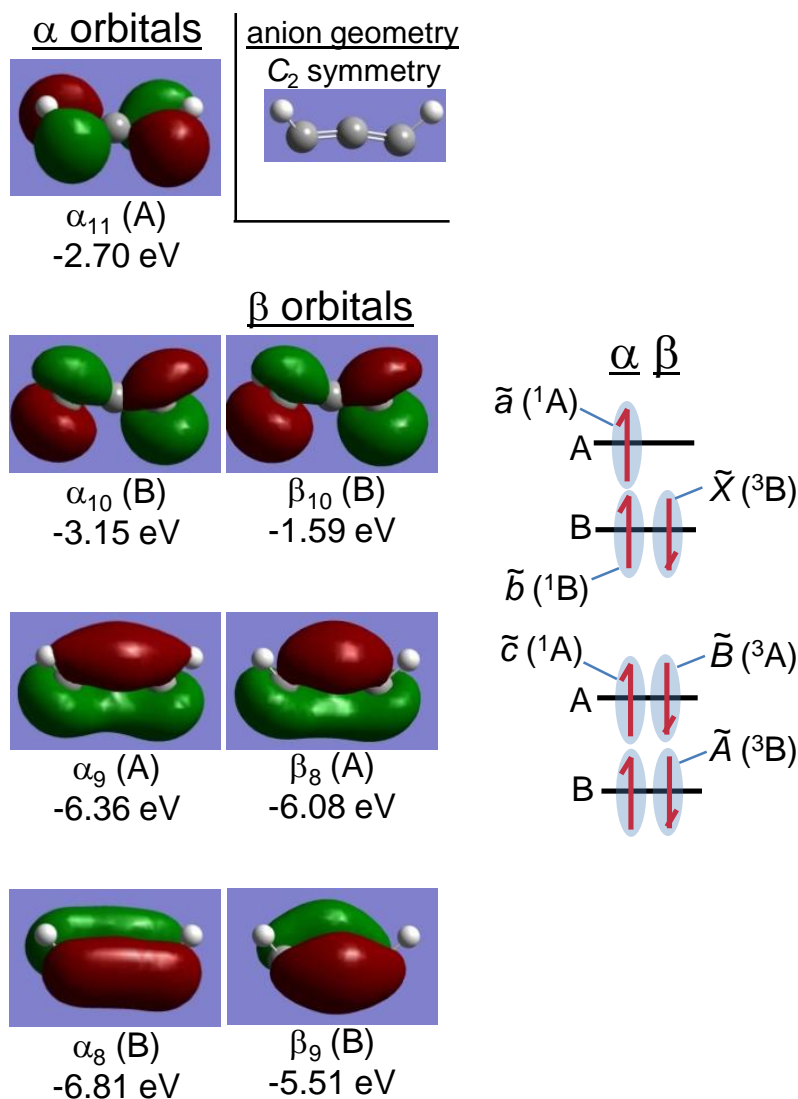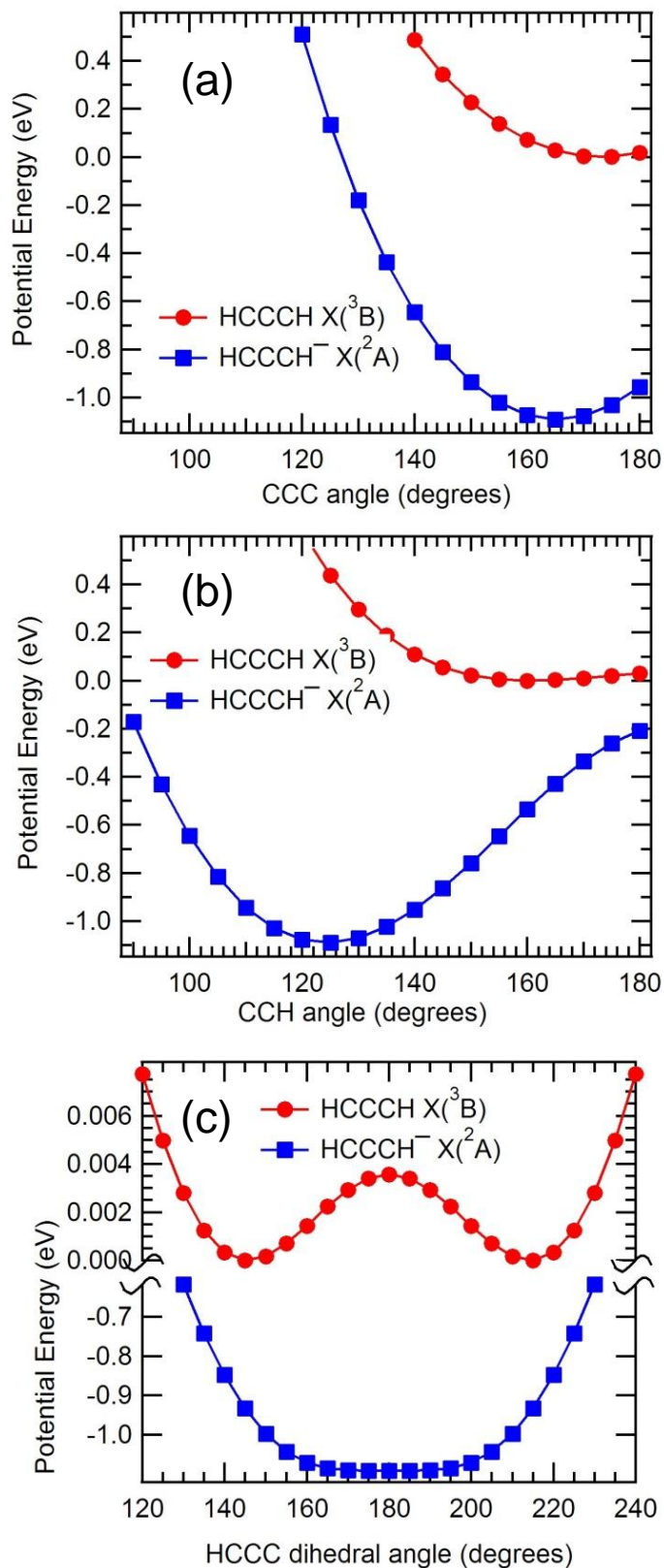Figure 7.12: Unrelaxed bending potentials of HCCCH$^-$ $\tilde{A}(^2A)$ and HCCCH $\tilde{X}(^3B)$, calculated at UCCSD(T)/aug-cc-pVTZ. Coordinates other than the scanned coordinate are fixed at their equilibrium value. The zero of energy is the minimum of $\tilde{X}(^3B)$ state. Note the difference of energy scales in the bottom panel.

anion well in this coordinate provides a more rigid structure for the anion, whereas the large change in geometry and well depth should lead to significant excitation in this coordinate. Finally, in the dihedral angle $\angle$HCCC, the barriers to linearity are only 2 and 29 cm^{-1} in the anion and neutral states, with a decrease in $\angle$HCCC by 28° upon detachment. The anion potential along this coordinate is flat-bottomed and highly anharmonic, with a strong quartic term. Noting the change in scale in the upper half of Fig. 7.12(c), the potential is very flat along all three bending coordinates in the neutral. Based on these plots one might assume that the vibrationally averaged structure of the HCCCH $\tilde{X}(^3B)$ state will be linear, although this conclusion does not agree with the infrared (IR) and electron spin resonance (ESR) data of Seburg and McMahon, who find substantial evidence for a C_2 structure of HCCCH $\tilde{X}(^3B)$.[195]

Due to the large geometry change upon photodetachment to the $\tilde{X}(^3B)$ state, the standard normal-mode Franck-Condon simulations are of no assistance in assigning the origin transition. Figure 7.13(a) shows an *ab initio* Cartesian normal coordinates Franck-Condon simulation of the photoelectron spectrum terminating in the $\tilde{X}(^3B)$ state. The simulation qualitatively fails to reproduce experiment. The main progression in the simulation is the totally-symmetric C-H stretching mode ν_9, with a secondary progression in ν_5. Inspection of Table 7.3 shows only a modest change in the C-H bond length of -0.02 Å, inconsistent with the very long progression seen in the simulation (even if the C-H stretch is removed from the PES simulation, the remaining main active mode, ν_5, does not account for the observed FC envelope). This type of artifact arises from large amplitude vibrations in the CCH bond angle.[24] The Cartesian normal mode vectors displace atoms in straight lines, an approximation usually sufficient for small amplitude vibrations. In large amplitude vibrations, such as observed upon $\tilde{X}(^3B) \leftarrow \tilde{X}(^2B)$ photodetachment, curvilinear coordinates form a more appropriate basis set, so that bending motions do not artificially excite stretching motions. Creating appropriate internal, curvilinear coordinates is challenging and outside the scope of this paper.

Simulated photoelectron spectra of $\tilde{a}(^1A) \leftarrow \tilde{X}(^2B)$ photodetachment are shown in Fig. 7.13(b) and Figs. 7.14(a) – (b). We expect that photodetachment from the *trans* $\tilde{X}(^2B)$ anion to the *cis*

Figure 7.13: Simulated photoelectron spectra using normal mode analysis in mass-weighted Cartesian coordinates compared with the $\theta = 54.7°$ polarization spectrum of HCCCH$^-$. (a) Simulated spectrum of $\tilde{X}(^3B) \leftarrow \tilde{X}(^2B)$ photodetachment. (b) Simulated spectrum of $\tilde{a}(^1A) \leftarrow \tilde{X}(^2B)$ photodetachment, where the initial anion state is *trans* and the final neutral state is *cis*.
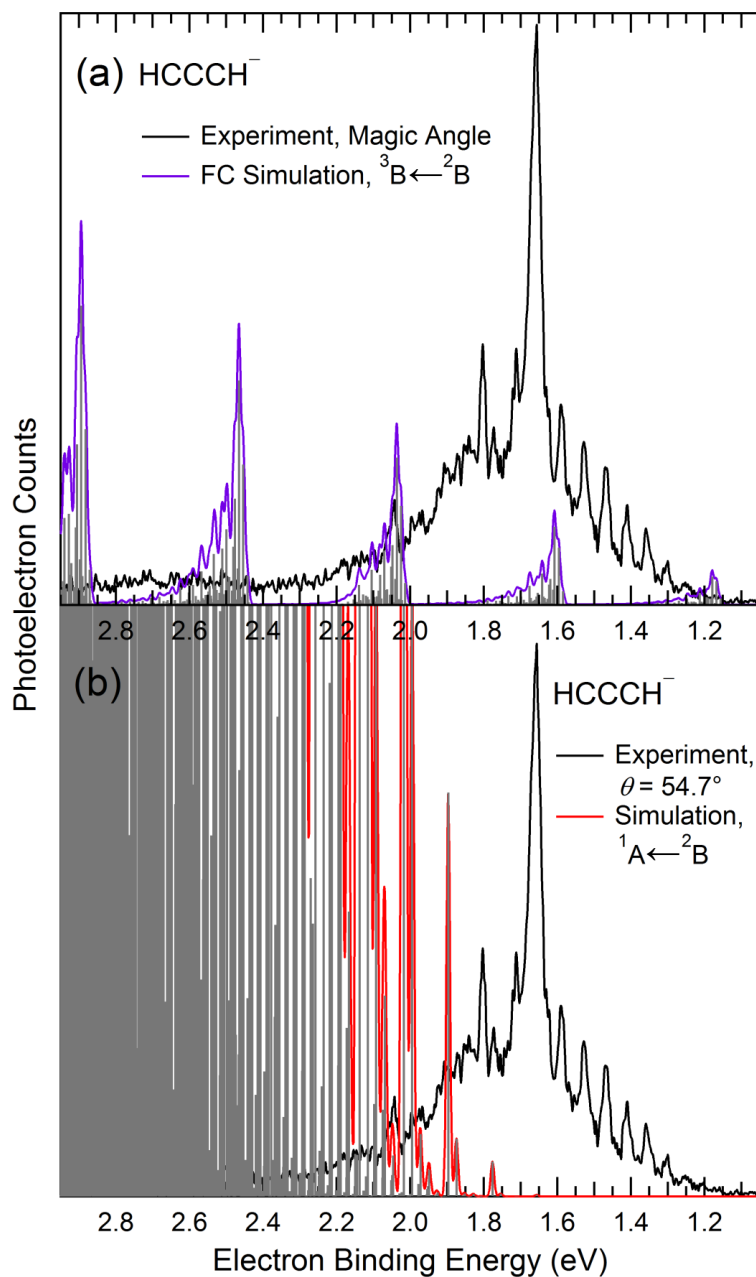
isomer of the $\tilde{a}(^1A)$ state of HCCCH will yield an extended vibrational progression with relatively little intensity at the origin. Indeed, the $\tilde{a}(^1A)$ (*cis*) $\leftarrow \tilde{X}(^2B)$ (*trans*) simulation (Fig. 7.13(b)) shows an extremely long vibrational progression with nearly no intensity at the origin, exaggerated by the inability of the normal-mode simulation in Cartesian coordinates to model large geometry changes. This simulation is inconsistent with the measured spectrum; thus, we do not see any evidence of $\tilde{a}(^1A)$ (*cis*) $\leftarrow \tilde{X}(^2B)$ (*trans*) photodetachment in our data.

The normal-mode Franck-Condon simulation is much more successful when the geometry change upon photodetachment is small, as illustrated in Figs. 7.14(a) and (b). The simulation of $\tilde{a}(^1A) \leftarrow \tilde{X}(^2B)$ photodetachment, in which both the initial anion state and the final neutral state have a *trans* geometry, is shown in Fig. 7.14(a); likewise, the simulation of $\tilde{a}(^1A) \leftarrow \tilde{A}(^2A)$ photodetachment, in which both the initial anion state and the final neutral state have a *cis* geometry, is shown in Fig. 7.14(b). In these cases, the small geometry change upon photodetachment to the $\tilde{a}(^1A)$ state leads to significant Franck-Condon overlap with vibrational levels near the bottom of the neutral potential well, where vibrations can be approximated as independent harmonic oscillators. Because the *cis* and *trans* isomers of HCCCH$^-$ and of the $\tilde{a}(^1A)$ state of HCCCH lie close in energy, we expect that both $\tilde{a}(^1A)$ (*trans*) $\leftarrow \tilde{X}(^2B)$ (*trans*) and $\tilde{a}(^1A)$ (*cis*) $\leftarrow \tilde{A}(^2A)$ (*cis*) photodetachment contribute signal to the observed photoelectron spectrum of HCCCH$^-$.

Although the harmonic approximation is clearly inadequate for the bending modes of HCCCH, it is still useful to consider the magnitude of the zero point energy in relation to the bending potentials of Fig. 7.12. At the CCSD(T)/aug-cc-pVTZ level, the zero point energies are 0.703 eV (5669 cm^{-1}) and 0.694 eV (5599 cm^{-1}), respectively, for HCCCH$^-$ $\tilde{A}(^2A)$ and HCCCH $\tilde{X}(^3B)$. Considering that the bending potentials in Fig. 7.12 are unrelaxed, we conclude that the zero point energy is generally greater than (or at least comparable to) the barriers to linearity in all the coordinates shown.

Figure 7.14: Simulated photoelectron spectra using normal mode analysis in mass-weighted Cartesian coordinates compared with the $\theta = 54.7°$ polarization spectrum of $HCCCH^-$. (a) Simulated spectrum of $\tilde{a}(^1A) \leftarrow \tilde{X}(^2B)$ photodetachment, where both states are *trans*. (b) Simulated spectrum of $\tilde{a}(^1A) \leftarrow \tilde{A}(^2A)$ photodetachment, where both states are *cis*.
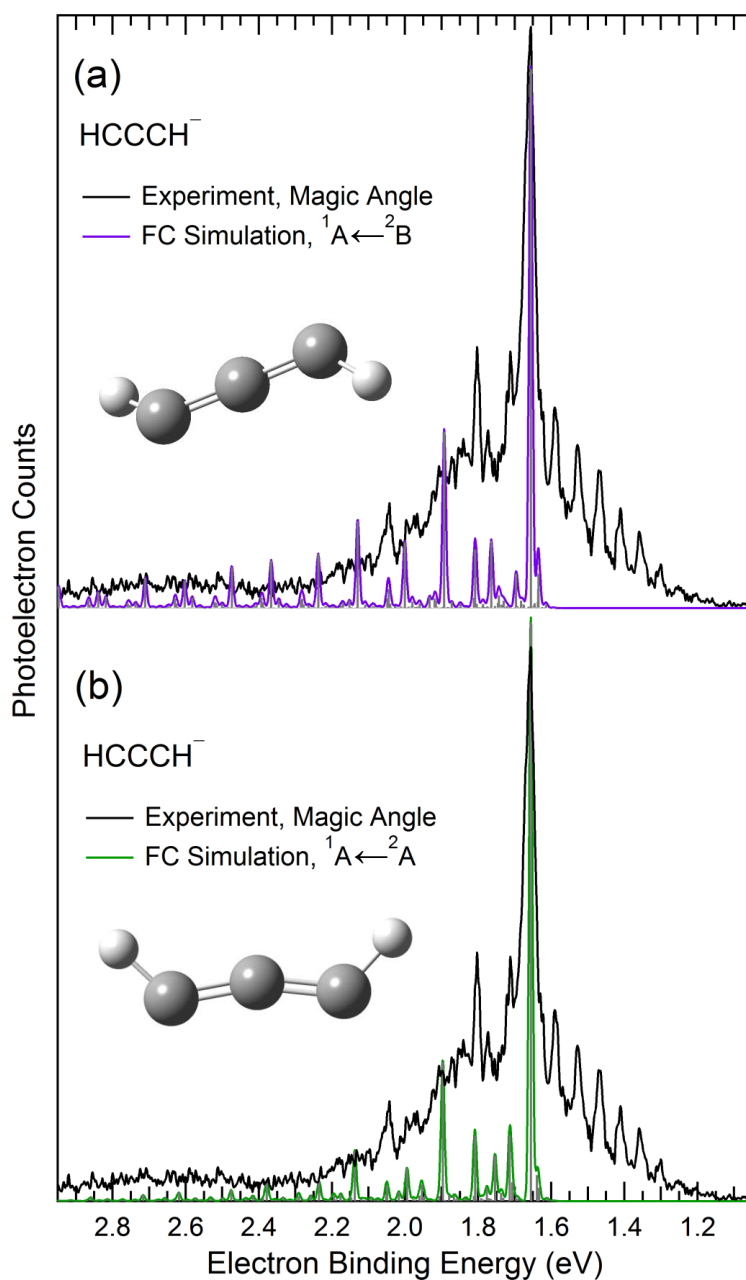
7.6   Discussion

7.6.1   Electronic Structure of HCCCH

The simplest carbene, methylene (CH_2), provides a good starting point for the discussion of propargylene. The ground state of CH_2^- is $\tilde{X}(^2B_1)$, with two electrons in an a_1 symmetry σ-type carbene orbital, and one electron in a b_1 symmetry π orbital perpendicular to the molecular plane (Scheme 7.4). In the first approximation, the detachment of each of these electrons produces the lowest three electronic states of neutral CH_2.

Scheme 7.4
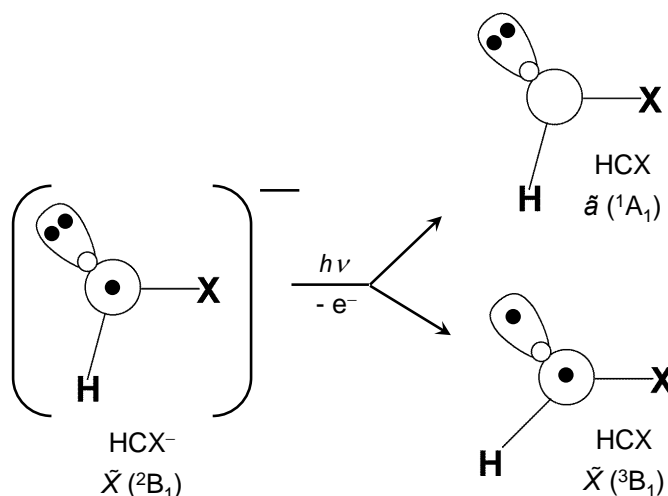
Detachment of the β electron from the σ orbital produces the $\tilde{X}(^3B_1)$ state (EA = 0.652 $\pm$ 0.006 eV); detachment of the α electron from the π orbital creates the $\tilde{a}(^1A_1)$ state ($T_0 = 0.392 \pm 0.002$ eV); detachment of the α electron from the σ orbital produces the higher lying open-shell singlet state $\tilde{b}(^1B_1)$ ($T_0 = 1.02 \pm 0.05$ eV).[34,222–226] The two electrons in the a_1 σ-type carbene orbital of the anion repel the C-H bonds, leading to a small HCH angle, whereas the single b_1 electron in the π orbital has no effect on the HCH angle. In this simple picture, removal of either σ electron (forming the $\tilde{X}(^3B_1)$ or $\tilde{b}(^1B_1)$ states) should increase $\angle$HCH, whereas removing the π electron to form the $\tilde{a}(^1A_1)$ state should have little influence on $\angle$HCH.

The propargylene molecule is simply an ethynyl-substituted methylene, HC-CCH. The richness of this molecule stems from the fact that both the C1 and C3 carbons can serve as carbene

centers, as shown in Scheme 7.1, with the added complexity that each center may have σ or π character, forming triplet and closed- or open-shell singlet states.

Given the electronic structure of CH_2 just described, assignment of the main features in the NIPES spectra of HCCCH and DCCCD (Fig. 7.6) is straightforward. Based on the work of Seburg and McMahon,[195] we assume that HCCCH belongs to the C_2 point group. Resolving the higher symmetry C_{2v} group of methylene to the C_2 point group is accomplished by removing the subscript on the symmetry labels (e.g., $^3B_1 \rightarrow {}^3B$). We assign the lowest energy electronic state of HCCCH as $\tilde{X}(^3B)$, with an experimental origin of $1.156 \pm \binom{0.010}{0.050}$ eV and a long vibrational progression indicative of a large geometry change compared to the anion. We expect, by analogy to CH_2, that a substantial increase in $\angle HCC$ is the genesis of the long vibrational progression. From the spectra we estimate that the peak at 1.71 eV represents the maximum of the Franck-Condon envelope of the $\tilde{X}(^3B)$ state and assign a VDE of 1.71 ± 0.06 eV, in reasonable agreement with the CCSD(T) VDE of 1.66 eV.

The sharp peak at eBE = 1.656 ± 0.005 eV, with β = -0.79, is consistent with the origin peak of the $\tilde{a}(^1A)$ state of HCCCH, providing a singlet-triplet splitting of $\Delta E_{TS} = 0.50 \pm \binom{0.050}{0.011}$ eV. Noting the $\beta \sim$ -0.41 value of the strong $\tilde{X}(^3B)$ peaks at 1.588 and 1.526 eV, we can use the negative peaks of $\beta(E)$ at higher binding energy to assign vibrational transitions belonging to the $\tilde{a}(^1A)$ state. Comparing the red spectrum in Fig. 7.6(a) (where transitions to $\tilde{a}(^1A)$ are disfavored) with the magic angle spectrum in black, the peak at 1.803 eV is the only other peak that can be conclusively assigned to the $\tilde{a}(^1A)$ state. The energy of this peak is 1186 ± 40 cm^{-1} above the $\tilde{a}(^1A)$ origin, consistent with the totally-symmetric CCC symmetric stretch vibration; the Franck-Condon simulation (Fig. 7.14) verifies this assignment. The experimental spectra are consistent with a small geometry change from anion to neutral for the $\tilde{a}(^1A)$ electronic state, consistent with our analogy to CH_2.

Finally, we assign a third electronic state, the $\tilde{b}(^1B)$ state, to the series of peaks from $\sim$ 2.4 – 2.95 eV with a VDE of 2.648 ± 0.020 eV. If the analogy with CH_2 holds, we expect the geometry of the $\tilde{b}(^1B)$ state to be similar to the $\tilde{X}(^3B)$ state, because they both arise from removal of an α or

β electron, respectively, from the same σ-type carbene orbital. This expectation is consistent with the red spectra in Figs. 7.6(a) and (b). If the geometries of these two neutral states are similar, it is reasonable to expect the energy difference between the VDEs and the ADEs to be similar. Using this energy difference from the $\tilde{X}(^3B)$ state, the approximate origin of the $\tilde{b}(^1B)$ lies at 2.648 - (1.71 - 1.156) $\sim$ 2.09 $\pm$ $\binom{0.06}{0.08}$ eV. This value is in good agreement with the ADE calculated using MRCI (offset by +0.14 eV, as discussed in Section 7.5.5) of 2.05 eV. As a result, our experimental estimate of the term energy for the third electronic state of HCCCH is $T_0[\tilde{b}(^1B)] = 0.94 \pm 0.08$ eV.

The assignment of the first three electronic states of neutral HCCCH by analogy with methylene is completely consistent with the electronic states predicted by a Koopmans' theorem analysis of our UCCSD(T)/aug-cc-pVTZ calculations. Figure 7.10 shows the seven highest orbitals of the HCCCH$^-$ anion, along with their orbital energies and symmetries. The anion geometry, while strictly C_2, is nearly planar. In the planar limit, the α_{11}, α_8, and β_9 orbitals are π orbitals, whereas the α_{10}, β_{10}, α_9, and β_8 orbitals are σ orbitals. If we make a further (small) distortion of the molecular frame so that it is linear, the lowest four orbitals become fully bonding, degenerate π_x and π_y orbitals with no transverse nodes. The highest three orbitals become approximately non-bonding, degenerate π_x and π_y orbitals with one transverse nodal plane. The shapes of these orbitals are reminiscent of the π system of the resonance-stabilized allyl radical (H$_2$C-CH-CH$_2$), where the unpaired electron is delocalized in a non-bonding orbital, with equal density on the two outer carbon atoms. The case of linear HCCCH is similar, except that this species is "doubly allylic," due to the delocalization of the three least bound electrons among the π orbitals in both the x- and the y-planes. Such delocalization should provide additional resonance stabilization compared with singly allylic species.

Remembering that the point group is in fact C_2 but close to planar and linear will provide several insights when interpreting the photoelectron spectra and angular distributions. Removal of the least bound electron (from the β_{10} orbital) creates a neutral state of (^3B) symmetry, consistent with our assignment of the ground electronic state. Furthermore, the σ-type β_{10} orbital is dominated by carbene lone pairs on the bottom of the molecule (as oriented in Fig. 7.10), but also shows a

bonding interaction on the top side that will reduce the CCH angle in the anion. Ejection of an electron from β_{10} (or α_{10}) implies a significant increase in the CCH angle in the neutral, consistent with the long vibrational progressions we observe for transitions to the $\tilde{X}(^3\mathrm{B})$ and $\tilde{b}(^1\mathrm{B})$ states. By contrast, removal of the second least bound electron from the π-type α_{11} orbital of the anion, creating an electronic state of ($^1\mathrm{A}$) symmetry, is expected to create very little geometry change, because this orbital is essentially non-bonding, or slightly CCC anti-bonding. In fact, Table 7.2 shows a slight increase in the CC bond length upon detachment to the $\tilde{a}(^1\mathrm{A})$ state, but overall only a minor geometry change, consistent with the short vibrational progression observed experimentally.

7.6.2   Interpretation of Photoelectron Angular Distribution Measurements

In the context of the molecular orbitals, the experimental angular distributions provide evidence that HCCCH^- should not be described as a planar structure, despite the relatively flat potential energy surfaces in the dihedral angle coordinate (see Fig. 7.12). To summarize, the experimental values of the anisotropy parameter upon detachment to different HCCCH electronic states are $\beta[\tilde{X}(^3\mathrm{B})] \sim$ -0.45, $\beta[\tilde{a}(^1\mathrm{A})] \sim$ -0.8, and $\beta[\tilde{b}(^1\mathrm{B})] =$ -0.1 to +0.2 with increasing eBE (decreasing eKE). In the limit that the anion is planar (a distortion of only 5.9° in the dihedral angle and 2 cm^{-1} in energy), the α_{10}, and β_{10} orbitals are σ orbitals, whereas the α_{11} orbital is a π orbital. Although not exact in molecules, in atomic systems detachment from an s orbital ejects an electron with a pure p-wave ($l = 1$) and $\beta = +2$, independent of eKE. Detachment from an atomic p-orbital creates both s-wave ($l = 0$; $\beta = 0$), and d-wave ($l = 2$; $\beta =$ -1) partial waves, which will interfere with each other to create anisotropy parameters between -1 and 0. At low eKE s-waves dominate, with d-waves dominating at eKE $\sim$ 1 eV. Applied to the present case with a planar molecular frame, we expect detachment from the π orbital α_{11} to be similar to an atomic p-orbital, and because the eKE of the $\tilde{a}(^1\mathrm{A})$ state origin is 1.752 eV, d-wave detachment should dominate, consistent with the observed very negative anisotropy parameter $\beta =$ -0.8.

For detachment from the β_{10} orbital (which would be purely σ-type if the anion were planar), we would expect $\beta \sim +2$ in the atomic case and $\beta > 0$ in the molecular case. For the $\tilde{X}(^3\mathrm{B})$ state,

however, we observe the opposite sign: β = -0.4, a qualitatively different result, implying that there is substantial π character in the β_{10} orbital. If the molecule were linear, we would expect pure π character for both the β_{10} and α_{11} orbitals and identical anisotropy parameters for the $\tilde{X}$ and $\tilde{a}$ states. Our observations are most consistent with a non-planar, non-linear structure, in which the β_{10} orbital will have both σ- and π-type contributions, the latter being responsible for d-wave character resulting in $\beta < 0$. However, the more negative anisotropy parameter for the $\tilde{a}$ state implies that the α_{11} orbital has more π character than β_{10}, again consistent with a somewhat non-planar, C_2 symmetry structure.

Finally, the $\tilde{b}(^1B)$ state is formed by removal of the α_{10} electron, again of purely σ character in the planar molecule, but with π-type contributions in the non-planar molecule adding s- and d-symmetry partial waves. However, in the $\tilde{b}(^1B)$ state the anisotropy parameter ranges from $\beta(\text{eKE} = 1.0) = -0.1$ to $\beta(\text{eKE} = 0.46) = +0.2$. The lower eKEs resulting from this higher-lying electronic state are again consistent with detachment from an orbital that has π character (a negative β component that decreases in magnitude as kinetic energy decreases) and σ character (contributing a positive β component independent of eKE, and dominating all other components at very low kinetic energy). These orbital characters, in turn, are consistent with a C_2 symmetry structure.

7.6.3   Higher Lying Electronic States of HCCCH

Assignments of the higher lying peaks from the VMI spectrometer (at eBE = 4.456, 4.589, 4.743, and 4.877 eV) are not as straightforward as in the NIPES spectra. Based on the intensities, it seems reasonable to assign the 4.456 eV peak as the origin of an electronic state. Due to background signals inherent in these experiments, the angular distributions from the VMI apparatus are not quantitative, which removes a key observable in the assignment of electronic states. The MRCI results in Table 7.2, corrected for the 0.14 eV offset, predict adiabatic detachment energies of $\tilde{c}(^1A) = 2.70$ eV, $\tilde{A}(^3B_2) = 4.10$ eV, $\tilde{d}(^1A_2) = 4.17$ eV, and $\tilde{B}(^3A_2) = 4.34$ eV. Inspection of the molecular orbitals of these states shows that all states are accessible by removal of one electron from the anion except the $\tilde{d}(^1A_2)$ state. The best match energetically with experiment is the $\tilde{B}(^3A_2)$

state. However, the VDE is calculated to be 0.3 eV above the ADE for this state, implying a fairly large geometry change. This prediction is somewhat at odds with the fact that the experimental peak at 4.456 eV in Fig. 7.3 is the strongest of the peaks in this range, implying a modest geometry change from the anion. All the other calculated electronic states in this region have even larger VDE - ADE gaps.

A final point can be raised about the high energy red spectra in Fig. 7.3. The spacing between the first and second peak is 0.133 eV (1070 cm^{-1}), a value consistent with a CCC stretching mode. However, the third peak is located 0.287 eV (2315 cm^{-1}) above the origin peak. It is difficult to rationalize this spacing as a vibrational fundamental or, based on the intensities, as a combination band built off the 4.456 eV origin peak. Therefore it seems likely that the peak at 4.743 eV represents the origin of an additional electronic state. In the absence of additional experimental observables, it is difficult to determine more about these high-lying electronic states of HCCCH.

7.6.4   Vibrational Assignments in the $\tilde{X}(^3\mathrm{B})$ State of HCCCH

The vibrational peak spacings in the main progressions of the $\tilde{X}(^3\mathrm{B})$ state of HCCCH and DCCCD are shown in Fig. 7.8 and can be derived from Table 7.1. Based on our assignment of the origin transition in the $\tilde{X}(^3\mathrm{B})$ state, the fundamental frequency of the main progression in HCCCH is 360 cm^{-1}, ($n = 0$ in Fig. 7.8). Note that peak spacings in both isotopologues increase with increasing energy in the potential well. This negative anharmonicity is arises from quartic terms in the 1-D vibrational potential and is indicative of a bending mode. The shapes of the potentials in both the CCH and the CCC coordinates of the neutral $\tilde{X}(^3\mathrm{B})$ state (Fig. 7.12) are consistent with negative anharmonicity.

Frequency changes upon deuteration may aid the assignment of vibrational modes. The ratios of DCCCD : HCCCH peak spacing for the main progression in the $\tilde{X}(^3\mathrm{B})$ state can be calculated from the data in Fig. 7.8. These ratios range from 0.76 – 0.71, with an average of 0.74. This value is only slightly larger than the 0.707 value expected for a vibrational mode involving pure H(D) motion, implying that the active mode has significant hydrogen atom displacement. Because the

peak spacings range from 360 to 500 cm^{-1} for HCCCH (306 – 403 cm^{-1} for DCCCD), a bending mode is the only reasonable choice for the active mode, and the only plausible choices consistent with the experimental isotopologue frequency ratios are 1(A), 2(B), and 5(A), as shown in Table 7.3. Mode 2(B) is non-totally symmetric, and therefore should not appear in the spectrum with the exception of even overtones. The 237 cm^{-1} calculated harmonic frequency of mode 1(A) appears too small to match the experimental progression, although the true, anharmonic fundamental frequency may be higher. The mostly likely assignment of the active mode is ν_5, the in-plane symmetric CCH bend. Both the calculated fundamental frequency (351 cm^{-1}) and the DCCCD : HCCCH frequency ratio (0.75) are in good agreement with our experimental measurements, supporting the assignment of the main progression to this mode. Nimlos et al., in their analysis of the isoelectronic HCCN molecule, identified a similar progression and assigned it to the ν_5 semi-rigid bender in this isoelectronic molecule.[142]

Our 360 cm^{-1} fundamental frequency of ν_5 is difficult to reconcile with the infrared matrix spectra of Seburg and McMahon,[184] where they observe four bending mode bands: 550 cm^{-1} (m), 403 cm^{-1} (m), 249 cm^{-1} (s), and 246 cm^{-1} (m). With the exception of a (normally) small matrix shift, the matrix isolation experiment should measure the true, anharmonic vibrational fundamental frequencies. One way to reconcile the two experiments is to invoke a 42 cm^{-1} matrix shift to the blue in this system. A shift of such magnitude is unusual, but there are few comparisons of gas phase vs. matrix frequencies below 400 cm^{-1}. It may be that at such low frequencies, large amplitude motions have dramatically increased matrix shifts. A blue shift in the matrix would also be consistent with significant repulsive interactions arising from confinement of large amplitude motions by the matrix.

7.7   Conclusions

We have used negative ion photoelectron spectroscopy to investigate the electronic and vibrational structure of propargylene. We prepare HCCCH$^-$ *via* removal of H$_2^+$ from propyne, which produces the C$_3$H$_2^-$ isomers propargylene and propadienylidene anions (m/z 38). The reaction of

O^- with allene, on the other hand, generates predominantly propadienylidene.[180,181] By subtracting the scaled propadienylidene spectra from the former spectra, we obtain the 364-nm photoelectron spectrum of the desired isomer: $HCCCH^-$.

It is notoriously difficult to assign the origin of a molecule that undergoes a substantial geometry change upon photodetachment. A large change in the $\angle CCH$ of $36°$ results in significant activity of the ν_5 symmetric CCH bend, which is manifested as an extended vibrational progression in the $\tilde{X}(^3B)$ ground state. Through comparison of the photoelectron spectra of $HCCCH^-$ and $DCCCD^-$, we assign the origin transition and measure the $EA(HCCCH) = 1.156 \pm \binom{0.010}{0.050}$ eV, in excellent agreement with our best calculated value of 1.146 eV.

At higher binding energy we observe transitions to the $\tilde{a}(^1A)$ excited state. Because the electron removed upon $\tilde{a}(^1A) \leftarrow \tilde{X}(^2B)$ photodetachment is essentially non-bonding in character, the geometry of the anion and the $\tilde{a}(^1A)$ state are very similar. Thus, we observe a sharp, intense peak at 1.656 eV corresponding to the origin of the $\tilde{a}(^1A)$ state. We measure $\Delta E_{TS} = 0.50 \pm \binom{0.050}{0.011}$ eV.

A third state of the neutral, with VDE of 2.648 ± 0.020 eV, is seen in the NIPES spectra (most prominently at $\theta = 0°$). The low signal intensity of this progression makes detailed analysis of this state difficult; however, the extended nature of the spectral envelope indicates that its geometry is quite different from that of the anion. Through comparison of the calculated ADE and VDE with the observed progression, we assign these features to the $\tilde{b}(^1B)$ state.

Considering the first three electronic states of neutral propargylene, we find both similarities and discrepancies with the simpler case of methylene. The geometry changes implied by the vibrational progressions we observe argue that the electronic structure of the carbene centers in propargylene are similar to that in methylene. In particular, removal of a σ-type electron from the anion leads to a large change in $\angle CCH$, whereas removal of a π-type electron has little effect on $\angle CCH$. In contrast with methylene, where β is positive for the origin of the ground state but negative for the excited $\tilde{a}$ state,[227] we measure a negative β for the two lowest states of HC-CCH. Presumably, this difference arises from the π character present in all the frontier orbitals of

HCCCH$^-$, whereas in methylene there is a strict delineation of σ and π orbital characters.

It is likely that a higher resolution photoelectron spectrum of the $\tilde{X}(^3\text{B})$ state would reveal much more complicated vibrational structure due to the quasilinear nature of HCCCH. In fact there are signs even in our spectra that more than one vibrational mode contributes to this progression, especially at high binding energies. However, a more sophisticated analysis awaits higher resolution spectroscopy.

Bibliography

[1] A. M. ELLIS, M. FEHER, and T. G. WRIGHT, Electronic and Photoelectron Spectroscopy: Fundamentals and Case Studies, Cambridge University Press, Cambridge, 2005.

[2] K. M. ERVIN and W. C. LINEBERGER, Photoelectron Spectroscopy of Molecular Anions, volume 1, p. 121, JAI, Greenwich, 1992.

[3] K. M. ERVIN, J. HO, and W. C. LINEBERGER, J. Chem. Phys. **89**, 4514 (1988).

[4] K. M. ERVIN, T. M. RAMOND, G. E. DAVICO, R. L. SCHWARTZ, S. M. CASEY, and W. C. LINEBERGER, J. Phys. Chem. A **105**, 10822 (2001).

[5] J. COOPER and R. N. ZARE, J. Chem. Phys. **48**, 942 (1968).

[6] D. HANSTORP, C. BENGTSSON, and D. J. LARSON, Phys. Rev. A **40**, 670 (1989).

[7] R. F. GUNION, M. K. GILLES, M. L. POLAK, and W. C. LINEBERGER, Int. J. Mass Spectrom. Ion Processes **117**, 601 (1992).

[8] T. E. SHARP and H. M. ROSENSTOCK, J. Chem. Phys. **41**, 3453 (1964).

[9] W. D. GWINN, J. Chem. Phys. **55**, 477 (1971).

[10] Molecular Vibrations, Dover, New York, 1980.

[11] F. DUSCHINSKY, Acta Physicochimica Urss **7**, 551 (1937).

[12] C. W. MULLER, J. J. NEWBY, C.-P. LIU, C. P. RODRIGO, and T. S. ZWIER, Phys. Chem. Chem. Phys. **12**, 2331 (2010).

[13] J. R. REIMERS, J. Chem. Phys. **115**, 9103 (2001).

[14] C. ECKART, Phys. Rev. **47**, 552 (1935).

[15] A. WARSHEL and M. KARPLUS, Chem. Phys. Lett. **17**, 7 (1972).

[16] J. T. HOUGEN and J. K. G. WATSON, Can. J. Phys. **43**, 298 (1965).

[17] N. J. D. LUCAS, J. Phys. B **6**, 155 (1973).

[18] I. OZKAN, J. Mol. Spectrosc. **139**, 147 (1990).

[19] R. BORRELLI and A. PELUSO, J. Chem. Phys. **125**, 194308 (2006).

[20] P. Chen, Unimolecular and Bimolecular Ion-Molecule Reaction Dynamics, Wiley & Sons, Chichester, 1994.

[21] K. M. Ervin, PESCAL, Fortran program (2010).

[22] J. R. Reimers and R. O. Watts, Mol. Phys. **52**, 357 (1984).

[23] J. R. Reimers, K. R. Wilson, E. J. Heller, and S. R. Langhoff, J. Chem. Phys. **82**, 5064 (1985).

[24] K. M. Vogelhuber, S. W. Wren, A. B. McCoy, K. M. Ervin, and W. C. Lineberger, J. Chem. Phys. **134**, 184306 (2011).

[25] H. Kikuchi, M. Kubo, N. Watanabe, and H. Suzuki, J. Chem. Phys. **119**, 729 (2003).

[26] R. Borrelli and A. Peluso, J. Chem. Phys. **128**, 044303 (2008).

[27] J. H. Frederick and C. Woywod, J. Chem. Phys. **111**, 7255 (1999).

[28] S. Califano, Vibrational States, Wiley, New York, 1976.

[29] E. V. Doktorov, I. A. Malkin, and V. I. Manko, J. Mol. Spectrosc. **56**, 1 (1975).

[30] A. Peluso, F. Santoro, and G. Del Re, Int. J. Quantum Chem. **63**, 233 (1997).

[31] C. H. DePuy, S. R. Kass, and G. P. Bean, J. Org. Chem. **53**, 4427 (1988).

[32] E. P. Clifford, P. G. Wenthold, W. C. Lineberger, G. B. Ellison, C. X. Wang, J. J. Grabowski, F. Vila, and K. D. Jordan, J. Chem. Soc., Perkin Trans. 2 , 1015 (1998).

[33] S. J. Blanksby and G. B. Ellison, Accounts Chem. Res. **36**, 255 (2003).

[34] D. G. Leopold, K. K. Murray, A. E. S. Miller, and W. C. Lineberger, J. Chem. Phys. **83**, 4849 (1985).

[35] F. C. Fehsenfeld, K. M. Evenson, and H. P. Broida, Rev. Sci. Instrum. **36**, 294 (1965).

[36] J. Lee and J. J. Grabowski, Chem. Rev. **92**, 1611 (1992).

[37] M. Marynowski, W. Franzen, and M. El-Batanouny, Rev. Sci. Instrum. **65**, 3718 (1994).

[38] S. W. Wren, Ph.D. Thesis , University of Colorado (2011).

[39] C. Douketis, D. Anex, G. Ewing, and J. P. Reilly, J. Phys. Chem. **89**, 4173 (1985).

[40] C. E. Tanner, B. P. Masterson, and C. E. Wieman, Opt. Lett. **13**, 357 (1988).

[41] K. M. Ervin, J. Ho, and W. C. Lineberger, J. Chem. Phys. **91**, 5974 (1989).

[42] I. C. Chang, Acousto-Optic Devices and Applications, pp. 12.1 – 12.54, McGraw-Hill, New York, 1995.

[43] C. S. Feigerle, Ph.D. Thesis , University of Colorado (1983).

[44] T. M. Ramond, Ph.D. Thesis , University of Colorado (2001).

[45] D. M. Neumark, K. R. Lykke, T. Andersen, and W. C. Lineberger, Phys. Rev. A **32**, 1890 (1985).

[46] C. E. Moore, Circular of the National Bureau of Standards 467 (1958).

[47] K. M. Ervin, W. Anusiewicz, P. Skurski, J. Simons, and W. C. Lineberger, J. Phys. Chem. A **107**, 8521 (2003).

[48] M. J. Frisch, G. W. Trucks, H. B. Schlegel, G. E. Scuseria, M. A. Robb, J. R. Cheeseman, J. J. A. Montgomery, T. Vreven, K. N. Kudin, J. C. Burant, J. M. Millam, S. S. Iyengar, J. Tomasi, V. Barone, B. Mennucci, M. Cossi, G. Scalmani, N. Rega, G. A. Petersson, H. Nakatsuji, M. Hada, M. Ehara, K. Toyota, R. Fukuda, J. Hasegawa, M. Ishida, T. Nakajima, Y. Honda, O. Kitao, H. Nakai, M. Klene, X. Li, J. E. Knox, H. P. Hratchian, J. B. Cross, V. Bakken, C. Adamo, J. Jaramillo, R. Gomperts, R. E. Stratmann, O. Yazyev, A. J. Austin, R. Cammi, C. Pomelli, J. W. Ochterski, P. Y. Ayala, K. Morokuma, G. A. Voth, P. Salvador, J. J. Dannenberg, V. G. Zakrzewski, S. Dapprich, A. D. Daniels, M. C. Strain, O. Farkas, D. K. Malick, A. D. Rabuck, K. Raghavachari, J. B. Foresman, J. V. Ortiz, Q. Cui, A. G. Baboul, S. Clifford, J. Cioslowski, B. B. Stefanov, G. Liu, A. Liashenko, P. Piskorz, I. Komaromi, R. L. Martin, D. J. Fox, T. Keith, M. A. Al-Laham, C. Y. Peng, A. Nanayakkara, M. Challacombe, P. M. W. Gill, B. Johnson, W. Chen, M. W. Wong, C. Gonzalez, and J. A. Pople, Gaussian 03, Revision B.05, Gaussian, Inc., Pittsburgh, 2003.

[49] A. D. Becke, J. Chem. Phys. **98**, 5648 (1993).

[50] C. T. Lee, W. T. Yang, and R. G. Parr, Phys. Rev. B **37**, 785 (1988).

[51] A. D. McLean and G. S. Chandler, J. Chem. Phys. **72**, 5639 (1980).

[52] R. Krishnan, J. S. Binkley, R. Seeger, and J. A. Pople, J. Chem. Phys. **72**, 650 (1980).

[53] K. Sendt, G. B. Bacskay, and J. C. Mackie, J. Phys. Chem. A **104**, 1861 (2000).

[54] J. M. Simmie and H. J. Curran, J. Phys. Chem. A **113**, 5128 (2009).

[55] J. W. Sebbar, N.; Bozzelli and H. Bockhorn, Int. J. Chem. Kinet. **37**, 633 (2005).

[56] The Structure and Reaction Processes of Coal, Plenum Press, New York, 1994.

[57] R. A. Meyers, Coal Structure, Academic Press, New York, 1982.

[58] J. Haggin, Chem. Eng. News **60**, 17 (1982).

[59] O. Beaumont, Wood and Fiber Science **17**, 228 (1985).

[60] J. Piskorz, D. Radlein, and D. S. Scott, J. Anal. Appl. Pyrolysis **9**, 121 (1986).

[61] R. J. Evans and T. A. Milne, Energy Fuels **1**, 123 (1987).

[62] R. J. Evans and T. A. Milne, Energy Fuels **1**, 311 (1987).

[63] F. Shafizadeh and Y. Z. Lai, J. Org. Chem. **37**, 278 (1972).

[64] F. Shafizadeh, G. D. McGinnis, and C. W. Philpot, Carbohydr. Res. **25**, 23 (1972).

[65] F. Shafizadeh, Y. Z. Lai, and C. R. McIntyre, J. Appl. Polym. Sci. **22**, 1183 (1978).

[66] S. Reale, A. Di Tullio, N. Spreti, and F. De Angelis, Mass Spectrom. Rev. **23**, 87 (2004).

[67] A. J. Ragauskas, C. K. Williams, B. H. Davison, G. Britovsek, J. Cairney, C. A. Eckert, W. J. Frederick, J. P. Hallett, D. J. Leak, C. L. Liotta, J. R. Mielenz, R. Murphy, R. Templer, and T. Tschaplinski, Science **311**, 484 (2006).

[68] S. Yaman, Energy Conv. Manage. **45**, 651 (2004).

[69] L. D. Gomez, C. G. Steele-King, and S. J. McQueen-Mason, New Phytol. **178**, 473 (2008).

[70] S. D. Phillips, Ind. Eng. Chem. Res. **46**, 8887 (2007).

[71] D. Fabbri, A. Adamiano, and C. Torri, Anal. Bioanal. Chem. **397**, 309 (2010).

[72] A. Oasmaa and D. Meier, J. Anal. Appl. Pyrolysis **73**, 323 (2005).

[73] H. Pakdel and C. Roy, Energy Fuels **5**, 427 (1991).

[74] P. A. Horne and P. T. Williams, Fuel **75**, 1051 (1996).

[75] A. Lifshitz, M. Bidani, and S. Bidani, J. Phys. Chem. **90**, 5373 (1986).

[76] P. P. Organ and J. C. Mackie, J. Chem. Soc., Faraday Trans. **87**, 815 (1991).

[77] D. Fulle, A. Dib, J. H. Kiefer, Q. Zhang, J. Yao, and R. D. Kern, J. Phys. Chem. A **102**, 7480 (1998).

[78] O. S. L. Bruinsma, P. J. J. Tromp, H. J. J. D. Nolting, and J. A. Moulijn, Fuel **67**, 334 (1988).

[79] M. A. Grela, V. T. Amorebieta, and A. J. Colussi, J. Phys. Chem. **89**, 38 (1985).

[80] N. R. Hore and D. K. Russell, New J. Chem. **28**, 606 (2004).

[81] A. Vasiliou, M. R. Nimlos, J. W. Daily, and G. B. Ellison, J. Phys. Chem. A **113**, 8540 (2009).

[82] E. B. Jochnowitz, X. Zhang, M. R. Nimlos, M. E. Varner, J. F. Stanton, and G. B. Ellison, J. Phys. Chem. A **109**, 3812 (2005).

[83] R. F. Liu, X. F. Zhou, and L. Zhai, J. Comput. Chem. **19**, 240 (1998).

[84] NIST Chemistry WebBook, chapter NIST Standard Reference Database Number 69, National Institute of Standards and Technology, accessed August 5, 2010.

[85] Y. L. Guo and J. J. Grabowski, Int. J. Mass Spectrom. Ion Processes **117**, 299 (1992).

[86] A. J. Gianola, T. Ichino, S. Kato, V. M. Bierbaum, and W. C. Lineberger, J. Phys. Chem. A **110**, 8457 (2006).

[87] S. M. Villano, A. J. Gianola, N. Eyet, T. Ichino, S. Kato, V. M. Bierbaum, and W. C. Lineberger, J. Phys. Chem. A **111**, 8579 (2007).

[88] A. J. Gianola, T. Ichino, R. L. Hoenigman, S. Kato, V. M. Bierbaum, and W. C. Lineberger, J. Phys. Chem. A **109**, 11504 (2005).

[89] A. J. Gianola, T. Ichino, R. L. Hoenigman, S. Kato, V. M. Bierbaum, and W. C. Lineberger, J. Phys. Chem. A **108**, 10326 (2004).

[90] H. Koppel, W. Domcke, and L. S. Cederbaum, Adv. Chem. Phys. **57**, 59 (1984).

[91] P. J. Derrick, L. Asbrink, O. Edqvist, B. O. Jonssen, and E. Lindholm, Int. J. Mass Spectrom. Ion Phys. **6**, 161 (1971).

[92] P. J. Derrick, L. Asbrink, O. Edqvist, and E. Lindholm, Spectrochim. Acta A **27**, 2525 (1971).

[93] P. J. Derrick, L. Asbrink, O. Edqvist, B. O. Jonssen, and E. Lindholm, Int. J. Mass Spectrom. Ion Phys. **6**, 177 (1971).

[94] P. J. Derrick, L. Asbrink, O. Edqvist, B. O. Jonssen, and E. Lindholm, Int. J. Mass Spectrom. Ion Phys. **6**, 191 (1971).

[95] K. Takeshita and Y. Yamamoto, J. Chem. Phys. **101**, 2198 (1994).

[96] K. Takeshita and Y. Yamamoto, Chem. Phys. **189**, 489 (1994).

[97] A. B. Trofimov, H. Koppel, and J. Schirmer, J. Chem. Phys. **109**, 1025 (1998).

[98] J. C. Mackie, M. B. Colket, P. F. Nelson, and M. Esler, Int. J. Chem. Kinet. **23**, 733 (1991).

[99] C. Barckholtz, T. A. Barckholtz, and C. M. Hadad, J. Am. Chem. Soc. **121**, 491 (1999).

[100] E. S. Whitney, T. Haeber, M. D. Schuder, A. C. Blair, and D. J. Nesbitt, J. Chem. Phys. **125** (2006).

[101] M. Schwartz, L. R. Peebles, R. J. Berry, and P. Marshall, J. Chem. Phys. **118**, 557 (2003).

[102] M. J. Molina, L. T. Molina, and C. E. Kolb, Ann. Rev. Phys. Chem. **47**, 327 (1996).

[103] B. J. Finlayson-Pitts, Chemistry of the Upper and Lower Atmosphere: Theory, Experiments, and Applications, Academic, New York, 1999.

[104] J. S. Francisco and M. M. Maricq, Advances in Photochemistry, volume 20, p. 79, Wiley, New York, 1995.

[105] L. J. CARPENTER, Chem. Rev. **103**, 4953 (2003).

[106] M. MCFARLAND and J. KAYE, Photochem. Photobio. **55**, 911 (1992).

[107] S. I. STOLIAROV, A. BENCSURA, E. SHAFIR, V. D. KNYAZEV, and I. R. SLAGLE, J. Phys. Chem. A **105**, 76 (2001).

[108] H. E. SIMMONS and R. D. SMITH, J. Am. Chem. Soc. **81**, 4256 (1959).

[109] D. C. BLOMSTROM, K. HERBIG, and H. E. SIMMONS, J. Org. Chem. **30**, 959 (1965).

[110] N. J. PIENTA and P. J. KROPP, J. Am. Chem. Soc. **100**, 655 (1978).

[111] P. J. KROPP, N. J. PIENTA, J. A. SAWYER, and R. P. POLNIASZEK, Tetrahedron **37**, 3236 (1981).

[112] P. J. KROPP, Accounts Chem. Res. **17**, 131 (1984).

[113] E. C. FRIEDRICH, J. M. DOMEK, and R. Y. PONG, J. Org. Chem. **50**, 4640 (1985).

[114] E. C. FRIEDRICH, S. E. LUNETTA, and E. J. LEWIS, J. Org. Chem. **54**, 2388 (1989).

[115] S. DURANDETTI, S. SIBILLE, and J. PERICHON, J. Org. Chem. **56**, 3255 (1991).

[116] J. M. CONCELLON, P. L. BERNAD, and J. A. PEREZ-ANDRES, Tetrahedron Lett. **39**, 1409 (1998).

[117] T. G. CARVER and L. ANDREWS, J. Chem. Phys. **50**, 4223 (1969).

[118] T. G. CARVER and L. ANDREWS, J. Chem. Phys. **50**, 4235 (1969).

[119] M. E. JACOX and D. E. MILLIGAN, J. Chem. Phys. **54**, 3935 (1971).

[120] B. S. AULT and L. ANDREWS, J. Chem. Phys. **63**, 1411 (1975).

[121] M. E. JACOX, Chem. Phys. **12**, 51 (1976).

[122] L. ANDREWS and F. T. PROCHASKA, J. Am. Chem. Soc. **101**, 1190 (1979).

[123] L. ANDREWS, F. T. PROCHASKA, and B. S. AULT, Journal of the American Chemical Society **101**, 9 (1979).

[124] T. D. FRIDGEN, X. K. K. ZHANG, J. M. PARNIS, and R. E. MARCH, Journal of Physical Chemistry A **104**, 3487 (2000).

[125] A. RICHTER, H. MEYER, T. KAUSCHE, T. MULLER, W. SPORLEDER, and A. SCHWEIG, Chem. Phys. **214**, 321 (1997).

[126] D. K. BOHME, L. B. YOUNG, and E. LEERUFF, Journal of the American Chemical Society **94**, 5153 (1972).

[127] J. L. HOLMES and F. P. LOSSING, J. Am. Chem. Soc. **110**, 7343 (1988).

[128] M. BORN, S. INGEMANN, and N. M. M. NIBBERING, International Journal of Mass Spectrometry **194**, 103 (2000).

[129] Q. S. Li, J. F. Zhao, Y. M. Xie, and H. F. Schaefer, Mol. Phys. **100**, 3615 (2002).

[130] S. W. Wren, K. M. Vogelhuber, K. M. Ervin, and W. C. Lineberger, Phys. Chem. Chem. Phys. **11**, 4745 (2009).

[131] H. Stoll, B. Metz, and M. Dolg, J. Comput. Chem. **23**, 767 (2002).

[132] M. A. Thompson, J. P. Martin, J. P. Darr, W. C. Lineberger, and R. Parson, J. Chem. Phys. **129**, 224304 (2008).

[133] M. A. Thompson, Ph.D. Thesis , University of Colorado (2007).

[134] G. R. Long and J. W. Hudgens, J. Phys. Chem. **91**, 5870 (1987).

[135] D. T. Colbert and W. H. Miller, J. Chem. Phys. **96**, 1982 (1992).

[136] D. Luckhaus, J. Chem. Phys. **113**, 1329 (2000).

[137] G. H. Gardeinier, M. A. Johnson, and A. B. McCoy, J. Phys. Chem. A **113**, 4772 (2009).

[138] K. M. Vogelhuber, S. W. Wren, L. Sheps, and W. C. Lineberger, J. Chem. Phys. **134**, 064302 (2011).

[139] W. C. Lineberger and W. T. Borden, Phys. Chem. Chem. Phys. **13**, 11792 (2011).

[140] Reactive Molecules, John Wiley & Sons, New York, 1984.

[141] R. L. Schwartz, G. E. Davico, T. M. Ramond, and W. C. Lineberger, J. Phys. Chem. A **103**, 8213 (1999).

[142] M. R. Nimlos, G. Davico, C. M. Geise, P. G. Wenthold, W. C. Lineberger, S. J. Blanksby, C. M. Hadad, G. A. Petersson, and G. B. Ellison, J. Chem. Phys. **117**, 4323 (2002).

[143] J. Y. Qi, M. D. Chen, W. Wu, Q. E. Zhang, and C. T. Au, Chem. Phys. **364**, 31 (2009).

[144] M. B. Bell, P. A. Feldman, M. J. Travers, M. C. McCarthy, C. A. Gottlieb, and P. Thaddeus, Astrophys. J. **483**, L61 (1997).

[145] M. C. McCarthy, J. U. Grabow, M. J. Travers, W. Chen, C. A. Gottlieb, and P. Thaddeus, Astrophys. J. **494**, L231 (1998).

[146] R. Nagarajan and J. P. Maier, Int. Rev. Phys. Chem. **29**, 521 (2010).

[147] M. C. McCarthy and P. Thaddeus, J. Mol. Spec. **232**, 351 (2005).

[148] C. D. Ball, M. C. McCarthy, and P. Thaddeus, J. Chem. Phys. **112**, 10149 (2000).

[149] K. Aoki, S. Ikuta, and A. Murakami, Chem. Phys. Lett. **209**, 211 (1993).

[150] M. C. McCarthy, A. J. Apponi, V. D. Gordon, C. A. Gottlieb, P. Thaddeus, T. D. Crawford, and J. F. Stanton, J. Chem. Phys. **111**, 6750 (1999).

[151] M. C. McCarthy, J. U. Grabow, M. J. Travers, W. Chen, C. A. Gottlieb, and P. Thaddeus, Astrophys. J. **513**, 305 (1999).

[152] K. Aoki and S. Ikuta, J. Chem. Phys. **98**, 7661 (1993).

[153] S. Ikuta, T. Tsuboi, and K. Aoki, J. Mol. Struct. (Theochem) **528**, 297 (2000).

[154] J. Kalcher, Chem. Phys. Lett. **403**, 146 (2005).

[155] M. Z. Kassaee, J. Azarnia, and S. Arshadi, J. Mol. Struct. (Theochem) **686**, 115 (2004).

[156] N. P. Bowling, R. J. Halter, J. A. Hodges, R. A. Seburg, P. S. Thomas, C. S. Simmons, J. F. Stanton, and R. J. McMahon, J. Am. Chem. Soc. **128**, 3291 (2006).

[157] D. J. Goebbert, K. Pichugin, D. Khuseynov, P. G. Wenthold, and A. Sanov, J. Chem. Phys. **132**, 224301 (2010).

[158] J. A. Tang, Y. Sumiyoshi, and Y. Endo, Chem. Phys. Lett. **315**, 69 (1999).

[159] J. Cernicharo, M. Guelin, and J. R. Pardo, Astrophys. J. **615**, L145 (2004).

[160] K. M. Vogelhuber, S. W. Wren, C. J. Shaffer, R. J. McMahon, A. B. McCoy, and W. C. Lineberger, J. Chem. Phys. **135**, 204307 (2011).

[161] S. W. Wren, K. M. Vogelhuber, J. M. Garver, S. Kato, L. Sheps, V. M. Bierbaum, and W. C. Lineberger, J. Am. Chem. Soc. **134**, 6584 (2012).

[162] C. Moller and M. S. Plesset, Phys. Rev. **46**, 618 (1934).

[163] J. T. Hougen, P. R. Bunker, and J. W. C. Johns, J. Mol. Spec. **34**, 136 (1970).

[164] T. Ichino, S. M. Villano, A. J. Gianola, D. J. Goebbert, L. Velarde, A. Sanov, S. J. Blanksby, X. Zhou, D. A. Hrovat, W. T. Borden, and W. C. Lineberger, J. Phys. Chem. A **115**, 1634 (2011).

[165] E. T. Seidl and H. F. Schaefer, J. Chem. Phys. **96**, 4449 (1992).

[166] D. J. Goebbert, D. Khuseynov, and A. Sanov, J. Phys. Chem. A **114**, 2259 (2010).

[167] D. J. Goebbert, D. Khuseynov, and A. Sanov, J. Chem. Phys. **131**, 161102 (2009).

[168] D. J. Goebbert, L. Velarde, D. Khuseynov, and A. Sanov, J. Phys. Chem. Lett. **1**, 792 (2010).

[169] P. Thaddeus, C. A. Gottlieb, R. Mollaaghababa, and J. M. Vrtilek, J. Chem. Soc. Faraday Trans. **89**, 2125 (1993).

[170] J. Cernicharo, C. A. Gottlieb, M. Guelin, T. C. Killian, P. Thaddeus, and J. M. Vrtilek, Astrophys. J. **368**, L43 (1991).

[171] J. Cernicharo, C. A. Gottlieb, M. Guelin, T. C. Killian, G. Paubert, P. Thaddeus, and J. M. Vrtilek, Astrophys. J. **368**, L39 (1991).

[172] J. M. Vrtilek, C. A. Gottlieb, E. W. Gottlieb, T. C. Killian, and P. Thaddeus, Astrophys. J. **364**, L53 (1990).

[173] M. C. McCarthy and P. Thaddeus, J. Mol. Spec. **211**, 235 (2002).

[174] C. A. Gottlieb, T. C. Killian, P. Thaddeus, P. Botschwina, J. Flugge, and M. Oswald, J. Chem. Phys. **98**, 4478 (1993).

[175] J. Gauss and J. F. Stanton, J. Mol. Struct. **485**, 43 (1999).

[176] J. A. Hodges, R. J. McMahon, K. W. Sattelmeyer, and J. F. Stanton, Astrophys. J. **544**, 838 (2000).

[177] J. F. Stanton, J. T. DePinto, R. A. Seburg, J. A. Hodges, and R. J. McMahon, J. Am. Chem. Soc. **119**, 429 (1997).

[178] P. Birza, A. Chirokolava, M. Araki, P. Kolek, and J. P. Maier, J. Mol. Spectr. **229**, 276 (2005).

[179] E. Achkasova, M. Araki, A. Denisov, and J. P. Maier, J. Mol. Spectr. **237**, 70 (2006).

[180] J. M. Oakes and G. B. Ellison, Tetrahedron **42**, 6263 (1986).

[181] M. S. Robinson, M. L. Polak, V. M. Bierbaum, C. H. Depuy, and W. C. Lineberger, J. Am. Chem. Soc. **117**, 6766 (1995).

[182] J. F. Stanton, E. Garand, J. Kim, T. I. Yacovitch, C. Hock, A. S. Case, E. M. Miller, Y.-J. Lu, K. M. Vogelhuber, S. W. Wren, T. I. Ichino, J. P. Maier, R. J. McMahon, D. L. Osborn, D. M. Neumark, and W. C. Lineberger, J. Chem. Phys. **136**, 134312 (2012).

[183] R. A. Seburg, J. T. DePinto, E. V. Patterson, and R. J. McMahon, J. Am. Chem. Soc. **117**, 835 (1995).

[184] R. A. Seburg, E. V. Patterson, J. F. Stanton, and R. J. McMahon, J. Am. Chem. Soc. **119**, 5847 (1997).

[185] J. P. Maier, G. A. H. Walker, D. A. Bohlender, F. J. Mazzotti, R. Raghunandan, J. Fulara, I. Garkusha, and A. Nagy, Astrophys. J. **726**, 41 (2011).

[186] H. Linnartz, N. Wehres, H. Van Winckel, G. A. H. Walker, D. A. Bohlender, A. G. G. M. Tielens, T. Motylewski, and J. P. Maier, Astron. Astrophys. **511**, L3 (2010).

[187] D. L. Osborn, K. M. Vogelhuber, S. W. Wren, E. M. Miller, Y.-J. Lu, A. S. Case, L. Sheps, R. J. McMahon, L. B. Harding, and W. C. Lineberger, J. Am. Chem. Soc. **in preparation** (2012).

[188] P. Thaddeus, J. M. Vrtilek, and C. A. Gottlieb, Astrophys. J. **299**, L63 (1985).

[189] J. Cernicharo, P. Cox, D. Fosse, and R. Gusten, Astron. and Astrophys. **351**, 341 (1999).

[190] H. Clauberg, D. W. Minsek, and P. Chen, J. Am. Chem. Soc. **114**, 99 (1992).

[191] M. Tulej, F. Guthe, M. V. Pachkov, K. Tikhomirov, R. Xu, M. Jungen, and J. P. Maier, Phys. Chem. Chem. Phys. **3**, 4674 (2001).

[192] R. A. Bernheim, R. J. Kempf, J. V. Gramas, and P. S. Skell, J. Chem. Phys. **43**, 196 (1965).

[193] F. K. Chi, Ph.D. Thesis , Michigan State University (1972).

[194] M. E. Jacox and D. E. Milligan, Chem. Phys. **4**, 45 (1974).

[195] R. A. Seburg, E. V. Patterson, and R. J. McMahon, J. Am. Chem. Soc. **131**, 9442 (2009).

[196] J. A. Miller, J. V. Volponi, and J. F. Pauwels, Combust. Flame **105**, 451 (1996).

[197] J. A. Miller and C. F. Melius, Combust. Flame **91**, 21 (1992).

[198] A. Bhargava and P. R. Westmoreland, Combust. Flame **113**, 333 (1998).

[199] W. Boullart, K. Devriendt, R. Borms, and J. Peeters, J. Phys. Chem. **100**, 998 (1996).

[200] C. A. Taatjes, S. J. Klippenstein, N. Hansen, J. A. Miller, T. A. Cool, J. Wang, M. E. Law, and P. R. Westmoreland, Phys. Chem. Chem. Phys. **7**, 806 (2005).

[201] P. Maksyutenko, F. T. Zhang, X. B. Gu, and R. I. Kaiser, Phys. Chem. Chem. Phys. **13**, 240 (2011).

[202] L. Vereecken and J. Peeters, J. Phys. Chem. A **103**, 5523 (1999).

[203] R. Guadagnini, G. C. Schatz, and S. P. Walch, J. Phys. Chem. A **102**, 5857 (1998).

[204] T. L. Nguyen, A. M. Mebel, S. H. Lin, and R. I. Kaiser, J. Phys. Chem. A **105**, 11549 (2001).

[205] S. P. Walch, J. Chem. Phys. **103**, 7064 (1995).

[206] F. Goulay, A. J. Trevitt, G. Meloni, T. M. Selby, D. L. Osborn, C. A. Taatjes, L. Vereecken, and S. R. Leone, J. Am. Chem. Soc. **131**, 993 (2009).

[207] C. P. Casey, S. Kraft, and D. R. Powell, J. Am. Chem. Soc. **122**, 3771 (2000).

[208] C. P. Casey, S. Kraft, and D. R. Powell, J. Am. Chem. Soc. **124**, 2584 (2002).

[209] A. Padwa, D. J. Austin, Y. Gareau, J. M. Kassir, and S. L. Xu, J. Am. Chem. Soc. **115**, 2637 (1993).

[210] E. C. Hansen and D. S. Lee, Acc. Chem. Res. **39**, 509 (2006).

[211] D. W. Chandler and P. L. Houston, J. Chem. Phys. **86**, 1445 (1987).

[212] A. Eppink and D. H. Parker, Rev. Sci. Instrum. **68**, 3477 (1997).

[213] L. Sheps, E. M. Miller, and W. C. Lineberger, J. Chem. Phys. **131**, 064304 (2009).

[214] W. C. Wiley and I. H. McLaren, Rev. Sci. Instrum. **26** (1955).

[215] K. Yokoyama, G. W. Leach, J. B. Kim, and W. C. Lineberger, J. Chem. Phys. **105**, 10696 (1996).

[216] W. H. Robertson, J. A. Kelley, and M. A. Johnson, Rev. Sci. Instrum. **71**, 4431 (2000).

[217] D. Hanstorp and M. Gustafsson, J. Phys. B **25**, 1773 (1992).

[218] M. J. Frisch, G. W. Trucks, H. B. Schlegel, G. E. Scuseria, M. A. Robb, J. R. Cheeseman, J. A. Montgomery Jr., T. Vreven, K. N. Kudin, J. C. Burant, J. M. Millam, S. S. Iyengar, J. Tomasi, V. Barone, B. Mennucci, M. Cossi, G. Scalmani, N. Rega, G. A. Petersson, H. Nakatsuji, M. Hada, M. Ehara, K. Toyota, R. Fukuda, J. Hasegawa, M. Ishida, T. Nakajima, Y. Honda, O. Kitao, H. Nakai, M. Klene, X. Li, J. E. Knox, H. P. Hratchian, J. B. Cross, V. Bakken, C. Adamo, J. Jaramillo, R. Gomperts, R. E. Stratmann, O. Yazyev, A. J. Austin, R. Cammi, C. Pomelli, J. W. Ochterski, P. Y. Ayala, K. Morokuma, G. A. Voth, P. Salvador, J. J. Dannenberg, V. G. Zakrzewski, S. Dapprich, A. D. Daniels, M. C. Strain, O. Farkas, D. K. Malick, A. D. Rabuck, K. Raghavachari, J. B. Foresman, J. V. Ortiz, Q. Cui, A. G. Baboul, S. Clifford, J. Cioslowski, B. B. Stefanov, G. Liu, A. Liashenko, P. Piskorz, I. Komaromi, R. L. Martin, D. J. Fox, T. Keith, M. A. Al-Laham, C. Y. Peng, A. Nanayakkara, M. Challacombe, P. M. W. Gill, B. Johnson, W. Chen, M. W. Wong, C. Gonzalez, and J. A. Pople, Gaussian 09, Revision A.1, Gaussian, Inc., Wallingford, CT, 2009.

[219] H.-J. Werner, P. J. Knowles, G. Knizia, F. R. Manby, and M. Schütz, MOLPRO, version 2010.1, a package of *ab initio* programs, 2010.

[220] S. Ikuta, J. Chem. Phys. **107**, 4579 (1997).

[221] T. R. Taylor, R. T. Bise, K. R. Asmis, and D. M. Neumark, Chem. Phys. Lett. **301**, 413 (1999).

[222] A. R. W. McKellar, P. R. Bunker, T. J. Sears, K. M. Evenson, R. J. Saykally, and S. R. Langhoff, J. Chem. Phys. **79**, 5251 (1983).

[223] A. R. W. McKellar, P. R. Bunker, T. J. Sears, K. M. Evenson, and S. R. Langhoff, Bull. Soc. Chim. Belg. **92**, 499 (1983).

[224] P. R. Bunker, T. J. Sears, A. R. W. McKellar, K. M. Evenson, and F. J. Lovas, J. Chem. Phys. **79**, 1211 (1983).

[225] G. Herzberg, Proc. R. Soc. London, Ser. A **295**, 106 (1966).

[226] G. V. Hartland, D. Qin, and H.-L. Dai, J. Chem. Phys. **102**, 6641 (1995).

[227] P. C. Engelking, R. R. Corderman, J. J. Wendoloski, G. B. Ellison, S. V. Oneil, and W. C. Lineberger, J. Chem. Phys. **74**, 5460 (1981).